A VARIATIONAL FRAMEWORK FOR MATHEMATICALLY NONSMOOTH PROBLEMS IN SOLID AND STRUCTURE MECHANICS

BY

PINLEI CHEN

DISSERTATION

Submitted in partial fulfillment of the requirements
for the degree of Doctor of Philosophy in Civil Engineering
in the Graduate College of the
University of Illinois at Urbana-Champaign, 2018

Urbana, Illinois

Doctoral Committee:

Professor Arif Masud, Chair and Director of Research
Professor C. Armando Duarte
Associate Professor Oscar Lopez-Pamies
Professor Philippe H. Geubelle

ABSTRACT

This dissertation presents a new paradigm for addressing multi-physics problems with interfaces in the field of Additive Manufacturing and the modeling of fibrous composite materials. The unique process of adding the material layer by layer in the AM techniques raises the issue about the stability of the interfaces between the layers and along the boundaries of multi-constituent materials. A stabilized interface formulation is developed to model debonding in monotonic loading, fatigue effects in cyclic loading, and thermal effects at interfaces which severely impact the functional life of those materials and structures.

The formulation is based on embedding Discontinuous Galkerin (DG) ideas in a Continuous Galerkin (CG) framework. Starting from a mixed method incorporating the Lagrange multiplier along the interface, a pure displacement formulation is derived using the Variational Multiscale Method (VMS). From a mathematical and computational perspective, the key factor influencing the accuracy and robustness of the interface formulation is the design of the numerical flux and the penalty or stability terms. Analytical expressions that are free from user-defined parameters are naturally derived for the numerical flux and stability tensor which are functions of the evolving geometric and material nonlinearity. The proposed framework is extended for debonding at finite strains across general bimaterial interfaces. An interfacial gap function is introduced that evolves subject to constraints imposed by opening and/or sliding interfaces. An internal variable formalism is derived together with the notion of irreversibility of damage results in a set of evolution equations for the gap function that seamlessly tracks interface debonding by treating damage and friction in a unified way. Tension debonding, compression damage, and frictional sliding are accommodated, and return mapping algorithms in the presence of evolving strong discontinuities are developed. This derivation variationally embeds the interfacial kinematic models that are crucial to capturing the physical and mathematical properties involving large strains and damage. The framework is extended for monolithic coupling of thermomechanical fields in the class of problems that have embedded weak and strong discontinuities in the mechanical and thermal fields. Since the derived expressions are a function of the mechanical and thermal fields, the resulting stabilized formulation contains numerical flux and stability tensors that provide an avenue to variationally embed interfacial kinetic and kinematic models for more robust

representation of interfacial physics.

Representative numerical tests involving large strains and rotations, damage phenomena, and thermal effects are performed to confirm the robustness and accuracy of the method. Comparison of the results with both experimental and numerical results from literature are presented.

ACKNOWLEDGEMENTS

First, I would like to say that I am especially indebted to my advisor, Professor Arif Masud, who has actively provided me with all the useful advice during my Ph.D. thesis and has been extensively supportive of my career goals. I am grateful to him for his patience and all the opportunities I was given to conduct my research at UIUC. Without his guidance and persistent help, this dissertation would not have been possible.

In addition, I would want to thank Professor Timothy Truster for his insight during the early stage of my Ph.D. work and providing me a good platform to build my own research topics. I also want to express my gratitude to each of my committee members: Professor Armando Duarte, Professor Oscar Lopez, and Professor Philippe Geubelle who have given me helpful comments and support.

I also want to thank the campus cluster from Computational Science and Engineering Program which enables me to run large scale problems in the parallel computing system. These numerical simulations became parts of my thesis dissertation.

I am grateful to all of those with whom I have had the pleasure to work and discuss with during my Ph.D. thesis: Dr. Timothy Truster, Dr. Harishanker Gajendran, Dr. JaeHyuk Kwack, Lixing Zhu, Marcelino Anguiano, Soonpil Kang, Ahmad Al-Naseem, Ignasius Pradipta Anugraha and my other colleagues for providing a vibrant and friendly environment for my growth in academia.

At last, I would like to thank my parents, whose love are with me in whatever I pursue. Most importantly, I wish to thank my love husband, Chenyi Pan for great support and advice throughout my years of study.

TABLE OF CONTENTS

CHAPTER 1: INTRODUCTION

1.1 Motivation

The rapid development of Additive Manufacturing (AM) has marked a departure from the traditional process of making three-dimensional (3D) objects, but what is not clear is the reliability of using AM technique especially in civil infrastructure undergoes extreme environmental loadings. While adding materials layer by layer is simple, one of the major impediment to the AM technique is the lack of knowledge about the reliability of the 3D produces. Questions have been raised about the stability of the interfaces between the layers. Broad applications are limited by a systematic understanding of how stable these 3D products are under various loading conditions.

The interfaces also exist in other physical applications, such as interphases boundaries of multi-constituents, welded steel tubular joints, and interfaces between bone and tissue in biomechanics. Failure modes such as debonding in monotonic loading and fatigue effects in cyclic loading along with thermal and chemical reactions at the interfaces severely impact the functional life of the structure. Because of the complex geometry and wide range of material applications, it is crucial to have a robust and consistent framework which can accurately represent the interface continuity conditions and track the debonding phenomena. To this end, these underlying features lead to a method with embedded damage feature in finite strain range with consistently evolving stabilization which will have various applications in mechanical, aerospace and civil engineering.

This dissertation seeks to establish a variationally consistent interface framework with evolving weak and strong discontinuities. To address the major concerns influencing the accuracy and robustness of the interfacial physics, accurate representation of the interface continuity conditions are consistently derived. These derived formulations are functions of the evolving material and geometry without user-defined variables. The framework is extended to incorporate damage and debonding phenomena by seamlessly tracking different damage kinematics in a unified way, and further enhanced by adding the thermal effects to demonstrate monolithic coupling of thermomechanical fields for problems that have embedded weak and strong discontinuities in the mechanical and thermal fields.

Recent developments in additive manufacturing have heightened the need for the accurate modeling of the interfacial behavior of the 3D manufactured objects such as debonding which

results in local failure. To incorporate damage phenomena, one of the most significant challenges is developing a stabilized and consistently driven framework that imposing displacement and traction continuity conditions. Many researchers have studied the methods of enforcing the interface continuity. Methods such as that developed in [80] are called Lagrange multiplier method, for which the unknown field is solved together with the newly introduced Lagrange multipliers. Similar to the incompressible elasticity or fluid flow problem, this method needs to fulfill the inf-sup condition [28,86] which necessitates different choices of the function spaces. Later, a modified Lagrange multiplier method which is named as mortar method [23] is proposed where an optimal approximation space is used for the multipliers. Series versions of the mortar methods have been proposed for contact problems in [105] considering two-dimensional (2D) linear kinematics and three-dimensional (3D) problems [131] within the context of large deformation. Although the Lagrange multiplier method has the advantage of easily establishing a global system to solve for, and has shown many applications, inf-sup conditions need to be satisfied. For problems of a very fine mesh overlays a coarse mesh, oscillations of the multiplier fields or mesh locking may occur which affect the overall accuracy and the rates of convergence [140].

Another method to avoid satisfying the inf-sup condition (LBB condition) is by using stabilization techniques. A good review of the stabilized methods is provided in [90] and the range of application of stabilized methods in fluids, solids, electronic structure modeling, and probabilistic mechanics is presented in [55,92,93,95,99,101,128]. This thesis pushes the envelope of stabilized methods to finite deformation nonlinear problems with weak and strong discontinuities. The notion of stabilization is employed in stabilized Lagrange multiplier method [11,15] and Discontinuous Galerkin (DG) type methods such as Nitsche's methods originally proposed in [120] which is used to weakly enforce the Dirichlet boundary conditions. This method is further extended for weak enforcement of interface continuity in [20,140] where the Lagrange multipliers are replaced via a physical representation of the primal variables, and a penalty type term is added. A close relation between the stabilized Lagrange multiplier method and Nitsche's method is discussed in [151] for problems with the weakly enforced essential boundary conditions. In the field of solid mechanics, DG type method such as the so-called Nitsche's method has been applied to incompressible elasticity [60], elliptic interface problems [58,61], linear elasticity [140] and nonlinear elasticity [107,53,122]. A detailed summary of the DG type methods for second order elliptic problems is discussed by Arnold et al. [1]. In recent years, Wang and coworkers [168, 167, 114] have developed

a weak Galerkin finite element method (WG-FEM) where a discrete weak gradient operator is introduced to replace the classical gradient operator. For interface problem, starting from the mixed formulation with the Lagrange multiplier field, WG-FEM enforces only weak continuity of variables via the discrete weak operators [113], and a parameter-free stabilized method is developed [114]. The idea of using WG-FEM for interface problem is similar as in hybridized discontinuous Galerkin (HDG) method [41,71] for solving elliptic interface problems where the global degree of freedom is reduced compared to the local discontinuous Galerkin (LDG) method [32] but replacing the gradient operator with the weak one. Although these types of DG methods have shown excellent performance in many applications in both solid and fluid mechanics, the mechanism by which the penalty parameter and numerical flux terms are systematically chosen has not been established. Studies show that these terms are functions of geometric weighting [58] and material weighting [140] which are treated either via simplified mesh scaling factors or user-defined parameters that are calibrated for particular numerical test cases. Several attempts have been made to study these parameters, such as using eigenvalue analysis given in [49,57] for linear problems, or an adaptive stabilization mechanism in [51] for nonlinear problems. Researchers [51,52] have shown that prescribing a value a priori may not lead to a robust method, especially when the simulated response involves large deformation or material instability. When extended to nonlinear elasticity at finite strains, the rubout and accuracy of the DG methods are highly dependent on the correct design of the biasing in numerical flux term and the penalty or stabilization parameters.

In addition to using DG and stabilized formulations to impose the interface displacement continuity in a weak sense, a natural extension is to allow jumps or discontinuities in both deformation map and the gradient of the deformation map [107]. To model the interfacial debonding or gaps, the cohesive zone method (CZM) is commonly used. This method is proposed initially by Barenblatt [16] and Dugdale [46] to model the evolution of crack in nonlinear fracture mechanics in solids and further extended by Needleman [115] and Hillerborg [65]. To date, the cohesive zone method can be separated into two different types: intrinsic cohesive zone method [25,49,82] and extrinsic cohesive zone method [107,85,175]. While the former one contains initial hardening portion in the traction-gap relation, this technique brings an additional elastic stiffness to the system that upsets the consistency of the discrete model and causes oscillation in dynamic simulations [25]. The extrinsic cohesive zone method, however, avoids the so-called artificial

compliance and enables the natural insertion of cracks [169]. However, in the meantime, additional issues arise with implementing the procedure and interpreting the results [175]. Another limitation of the CZM method is the needs for a conforming mesh [174]. Succeeding researchers [169] suggest using the extended finite element method (XFEM) [1,109,153] to arbitrary insert strong discontinuities using Heaviside functions as the enrichment functions and to enable the failure grows inside elements based on the partition of unity concept. This method, however, introduces additional global degrees of freedom to capture the discontinuities. Another method for tracing the interface failure is called hybrid DG method, or DG/CZM method [106,119,142,172] where DG method is used for the pre-failure process with weak discontinuity and CZM method is used for the post-failure process with strong discontinuity. This specific switch is achieved via the change of the underlying mathematical formulation through the existence of an embedded parameter result in a formulation where consistency is not maintained throughout.

Another important class of problems for interface damage is the failure due to fatigue effects under cyclic loadings. Classical numerical approaches to model fatigue effects have divided into two categories: Continuous damage mechanical (CDM) and discretization method. The initial work of CDM idea is introduced by Kachanov [74] for studying creep. Lemaitre [81] and Chaboche [35,36] have further extended the CDM idea to provide a better life prediction with different damage growth models, such as fatigue, creep, and creep-fatigue. Although this method is thermodynamically consistent and can provide a good approximation of different types of fatigue, such as low cycle fatigue [34,24], high cycle fatigue [166], the detailed cracked information at crack tips or crack surfaces is difficult to achieve. Later, other researchers adopted the cohesive zone method (CZM) to model the fatigue effects by introducing a cohesive law with unloading and reloading hysteresis [117], and works have been shown for the ability to predict the fatigue crack growth and life [136,143].

To keep the framework complete, the thermal field coupled with the mechanical field within the DG context is another important issue to be addressed. In recent years, the coupled thermomechanical problems with no interface elements have been studied by many researchers on topics including developing staggered algorithms by Armero and Simo [6], Rieger and Wriggers [135], Romero [137] and Martins et al. [88]. While the staggered algorithms are easy to implement and cost-effective, specific treatments of the splitting strategy need to be analyzed and implemented. For problems with interfaces, how to decompose the system of equations remains a

question.

In this dissertation, we first propose a linear version of stabilized mixed Discontinuous Galerkin (DG) method is presented for monolithic coupling of thermomechanical fields in the class of problems that have embedded discontinuities in both mechanical and thermal fields. A Variational multiscale method (VMS) based interface formulation at finite strains is developed from the underlying Lagrange multiplier method. The derivation depends on the key feature in the VMS approach [68,69] where the total solution field is decomposed into coarse and fine scales. The VMS method has been applied in both fluid and solid mechanical problems, such as advection-diffusion equation [94], incompressible fluid flow [92], and incompressible elasticity [101, 102]. The method is also capable of measuring the error in the numerical simulations [99,101] which do not have exact solutions. In the application of interface problem in particular, by representing the fine scales via edge bubble functions, the primal interface formulation is systematically derived. In particular, these derived quantities naturally account for the evolving geometric nonlinearity as well as discontinuous material properties. This method handles problems with nonfoaming meshes, with different element types, with fully discontinuities within specified or every element boundary, and with problems with different material types.

Subsequently, an inelastic gap function is introduced to model the damage or debonding along multi-material interfaces. This inelastic gap and its corresponding interface traction are treated as a strain-like variable which is tracked at each integration point by adopting the idea from [146]. Similar ideas have been adopted by Annavarapu and coworkers [1] for frictional sliding problems. Various nonlinear interfacial debonding models are variationally embedded at interfacial boundaries. Specifically, the combination of damage and friction along the debonding surface is easily accommodated by borrowing concepts from multi-surface plasticity [146]. Also, rate dependency and other advanced phenomena can be more easily treated in the present framework. This method avoids using the intrinsic cohesive elements which will introduce artificial elastic interface stiffness that affects the consistency. With the fine-scale model evolves with the material and geometric nonlinearity exhibited in the vicinity of the interface, the algorithmic interface parameters are updated accordingly with the evolution of the nonlinear problems. This proposed method is applied to model practical problems such as damage phenomena in fibrous composites or tearing of soft materials out of hard materials.

Lastly, a novel stabilized interface formulation with a fully coupled thermomechanical problem to overcome the issues with the staggered algorithm. The systems of balance equations are solved in a fully coupled fashion. Starting from the Lagrange multiplier method to enforce the temperature and displacement continuity across the embedded interfaces, a fully coupled system of stabilized interface formulations is developed by employing the ideas from VMS based stabilization. The idea follows the same line of thoughts as for primal interface formulation for a pure mechanical problem such that the naturally derived expressions for both mechanical and thermal fields are free of any ad hoc or user-defined parameters.

1.2 Dissertation outline

The stabilized framework to solve mathematically non-smooth problems at finite strains and the thermomechanical coupled problems is developed in the following chapters:

In Chapter 2, a stabilized mixed Discontinuous Galerkin (DG) method is presented for monolithic coupling of thermomechanical fields to address problems with discontinuities. Starting from a thermo-mechanically coupled formulation, the Lagrange multiplier method is used to constrain the interface continuities for both thermal and mechanical fields. VMS method is used to convert the mixed interface formulations with Lagrange multipliers into two primal interface formulations. The interfacial fine scales are expanded via edge bubbles and are resolved locally to extract analytical models for Lagrange multipliers in terms of the jumps in the fields and their fluxes. Several benchmark problems within one-dimension (1D) and two-dimension (2D) are presented to show stability and variational consistency of the method.

In Chapter 3, a framework that accommodates nonconforming finite element meshes and large deformation and rotation is proposed. A stabilized Discontinuous Galerkin method is developed for general hyperelastic materials at finite strains. Starting from a mixed method incorporating Lagrange multipliers along the interface, the displacement formulation is systematically derived through a Variational Multiscale (VMS) approach whereby the numerical fine scales are modeled via edge bubble functions. This pure displacement formulation contains the area and stress weighting terms along with the stability tensors which account for geometric and material nonlinearities. Representative numerical tests involving large strains and rotations are performed to confirm the robustness of the method.

Following the previous work done in Chapter 3, the damage model is embedded into the DG framework in Chapter 4. The specific objective of this Chapter is to accurately model the transition between the bonded area and the unbonded area. By releasing the constraint of the continuity at the interface, an inelastic gap function is employed to model the damage or separation of the interface. In the present method, the combination of damage and friction along the debonding surfaces was easily accommodated by borrowing concepts from multi-surface inelasticity. Thus, the proposed method provides a general framework to incorporate friction, rate-dependency, and softening, as desired. Simulations of tensile and compressive debonding tests show the robustness of the method. In a subsequent study, we simulated a fiber-matrix debonding test and a fiber pushout test and compared the results against the experimental data and other numerical tests to show the robustness and accuracy.

In Chapter 5, we present a framework to simulate the interface fatigue growth which is developed from the interface damage model presented earlier. When studying the strength of materials with weak interfaces, the weakness of the interphase cohesion between two or more constituents, especially due to fatigue effects under cyclic loadings, is one of the leading cause of structural failure. As our interface damage model is based on inelasticity theory, it is a new hysteretic damage model different than the traditional cohesive zone model. Low-cycle fatigue effects are accommodated, and the fatigue behavior of steel materials is investigated. By comparing the computational results with both the numerical and experimental results, we validate the proposed framework.

In Chapter 6, the framework is extended to Multiphysics regime at finite strains. Thermal and mechanical properties are assumed to vary sharply across embedded interfaces giving rise to weak discontinuities in the computed field. The new interface coupling framework is developed by embedding Discontinuous Galerkin (DG) ideas in the Continuous Galerkin (CG) method within the context of Variational Multiscale (VMS) framework. Starting from a thermomechanically coupled formulation over the elastic domain, a Lagrange multiplier method is developed that couples fields along the interfaces. The interfacial fine-scale problem facilitated by VMS framework is expanded via edge bubbles and resolved locally to extract analytical expressions for Lagrange multipliers. The derived terms for interfacial stabilization are a function of the residual of Euler-Lagrange equations along the embedded interface. Stabilization tensors are functions of the evolving mechanical and thermal fields and therefore free of user-defined parameters. A

significant contribution of the method is that evolution of interfacial kinematics is easily handled via embedding phenomenological models along the embedded interfaces. Several test cases show the to illustrate its versatility and applicability of the method.

In Chapter 7, concluding remarks and significant contribution of this thesis dissertation and future work directions are presented. The future research directions include extending the current computational framework for modeling incompressible materials, merging the DG formulation with a homogenized model. Simulation-based material modeling for additively manufactured civil infrastructure under extreme loading conditions, and application with thermal and chemical reactions are also presented.

CHAPTER 2: A FULLY COUPLED THERMOMECHANICAL INTERFACE FORMULATION WITH A CONSISTENTLY EVOLVING STABILIZATION THROUGH VARIATIONAL MULTISCALE METHOD

2.1 Introduction

DG frameworks [5,17,25,29,31,51,60,70,106,140] provide the platform to develop advanced numerical methods where interfacial terms provide an avenue to embed kinetic and kinematic models. Classically the coupled thermomechanical methods have been proposed in the context of continuous Galerkin methods. The emphasis in these works [135,144,162,139,138,108] has been on the development of coupled solution algorithms that are based on underlying operator splitting methodology which leads to staggered solution schemes. Staggered algorithms are invariably first order accurate, and developing second order accurate staggered algorithms is not straightforward. The work by Armero and Simo [6] is based on continuous Galerkin method and it presents fractional step methods for thermomechanical problems. Two strategies, termed as (i) isothermal split, and (ii) adiabatic split are presented. With a smart implementation strategy proposed in Chapter 2, the adiabatic method attains second order accuracy under certain conditions. In the work of Miche [108], these methods are extended to finite strain thermoelasticity. Relatively recently, several works have appeared in the literature that address this important class of problem [139,138,108].

This Chapter presents a novel stabilized method for coupled field problem of thermoelasticity. The objective of this work has been to develop a monolithic method where all fields are resolved in a fully coupled fashion and therefore higher order accurate numerical solution algorithms can be proposed. The emphasis throughout has been that the resulting coupled formulation accommodates weak and strong discontinuities embedded in the interior of the domain. Starting from a thermo-mechanically coupled formulation, a Lagrange multiplier method along the interface is developed. Employing ideas for VMS based stabilization, the interfacial fine-scale problem is expended via edge bubbles and resolved locally to extract an analytical expression for Lagrange multipliers. The derived expression is a function of evolving mechanical and thermal fields and therefore the derived stabilized formulation contains the numerical flux and stability tensor which are free from user-defined parameters.

We start with the governing system of equations for small strain linear thermoelasticity, and employ the notion of discontinuity of the spatial functions across embedded interfaces. Calls for the coupling terms to enforce the continuum requirements of the continuity of the fields and their fluxes across these interfaces. In the context of thermomechanical problems, we need to enforce the continuity of displacement and stress for the mechanical fields and continuity of temperature and its flux for the thermal field. Although DG methods that are based on Lagrange multipliers [26,61] have been proposed to enforce this continuity, they lack the provision for the development of strong discontinuities which is an important mode of deformation that represent a mechanical failure of the physical system. Our objective is to develop analytical models for Lagrange multipliers in terms of the underlying fields so that interfacial kinetic and kinematic models can be embedded at the interfaces.

An outline of the Chapter is as follows: section 2.2 presents the governing equations for fully coupled thermomechanics. Section 2.3 presents the stabilized interface formulation of both the thermal and mechanical sub-problems. The derivation of the system matrices for the 1-D case is presented in section 2.4. Several benchmark problems within one dimension (1D) and two-dimension (2D) are presented to show stability and variational consistency of the method are shown in section 2.5, and conclusions are drawn in section 2.6.

2.2 Governing Equations and Mixed Interfacial Weak Form

The Lagrangian form of balance of momentum, the balance of energy, the interface continuity equations, boundary conditions and initial conditions are presented below. For the sake of simplicity and in the interest of ease of presentation of the main ideas we limit our discussion to quasi-static thermoelasticity. Throughout, we denote quantities with counterparts in both regions by a superscript (α), where α takes the value 1 or 2.

Balance of momentum and balance of energy:

$$\operatorname{div}\left[\boldsymbol{\sigma}^{(\alpha)}\right]+\rho\boldsymbol{b}^{(\alpha)}=\mathbf{0} \qquad \text{in} \quad \Omega^{(\alpha)}\times]0,\mathrm{T}[\quad \alpha=1,2 \tag{2-1}$$

$$\rho^{(\alpha)}c_p{}^{(\alpha)}\dot{\theta}^{(\alpha)}=-\operatorname{div}\left(\boldsymbol{q}^{(\alpha)}\right)-\boldsymbol{m}^{(\alpha)}:\nabla\boldsymbol{v}^{(\alpha)}+\overline{r}^{(\alpha)} \qquad \text{in} \quad \Omega^{(\alpha)}\times]0,\mathrm{T}[\quad \alpha=1,2 \tag{2-2}$$

Interface continuity equations:

$$\boldsymbol{u}^{(1)}-\boldsymbol{u}^{(2)}=[\![\boldsymbol{u}]\!]=\mathbf{0} \qquad \text{on} \quad \Gamma_{\mathrm{I}} \tag{2-3}$$

$$\theta^{(1)}-\theta^{(2)}=[\![\theta]\!]=0 \qquad \text{on} \quad \Gamma_{\mathrm{I}} \tag{2-4}$$

$$\boldsymbol{\sigma}^{(1)} \cdot \boldsymbol{n}^{(1)} - \boldsymbol{\lambda}_1 = \mathbf{0} \qquad \text{on } \Gamma_{\mathrm{I}} \tag{2-5}$$

$$\boldsymbol{\sigma}^{(2)} \cdot \boldsymbol{n}^{(2)} + \boldsymbol{\lambda}_1 = \mathbf{0} \qquad \text{on } \Gamma_{\mathrm{I}} \tag{2-6}$$

$$-\boldsymbol{q}^{(1)} \cdot \boldsymbol{n}^{(1)} - \lambda_2 = \mathbf{0} \qquad \text{on } \Gamma_{\mathrm{I}} \tag{2-7}$$

$$-\boldsymbol{q}^{(2)} \cdot \boldsymbol{n}^{(2)} + \lambda_2 = \mathbf{0} \qquad \text{on } \Gamma_{\mathrm{I}} \tag{2-8}$$

Dirichlet and Neumann boundary conditions:

$$\boldsymbol{u}^{(\alpha)} = \overline{\boldsymbol{u}}^{(\alpha)}\left(\boldsymbol{x}, t\right) \qquad \text{on } \Gamma_{\mathrm{g}}^{(\alpha)} \times]0, \mathrm{T}[\tag{2-9}$$

$$\theta^{(\alpha)} = \overline{\theta}^{(\alpha)}\left(\boldsymbol{x}, t\right) \qquad \text{on } \Gamma_{\mathrm{g}}^{(\alpha)} \times]0, \mathrm{T}[\tag{2-10}$$

$$\boldsymbol{\sigma}^{(\alpha)} \cdot \boldsymbol{n}^{(\alpha)} = \overline{\boldsymbol{t}}^{(\alpha)}\left(\boldsymbol{x}, t\right) \qquad \text{on } \Gamma_{\mathrm{h}}^{(\alpha)} \times]0, \mathrm{T}[\tag{2-11}$$

$$\boldsymbol{q}^{(\alpha)} \cdot \boldsymbol{n}^{(\alpha)} = \overline{q}^{(\alpha)}\left(\boldsymbol{x}, t\right) \qquad \text{on } \Gamma_{\mathrm{h}}^{(\alpha)} \times]0, \mathrm{T}[\tag{2-12}$$

The stress tensor $\left[\boldsymbol{\sigma}^{(\alpha)}\right]$ is obtained from the internal energy e by employing the usual hyperelastic relations. To keep the presentation simple, we assume a linear thermomechanical internal energy function that yields the Cauchy stress $\left[\boldsymbol{\sigma}^{(\alpha)}\right] = \dfrac{\partial e}{\partial \boldsymbol{\varepsilon}} = \boldsymbol{\sigma}^{(\alpha)} - \boldsymbol{m}^{(a)}\theta^{(a)} = \mathbb{C}^{(a)} : \boldsymbol{\varepsilon}^{(a)} - \boldsymbol{m}^{(a)}\theta^{(a)}$. Eqn.(2-1) gets embedded with this thermomechanical stress tensor. In the balance of momentum and energy equations, $\theta^{(a)} = T^{(\alpha)} - T_{\mathrm{ref}}^{(\alpha)}$ is the change of the temperature with respect to the reference temperature $T_{\mathrm{ref}}^{(\alpha)}$. In Eqn. (2-2), $c_p^{(\alpha)}$ is the specific heat, $\boldsymbol{m}^{(\alpha)}$ is a second-order structural tensor coupling thermal and mechanical parts, $\boldsymbol{b}^{(\alpha)}$ is the mass-specific body force, $\rho^{(\alpha)} > 0$ is the referential mass density, $\mathrm{div}\left(\bullet\right) = \mathrm{tr}\left[\mathrm{grad}\left(\bullet\right)\right]$ is the material divergence operator, $\boldsymbol{n}^{(\alpha)}$ is the unit outward normal to the interface boundary Γ_{I} as well as to the Neumann boundary Γ_{h}, and $\overline{r}$ is the heat resource, and $\boldsymbol{n}^{(1)} = -\boldsymbol{n}^{(2)}$.

At this point, we assume that the system obeys the Fourier's law for heat conduction to ensure the satisfaction of the Clausius-Duhem inequality. The heat flux or thermal flux term is taken to be:

$$\boldsymbol{q}^{(\alpha)} = -\overline{\boldsymbol{k}}^{(\alpha)} \nabla \theta^{(\alpha)} \tag{2-13}$$

where $\overline{\boldsymbol{k}} = k_\theta \mathbf{I}$ is the thermal conductivity tensor and coefficient k_θ is taken of the form:

$$k_\theta(\theta) = k_0(\theta_{\text{ref}})\left[1 - \omega_k(\theta - \theta_{\text{ref}})\right] \tag{2-14}$$

where $k_0(\theta_{\text{ref}})$ is the thermal conductivity at $T = \theta_{\text{ref}}$ and ω_k is the softening parameter. In this Chapter, we assume $\omega_k = 0$.

The thermomechanical coupling tensor is of the form $\boldsymbol{m} = m\mathbf{I}$, where $m = 3\kappa\beta$. $\kappa = \lambda + \frac{2}{3}\mu$ is the bulk modulus and β is the coefficient of thermal expansion [6].

Eqn. (2-3) constrains the continuity of the displacement field while Eqn. (2-4) constrains the continuity of the temperature field over the two adjoining sub-domains. The Lagrange multipliers $\boldsymbol{\lambda}_1$ and λ_2 are introduced to enforce the equilibrium of tractions and the equilibrium of heat flux across the interface Γ_{I}. The traction terms are only operational when the two subdomains are in contact at Γ_{I}. Once fully debonded, the traction terms vanish automatically and uniformly. We specify the functional spaces as follows:

$$\mathcal{S}_u^{(\alpha)} = \left\{ \boldsymbol{u}^{(\alpha)} \,\middle|\, \boldsymbol{u}^{(\alpha)} \in \left[H^1\left(\Omega^{(\alpha)}\right) \right]^{n_{\text{sd}}} \right\} \tag{2-15}$$

$$\mathcal{S}_\theta^{(\alpha)} = \left\{ \theta^{(\alpha)} \,\middle|\, \theta^{(\alpha)} \in \left[H^1\left(\Omega^{(\alpha)}\right) \right]^{n_{\text{sd}}} \right\} \tag{2-16}$$

$$\mathcal{V}_\phi^{(\alpha)} = \left\{ \boldsymbol{\eta}^{(\alpha)} \,\middle|\, \boldsymbol{\eta}^{(\alpha)} \in \left[H_o^1\left(\Omega^{(\alpha)}\right) \right]^{n_{\text{sd}}},\ \boldsymbol{\eta}^{(\alpha)}\big|_{\Gamma^{(\alpha)} \setminus \Gamma_{\text{I}}} = \mathbf{0} \right\} \tag{2-17}$$

$$\mathcal{V}_\theta^{(\alpha)} = \left\{ \omega^{(\alpha)} \,\middle|\, \omega^{(\alpha)} \in \left[H_o^1\left(\Omega^{(\alpha)}\right) \right],\ \omega^{(\alpha)}\big|_{\Gamma^{(\alpha)} \setminus \Gamma_{\text{I}}} = 0 \right\} \tag{2-18}$$

$$\mathcal{Q} = \left\{ \boldsymbol{\lambda}_\alpha \,\middle|\, \boldsymbol{\lambda}_\alpha \in \left[H^{-\frac{1}{2}}\left(\Gamma_{\text{I}}\right) \right]^{n_{\text{sd}}} \right\} \tag{2-19}$$

The associated weak form is derived via standard procedures. A formal statement is: Find $\left\{ \boldsymbol{u}^{(\alpha)}, \theta^{(\alpha)}, \boldsymbol{\lambda}_\alpha \right\} \in \mathcal{S}_\phi^{(\alpha)} \times \mathcal{S}_\theta^{(\alpha)} \times \mathcal{Q}$ such that for all $\left\{ \boldsymbol{\eta}^{(\alpha)}, \omega^{(\alpha)} \right\} \in \mathcal{V}_\phi^{(\alpha)} \times \mathcal{V}_\theta^{(\alpha)}$, the following equations are satisfied:

Weak form of balance of momentum

$$\begin{aligned} &\sum_{\alpha=1}^{2} \int_{\Omega^{(\alpha)}} \left[\operatorname{div} \boldsymbol{\eta}^{(\alpha)} \cdot \left(\mathbb{C}^{(a)} : \boldsymbol{\varepsilon}^{(a)} - \boldsymbol{m}^{(\alpha)} \theta^{(\alpha)} \right) - \rho \boldsymbol{b}^{(\alpha)} \cdot \boldsymbol{\eta}^{(\alpha)} \right] \mathrm{d}V \\ &- \sum_{\alpha=1}^{2} \int_{\Gamma_{\text{h}}} \overline{\boldsymbol{t}}^{(\alpha)} \cdot \boldsymbol{\eta}^{(\alpha)} \mathrm{d}\Gamma_{\text{h}} - \int_{\Gamma_{\text{I}}} \boldsymbol{\lambda}_1 \cdot [\![\boldsymbol{\eta}]\!] \, \mathrm{d}\Gamma_{\text{I}} = 0 \end{aligned} \tag{2-20}$$

Continuity equation for displacement

$$-\int_{\Gamma_I} \boldsymbol{\mu}_1 \cdot \left([\![\boldsymbol{u}]\!] \right) \mathrm{d}\Gamma_I = 0 \tag{2-21}$$

Balance of energy

$$\sum_{\alpha=1}^{2} \int_{\Omega^{(\alpha)}} \left[\overline{c} \dot{\theta}^{(\alpha)} \cdot \omega^{(\alpha)} + \mathrm{div}\, \omega^{(\alpha)} \cdot \left(\overline{\boldsymbol{k}}^{(\alpha)} \nabla \theta^{(\alpha)} \right) + \left(\boldsymbol{m}^{(\alpha)} : \nabla \boldsymbol{v}^{(\alpha)} \right) \cdot \omega^{(\alpha)} - \overline{r}^{(\alpha)} \cdot \omega^{(\alpha)} \right] \mathrm{d}V + \sum_{\alpha=1}^{2} \int_{\Gamma_h} \overline{q}^{(\alpha)} \cdot \omega^{(\alpha)} \, \mathrm{d}\Gamma_h - \underbrace{\int_{\Gamma_I} \lambda_2 \cdot [\![\omega]\!] \, \mathrm{d}\Gamma_I}_{\text{heat flux cont.}} = 0 \tag{2-22}$$

Continuity equation for temperature

$$\underbrace{-\int_{\Gamma_I} \mu_2 \cdot \left([\![\theta]\!] \right) \mathrm{d}\Gamma_I}_{\text{temperature cont.}} = 0 \tag{2-23}$$

where $\overline{\boldsymbol{t}} = \boldsymbol{\sigma} \cdot \boldsymbol{n}$ is the traction and $\overline{q} = \boldsymbol{q} \cdot \boldsymbol{n}$ is heat flux at boundaries Γ_h. We define $\overline{c} = \rho^{(\alpha)} c_p{}^{(\alpha)}$ as the volumetric heat capacity [6]. As mentioned earlier, the Lagrange multiplier field $\boldsymbol{\lambda}_1$ in (2-20) has the connotation of the traction field on Γ_I [9]. In this section, we introduce another unknown Lagrange multiplier field λ_2 which has the connotation of the heat flux field on Γ_I. Eqn. (2-21) and (2-23) weakly enforce the jump continuity where $[\![\bullet]\!] = (\bullet)^{(1)} - (\bullet)^{(2)}$ is the jump operator defined for vector-valued fields on the interface Γ_I. Although this definition depends on the ordering of the domains as in [70], the final weak form is independent of sub-domain ordering.

In the following sections, we focus on the development of the stabilized interface thermal formulations (2-22) and (2-23). Since stabilization of the mechanical field is presented in [100,162], in this work we focus our attention primarily on the thermal problem. Interested reader is referred to [162] for the more detailed derivation of the stabilized interfacial mechanical formulation.

Remark: *This system involves two unknown fields to be solved for: temperature for the thermal problem and displacement for the mechanical problem.*

Remark: *In section 2.3.2 we bring together thermal and mechanical problems and present the combined thermomechanical stabilized interface formulation.*

2.3 Multiscale Decomposition and Stabilized Interface Formulation

A stabilized method for convective-diffusive heat transfer was proposed in Ayub and Masud [10] that was based on the notion of the additive split of the underlying temperature field and its flux.

The formulation was shown to be stable and convergent for a variety of interpolation polynomials for the temperature and flux fields. In this work we focus on the temperature field alone, and employing VMS ideas, develop a stabilized method.

The multiscale decomposition for the temperature field is shown in Figure 2.1 where we assume that the total solution is an additive combination of the coarse scale solution $\hat{\theta}$ and the fine scale solution $\tilde{\theta}$.

$$\theta^{(\alpha)} = \hat{\theta}^{(\alpha)} + \tilde{\theta}^{(\alpha)} \tag{2-24}$$

We also apply the same additive decomposition to the weighing function ω:

$$\omega^{(\alpha)} = \hat{\omega}^{(\alpha)} + \tilde{\omega}^{(\alpha)} \tag{2-25}$$

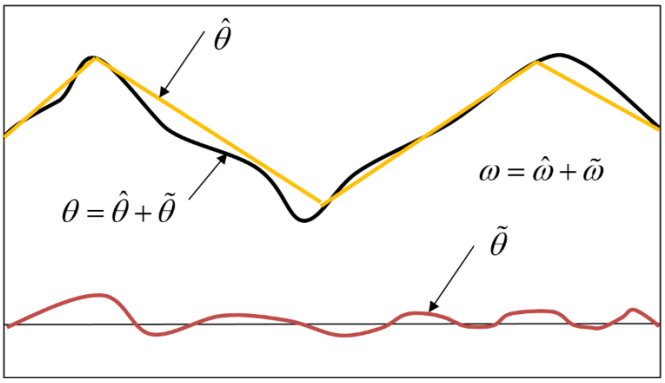

Figure 2.1. Additive decomposition of the temperature trial solution and the weighting function.

The decomposition of the displacement field can be found in [100]. Following the same idea, the additive decomposition of the mechanical trial solution and its corresponding weighting function can be represented as

$$\boldsymbol{u}^{(\alpha)} = \hat{\boldsymbol{u}}^{(\alpha)} + \tilde{\boldsymbol{u}}^{(\alpha)} \tag{2-26}$$

$$\boldsymbol{\eta}^{(\alpha)} = \tilde{\boldsymbol{\eta}}^{(\alpha)} + \hat{\boldsymbol{\eta}}^{(\alpha)} \tag{2-27}$$

Accordingly, the weak forms (2-20)-(2-23) can be separated into following multiscale interface problems.

Coarse-Scale Problem $\mathcal{C}_{\text{Thermal}}$:

$$\sum_{\alpha=1}^{2}\int_{\Omega^{(\alpha)}}\left[\overline{c}\left(\dot{\tilde{\theta}}_{n+1}^{(\alpha)}+\dot{\hat{\theta}}_{n+1}^{(\alpha)}\right)\cdot\hat{\omega}^{(\alpha)}+\operatorname{div}\left(\hat{\omega}^{(\alpha)}\right)\cdot\left(\overline{\boldsymbol{k}}^{(\alpha)}\cdot\nabla\theta_{n+1}^{(\alpha)}\right)-\overline{r}\cdot\hat{\omega}^{(\alpha)}\right]\mathrm{d}V$$
$$+\sum_{\alpha=1}^{2}\int_{\Omega^{(\alpha)}}\left(\boldsymbol{m}^{(\alpha)}:\nabla\boldsymbol{v}^{(\alpha)}\right)\cdot\hat{\omega}^{(\alpha)}\mathrm{d}V \tag{2-28}$$
$$+\sum_{\alpha=1}^{2}\int_{\Gamma_{\mathrm{h}}}\overline{q}^{(\alpha)}\cdot\hat{\omega}^{(\alpha)}\,\mathrm{d}\Gamma_{\mathrm{h}}-\underbrace{\int_{\Gamma_{\mathrm{I}}}\lambda_2\cdot[\![\hat{\omega}]\!]\,\mathrm{d}\Gamma_{\mathrm{I}}}_{\text{heat flux cont.}}=0$$

$$\underbrace{-\int_{\Gamma_{\mathrm{I}}}\mu_2\cdot\left([\![\hat{\theta}]\!]+[\![\tilde{\theta}]\!]\right)\mathrm{d}\Gamma_{\mathrm{I}}}_{\text{temperature cont.}}=0 \tag{2-29}$$

Coarse-Scale Problem $\mathcal{C}_{\mathrm{Mech}}$:

$$\sum_{\alpha=1}^{2}\int_{\Omega^{(\alpha)}}\left[\operatorname{div}\hat{\boldsymbol{\eta}}^{(\alpha)}\cdot\left(\mathbb{C}^{(a)}:\boldsymbol{\varepsilon}^{(a)}-\boldsymbol{m}^{(\alpha)}\theta^{(\alpha)}\right)-\rho\boldsymbol{b}^{(\alpha)}\cdot\hat{\boldsymbol{\eta}}^{(\alpha)}\right]\mathrm{d}V$$
$$-\sum_{\alpha=1}^{2}\int_{\Gamma_{\mathrm{h}}}\overline{\boldsymbol{t}}^{(\alpha)}\cdot\hat{\boldsymbol{\eta}}^{(\alpha)}\mathrm{d}\Gamma_{\mathrm{h}}-\int_{\Gamma_{\mathrm{I}}}\boldsymbol{\lambda}_1\cdot[\![\hat{\boldsymbol{\eta}}\,]\!]\,\mathrm{d}\Gamma_{\mathrm{I}}=0 \tag{2-30}$$

$$-\int_{\Gamma_{\mathrm{I}}}\boldsymbol{\mu}_1\cdot\left([\![\tilde{\boldsymbol{u}}]\!]+[\![\hat{\boldsymbol{u}}]\!]\right)\mathrm{d}\Gamma_{\mathrm{I}}=0 \tag{2-31}$$

Fine-Scale Problem $\mathcal{F}_{\mathrm{Thermal}}$:

$$\sum_{\alpha=1}^{2}\int_{\Omega^{(\alpha)}}\left[\overline{c}\cdot\left(\dot{\tilde{\theta}}_{n+1}^{(\alpha)}+\dot{\hat{\theta}}_{n+1}^{(\alpha)}\right)\tilde{\omega}^{(\alpha)}+\operatorname{div}\left(\tilde{\omega}^{(\alpha)}\right)\cdot\left(\overline{\boldsymbol{k}}^{(\alpha)}\cdot\nabla\theta_{n+1}^{(\alpha)}\right)-\overline{r}\cdot\tilde{\omega}^{(\alpha)}\right]\mathrm{d}V$$
$$+\sum_{\alpha=1}^{2}\int_{\Gamma_{\mathrm{h}}}\overline{q}^{(\alpha)}\cdot\tilde{\omega}^{(\alpha)}\,\mathrm{d}\Gamma_{\mathrm{h}}-\underbrace{\int_{\Gamma_{\mathrm{I}}}\lambda_2\cdot[\![\tilde{\omega}]\!]\,\mathrm{d}\Gamma_{\mathrm{I}}}_{\text{heat flux cont.}}=0 \tag{2-32}$$

Fine-Scale Problem $\mathcal{F}_{\mathrm{Mech}}$:

$$\sum_{\alpha=1}^{2}\int_{\Omega^{(\alpha)}}\left[\operatorname{div}\tilde{\boldsymbol{\eta}}^{(\alpha)}\cdot\mathbb{C}^{(a)}:\boldsymbol{\varepsilon}^{(a)}-\rho\boldsymbol{b}^{(\alpha)}\cdot\tilde{\boldsymbol{\eta}}^{(\alpha)}\right]\mathrm{d}V$$
$$-\sum_{\alpha=1}^{2}\int_{\Gamma_{\mathrm{h}}}\overline{\boldsymbol{t}}^{(\alpha)}\cdot\tilde{\boldsymbol{\eta}}^{(\alpha)}\mathrm{d}\Gamma_{\mathrm{h}}-\int_{\Gamma_{\mathrm{I}}}\boldsymbol{\lambda}_1\cdot[\![\tilde{\boldsymbol{\eta}}\,]\!]\,\mathrm{d}\Gamma_{\mathrm{I}}=0 \tag{2-33}$$

As in Eqn. (2-28) to (2-33), the Lagrange multipliers $\boldsymbol{\lambda}_1$ and λ_2, the coarse and fine temperature field $\hat{\theta}^{(\alpha)}$ and $\tilde{\theta}^{(\alpha)}$, and the coarse and fine displacement field $\hat{\boldsymbol{u}}^{(\alpha)}$ and $\tilde{\boldsymbol{u}}^{(\alpha)}$ are the unknowns. Specifically, the coarse scale problem $\mathcal{C}_{\mathrm{Thermal}}$ (2-28) contains the mechanical velocity unknowns $\boldsymbol{v}^{(\alpha)}$, temperature unknowns $\theta^{(\alpha)}$ and the Lagrange multiplier λ_2. The fine-scale problem $\mathcal{F}_{\mathrm{Thermal}}$

(2-32) contains both the Lagrange multiplier λ_2 and temperature $\theta^{(\alpha)}$ as the unknowns. In addition, the coarse scale problem $\mathcal{C}_{\text{Mech}}$ has the thermal unknowns $\theta^{(\alpha)}$, mechanical displacement unknowns $\boldsymbol{u}^{(\alpha)}$, and the Lagrange multiplier $\boldsymbol{\lambda}_1$. The fine-scale problem $\mathcal{F}_{\text{Mech}}$ contains both the Lagrange multiplier $\boldsymbol{\lambda}_1$ and the displacement unknowns $\boldsymbol{u}^{(\alpha)}$.

For both the mechanical and thermal part, we adopt a strategy that is similar to our earlier work in the context of mechanical field problem [100,162]. The stabilized form for the thermal problem is developed via a three-stage modeling process. The process to derive the stabilized formulation for the mechanical part from equations (2-30)-(2-31) and (2-33) is similar. First, by localizing the fine-scale equation (2-32) to the vicinity of the interface Γ_I and expanding the fine-scale solution via bubble functions, we obtain the expression for the fine scale solution as a function of the Lagrange multiplier, the given bubble function, and the residual of coarse scales. Secondly, substituting the fine-scale solution $\tilde{\theta}^{(\alpha)}$ into the continuity equation (2-29), and assuming a piecewise constant λ_2, we solve for the Lagrange multiplier in terms of the coarse-scale solution $\hat{\theta}^{(\alpha)}$. Thirdly, we variationally embed λ_2 and $\tilde{\theta}^{(\alpha)}$ into the coarse-scale formulation (2-28) to remove the explicit appearance of $\tilde{\theta}^{(\alpha)}$ and λ_2.

Remark: *One main difference from our earlier work [162] is the existence of the thermomechanical coupling terms. To keep the fine scale sub-problem simple, the thermomechanical coupling term only appears in the coarse scale problem equation (2-28) and (2-33).*

2.3.1 Derivation of Fine-scale Interfacial Models

At this point, our objective is to develop a model for the fine-scale temperature field at the boundary of the elements that lie in the vicinity of Γ_I. To keep the model simple, we assume a piece-wise constant-in-time approximation for the fine-scale temperature field, i.e., $\dot{\tilde{\theta}}^{(\alpha)} = 0$. This helps drop the time rate of change of temperature field from (2-32). In this case, $\dot{\hat{\theta}}^{(\alpha)} = \dot{\theta}^{(\alpha)}$.

As adopted in [162], we approximate the fine scales using edge bubble functions which are only supported within the sectors $\omega_s^{(\alpha)}$ next to the interface segments γ_s as shown in Figure 2.2. The

expressions for fine scale edge bubble functions are as follows:

$$\tilde{\theta}^{(\alpha)}\Big|_{\omega_s^{(\alpha)}} = \beta_s^{\theta(\alpha)} b_s^{\theta(\alpha)}(\boldsymbol{x}), \qquad \tilde{\omega}^{(\alpha)}\Big|_{\omega_s^{(\alpha)}} = \chi_s^{\theta(\alpha)} b_s^{\theta(\alpha)}(\boldsymbol{x}) \tag{2-34}$$

$$\tilde{\boldsymbol{u}}^{(\alpha)}\Big|_{\omega_s^{(\alpha)}} = \beta_s^{(\alpha)} \boldsymbol{b}_s^{(\alpha)}(\boldsymbol{x}), \qquad \tilde{\boldsymbol{\eta}}^{(\alpha)}\Big|_{\omega_s^{(\alpha)}} = \chi_s^{(\alpha)} \boldsymbol{b}_s^{(\alpha)}(\boldsymbol{x}) \tag{2-35}$$

where terms with the superscript $\boldsymbol{\theta}$ expressed as $(\cdot)_s^{\theta(\alpha)}$ are the coefficients or bubble functions for the thermal part and normal terms $(\cdot)_s^{(\alpha)}$ are the coefficient or bubble functions for the mechanical part.

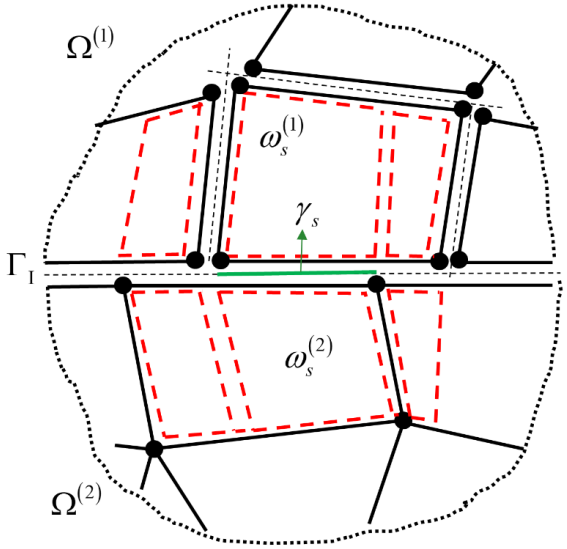

Figure 2.2. Description of the interface sectors $\omega_s^{(\alpha)}$ and segment γ_s.

Next, we rearrange (2-32) and apply the divergence theorem

$$\begin{aligned}
&\sum_{\alpha=1}^{2} \int_{\omega_s^{(\alpha)}} \left[\operatorname{div}\left(\tilde{\omega}^{(\alpha)}\right) \cdot \left(\overline{\boldsymbol{k}}^{(\alpha)} \cdot \nabla \tilde{\theta}_{n+1}^{(\alpha)} \right) \right] \mathrm{d}V \\
&= \sum_{\alpha=1}^{2} \int_{\omega_s^{(\alpha)}} \left[-\overline{c} \left(\hat{\dot{\theta}}_{n+1}^{(\alpha)} \right) + \operatorname{div}\left(\overline{\boldsymbol{k}}^{(\alpha)} \cdot \nabla \hat{\theta}_{n+1}^{(\alpha)} \right) + \overline{r} \right] \cdot \tilde{\omega}^{(\alpha)} \mathrm{d}V \\
&\quad + \int_{\gamma_s} \left(\lambda_2 + \boldsymbol{q}^{(1)} \boldsymbol{n}^{(1)} \right) \cdot \tilde{\omega}^{(1)} \, \mathrm{d}\gamma_s + \int_{\gamma_s} \left(-\lambda_2 + \boldsymbol{q}^{(2)} \boldsymbol{n}^{(2)} \right) \cdot \tilde{\omega}^{(2)} \, \mathrm{d}\gamma_s
\end{aligned} \tag{2-36}$$

We then solve for (2-36) by substituting the expression for fine scales (2-34).

$$
\begin{aligned}
&\sum_{\alpha=1}^{2}\int_{\omega_s^{(\alpha)}}\left[\operatorname{div}\left(\chi_s^{\theta(\alpha)}b_s^{\theta(\alpha)}\right)\cdot\left(\overline{\boldsymbol{k}}^{(\alpha)}\cdot\nabla\left(\beta_s^{\theta(\alpha)}b_s^{\theta(\alpha)}\right)\right)\right]\mathrm{d}V\\
&=\sum_{\alpha=1}^{2}\int_{\omega_s^{(\alpha)}}\left[-\overline{c}\left(\hat{\dot{\theta}}_{n+1}^{(\alpha)}\right)+\operatorname{div}\left(-\hat{\boldsymbol{q}}^{(\alpha)}\right)+\overline{r}\right]\cdot\left(\chi_s^{\theta(\alpha)}b_s^{\theta(\alpha)}\right)\mathrm{d}V\\
&\quad+\int_{\gamma_s}\left(\lambda_2+\boldsymbol{q}^{(1)}\boldsymbol{n}^{(1)}\right)\cdot\left(\chi_s^{\theta(1)}b_s^{\theta(1)}\right)\mathrm{d}\gamma_s+\int_{\gamma_s}\left(-\lambda_2+\boldsymbol{q}^{(2)}\boldsymbol{n}^{(2)}\right)\cdot\left(\chi_s^{\theta(2)}b_s^{\theta(2)}\right)\mathrm{d}\gamma_s
\end{aligned}
\tag{2-37}
$$

Since the fine scale variational problem (2-37) holds for all admissible weighting functions, we obtain the fine scale solution coefficient $\beta_s^{\theta(\alpha)}$ as follows

$$
\begin{aligned}
\beta_s^{\theta(\alpha)}=&\int_{\omega_s^{(\alpha)}}\left[\boldsymbol{\varepsilon}\left(b_s^{\theta(\alpha)}\right)\cdot\left(\overline{\boldsymbol{k}}^{(\alpha)}\cdot\boldsymbol{\varepsilon}\left(b_s^{\theta(\alpha)}\right)\right)\right]\mathrm{d}V^{-1}\\
&\cdot\left\{\begin{array}{l}\displaystyle\int_{\omega_s^{(\alpha)}}\left(b_s^{\theta(\alpha)}\right)\cdot\left(-\overline{c}\left(\hat{\dot{\theta}}_{n+1}^{(\alpha)}\right)+\operatorname{div}\left(\overline{\boldsymbol{k}}^{(\alpha)}\cdot\nabla\hat{\theta}_{n+1}^{(\alpha)}\right)+\overline{r}\right)\mathrm{d}V\\ \displaystyle+\int_{\gamma_s}\left(\left(-1\right)^{\alpha-1}\lambda_2+\boldsymbol{q}^{(\alpha)}\boldsymbol{n}^{(\alpha)}\right)\cdot\left(b_s^{\theta(\alpha)}\right)\mathrm{d}\gamma_s\end{array}\right\}
\end{aligned}
\tag{2-38}
$$

Following the same steps, the fine scale coefficient $\boldsymbol{\beta}_s^{(\alpha)}$ for the mechanical part can be written as below.

$$
\begin{aligned}
\boldsymbol{\beta}_s^{(\alpha)}=&\int_{\omega_s^{(\alpha)}}\left[\boldsymbol{\varepsilon}\left(\boldsymbol{b}_s^{(\alpha)}\right):\left(\mathbb{C}^{(a)}:\boldsymbol{\varepsilon}\left(\boldsymbol{b}_s^{(\alpha)}\right)\right)\right]\mathrm{d}V^{-1}\\
&\cdot\left\{\begin{array}{l}\displaystyle\int_{\omega_s^{(\alpha)}}\left(\boldsymbol{b}_s^{(\alpha)}\right):\left(\operatorname{div}\left[\mathbb{C}^{(a)}:\boldsymbol{\varepsilon}^{(a)}-\boldsymbol{m}^{(\alpha)}\theta^{(\alpha)}\right]+\rho\boldsymbol{b}^{(\alpha)}\right)\mathrm{d}V\\ \displaystyle+\int_{\gamma_s}\left(\left(-1\right)^{\alpha-1}\boldsymbol{\lambda}_1-\boldsymbol{\sigma}^{(\alpha)}\boldsymbol{n}^{(\alpha)}\right)\cdot\left(\boldsymbol{b}_s^{(\alpha)}\right)\mathrm{d}\gamma_s\end{array}\right\}
\end{aligned}
\tag{2-39}
$$

As adopted in [162], the following assumptions are applied to further simplify Eqn. (2-38). Firstly, we apply the mean value theorem to the residual of the Euler-Lagrange equation over each sector $\omega_s^{(\alpha)}$ to extract it out of the integral. Especially, we consider a piecewise constant L_2 projection of the interface residual term $\left(\left(-1\right)^{\alpha-1}\lambda_2+\boldsymbol{q}^{(\alpha)}\boldsymbol{n}^{(\alpha)}\right)$ and $\left(\left(-1\right)^{\alpha-1}\boldsymbol{\lambda}_1-\boldsymbol{t}^{(\alpha)}\boldsymbol{n}^{(\alpha)}\right)$ over the sector boundaries. Secondly, although the bubbles $b_s^{\theta(\alpha)}$ and $\boldsymbol{b}_s$ are not precisely residual free bubbles, we assume the fine scale edge bubbles are orthogonal to the internal residual. Consequently, we assume $\int_{\omega_s^{(\alpha)}}\left(b_s^{\theta(\alpha)}\right)\cdot\left(-\overline{c}\left(\hat{\dot{\theta}}_{n+1}^{(\alpha)}\right)+\operatorname{div}\left(\overline{\boldsymbol{k}}^{(\alpha)}\cdot\nabla\hat{\theta}_{n+1}^{(\alpha)}\right)+\overline{r}\right)\mathrm{d}V\approx 0$ and $\int_{\omega_s^{(\alpha)}}\left(\boldsymbol{b}_s^{(\alpha)}\right):\left(\operatorname{div}\left[\mathbb{C}^{(a)}:\boldsymbol{\varepsilon}^{(a)}-\boldsymbol{m}^{(\alpha)}\theta^{(\alpha)}\right]+\rho\boldsymbol{b}^{(\alpha)}\right)\mathrm{d}V\approx\mathbf{0}$. Thirdly, we use the unique attribute of VMS-based stabilization that arbitrary combinations of interpolation functions can be employed

for expanding the temperature and Lagrange multiplier fields. Lastly, we focus on the trace of the fine scales along the interface and make the following assumption which is analogous to employing the average value of the bubble function on the element boundaries.

$$b_s^{\theta(\alpha)} \int_{\gamma_s} \left(b_s^{\theta(\alpha)} \right) \mathrm{d}\gamma_s = meas\left(\gamma_s \right)^{-1} \left(\int_{\gamma_s} \left(b_s^{\theta(\alpha)} \right) \mathrm{d}\gamma_s \right)^2 \tag{2-40}$$

Applying (2-40) to (2-38) and substituting back in Eqn. (2-34), the fine scale solution $\tilde{\theta}^{(\alpha)}$ is obtained as follows

$$\tilde{\theta}^{(\alpha)} = \tau_s^{\theta(\alpha)} \cdot \left(\left(-1 \right)^{\alpha - 1} \lambda_2 + \boldsymbol{q}^{(\alpha)} \boldsymbol{n}^{(\alpha)} \right) \tag{2-41}$$

where

$$\tau_s^{\theta(\alpha)} = \left[\mathrm{meas}\left(\gamma_s \right) \right]^{-1} \left(\int_{\gamma_s} b_s^{\theta(\alpha)} \, \mathrm{d}\gamma_s \right)^2 \tilde{\tau}_s^{\theta(\alpha)} \tag{2-42}$$

$$\tilde{\tau}_s^{\theta(\alpha)} = \left[\int_{\omega_s^{(\alpha)}} \boldsymbol{\varepsilon}\left(b_s^{\theta(\alpha)} \right) \cdot \left(\overline{\boldsymbol{k}}^{(\alpha)} \cdot \boldsymbol{\varepsilon}\left(b_s^{\theta(\alpha)} \right) \right) \mathrm{d}V \right]^{-1} \tag{2-43}$$

The mechanical fine scale solution $\tilde{\boldsymbol{u}}$ is obtained accordingly as follows

$$\tilde{\boldsymbol{u}}^{(\alpha)} = \boldsymbol{\tau}_s^{(\alpha)} \cdot \left(\left(-1 \right)^{\alpha - 1} \boldsymbol{\lambda}_1 - \boldsymbol{\sigma}^{(\alpha)} \boldsymbol{n}^{(\alpha)} \right) \tag{2-44}$$

where

$$\boldsymbol{\tau}_s^{(\alpha)} = \left[\mathrm{meas}\left(\gamma_s \right) \right]^{-1} \left(\int_{\gamma_s} b_s^{(\alpha)} \, \mathrm{d}\gamma_s \right)^2 \tilde{\boldsymbol{\tau}}_s^{(\alpha)} \tag{2-45}$$

$$\tilde{\boldsymbol{\tau}}_s^{(\alpha)} = \left[\int_{\omega_s^{(\alpha)}} \boldsymbol{\varepsilon}\left(\boldsymbol{b}_s^{\theta(\alpha)} \right) : \left(\mathbb{C}^{(a)} : \boldsymbol{\varepsilon}\left(\boldsymbol{b}_s^{(\alpha)} \right) \right) \mathrm{d}V \right]^{-1} \tag{2-46}$$

One significant attribute of this method is that the expression for the fine scale $\tilde{\theta}^{(\alpha)}$ is similar in form to the expression given in [162], but since the temperature field is a scalar, all the bubble functions and stability terms $\tau_s^{\theta(\alpha)}$ and $\tilde{\tau}_s^{\theta(\alpha)}$ are scalar fields. Interested readers are referred to [162] for a detailed discussion of the mechanical fine scale solutions. The key contribution here is that the fine scale solution incorporates the effects of evolving thermal field from either side of the interface via the appearance of the conductivity tensor $\overline{\boldsymbol{k}}^{(\alpha)}$. These dependencies play a key role in the mathematical properties of the numerical flux and penalty parameter derived in the next section.

Remark: *The fine scale derivation stays form identical to our previous work in [162] in the small strain regime. Interested reader is referred to [162] for the evolution of the fine scales for different PDEs.*

Remark: *As shown in Figure 2.2, for sector $\omega_s^{(\alpha)}$, the interface segments lie not only between bimaterial interphases or pre-defined boundaries. Every element boundary can potentially become the interface segment. Furthermore, nonconforming meshes or different types of elements are fully compatible since node on node contact is not required.*

2.3.2 Variational embedding in the coarse-scale problem

The fine scale temperature field $\tilde{\theta}^{(\alpha)}$ in (2-41) is a function of the Lagrange multiplier field λ_2 which is still an unknown. We therefore focus on the continuity equation (2-29) to obtain an expression for the Lagrange multiplier field λ_2. Following our earlier work in [162], we require that (2-29) holds for all Lagrange multipliers μ_2 locally along the interface. We take the piecewise constant projection of μ_2 over element interfaces that take it out of the integral expression and therefore, the quantity in square brackets of (2-29) must vanish everywhere. We then apply the same assumption to the displacement continuity equation (2-31).

$$\left(\left[\!\left[\hat{\theta}\right]\!\right]+\left[\!\left[\tilde{\theta}\right]\!\right]\right)=0 \tag{2-47}$$

$$\left(\left[\!\left[\tilde{\boldsymbol{u}}\right]\!\right]+\left[\!\left[\hat{\boldsymbol{u}}\right]\!\right]\right)=\mathbf{0} \tag{2-48}$$

Noting that $\left[\!\left[\cdot\right]\!\right]=\left(\cdot\right)^{(1)}-\left(\cdot\right)^{(2)}$ and solving (2-47) for λ_2 by substituting (2-41) and solving (2-48) by substituting (2-44), we arrive at an explicit form for λ_2 as a function of heat flux term $\boldsymbol{q}^{(\alpha)}$ and coarse scale temperature field $\hat{\theta}$:

$$\lambda_2=\left[-\delta_s^{\theta(1)}\cdot\left(\boldsymbol{q}^{(1)}\boldsymbol{n}^{(1)}\right)+\delta_s^{\theta(2)}\cdot\left(\boldsymbol{q}^{(2)}\boldsymbol{n}^{(2)}\right)\right]-\tau_s^{\theta}\cdot\left(\left[\!\left[\hat{\theta}\right]\!\right]\right) \tag{2-49}$$

where $\tau_s^{\theta}=\left(\tau_s^{\theta(1)}+\tau_s^{\theta(2)}\right)^{-1}$ is the stability tensor term and $\delta_s^{\theta(\alpha)}=\tau_s^{\theta}\cdot\tau_s^{\theta(\alpha)}$ is the flux weighting tensor consisting of the stabilization tensor from both subdomains.

In addition, the explicit form for $\boldsymbol{\lambda}_1$ is obtained as a function of the traction field $\boldsymbol{\sigma}^{(\alpha)}\boldsymbol{n}^{(\alpha)}$ and the coarse scale displacement field is given as follows.

$$\boldsymbol{\lambda}_1 = \left[\boldsymbol{\delta}_s^{(1)} \cdot \left(\boldsymbol{\sigma}^{(1)} \boldsymbol{n}^{(1)} \right) - \boldsymbol{\delta}_s^{(2)} \cdot \left(\boldsymbol{\sigma}^{(2)} \boldsymbol{n}^{(2)} \right) \right] - \boldsymbol{\tau}_s \cdot \left(\left[\!\left[\hat{\boldsymbol{u}} \right]\!\right] \right) \tag{2-50}$$

By substituting λ_2 into (2-41) and $\boldsymbol{\lambda}_1$ into (2-44), simplified expressions for the fine scales $\tilde{\theta}^{(\alpha)}$ and $\tilde{\boldsymbol{u}}$ results:

$$\tilde{\theta}^{(\alpha)} = \delta_s^{\theta} \left[\boldsymbol{q}^{(1)} \cdot \boldsymbol{n}^{(1)} + \boldsymbol{q}^{(2)} \cdot \boldsymbol{n}^{(2)} \right] + (-1)^{(\alpha)} \delta_s^{\theta(\alpha)T} \cdot \left(\left[\!\left[\hat{\theta} \right]\!\right] \right) \tag{2-51}$$

$$\tilde{\boldsymbol{u}}^{(\alpha)} = - \boldsymbol{\delta}_s \left[\boldsymbol{\sigma}^{(1)} \cdot \boldsymbol{n}^{(1)} + \boldsymbol{\sigma}^{(2)} \cdot \boldsymbol{n}^{(2)} \right] + (-1)^{(\alpha)} \boldsymbol{\delta}_s^{(\alpha)T} \cdot \left(\left[\!\left[\hat{\boldsymbol{u}} \right]\!\right] \right) \tag{2-52}$$

where

$$\delta_s^{\theta} = \tau_s^{\theta(1)} \cdot \delta_s^{\theta(2)} = \tau_s^{\theta(2)} \cdot \delta_s^{\theta(1)} \quad \boldsymbol{\delta}_s^{\theta} = \boldsymbol{\tau}_s^{(1)} \cdot \boldsymbol{\delta}_s^{(2)} = \boldsymbol{\tau}_s^{(2)} \cdot \boldsymbol{\delta}_s^{(1)} \tag{2-53}$$

Now we focus on the coarse-scale problems (2-28) and (2-30) and segregate coarse and fine terms. We then substitute fine scale solution (2-51) and Lagrange multiplier (2-49) and obtain the stabilized form.

$$\begin{aligned}
&\sum_{\alpha=1}^{2} \int_{\Omega^{(\alpha)}} \left[\overline{c} \left(\dot{\theta}_{n+1}^{(\alpha)} \right) \cdot \hat{\omega}^{(\alpha)} + \mathrm{div} \left(\hat{\omega}^{(\alpha)} \right) \cdot \left(\overline{\boldsymbol{k}}^{(\alpha)} \cdot \nabla \hat{\theta}_{n+1}^{(\alpha)} \right) - \overline{r} \cdot \hat{\omega}^{(\alpha)} \right] \mathrm{d}V \\
&- \int_{\Gamma_{\mathrm{I}}} \left\{ \left(\overline{\boldsymbol{k}} \nabla \hat{\theta}_{n+1} \right) \boldsymbol{n} \right\} \cdot \left[\!\left[\hat{\omega} \right]\!\right] \mathrm{d}\Gamma_{\mathrm{I}} - \int_{\Gamma_{\mathrm{I}}} \left\{ \left(\overline{\boldsymbol{k}} \nabla \hat{\omega} \right) \boldsymbol{n} \right\} \cdot \left(\left[\!\left[\hat{\theta}_{n+1} \right]\!\right] - \theta_g \right) \mathrm{d}\Gamma_{\mathrm{I}} \\
&+ \int_{\Gamma_{\mathrm{I}}} \left[\!\left[\hat{\omega} \right]\!\right] \cdot \boldsymbol{\tau}_s^{\theta} \cdot \left(\left[\!\left[\hat{\theta}_{n+1} \right]\!\right] - \theta_g \right) \mathrm{d}\Gamma_{\mathrm{I}} - \int_{\Gamma_{\mathrm{I}}} \left[\!\left[\left(\overline{\boldsymbol{k}} \nabla \hat{\omega} \right) \boldsymbol{n} \right]\!\right] \cdot \delta_s^{\theta} \cdot \left[\!\left[\left(\overline{\boldsymbol{k}} \nabla \hat{\theta}_{n+1} \right) \boldsymbol{n} \right]\!\right] \mathrm{d}\Gamma_{\mathrm{I}} \\
&+ \sum_{\alpha=1}^{2} \int_{\Omega^{(\alpha)}} \left[\left(\boldsymbol{m}^{(\alpha)} : \nabla \boldsymbol{v}^{(\alpha)} \right) \cdot \hat{\omega}^{(\alpha)} \right] \mathrm{d}V + \sum_{\alpha=1}^{2} \int_{\Gamma_{\mathrm{h}}} \overline{q}^{(\alpha)} \cdot \hat{\omega}^{(\alpha)} \, \mathrm{d}\Gamma_{\mathrm{h}} = 0
\end{aligned} \tag{2-54}$$

where $\left\{ (\bullet) \boldsymbol{n} \right\}$ is the average operator and $\left[\!\left[(\bullet) \boldsymbol{n} \right]\!\right]$ is the jump operator defined as:

$$\left\{ (\bullet) \boldsymbol{n} \right\} = \boldsymbol{\delta}_s^{\theta(1)} \cdot \left((\bullet)^{(1)} \boldsymbol{n}^{(1)} \right) - \boldsymbol{\delta}_s^{\theta(2)} \cdot \left((\bullet)^{(2)} \boldsymbol{n}^{(2)} \right) \tag{2-55}$$

$$\left[\!\left[(\bullet) \boldsymbol{n} \right]\!\right] = \boldsymbol{\delta}_s^{\theta(1)} \cdot \left((\bullet)^{(1)} \boldsymbol{n}^{(1)} \right) + \boldsymbol{\delta}_s^{\theta(2)} \cdot \left((\bullet)^{(2)} \boldsymbol{n}^{(2)} \right) \tag{2-56}$$

2.3.3 Stabilized Interface Formulation for Both mechanical and Thermal Field

Incorporating the expressions (2-49) for λ_2 and the fine-scale fields $\tilde{\theta}^{(\alpha)}$ (2-51) into the linearized coarse-scale problem (2-55) yields the stabilized interface formulation. Following along our earlier work [99,100], we drop the jump in the flux term both in the mechanical $\left(\left[\!\left[\mathbb{C} : \boldsymbol{\varepsilon} \left(\boldsymbol{\eta}_o \right) \boldsymbol{n} \right]\!\right], \boldsymbol{\delta}_s \cdot \left[\!\left[\mathbb{C} : \boldsymbol{\varepsilon} \left(\boldsymbol{u}_{n+1} \right) \boldsymbol{n} + \left(\boldsymbol{m} \theta \right) \boldsymbol{n} \right]\!\right] \right)_{\Gamma_{\mathrm{I}}}$ and in the thermal fields

$\left(\left[\!\left[\left(\overline{\boldsymbol{k}}\nabla\hat{\omega}\right)\boldsymbol{n}\right]\!\right]\cdot\boldsymbol{\delta}_s^{\theta}\cdot\left[\!\left[\left(\overline{\boldsymbol{k}}\nabla\hat{\theta}_{n+1}\right)\boldsymbol{n}\right]\!\right]\right)_{\Gamma_{\mathrm{I}}}$ to keep the formulation simple,.

Let $\boldsymbol{\mathcal{V}}=\left\{\boldsymbol{u},\theta\right\}$ and $\boldsymbol{\mathcal{W}}=\left\{\boldsymbol{\eta},\omega\right\}$ such that

$$\mathbb{B}_{\text{mech}}\left(\boldsymbol{\mathcal{W}},\boldsymbol{\mathcal{V}}\right)+\mathbb{B}_{\text{thermal}}\left(\boldsymbol{\mathcal{W}},\boldsymbol{\mathcal{V}}\right)=\mathbb{F}_{\text{mech}}\left(\boldsymbol{\mathcal{W}}\right)+\mathbb{F}_{\text{thermal}}\left(\boldsymbol{\mathcal{W}}\right) \tag{2-57}$$

and

$$\mathbb{B}_{\text{mech}}\left(\boldsymbol{\mathcal{W}},\boldsymbol{\mathcal{V}}\right)=\mathbb{B}_{\text{mech}}^{\text{Gal}}\left(\boldsymbol{\mathcal{W}},\boldsymbol{\mathcal{V}}\right)+\mathbb{B}_{\text{mech}}^{\text{Interfacial}}\left(\boldsymbol{\mathcal{W}},\boldsymbol{\mathcal{V}}\right) \tag{2-58}$$

$$\mathbb{B}_{\text{thermal}}\left(\boldsymbol{\mathcal{W}},\boldsymbol{\mathcal{V}}\right)=\mathbb{B}_{\text{thermal}}^{\text{Gal}}\left(\boldsymbol{\mathcal{W}},\boldsymbol{\mathcal{V}}\right)+\mathbb{B}_{\text{thermal}}^{\text{Interfacial}}\left(\boldsymbol{\mathcal{W}},\boldsymbol{\mathcal{V}}\right) \tag{2-59}$$

Eqn. (2-58) and (2-59) contain both the standard Galerkin terms and the newly derived interfacial terms.

Mechanical formulation:

$$\mathbb{B}_{\text{mech}}^{\text{Gal}}\left(\boldsymbol{\mathcal{W}},\boldsymbol{\mathcal{V}}\right)=\sum_{\alpha=1}^{2}\int_{\Omega^{(\alpha)}}\left[\operatorname{div}\boldsymbol{\eta}^{(\alpha)}\cdot\left(\mathbb{C}^{(\alpha)}:\boldsymbol{\varepsilon}\left(\boldsymbol{u}_{n+1}^{(\alpha)}\right)-\boldsymbol{m}^{(\alpha)}\theta_{n+1}^{(\alpha)}\right)\right]\mathrm{d}V \tag{2-60}$$

$$\begin{aligned}\mathbb{B}_{\text{mech}}^{\text{Interfacial}}\left(\boldsymbol{\mathcal{W}},\boldsymbol{\mathcal{V}}\right)=&-\int_{\Gamma_{\mathrm{I}}}\left[\!\left[\boldsymbol{\eta}\right]\!\right]\cdot\left\{\left(\mathbb{C}:\boldsymbol{\varepsilon}\left(\boldsymbol{u}_{n+1}\right)-\boldsymbol{m}\theta_{n+1}\right)\boldsymbol{n}\right\}\mathrm{d}\Gamma_{\mathrm{I}}\\&-\int_{\Gamma_{\mathrm{I}}}\left\{\left(\mathbb{C}:\boldsymbol{\varepsilon}\left(\boldsymbol{\eta}\right)\right)\boldsymbol{n}\right\}\cdot\left(\left[\!\left[\boldsymbol{u}_{n+1}\right]\!\right]-\boldsymbol{\zeta}\right)\mathrm{d}\Gamma_{\mathrm{I}}\\&+\int_{\Gamma_{\mathrm{I}}}\left[\!\left[\boldsymbol{\eta}\right]\!\right]\cdot\boldsymbol{\tau}_s\left(\left[\!\left[\boldsymbol{u}_{n+1}\right]\!\right]-\boldsymbol{\zeta}\right)\mathrm{d}\Gamma_{\mathrm{I}}\end{aligned} \tag{2-61}$$

$$\mathbb{F}_{\text{mech}}\left(\boldsymbol{\mathcal{W}}\right)=\sum_{\alpha=1}^{2}\int_{\Omega^{(\alpha)}}\left[\rho\boldsymbol{b}_{n+1}^{(\alpha)}\cdot\boldsymbol{\eta}^{(\alpha)}\right]\mathrm{d}V+\sum_{\alpha=1}^{2}\int_{\Gamma_{\mathrm{h}}}\overline{\boldsymbol{t}}^{(\alpha)}\cdot\boldsymbol{\eta}^{(\alpha)}\mathrm{d}\Gamma_{\mathrm{h}} \tag{2-62}$$

Thermal formulation:

$$\begin{aligned}\mathbb{B}_{\text{thermal}}^{\text{Gal}}\left(\boldsymbol{\mathcal{W}},\boldsymbol{\mathcal{V}}\right)=&\sum_{\alpha=1}^{2}\int_{\Omega^{(\alpha)}}\overline{c}\left(\frac{\theta_{n+1}^{(\alpha)}}{\Delta t}\right)\cdot\omega^{(\alpha)}+\operatorname{div}\left(\omega^{(\alpha)}\right)\cdot\left(\overline{\boldsymbol{k}}^{(\alpha)}\cdot\nabla\theta_{n+1}^{(\alpha)}\right)\mathrm{d}V\\&+\sum_{\alpha=1}^{2}\int_{\Omega^{(\alpha)}}\left(\boldsymbol{m}^{(\alpha)}:\nabla\left(\frac{\boldsymbol{u}_{n+1}^{(\alpha)}}{\Delta t}\right)\right)\cdot\omega^{(\alpha)}\mathrm{d}V\end{aligned} \tag{2-63}$$

$$\begin{aligned}\mathbb{B}_{\text{thermal}}^{\text{Interfacial}}\left(\boldsymbol{\mathcal{W}},\boldsymbol{\mathcal{V}}\right)=&-\int_{\Gamma_{\mathrm{I}}}\left\{\left(\overline{\boldsymbol{k}}\nabla\theta_{n+1}\right)\boldsymbol{n}\right\}\cdot\left[\!\left[\omega\right]\!\right]\mathrm{d}\Gamma_{\mathrm{I}}-\int_{\Gamma_{\mathrm{I}}}\left\{\left(\overline{\boldsymbol{k}}\nabla\omega\right)\boldsymbol{n}\right\}\cdot\left(\left[\!\left[\theta_{n+1}\right]\!\right]-\theta_g\right)\mathrm{d}\Gamma_{\mathrm{I}}\\&+\int_{\Gamma_{\mathrm{I}}}\left[\!\left[\omega\right]\!\right]\cdot\boldsymbol{\tau}_s^{\theta}\cdot\left(\left[\!\left[\theta_{n+1}\right]\!\right]-\theta_g\right)\mathrm{d}\Gamma_{\mathrm{I}}\end{aligned} \tag{2-64}$$

$$\mathcal{F}_{\text{thermal}}\left(\mathcal{W}\right)=\sum_{\alpha=1}^{2}\int_{\Omega^{(\alpha)}}\overline{c}\left(\frac{\theta_n^{(\alpha)}}{\Delta t}\right)\cdot\omega^{(\alpha)}+\left(\boldsymbol{m}^{(\alpha)}:\nabla\left(\frac{\boldsymbol{u}_n^{(\alpha)}}{\Delta t}\right)\right)\cdot\omega^{(\alpha)}\mathrm{d}V$$
$$+\sum_{\alpha=1}^{2}\int_{\Omega^{(\alpha)}}\overline{r}\cdot\omega^{(\alpha)}\mathrm{d}V-\sum_{\alpha=1}^{2}\int_{\Gamma_{\mathrm{h}}}\overline{q}^{(\alpha)}\cdot\hat{\omega}^{(\alpha)}\,\mathrm{d}\Gamma_{\mathrm{h}} \tag{2-65}$$

It is important to note that the structural form of the penalty term $\boldsymbol{\tau}_s$ and the stability tensor $\boldsymbol{\tau}_s^{(\alpha)}$ are not altered by the present developments and they form identical to the ones presented in [162]. Variationally consistent updating of these tensors results in a stabilized formulation that yields a robust numerical method as shown via numerical test cases in section 2.7.

Remark: *The second order tensor* $\boldsymbol{m}$ *is positive semidefinite and it couples the mechanical and thermal fields.*

Remark: *To keep the formulation simple, and without any loss in generality, we neglect the contribution of the fine scale in the structural heating term.*

2.4 1D Derivation and Implementation

To provide a deeper insight into the formulation, we present the 1D version of the stabilized DG formulations (2-57). Using linear shape functions and one-point integration rule, we evaluate the stiffness matrix for the two elements mesh with the interface in the middle as shown in Figure 2.3. We show the explicit form of matrices that emanate from the interfacial terms to provide insight into the structure of these terms. The domain interior terms that are also presented in the standard Galerkin method are summarized in Appendix A.

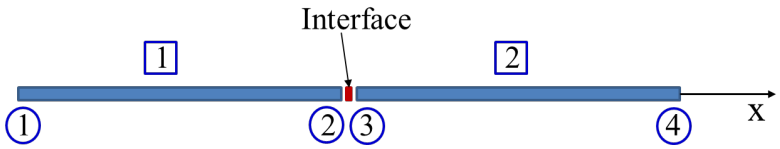

Figure 2.3. DG element description.

2.4.1 Evaluating the Consistent Tangent (Element-wise)

Now we focus on the interface terms that involve stabilization parameters and first evaluate the stability tensor $\boldsymbol{\tau}_s$ and $\boldsymbol{\delta}_s^{(\alpha)T}=\boldsymbol{\tau}_s^{(\alpha)}\cdot\boldsymbol{\tau}_s$.

$$\boldsymbol{\tau}_s=\left(\boldsymbol{\tau}_s^{(1)}+\boldsymbol{\tau}_s^{(2)}\right)^{-1} \tag{2-66}$$

$$\boldsymbol{\tau}_s^{(\alpha)} = \left[\text{meas}\left(\gamma_s\right)\right]^{-1}\left(\int_{\gamma_s} b_s^{(\alpha)}\,\mathrm{d}A\right)^2 \tilde{\boldsymbol{\tau}}_s^{(\alpha)} \tag{2-67}$$

$$\tilde{\boldsymbol{\tau}}_s^{(\alpha)} = \left[\int_{\omega_s^{(\alpha)}} \nabla \boldsymbol{b}_s^{(\alpha)} : \mathbb{C}^{(\alpha)} : \nabla \boldsymbol{b}_s^{(\alpha)}\,\mathrm{d}V\right]^{-1} \tag{2-68}$$

For the 1D case, the edge bubble function can be approximated by two linear shape functions with a value 1.0 at the element boundary and vanish to zero in the interiors. Adopting the idea from [162], we truncate the bubble function so that the direction in the x-direction equals to the width of the interface, as shown in Figure 2.4.

$$b_s^a\left(\xi\right) = \xi_a \xi,\ b_{s,x}^a\left(\xi\right) = \frac{2\xi_a}{l},\ \xi_a = \left(-1\right)^a, a = \left\{1,2\right\} \tag{2-69}$$

$$b_s\left(\xi\right) = \xi^2,\ b_{s,x}\left(\xi\right) = \frac{4\xi}{t}\ \text{(quadratic bubble)} \tag{2-70}$$

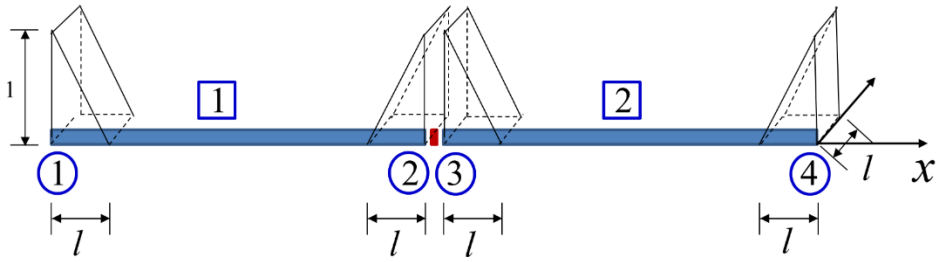

Figure 2.4. Description of the interfacial bubble functions in 1D.

With this in hand we can now evaluate the variationally derived stabilization parameters as follows:

$$\int_{\omega_s^{(\alpha)}} \nabla \boldsymbol{b}_s^{(\alpha)} : \mathbb{C}^{(\alpha)} : \nabla \boldsymbol{b}_s^{(\alpha)}\,\mathrm{d}V = E^{(\alpha)}\int_{x_2-l}^{x_2} \frac{4}{\left(l\right)^2}\mathrm{A}\mathrm{d}x = \left[\frac{4E^{(\alpha)}\mathrm{A}}{l}\right] \tag{2-71}$$

$$\tilde{\boldsymbol{\tau}}_s^{(\alpha)} = \left[\int_{\omega_s^{(\alpha)}} \nabla \boldsymbol{b}_s^{(\alpha)} : \mathbb{C}^{(\alpha)} : \nabla \boldsymbol{b}_s^{(\alpha)}\,\mathrm{d}V\right]^{-1} = \left[\frac{l}{4E^{(\alpha)}\mathrm{A}}\right] \tag{2-72}$$

$$\boldsymbol{\tau}_s^{(\alpha)} = \left[\text{meas}\left(\gamma_s\right)\right]^{-1}\left(\int_{\gamma_s} b_s^{(\alpha)}\,\mathrm{d}A\right)^2 \tilde{\boldsymbol{\tau}}_s^{(\alpha)} = \left[\frac{l^2 t^2}{4E^{(\alpha)}\mathrm{A}}\right] \tag{2-73}$$

$$\boldsymbol{\tau}_s = \left(\boldsymbol{\tau}_s^{(1)} + \boldsymbol{\tau}_s^{(2)}\right)^{-1} = \frac{\mathrm{A}}{l^2 t^2}\frac{1}{\left[\frac{1}{4E^{(1)}}\right] + \left[\frac{1}{4E^{(2)}}\right]} \tag{2-74}$$

$$\boldsymbol{\delta}_s^{(\alpha)T} = \boldsymbol{\tau}_s^{(\alpha)} \cdot \boldsymbol{\tau}_s = \frac{\left[\frac{1}{4E^{(\alpha)}}\right]}{\left[\frac{1}{4E^{(1)}}\right] + \left[\frac{1}{4E^{(2)}}\right]} \tag{2-75}$$

$$\boldsymbol{\delta}_s = \boldsymbol{\tau}_s^{(1)} \cdot \boldsymbol{\delta}_s^{(2)} = \boldsymbol{\tau}_s^{(2)} \cdot \boldsymbol{\delta}_s^{(1)} = \frac{l^2 t^2}{\mathrm{A}} \frac{\left[\frac{1}{4E^{(1)}}\right]\left[\frac{1}{4E^{(2)}}\right]}{\left[\frac{1}{4E^{(1)}}\right]+\left[\frac{1}{4E^{(2)}}\right]} \tag{2-76}$$

- Interface term 1: We can now evaluate the explicit contributions from the interface terms.

The nomenclature L and R correspond to the elements to the left and right of the interface node, respectively.

$$\left(\left\{\mathbb{C}:\boldsymbol{\varepsilon}(\boldsymbol{\eta})\boldsymbol{n}\right\},\left(\left[\!\left[\boldsymbol{u}_{n+1}\right]\!\right]\right)\right)_{\Gamma_\mathrm{I}} = \int_{\Gamma_\mathrm{I}} \left\{\begin{array}{l}\left(\delta_s^{(1)} \cdot E^{(1)} \varepsilon\left(\eta^{(1)}\right) n^{(1)} + \delta_s^{(2)} \cdot E^{(2)} : \varepsilon\left(\eta^{(2)}\right) n^{(1)}\right) \\ \cdot\left(u_{n+1}^{(1)} - u_{n+1}^{(2)}\right)\end{array}\right\} \mathrm{d}\Gamma_\mathrm{I} \tag{2-77}$$

There are four terms in (2-77). We will evaluate each term individually to show where the explicit computed quantities contribute to the element stiffness matrix.

$$\int_{\Gamma_\mathrm{I}} \left(\delta_s^{(1)} \cdot E^{(1)} \varepsilon\left(\eta^{(1)}\right) n^{(1)}\right) u_{n+1}^1 \, \mathrm{d}\Gamma_\mathrm{I} = \delta\eta^{(1)T} K_{\text{Interface1}}^{(\mathrm{LL})} \delta u^{(1)}$$

$$\Rightarrow \quad K_{\text{Interface1}}^{(\mathrm{LL})} = \delta_s^{(1)} E^{(1)} n^{(1)} \int_{-1}^{1} \left(\frac{(-1)^a}{h^e} \frac{1}{2}\left(1+\xi_b \xi\right) \right)\Bigg|_{x=x_2} \frac{lt}{2} d\xi_2 = \delta_s^{(1)} E^{(1)} \cdot \frac{lt}{h^e} \begin{bmatrix} 0 & -1 \\ 0 & 1 \end{bmatrix} \tag{2-78}$$

$$-\int_{\Gamma_\mathrm{I}} \left(\delta_s^{(1)} \cdot E^{(1)} \varepsilon\left(\eta^{(1)}\right) n^{(1)}\right) u_{n+1}^2 \, \mathrm{d}\Gamma_\mathrm{I} = \delta\eta^{(1)T} K_{\text{Interface1}}^{(\mathrm{LR})} \delta u^{(2)}$$

$$\Rightarrow \quad K_{\text{Interface1}}^{(\mathrm{LR})} = -\delta_s^{(1)} E^{(1)} n^{(1)} \int_{-1}^{1} \left(\frac{(-1)^a}{h^e} \frac{1}{2}\left(1+\xi_b \xi\right) \right)\Bigg|_{x=x_3} \frac{lt}{2} d\xi_2 = \delta_s^{(1)} E^{(1)} \cdot \frac{lt}{h^e} \begin{bmatrix} 1 & 0 \\ -1 & 0 \end{bmatrix} \tag{2-79}$$

$$\int_{\Gamma_\mathrm{I}} \left(\delta_s^{(2)} \cdot E^{(2)} \varepsilon\left(\eta^{(2)}\right) n^{(1)}\right) u_{n+1}^{(1)} \, \mathrm{d}\Gamma_\mathrm{I} = \delta\eta^{(2)T} K_{\text{Interface1}}^{(\mathrm{RL})} \delta u^{(1)}$$

$$\Rightarrow \quad K_{\text{Interface1}}^{(\mathrm{RL})} = \delta_s^{(2)} E^{(2)} n^{(1)} \int_{-1}^{1} \left(\frac{(-1)^a}{h^e} \frac{1}{2}\left(1+\xi_b \xi\right) \right)\Bigg|_{x=x_2} \frac{lt}{2} d\xi_2 = \delta_s^{(2)} E^{(2)} \frac{lt}{h^e} \begin{bmatrix} 0 & -1 \\ 0 & 1 \end{bmatrix} \tag{2-80}$$

$$-\int_{\Gamma_\mathrm{I}} \left(\delta_s^{(2)} \cdot E^{(2)} \varepsilon\left(\eta^{(2)}\right) n^{(1)}\right) u_{n+1}^{(2)} \, \mathrm{d}\Gamma_\mathrm{I} = \delta\eta^{(2)T} K_{\text{Interface1}}^{(\mathrm{RR})} \delta u^{(2)}$$

$$\Rightarrow \quad K_{\text{Interface1}}^{(\mathrm{RR})} = -\delta_s^{(2)} E^{(2)} n^{(1)} \int_{-1}^{1} \left(\frac{(-1)^a}{h^e} \frac{1}{2}\left(1+\xi_b \xi\right) \right)\Bigg|_{x=x_3} \frac{lt}{2} d\xi_2 = \delta_s^{(2)} E^{(2)} \frac{lt}{h^e} \begin{bmatrix} 1 & 0 \\ -1 & 0 \end{bmatrix} \tag{2-81}$$

- Interface term 2.1:

$$\left(\left[\!\left[\boldsymbol{\eta}\right]\!\right],\left\{\mathbb{C}:\boldsymbol{\varepsilon}\left(\boldsymbol{u}_{n+1}\right)\boldsymbol{n}\right\}\right)_{\Gamma_\mathrm{I}} = \int_{\Gamma_\mathrm{I}} \left(\eta^{(1)} - \eta^{(2)}\right)\left(\delta_s^{(1)} \cdot E^{(1)} \varepsilon\left(u_{n+1}^{(1)}\right) n^{(1)} + \delta_s^{(2)} \cdot E^{(2)} : \varepsilon\left(u_{n+1}^{(2)}\right) n^{(1)}\right) \tag{2-82}$$

Again, we see that there are four terms that emanate from (2-82) that can be evaluated via the standard procedure. It is to be noted that these terms are the transpose of the terms arising from

(2-78) to (2-81).

- Interface term 2.2

$$\left(\left[\!\left[\boldsymbol{\eta}\right]\!\right],\left\{\left(\boldsymbol{m}\theta\right)\boldsymbol{n}\right\}\right)_{\Gamma_{\mathrm{I}}}=\int_{\Gamma_{\mathrm{I}}}\left(\eta^{(1)}-\eta^{(2)}\right)\left(\delta_s^{(1)}\cdot m^{(1)}\theta_{n+1}^{(1)}n^{(1)}+\delta_s^{(2)}\cdot m^{(2)}\theta_{n+1}^{(2)}n^{(1)}\right)\mathrm{d}\Gamma_{\mathrm{I}} \tag{2-83}$$

Four terms arise from (2-83).

$$\begin{aligned}&\int_{\Gamma_{\mathrm{I}}}\eta^{(1)}\left(\delta_s^{(1)}\cdot m^{(1)}\theta_{n+1}^{(1)}n^{(1)}\right)\mathrm{d}\Gamma_{\mathrm{I}}=\delta\eta^{(1)T}K_{\mathrm{Interface2.2}}^{(\mathrm{LL})}\delta\theta^{(1)}\\&\Rightarrow\quad K_{\mathrm{Interface2.2}}^{(\mathrm{LL})}=\delta_s^{(1)}m^{(1)}n^{(1)}\int_{-1}^{1}\left(\frac{1}{2}\left(1+\xi_a\xi\right)\frac{1}{2}\left(1+\xi_b\xi\right)\right)\Bigg|_{x=x_2}\frac{lt}{2}d\xi_2\\&\qquad=\delta_s^{(1)}m^{(1)}\frac{lt}{2}\overbrace{\begin{bmatrix}0&0\\0&1\end{bmatrix}}^{(\theta_1\ \ \theta_2)}\begin{matrix}\}d_1\\\}d_2\end{matrix}\end{aligned} \tag{2-84}$$

And likewise, the remaining three terms can be calculated.

- Interface term 3: This term corresponds to the interfacial jump in the displacement field.

$$\left(\left[\!\left[\boldsymbol{\eta}_o\right]\!\right],\boldsymbol{\tau}_s\left(\left[\!\left[\boldsymbol{u}_{n+1}\right]\!\right]\right)\right)_{\Gamma_{\mathrm{I}}}=\int_{\Gamma_{\mathrm{I}}}\left(\eta_o^{(1)}-\eta_o^{(2)}\right)\cdot\tau_s\cdot\left(u_{n+1}^{(1)}-u_{n+1}^{(2)}\right)\mathrm{d}\Gamma_{\mathrm{I}} \tag{2-85}$$

We can now assemble the interface contribution for $\mathbb{B}_{\mathrm{mech}}^{\mathrm{Interfacial}}$:

$$K_{\mathrm{Interface\_me}}^{1}=\frac{lt}{h^e}\overbrace{\begin{bmatrix}0&-\delta E^{(1)}&\delta E^{(1)}&0\\0&\delta E^{(1)}&-\delta E^{(1)}&0\\0&-\delta E^{(2)}&\delta E^{(2)}&0\\0&\delta E^{(2)}&-\delta E^{(2)}&0\end{bmatrix}}^{d_1\quad d_2\quad d_3\quad d_4} \tag{2-86}$$

$$K_{\mathrm{Interface\_me}}^{2.1}=\left(K_{\mathrm{Interface\_me}}^{1}\right)^T=\frac{lt}{h^e}\overbrace{\begin{bmatrix}0&0&0&0\\-\delta E^{(1)}&\delta E^{(1)}&-\delta E^{(2)}&\delta E^{(2)}\\\delta E^{(1)}&-\delta E^{(1)}&\delta E^{(2)}&-\delta E^{(2)}\\0&0&0&0\end{bmatrix}}^{d_1\quad d_2\quad d_3\quad d_4} \tag{2-87}$$

$$K_{\mathrm{Interface\_me}}^{2.2}=\frac{lt}{2}\overbrace{\begin{bmatrix}0&0&0&0\\0&\delta m^{(1)}&-\delta m^{(2)}&0\\0&-\delta m^{(1)}&\delta m^{(2)}&0\\0&0&0&0\end{bmatrix}}^{\theta_1\quad\theta_2\quad\theta_3\quad\theta_4}\begin{matrix}\}d_1\\\}d_2\\\}d_3\\\}d_4\end{matrix} \tag{2-88}$$

$$K^{3}_{\text{Interface\_me}} = \tau_s \frac{lt}{2} \overbrace{\begin{bmatrix} 0 & 0 & 0 & 0 \\ 0 & 1 & -1 & 0 \\ 0 & -1 & 1 & 0 \\ 0 & 0 & 0 & 0 \end{bmatrix}}^{d_1 \quad d_2 \quad d_3 \quad d_4} \tag{2-89}$$

where $\delta E^{(1)} = \delta_s^{(1)} E^{(1)}$ and $\delta E^{(2)} = \delta_s^{(2)} E^{(2)}$.

- Coupling term in thermal phase:

$$\left(\omega_o^{(\alpha)}, m^{(\alpha)} \nabla v_{n+1}^{(\alpha)}\right) = \delta\omega^T \underbrace{\left(N_{\text{a}}, m^{(\alpha)} \frac{1}{\Delta t} N_{\text{b},x}\right)}_{K^{ab}_{\text{Thermal Couple}}} \delta u \tag{2-90}$$

$$\Rightarrow \quad K^{(\alpha)}_{\text{Thermal Couple}} = \frac{m^{(\alpha)}}{\Delta t} \int_{\Omega^{(\alpha)}} N_{\text{a}} N_{\text{b},x} \mathrm{d}V = \frac{m^{(\alpha)} \mathrm{A}}{2\Delta t} \overbrace{\begin{bmatrix} -1 & 1 \\ -1 & 1 \end{bmatrix}}^{(d_1 \quad d_2)} \begin{matrix} \theta_1 \\ \theta_2 \end{matrix} \tag{2-91}$$

- Interface terms $\mathbb{B}^{\text{Interfacial}}_{\text{thermal}}$: We now assemble the interface contribution for thermal phase.

$$K^{1}_{\text{Interface\_th}} = \frac{lt}{h^e} \overbrace{\begin{bmatrix} 0 & -\delta k^{(1)} & \delta k^{(1)} & 0 \\ 0 & \delta k^{(1)} & -\delta k^{(1)} & 0 \\ 0 & -\delta k^{(2)} & \delta k^{(2)} & 0 \\ 0 & \delta k^{(2)} & -\delta k^{(2)} & 0 \end{bmatrix}}^{\theta_1 \quad \theta_2 \quad \theta_3 \quad \theta_4} \tag{2-92}$$

$$K^{2}_{\text{Interface\_th}} = \left(K^{1}_{\text{Interface\_th}}\right)^T = \frac{lt}{h^e} \overbrace{\begin{bmatrix} 0 & 0 & 0 & 0 \\ -\delta k^{(1)} & \delta k^{(1)} & -\delta k^{(2)} & \delta k^{(2)} \\ \delta k^{(1)} & -\delta k^{(1)} & \delta k^{(2)} & -\delta k^{(2)} \\ 0 & 0 & 0 & 0 \end{bmatrix}}^{\theta_1 \quad \theta_2 \quad \theta_3 \quad \theta_4} \tag{2-93}$$

$$K^{3}_{\text{Interface\_th}} = \tau_s^{\theta} \frac{lt}{2} \overbrace{\begin{bmatrix} 0 & 0 & 0 & 0 \\ 0 & 1 & -1 & 0 \\ 0 & -1 & 1 & 0 \\ 0 & 0 & 0 & 0 \end{bmatrix}}^{\theta_1 \quad \theta_2 \quad \theta_3 \quad \theta_4} \tag{2-94}$$

where $\delta k^{(1)} = \delta_s^{\theta(1)} k^{(1)}$ and $\delta k^{(2)} = \delta_s^{\theta(2)} k^{(2)}$.

2.5 Numerical Results

2.5.1 1D Elliptic Problem for Heat Equation

The 1D elliptic equation for heat conduction is given as [58]:

$$-\sum_{i=1}^{2}\frac{\mathrm{d}}{dx}\left(k_i\frac{\mathrm{d}\theta_i}{dx}\right)=1;\quad \left[\!\left[\theta\left(\frac{1}{2}\right)\right]\!\right]=0;\quad \alpha_1\frac{\mathrm{d}\theta_1}{dx}\left(\frac{1}{2}\right)=\alpha_2\frac{\mathrm{d}\theta_2}{dx}\left(\frac{1}{2}\right) \tag{2-95}$$

where $i=1,2$ represents two different elements. We consider only two elements with the given data as follows: thermal conductivity $k_1=0.5$ and $k_2=3$, $h_e=1/2$, the width of the interface =0.001, $\mathrm{t}=$ thickness =0.001, $\mathrm{A}=$ cross-section area $=l\times t$, and the boundary conditions are shown in Figure 2.5 with the prescribed temperature field on both ends.

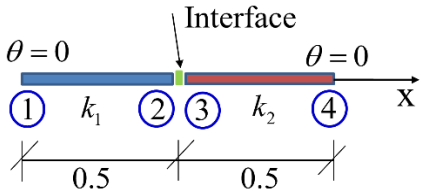

Figure 2.5. Problem description of the 1D elliptic problem with boundary conditions.

The exact solution [58] is given as

$$u_1(x)=\frac{(3k_1+k_2)x}{4k_1^2+4k_1k_2}-\frac{x^2}{2k_1},\qquad x\in[0,0.5] \tag{2-96}$$

$$u_2(x)=\frac{k_2-k_1+(3k_1+k_2)x}{4k_1^2+4k_1k_2}-\frac{x^2}{2k_2},\qquad x\in[0.5,1] \tag{2-97}$$

The element stiffness matrices are calculated as follows:

$$K^{(1)}_{\text{Heat Conduction}}=\frac{\bar{k}^{(1)}\mathrm{A}}{h^e}\overbrace{\begin{bmatrix}1 & -1\\ -1 & 1\end{bmatrix}}^{(\theta_1\ \ \theta_2)};\quad K^{(2)}_{\text{Heat Conduction}}=\frac{\bar{k}^{(2)}\mathrm{A}}{h^e}\overbrace{\begin{bmatrix}1 & -1\\ -1 & 1\end{bmatrix}}^{(\theta_3\ \ \theta_4)} \tag{2-98}$$

The variationally derived interfacial coefficients for this 1-D problem are computed as follows:

$$\tau_s^{\theta}=\left(\tau_s^{\theta(1)}+\tau_s^{\theta(2)}\right)^{-1}=\frac{\mathrm{A}}{t^2}\frac{1}{\left[\frac{1}{4k^{(1)}}\right]+\left[\frac{1}{4k^{(2)}}\right]}=\frac{\mathrm{A}}{l^2t^2}\frac{12}{7} \tag{2-99}$$

$$\delta_s^{\theta(1)T} = \tau_s^{\theta(1)} \cdot \tau_s^{\theta} = \frac{\left[\frac{1}{4k^{(1)}}\right]}{\left[\frac{1}{4k^{(1)}}\right]+\left[\frac{1}{4k^{(2)}}\right]} = \frac{6}{7} \tag{2-100}$$

$$\delta_s^{\theta(2)T} = \tau_s^{\theta(2)} \cdot \tau_s^{\theta} = \frac{\left[\frac{h^e}{2\overline{k}^{(1)}}\right]}{\left[\frac{h^e}{2\overline{k}^{(1)}}\right]+\left[\frac{h^e}{2\overline{k}^{(2)}}\right]} = \frac{1}{7} \tag{2-101}$$

$$\delta_s^{\theta} = \tau_s^{\theta(1)} \cdot \delta_s^{\theta(2)} = \tau_s^{\theta(2)} \cdot \delta_s^{\theta(1)} = \frac{l^2 t^2}{\mathrm{A}} \frac{\left[\frac{1}{4k^{(1)}}\right]\left[\frac{1}{4k^{(2)}}\right]}{\left[\frac{1}{4k^{(1)}}\right]+\left[\frac{1}{4k^{(2)}}\right]} = \frac{l^2 t^2}{\mathrm{A}} \cdot \frac{1}{14} \tag{2-102}$$

Using these coefficients, the interfacial matrices given in Eqn. (2-64) are derived as follows:

$$-\int_{\Gamma_{\mathrm{I}}} \left\{\left(\overline{\boldsymbol{k}} \nabla \theta_{n+1}\right)\boldsymbol{n}\right\} \cdot [\![\omega]\!] \mathrm{d}\Gamma_{\mathrm{I}} \;\Rightarrow\; K^1_{\text{Interface\_th}} = \frac{\tau_s^{\theta} l^3 t^3}{4h^e A} \overbrace{\begin{bmatrix} 0 & -1 & 1 & 0 \\ 0 & 1 & -1 & 0 \\ 0 & 1 & -1 & 0 \\ 0 & -1 & 1 & 0 \end{bmatrix}}^{\theta_1 \quad \theta_2 \quad \theta_3 \quad \theta_4} \tag{2-103}$$

$$-\int_{\Gamma_{\mathrm{I}}} \left\{\left(\overline{\boldsymbol{k}} \nabla \omega\right)\boldsymbol{n}\right\} \cdot \left([\![\theta_{n+1}]\!] - \theta_g\right) \mathrm{d}\Gamma_{\mathrm{I}} \;\Rightarrow\; K^2_{\text{Interface\_th}} = \frac{\tau_s^{\theta} l^3 t^3}{4h^e A} \overbrace{\begin{bmatrix} 0 & 0 & 0 & 0 \\ -1 & 1 & 1 & -1 \\ 1 & -1 & -1 & 1 \\ 0 & 0 & 0 & 0 \end{bmatrix}}^{\theta_1 \quad \theta_2 \quad \theta_3 \quad \theta_4} \tag{2-104}$$

$$\int_{\Gamma_{\mathrm{I}}} [\![\omega]\!] \cdot \boldsymbol{\tau}_s^{\theta} \cdot \left([\![\theta_{n+1}]\!] - \theta_g\right) \mathrm{d}\Gamma_{\mathrm{I}} \;\Rightarrow\; K^3_{\text{Interface\_th}} = \frac{\tau_s^{\theta} l t}{2} \overbrace{\begin{bmatrix} 0 & 0 & 0 & 0 \\ 0 & 1 & 1 & 0 \\ 0 & 1 & 1 & 0 \\ 0 & 0 & 0 & 0 \end{bmatrix}}^{\theta_1 \quad \theta_2 \quad \theta_3 \quad \theta_4} \tag{2-105}$$

Right-hand side body force term is calculated as follows:

$$f^{(\alpha)}_{\text{body force}} = \int_{\Omega^{(\alpha)}} \left(N_{\mathrm{a}}\right) \overline{r} \mathrm{d}V = \int_{x_1}^{x_2} \frac{1}{2}\left(1 + \xi_a \xi\right) \cdot 1 \mathrm{d}V = \mathrm{A} \begin{bmatrix} \frac{h_e}{2} \\ \frac{h_e}{2} \end{bmatrix} = \mathrm{A} \begin{bmatrix} 0.25 \\ 0.25 \end{bmatrix} \tag{2-106}$$

In the next step, we add together all the contributions from both interior and interface terms, and form the stiffness matrix and the external force vector.

$$\overbrace{\begin{bmatrix} 1 & -0.1429 & -0.8572 & 2.0991\times10^{-5} \\ -0.1429 & 8.5707\times10^{3} & -8.5797\times10^{3} & -0.8572 \\ -0.8572 & -8.5797\times10^{3} & 8.5707\times10^{3} & -5.1429 \\ 2.0991\times10^{-5} & -0.8572 & -5.1429 & 6 \end{bmatrix}}^{\theta_1 \quad \theta_2 \quad \theta_3 \quad \theta_4} \begin{bmatrix} \theta_1 \\ \theta_2 \\ \theta_3 \\ \theta_4 \end{bmatrix} = \begin{bmatrix} 0.25 \\ 0.25 \\ 0.25 \\ 0.25 \end{bmatrix} \tag{2-107}$$

Applying the boundary condition $\theta_1 = \theta_4 = 0$, and solving for θ_2 and θ_3, we get $x = 0.5$ at $\theta_2 = \theta_3 = 0.0714$. The exact solution computed through Eqn. (2-96) and (2-97) is: $u_1(x = 0.5) = u_2(x = 0.5) = 0.0714$, and the computed results with only two elements match the exact solution as shown in Figure 2.6. The problem was run with mesh refinement in 1D and the nodally exact solution was observed as shown in Figure 2.6. Figure 2.7 presents $L_2(\Omega)$ norm of the temperature error that converges at the optimal rate for linear elements.

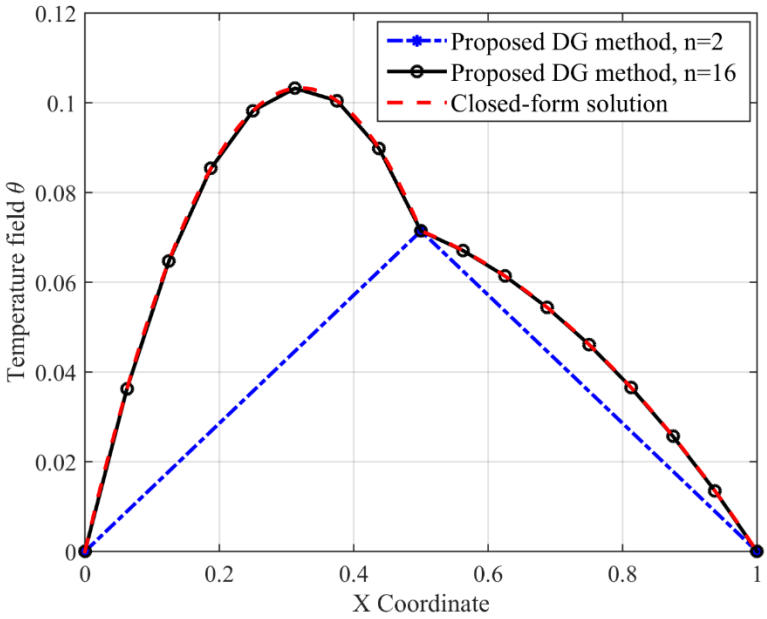

Figure 2.6. Spatial distribution of temperature field for the pure thermal problem.

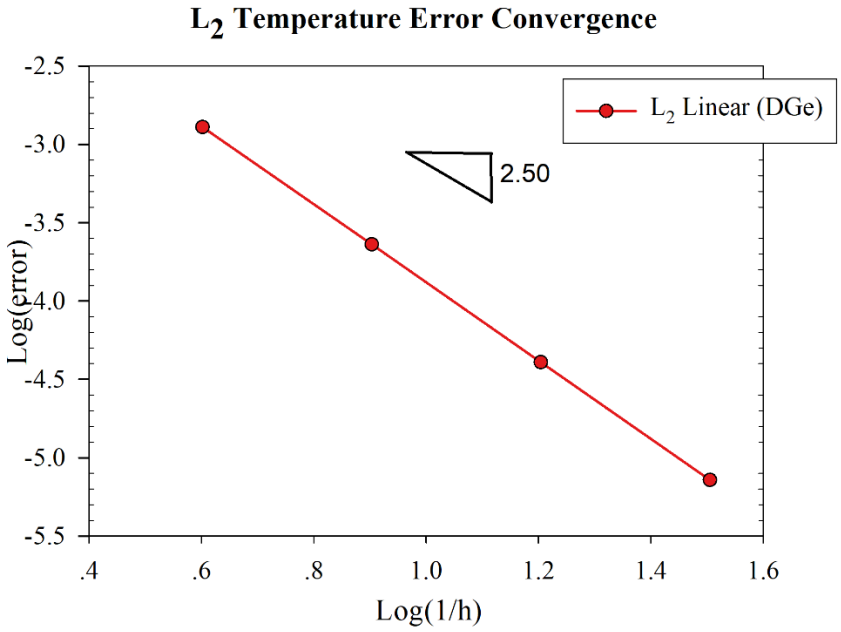

Figure 2.7. $L_2(\Omega)$ Temperature error convergence plot.

2.5.2 2D Heat Equations with Interfaces

This section investigates the performance of the proposed interface method with standard four-node quadrilaterals (Q4) and three-node triangles (T3). All integral expressions for lines and surfaces are evaluated using Gauss quadrature rules of sufficiently high order.

The problem is an extension of the test case employed in section 2.5.1, but now extended to 2D and involves pure thermal loading and no mechanical loading. This problem is inspired by [58] wherein an ordinary differential equation is considered as given in Eqn. (2-95). The biunit domain is (0,1) as shown in Figure 2.8, and the interface is set at $x = 0.5$. As given in [58], there is a closed form solution for this problem as given in Eqn. (2-96) and (2-97).

The geometry is comprised of two rectangular blocks with an interface in the middle as shown in Figure 2.8. Problem is driven with a prescribed heat source of strength $R = 1$. The two blocks have different thermal conductivity properties indicated as k_1 and k_2. Dirichlet boundary conditions are prescribed along the x direction at $y = 0$ and $y = 1$, such that $\theta(y = 0) = \theta(y = 1) = 0$.

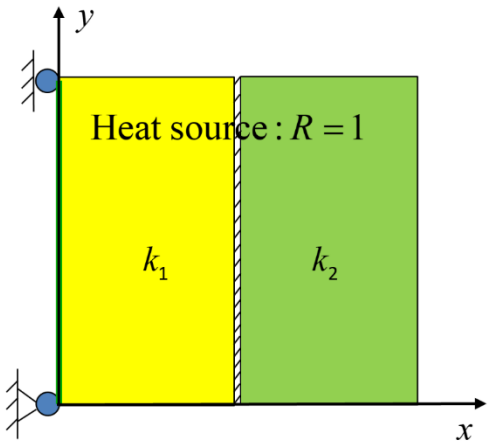

Figure 2.8. Geometry and boundary conditions.

We consider two formulations: one in which interfacial discontinuity is embedded only at $x = 0.5$, while elements within each block have inter-element continuity of the temperature field. This type of formulation is indicated as Q4DG and T3DG. A second formulation considers full DG across every element interface and is indicated as Q4DGe and T3DGe.

For the two mesh types, i.e., Q4 and T3 element meshes, we consider a mesh refinement of $n = [4,8,16,32]$, where n is the number of elements in any direction. The contour plots of the thermal field for mesh size $n = 4$ and $n = 16$ are given in Figure 2.9 (a) and (b), respectively. Figure 2.10 presents the line plots for Q4 element mesh with $n = 4$ and $n = 16$, and the nodally exact solution is attained even with the cruder discretization.

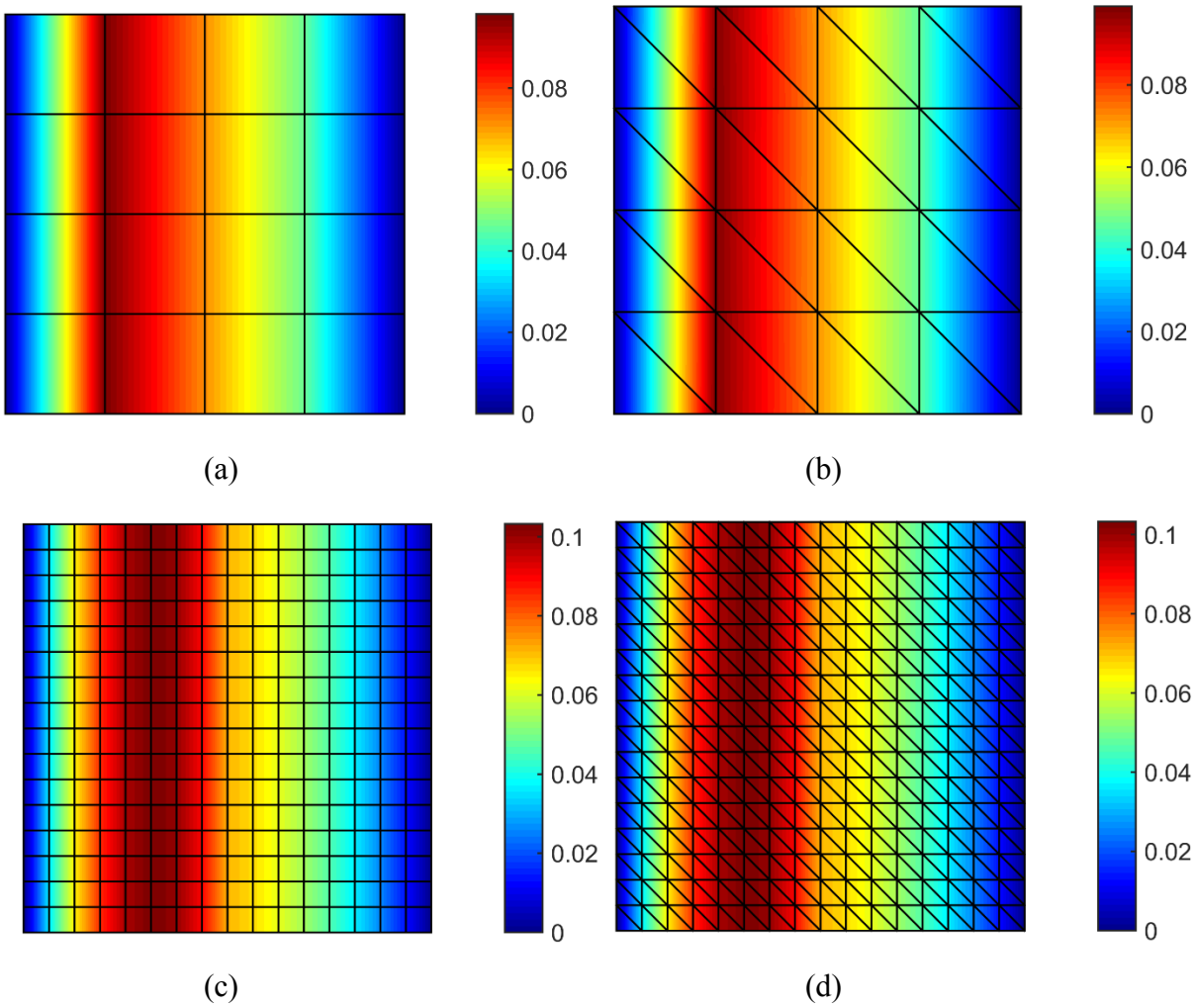

Figure 2.9. Contour plot of the thermal field for the pure thermal problem: (a) Q4 element ($n = 4$); (b) T3 element ($n = 8$); (c) Q4 element ($n = 16$); (d) T3 element ($n = 32$).

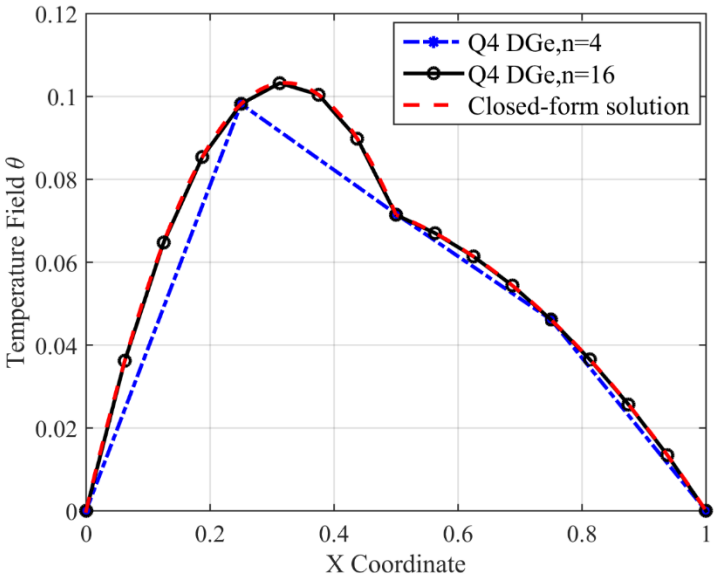

Figure 2.10. Line plot of the thermal field for Q4DGe mesh: $n=4$ and $n=16$.

We have conducted the temperature error convergence study in the $L_2(\Omega)$ norm and $H_1(\Omega)$ semi-norm, and optimal convergence is attained for all element types.

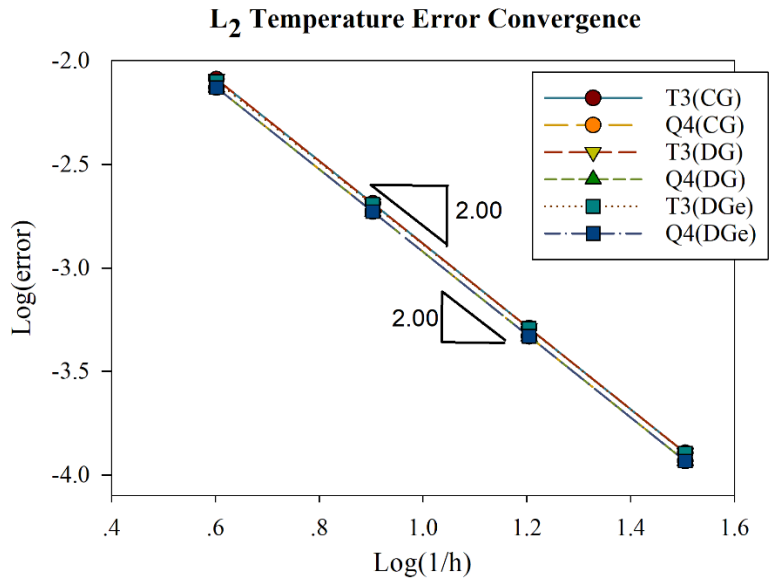

(a)

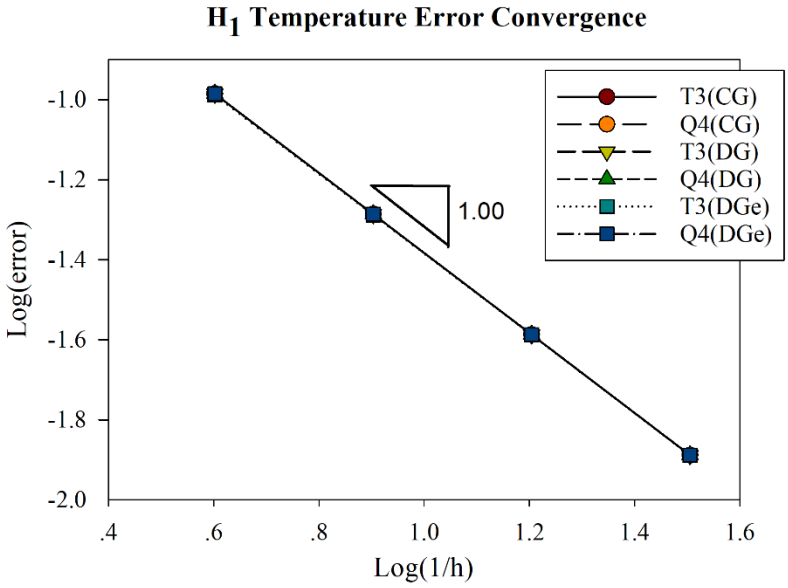

(b)

Figure 2.11. Error convergence plots: (a) $L_2(\Omega)$ norm; (b) $H_1(\Omega)$ semi-norm.

We choose different element types as a distorted T3 element, Highly heterogeneous Q4 element, and composite element with a combination of T3 and Q4 elements. The contour plots with DG at every element boundaries (DGe) are shown in Figure 2.12 to Figure 2.14.

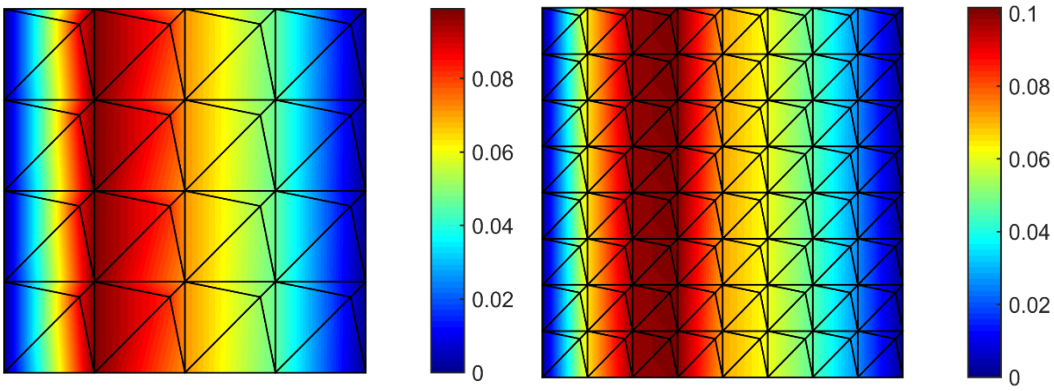

(a) (b)

Figure 2.12. Contour plot of the thermal field for the pure thermal problem (Brezzi T3 element) with different mesh refinements: (a) $n = 4$; (b) $n = 8$.

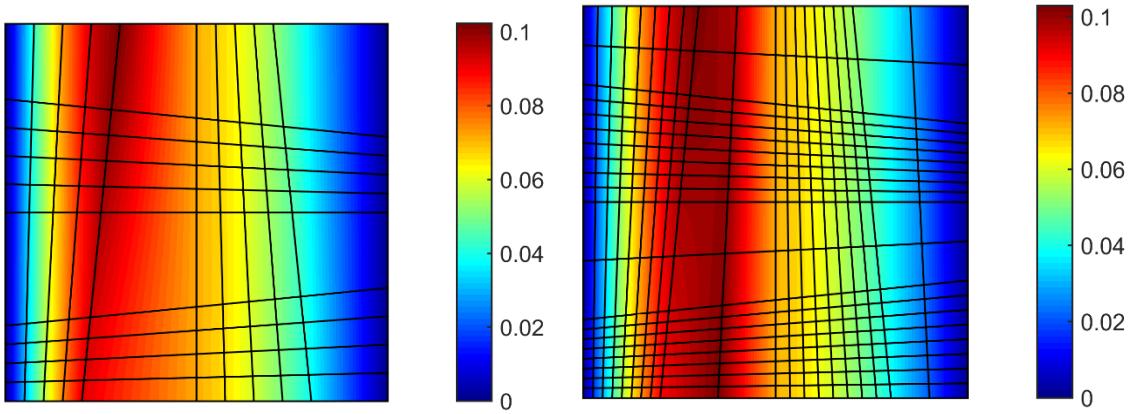

(a) (b)

Figure 2.13. Contour plot of the thermal field for the pure thermal problem (Highly heterogeneous Q4 element) with different mesh refinements: (a) $n = 10$; (b) $n = 20$.

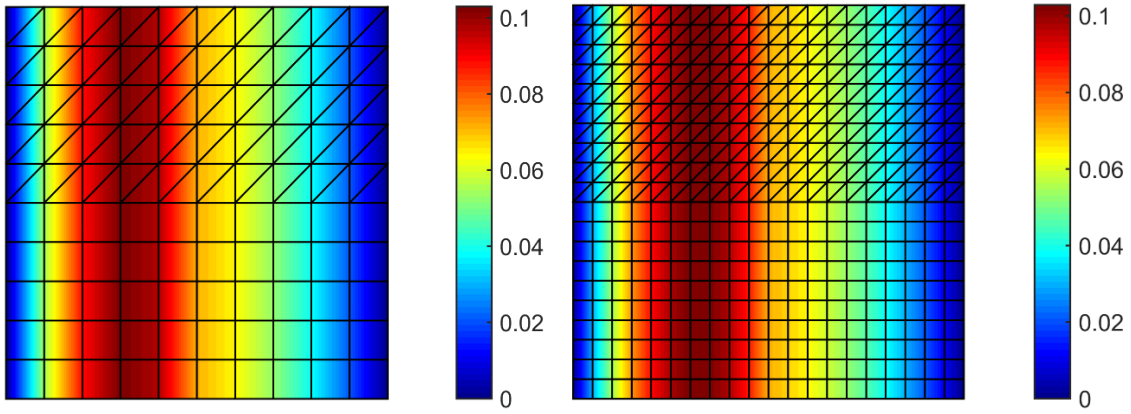

(a) (b)

Figure 2.14. Contour plot of the thermal field for the pure thermal problem (Composite element) with different mesh refinements: (a) $n = 10$; (b) $n = 20$.

We have also chosen a composite mesh type with Q4 and T3 elements, with mesh mismatching on the interface as shown in Figure 2.15.

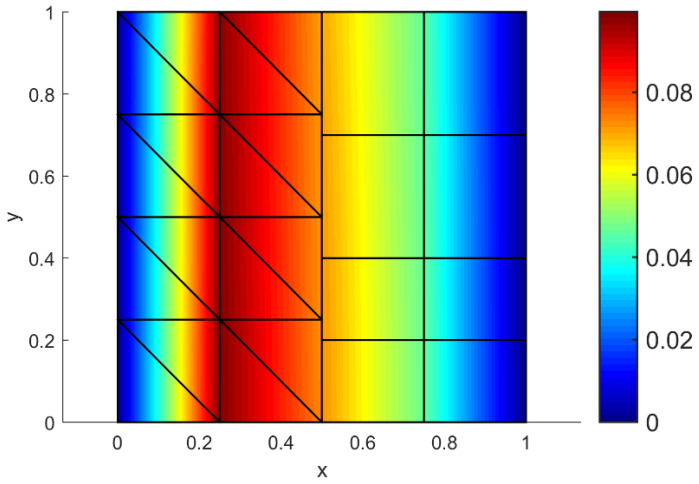

Figure 2.15. Contour plot of the thermal field for the pure thermal problem (Composite element) with nonconforming mesh.

We then combine the normal mesh with the distorted mesh and have conducted the $L_2(\Omega)$ temperature error and $H_1(\Omega)$ temperature error convergence study as given in Figure 2.16 (a) to (d) by comparing the computed values from different element types to the exact solution. Optimal

convergence rates for both $L_2(\Omega)$ and $H_1(\Omega)$ is attained for linear elements Q4 and T3, distorted Q4 and T3 element, and composite element. We have also found that DGe element, DG element and CG element have the similar error norm for this pure thermal problem.

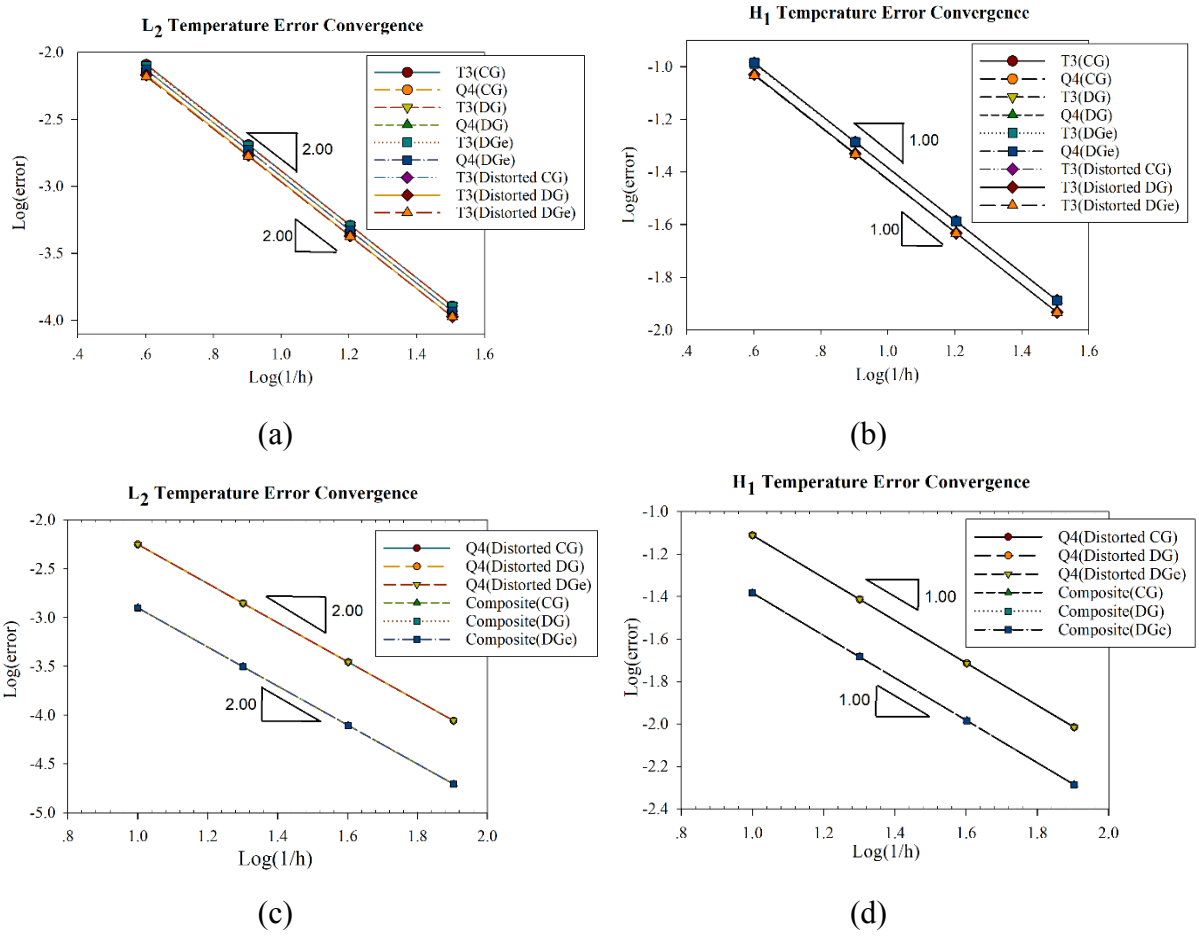

Figure 2.16. Temperature error convergence rate plot: (a) $L_2(\Omega)$ temperature error; (b) $H_1(\Omega)$ temperature error; (c) $L_2(\Omega)$ temperature error; (d) $H_1(\Omega)$ temperature error;

2.5.3 Highly heterogeneous material problem: Case of non-smooth problem

This is the test case of a non-smooth problem that involves sharp material discontinuities with weak singularities at the corners of the material blocks. The geometry is a biunit domain $\Omega = \{(x_1, x_2) \,|\, x_1, x_2 \in (0,1)\mathrm{m}\}$ which is comprised of two different homogeneous materials with different thermal conductivity, arranged in a checkerboard microstructure of 10×10 rows and columns, as shown in Figure 2.17. The thermal conductivity properties are given as: $\boldsymbol{k}^{(1)} = k^{(1)}\boldsymbol{I}$

(black color) with $k^{(1)} = 25\ \mathrm{W}/^{\circ}C$, and $\boldsymbol{k}^{(2)} = k^{(2)}\boldsymbol{I}$ (white color) with $k^{(2)} = 1\ \mathrm{W}/^{\circ}C$.

The objective of this test case is to determine the macroscopic thermal conductivity properties of the specimen. A boundary value problem is set up with prescribed temperature field applied at the boundaries as follows.

$$\theta = 0^{\circ}C \quad \text{on}\,[0, x_2]; \qquad \theta = 1^{\circ}C \quad \text{on}\,[1, x_2] \tag{2-108}$$

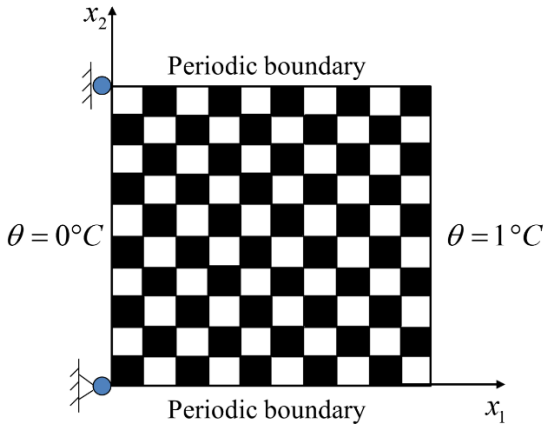

Figure 2.17. Geometric description of the checkerboard problem.

Periodic boundary conditions are applied at the top and bottom surfaces which ensures that the temperature field along these two surfaces is identical to simulate an infinitely long domain.

In a homogenized sense, the average heat flux can be determined as $\overline{q}_i^h = |\Omega|^{-1} \int_\Omega -k(\boldsymbol{x}) \dfrac{\partial T^h}{\partial x_i} d\boldsymbol{x}$. By the definition of the heat flux, we define the associated 'effective' thermal conductivity of the specimen $\tilde{k}^h$ as follows.

$$\overline{q}_i^h = -\tilde{k}^h \overline{\nabla \theta_i} \tag{2-109}$$

The exact solution for the thermal conductivity obtained via homogenization of a checkerboard of infinitely many rows and columns is $\tilde{k} = \sqrt{k^{(1)} k^{(2)}}$, which is first proved by Dychne [3] using duality argument and is extended in other works [43,123]. As stated in [13,64], For high k_1 / k_2 ratio, it is not possible to obtain good approximation of the solution via standard Finite Element method. The strength of the singularity can approach s^{-1} for large k_1 / k_2 value [64]. In this

problem, we compare the computed effective thermal conductivity $\tilde{k}^h$ obtained with the full DG formulation with the exact homogenized thermal conductivity $\tilde{k}$ and CG formulation for different mesh refinements.

Figure 2.18 to Figure 2.22 show the computed temperature field and the heat flux $q = -k(\boldsymbol{x})\dfrac{\partial T^h}{\partial x_i}$ over the domain, with mesh refinement using $\mathrm{n} = [10, 20, 50, 100, 200]$ where n is the number of the element per direction. With full DG elements, we can capture the sharp flux discontinuities over elements, as shown in Figure 2.18 (b) to Figure 2.22 (b). At the two periodic boundaries, the significant singularity is shown in Figure 2.20 (b) to Figure 2.22 (b) with mesh refinement.

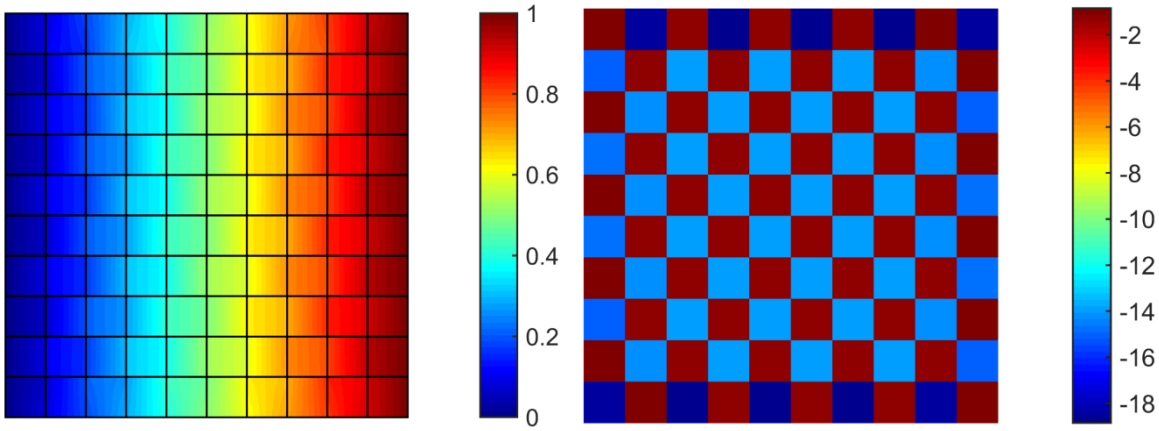

(a) (b)

Figure 2.18. Contour plots with Q4-DGe for the mesh size $n = 10$: (a) temperature field; (b) heat flux field.

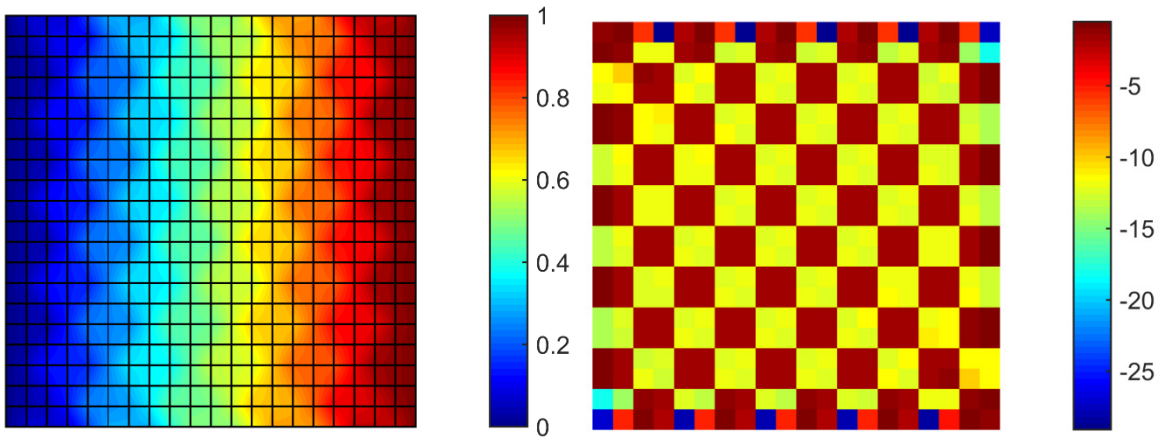

(a) (b)

Figure 2.19. Contour plots with Q4-DGe for the mesh size $n = 20$: (a) temperature field; (b) heat flux field.

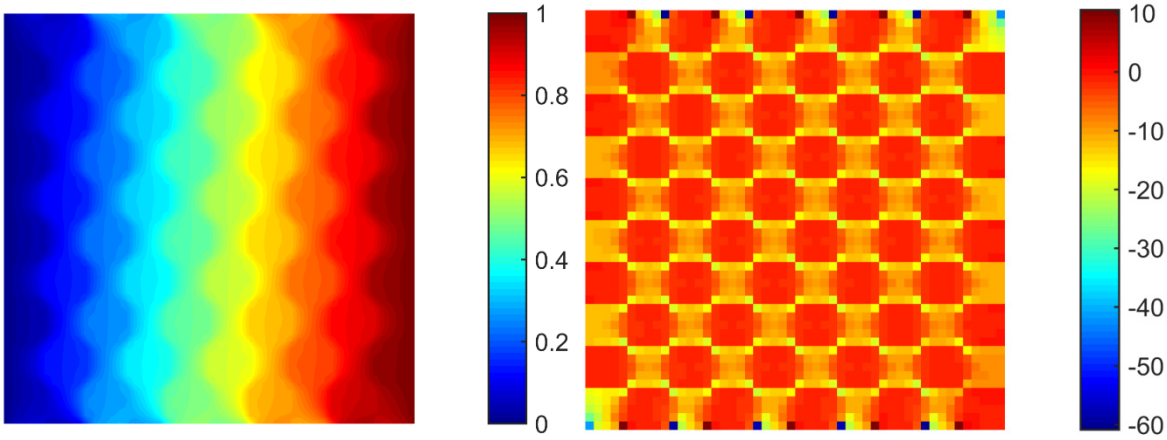

(a) (b)

Figure 2.20. Contour plots with Q4-DGe for the mesh size $n = 50$: (a) temperature field; (b) heat flux field.

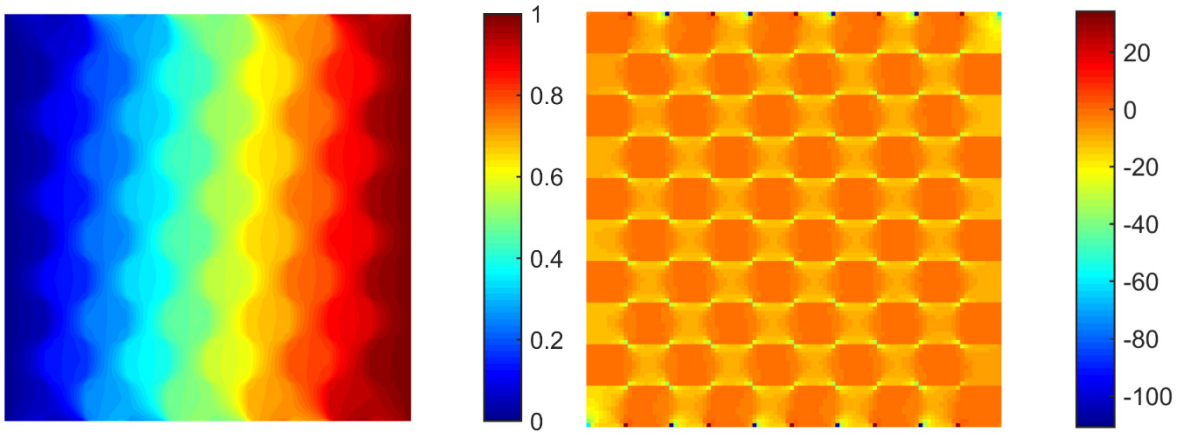

(a) (b)

Figure 2.21. Contour plots with Q4-DGe for the mesh size $n = 100$: (a) temperature field; (b) heat flux field.

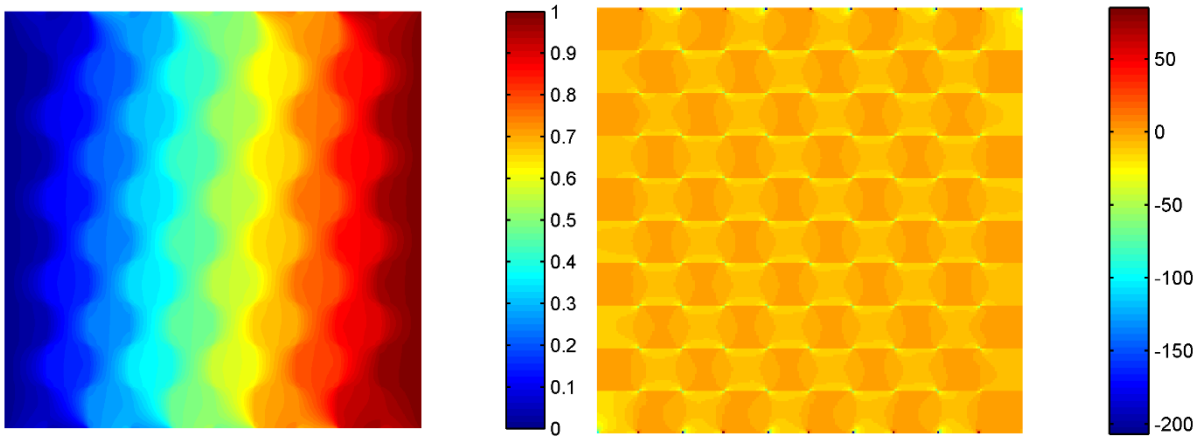

(a) (b)

Figure 2.22. Contour plots with Q4-DGe for the mesh size $n = 200$: (a) temperature field; (b) heat flux field.

The computed average heat flux $\tilde{k}^h$ for different mesh refinements are summarized in Table 2.1, for standard CG, interface DG, and full DG methods (DGe). CG stands for the standard continuous Galerkin formulation. Interface DG stands for the case where interface exists only across the lines of material discontinuity, while elements in the interior of each block have inter-element continuity of the temperature field. Acronym DGe stands for the fully discontinuous formulation from section 2.5. Table 2.1 shows that the DGe method yields solution which is asymptotically close to the exact solution. Furthermore, even with a coarse mesh with $n = 10$, DGe method results in

enhanced accuracy as compared to both CG and DG methods. The results from Table 2.1 are plotted in Figure 2.23, with the average thermal conductivity versus mesh refinement plot, and the engineering convergence rate plot.

Table 2.1. Comparison of the average thermal conductivity $\tilde{k}^h$ between CG, DG, and DGe results.

	$h=10$	$h=20$	$h=50$	$h=100$	$h=200$
CG	13	9.13	7.38	6.69	6.25
DG	13	9.13	7.38	6.69	6.25
DGe	8.14	7.05	6.36	6.06	5.85

In Figure 2.23, the plot shows the comparison of full DG solution with the standard CG solution and the exact solution. The full DG solution has better convergence properties as compared to the standard CG solution.

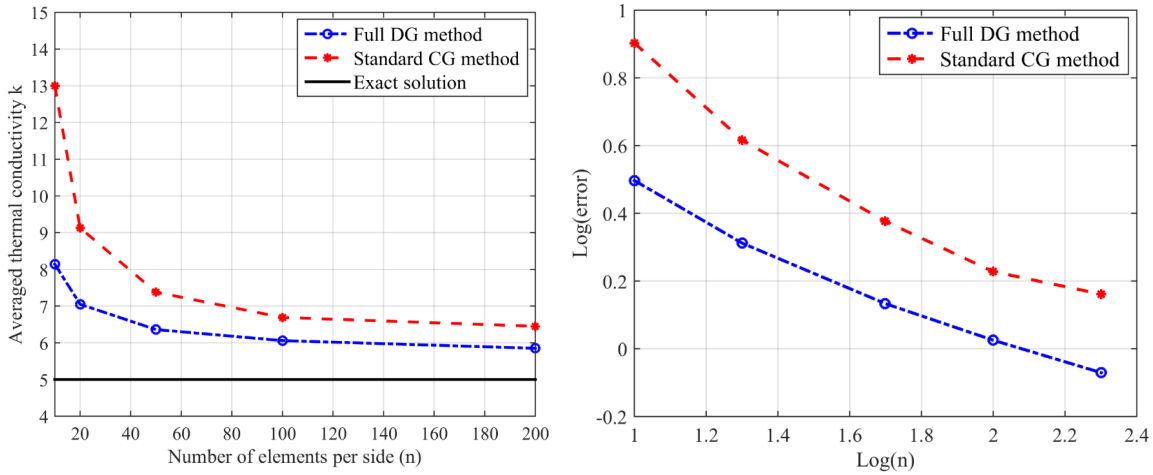

(a) (b)

Figure 2.23. (a) Average thermal conductivity $\tilde{k}^h$ and the exact solution $\tilde{k}$ plot; (b) Engineering convergence plot of the average thermal conductivity.

2.5.4 Thermo-mechanical coupled problem: Thick-walled hollow cylinder

This problem is a test case of the fully coupled thermomechanical problem. We solve a quasi-static thermoelasticity problem in an infinitely long thick-walled cylinder. The schematic description of the problem is shown in Figure 2.24 (a). Considering that the cylinder is long in the z-direction

and it is made of a homogeneous isotropic material, we assume plane strain conditions, and therefore a simplified model is given in Figure 2.24 (b) with the geometry and prescribed boundary conditions. This problem is modeled with full DG method with interfaces along all element boundaries through the radial direction. As shown in Figure 2.24 (b), the inner surface is subjected to a constant pressure $P = 100$ MPa , while the outer surface has a prescribed fixed displacement. Rollers are placed along all the top and bottom surface to convert this 2D problem into a 1D axisymmetric problem. A time-dependent thermal field $\theta = \theta(a,t)$ is applied at the inner surface while the temperature is kept constant at the outer surface $\theta(b,t) = 0$.

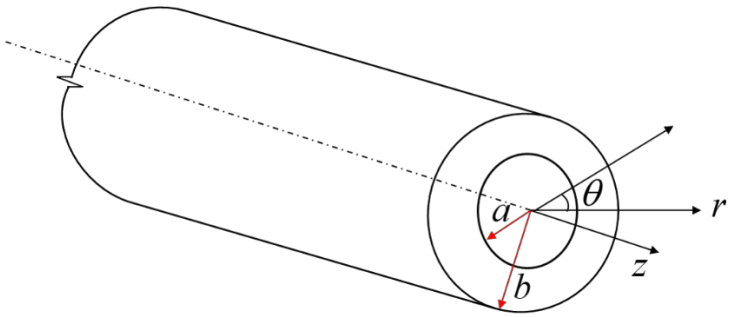

(a)

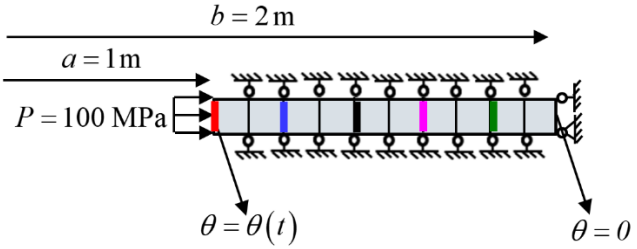

(b)

Figure 2.24. Schematic description: (a) Hollow thick-walled problem; (b) Simplified 2D model in the cylindrical coordinates.

The axisymmetric balance equations of quasi-static thermoelasticity for this problem need to be written in the cylindrical coordinates. By transforming the balance equations (2-1) and (2-2) into cylindrical coordinates, the following strong forms are derived [1, 144].

$$\frac{\partial \sigma_r^{(\alpha)}}{\partial r} + \frac{\left(\sigma_r^{(\alpha)} - \sigma_\theta^{(\alpha)}\right)}{r} = 0 \tag{2-110}$$

$$\rho^{(\alpha)} c_p^{(\alpha)} \dot{\theta}^{(\alpha)} = -\frac{\partial q^{(\alpha)}}{\partial r} - \frac{1}{r} q^{(\alpha)} - m^{(\alpha)} \left(\frac{\partial v^{(\alpha)}}{\partial r} + \frac{v^{(\alpha)}}{r} \right) \tag{2-111}$$

Assuming plain strain conditions, $\sigma_r^{(\alpha)}$ is the radial stress and $\sigma_\theta^{(\alpha)}$ is the hoop stress taking the form:

$$\sigma_r^{(\alpha)} = E^{(\alpha)} \varepsilon_r^{(\alpha)} + \lambda^{(\alpha)} \varepsilon_\theta^{(\alpha)} - m^{(\alpha)} \theta^{(\alpha)} \tag{2-112}$$

$$\sigma_\theta^{(\alpha)} = \lambda^{(\alpha)} \varepsilon_r^{(\alpha)} + E^{(\alpha)} \varepsilon_\theta^{(\alpha)} - m^{(\alpha)} \theta^{(\alpha)} \tag{2-113}$$

where two strains are represented as $\varepsilon_r^{(\alpha)} = \frac{\partial u^{(\alpha)}}{\partial r}$, and $\varepsilon_\theta^{(\alpha)} = \frac{u^{(\alpha)}}{r}$.

We take the material properties from [144] and they are listed in Table 2.2. We consider two different prescribed temperature profiles at inner surface: case (i) Constant temperature profile $\theta(a,t) = \theta_0 = 100\,°C$, and case (ii) Exponentially decaying temperature profile $\theta(a,t) = \theta_0 e^{-\omega t}$. The thermal diffusivity in Table 2.2 is defined as $\alpha = \frac{k}{\rho c_p}$.

Figure 2.25 presents the computed temperature profiles at various time levels plotted along the radial thickness of the cylinder for both case (i) and case (ii). The obtained results compare well with the solution given in [144]. The radial stress $\sigma_r^{(\alpha)}$ and the hoop stress $\sigma_\theta^{(\alpha)}$ are presented in Figure 2.26 and Figure 2.27, respectively, and show that the obtained results from the proposed interfacial DG formulation are stable and accurate in terms of both thermal and mechanical fields.

Table 2.2. Material and geometric properties of the thick-wall cylinder problem.

Elastic modulus E	208 GPa	Inner radius a	1 m
Poisson's ratio v	0.3	Outer radius b	2 m
Thermal diffusivity α	$1\times10^{-5}\,\frac{\mathrm{m}}{\mathrm{s}^2}$	Thermal decay parameter ω	0.001
Thermal expansion β	$12\times10^{-6}\,\frac{1}{°C}$	Density ρ	$7800\,\frac{kg}{m^3}$

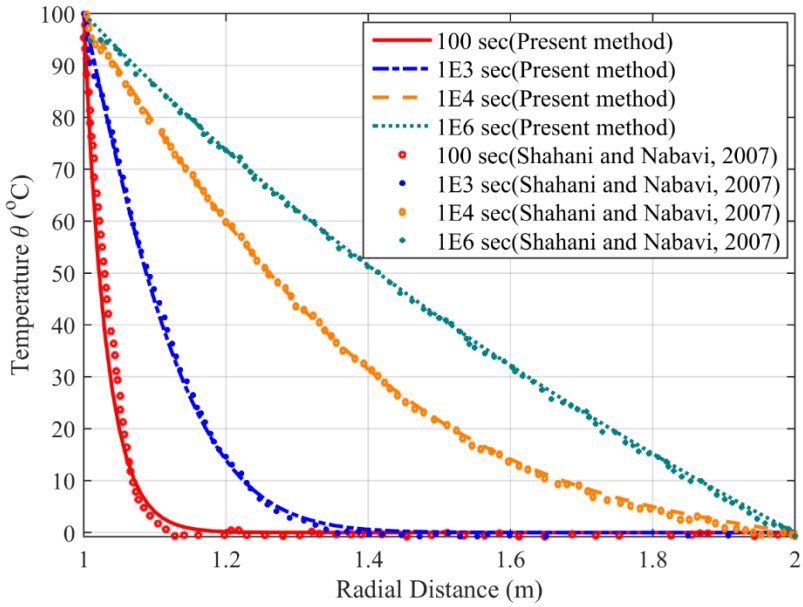

(a)

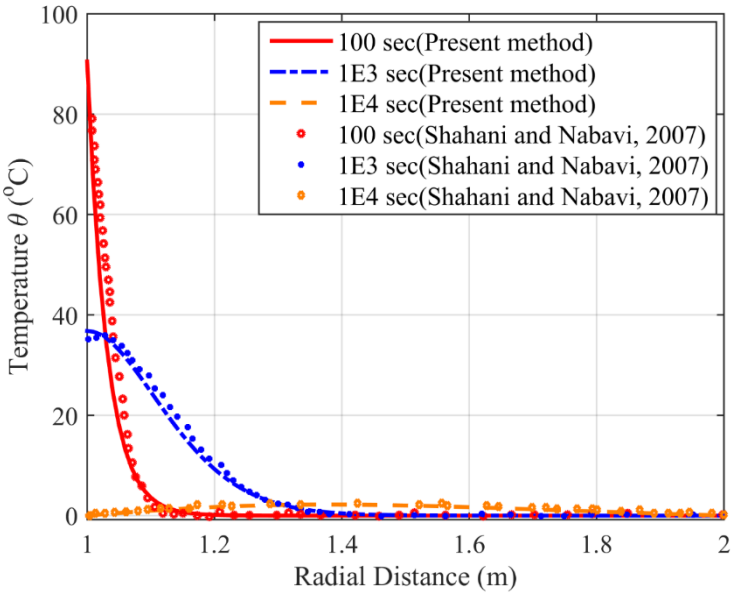

(b)

Figure 2.25. Temperature distribution through the radial direction: (a) Constant temperature; (b) Exponentially decaying temperature.

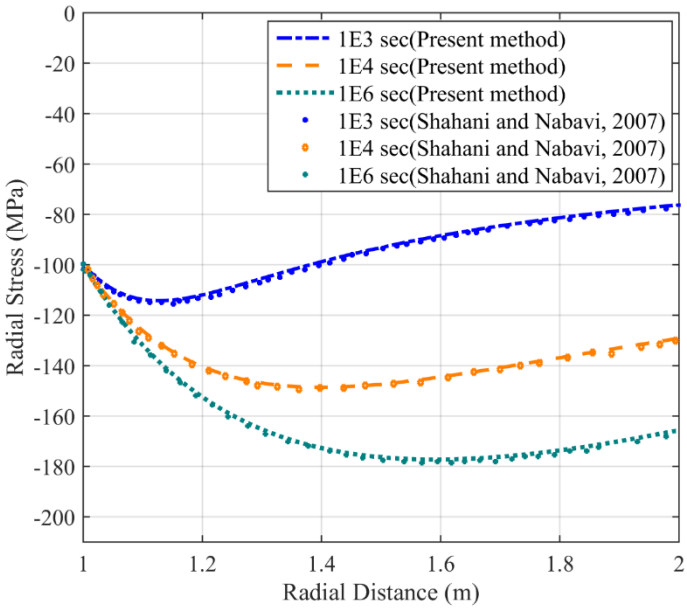

(a)

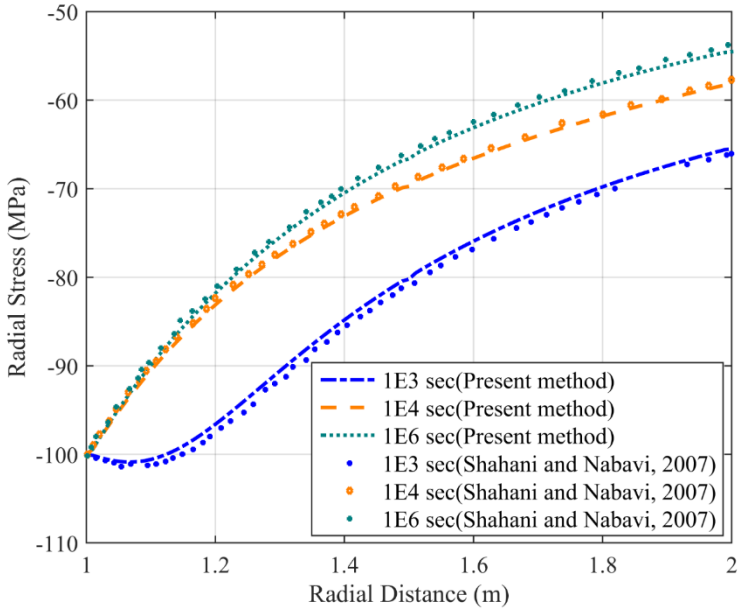

(b)

Figure 2.26. Radial stress distribution through the radial direction: (a) Constant temperature; (b) Exponentially decaying temperature.

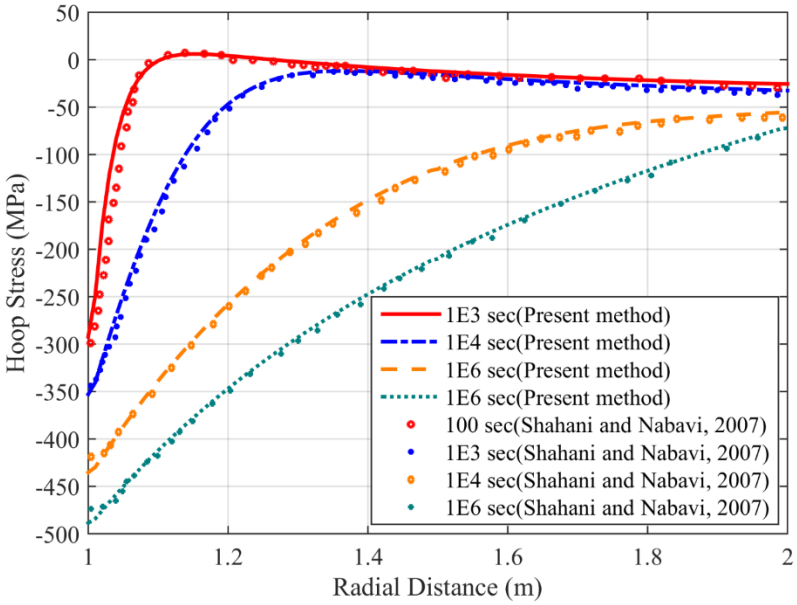

(a)

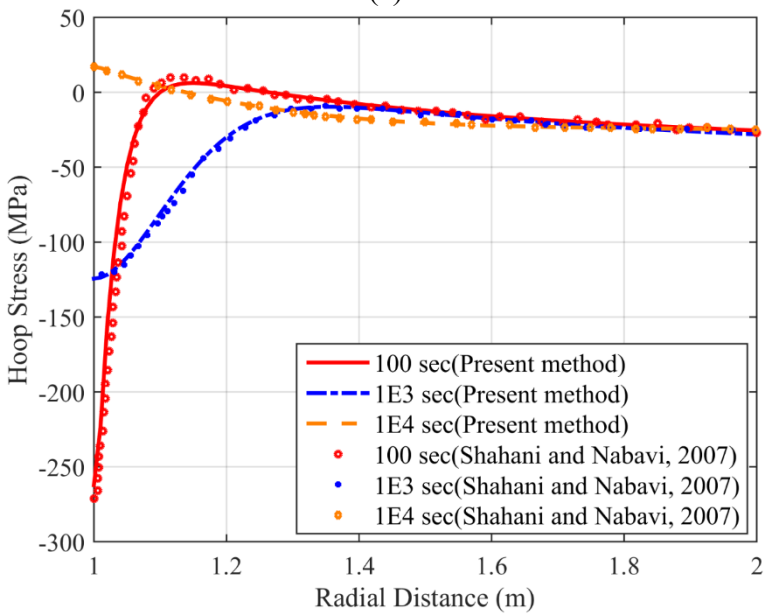

(b)

Figure 2.27. Hoop stress distribution through the radial direction: (a) Constant temperature; (b) Exponentially decaying temperature.

2.6 Conclusions

We have developed a stabilized DG method to accommodate weak and strong discontinuities in mixed field thermomechanical problems. Two formulations are presented. The first formulation is based on the notion of embedding interfaces in otherwise continuous Galerkin formulation and is appropriate for problems with embedded weak and strong continuities. This formulation enjoys

the variational structure of interface terms that can be used to embed physically based models of interfacial kinematics. It is computationally economic because of the reduced computational cost facilitated by the continuous Galerkin ideas in the interior of the subdomains. Since additive manufacturing involves layered deposition of material, rapid curing of material leads to interlayer thermal and residual mechanical stresses that give rise to embedded interfaces. These are sites for development of strong discontinuities, and therefore computational method as presented in this Chapter provide the framework to accommodate these processes.

Starting from a Lagrange multiplier formulation, interface coupling terms for the mechanical and thermal fields are uniformly derived. These DG terms accommodate different mechanical material properties and thermal coefficients across element interfaces. The method is shown to have variational convergence, and optimal rates are attained for 1D and 2D Lagrange elements.

A series of numerical test cases are presented to show the stability and variational convergence properties of the two methods. 1D test problem is presented to describe the evaluation of interfacial terms, and highlight nodal exact computed solution. It also serves as a model problem for implementation of the method. The 2D problem which embedded discontinuity in the thermal conduction property shows optimal convergence in the $L_2(\Omega)$ norm and $H_1(\Omega)$ semi-norm for 4-node quadrilateral and 3-node triangular elements. These elements are tested on a thermal problem with rough coefficients that give rise to domain interior singularities that intensify with mesh refinement. The case with sharp discontinuities in constitutive coefficients highlights the enhanced stability feature of the proposed method for problems with rough coefficients.

CHAPTER 3: FINITE STRAIN PRIMAL INTERFACE FORMULATION WITH CONSISTENTLY EVOLVING STABILIZATION[1]

3.1 Introduction

Finite strain finite element methods have been an area of active interest in the literature [6,89,91,96,131,149,155]. When applied to real materials, weak discontinuities invariably appear, and accurate modeling of these effects has been a focus of several research efforts. Earlier efforts have largely concentrated on continuous Galerkin methods. It was realized that strong discontinuities could still give rise to numerical instabilities in these methods. Considering that the new classes of problems that mechanics is confronted with are comprised of both weak and strong discontinuities, an attempt to embed the provision for accommodating strong discontinuities in the formulation and the method is very attractive. This is the objective of the present chapter.

The Discontinuous Galerkin (DG) method provides an attractive technique for imposing strong consistent formulations compared to the penalty method and does not introduce additional unknown fields as required in Lagrange multiplier methods. Examples from solid mechanics include the relaxation of continuity across element boundaries to treat incompressibility [60,53] as well as the modeling of material interfaces both along element boundaries [161] and within element interiors [5,140].

Some of the earliest methods applying discontinuous approximations to solve boundary value problems include the approaches for hyperbolic problems by Johnson [73] and elliptical problems by Arnold [8]. The latter is commonly termed as an interior penalty method, which was influenced by a method proposed by Nitsche [120] for weakly impose Dirichlet boundary conditions. Subsequently, the Nitsche method has been applied in the area of solid mechanics to treat incompressibility [100] and to handle embedded interfaces and cracks within the FE mesh [5,140,107]. Similar applications exist in the context of fluid mechanics, such as the weak imposition of no-slip conditions for wall bounded flows [18]. An extensive summary of the DG

1 This Chapter has been adapted from "T.J. Truster, P. Chen, A. Masud, Finite strain primal interface formulation with consistently evolving stabilization, Int. J. Numer. Meth. Eng. 102 (2015) 278–315." The copyright owner has provided written permission to reprint the work.

method for linear problems is given by Arnold et al. [9].

The key factors impacting the robustness and efficiency of the DG method are the design of the so-called numerical flux and the penalty or stabilization parameter. Regarding the penalty parameter, studies for embedded interface problems [140] as well as discontinuous discrete approximations [53,31] have shown that selecting a value outside of an optimal range leads to issues with accuracy and stability. Choosing a value that is too low leads to loss of coercivity and results in an ill-posed discrete problem. On the other hand, choosing a value that is too high leads to ill-conditioning in the stiffness matrix as well as to overly strict enforcement of the displacement jump condition. When the jump condition is strictly enforced, the computed response approaches that of a continuous Galerkin method, and the rationale for employing DG is lost. Dimensional analyses indicate that the stability parameter is a function of the element geometry, polynomial order, material properties, and the local interface topology; however, its magnitude can be elusive. The classical approach in the context of linear problems is to estimate the parameter through eigenvalue analyses [49,57]. More recently, in the context of embedded interface problems [5], the values of the parameter for linear simplex elements were determined by conducting a mathematical analysis of the coercivity condition. In particular, definitions for the numerical flux and penalty parameter emerged that involved a weighting of the element size and material properties across the interface. In contrast, the standard definition for the numerical flux in DG methods [9] assumes an equal weighting of the flux field from each side of the interface, which is postulated based on the assumption of mesh uniformity. Other interface methods have previously employed either area weighting [58] or stiffness weighting [140] alone. Additional techniques for defining the penalty parameter for linear problems include developments using bubble functions [45,111] and the Variational Multiscale method [162].

For the case of finite strain solid mechanics problems, the design of the stability parameter becomes more delicate because the material constitutive law evolves with the deformation, thereby implying that the stability estimates also evolve. In recent years, multiple nonlinear DG methods have been proposed for solving elasticity and plasticity problems, for which we cite [53, 107, 52,84,104,170,118,141,122]. Across each of these studies, the value of the penalty parameter was treated as a user-defined parameter that was calibrated for particular numerical test cases; only a few mathematical analyses have been undertaken for the nonlinear problem [51,125]. However other researchers have shown [52,51] that prescribing a value a priori may not lead to a robust

method, particularly when the simulated response involves large deformations or material instability. These authors proposed an adaptive/intelligent yet heuristic method for evolving the penalty parameter separately along each element interface by evaluating the minimum eigenvalue of the acoustic tensor of material moduli. These studies indicate that the increasing degrees of complexity encountered in finite strain problems calls for a sophistication of the underlying variational formulation of the DG method. In particular, the lack of a well-defined value for the penalty parameter has been a cause for concern that has limited the adoption of this method by the general research community [5].

In this work, we set out to derive a DG method for large strain kinematics in which computable expressions for the numerical flux and penalty parameter naturally arise. The derivation parallels our previous work for linear elasticity [162], where an underlying Lagrange multiplier formulation for the interface constraints is converted into a primal formulation. By viewing the problem in light of the Variational Multiscale philosophy, the mixed formulation gives rise to numerical fine scales locally at the interface due to sources of instability such as mesh nonconformity or significant material mismatch. Herein, the associated fine-scale weak form is approximated locally over segments of the interface by representing the fine-scale fields using edge bubble functions, resulting in fine-scale models that account for the constitutive response and element geometry on each side of the interface. By embedding these models into the coarse-scale weak form, a displacement-based interface formulation is obtained through local condensation of the multiplier field. The terms in the formulation share a resemblance with nonlinear interior penalty DG methods, such as the interface method presented in [107]. However, the present formulation contains consistent definitions for the penalty parameter along with a weighted numerical flux that is directly linked to the fine-scale models. Namely, the value of the penalty parameter and flux weights can vary spatially along the interface from element to element due to the local characteristics of the fine-scale models, a feature that is reported in [162].

A distinguishing feature in the present context is that the fine-scale models evolve with the material and geometric nonlinearity exhibited near the interface. Therefore, through their dependence on the fine-scale models, the algorithmic interface parameters are updated automatically in a consistent fashion as the nonlinear problem evolves. The resulting method is free from tunable parameters and capable of handling nonconforming meshes and material mismatch along discrete interfaces undergoing general large deformations. A straightforward generalization of the

derivations enables fully discontinuous functional approximations throughout the domain in line with the traditional meaning for Discontinuous Galerkin, see, e.g. [53,51]. A series of numerical tests are conducted employing nonconforming interfaces or discontinuous approximations across a spectrum of deformation modes to assess the stability and robustness of the method.

In the following section, we begin by discussing the underlying Lagrange multiplier formulation for imposing continuity across interfaces in the finite deformation context in section 3.2. The derivation of the stabilized interface formulation employing the Variational Multiscale method is presented in section 3.3. The approach is subsequently extended to domains containing multiple interfaces in section 3.4. Key aspects regarding the implementation of the fine-scale models are discussed in section 3.5. In section 3.6, multiple benchmark problems are considered, including an error convergence analysis. Finally, we give concluding remarks in section 3.7.

3.2 Governing Equations and Mixed Interfacial Weak Form

As a model problem, we consider a deformable body $\Omega \subset \mathbb{R}^{n_{sd}}$ that is cut into two disjoint regions $\Omega^{(1)}$ and $\Omega^{(2)}$ by an interface of interest Γ_I; an illustration is given in Figure 3.1 (a) – (b), in which the regions are visibly separated for clarity. The case of multiple interfaces, such as encountered in the context of Discontinuous Galerkin methods, is accommodated by a straightforward generalization of the following developments. Throughout, we denote quantities with counterparts in both regions by a superscript (α), where α takes the value 1 or 2. Additionally, we suppress the superscripts in some expressions that apply equally to both regions in order to simplify the presentation.

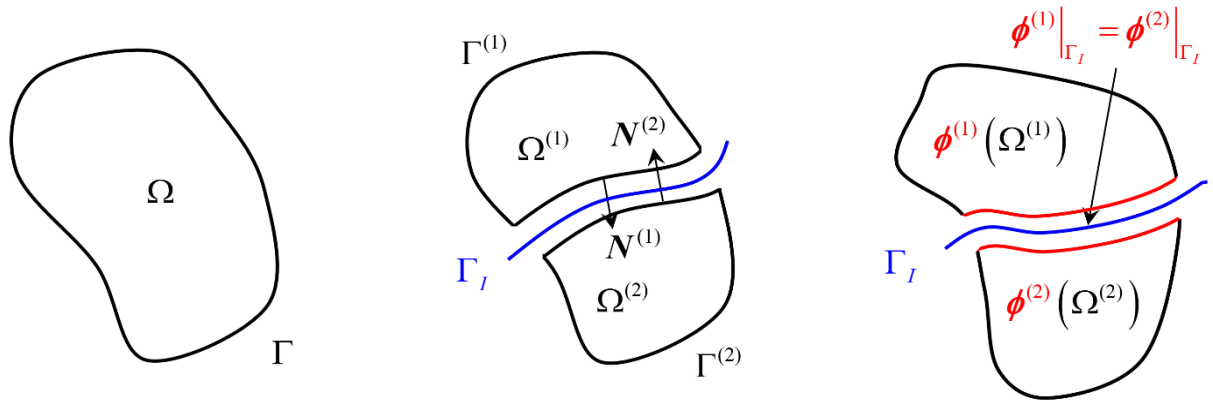

(a) (b) (c)

Figure 3.1. (a) Single domain Ω; imposition of interface Γ_I; (c) deformed configuration generated by $\boldsymbol{\phi}^{(1)}$ and $\boldsymbol{\phi}^{(2)}$.

We denote points in the reference configuration by $\boldsymbol{X} \in \Omega^{(1)} \bigcup \Omega^{(2)}$ and their corresponding images in the current configuration by $\boldsymbol{x}$. The current position of each region $\Omega^{(\alpha)}$ at time t is given by the image of all points $\boldsymbol{X} \in \Omega^{(\alpha)}$ under the deformation map $\boldsymbol{\phi}^{(\alpha)}(\boldsymbol{X},t)$ such that $\boldsymbol{x}(\boldsymbol{X},t) = \boldsymbol{\phi}^{(\alpha)}(\boldsymbol{X},t)$. An example of the deformed configuration is depicted in Figure 3.1 (c). We also define the displacement field associated with the deformation $\boldsymbol{\phi}^{(\alpha)}$ as $\boldsymbol{u}^{(\alpha)}(\boldsymbol{X},t) = \boldsymbol{x}(\boldsymbol{X},t) - \boldsymbol{X}$. Finally, the deformation gradient $\boldsymbol{F}^{(\alpha)}(\boldsymbol{X},t)$ emanating from $\boldsymbol{\phi}^{(\alpha)}(\boldsymbol{X},t)$ is obtained as:

$$\boldsymbol{F}(\boldsymbol{X},t) \equiv \frac{\partial \boldsymbol{x}}{\partial \boldsymbol{X}} = \text{GRAD}\ \boldsymbol{x} \tag{3-1}$$

Although the deformations $\boldsymbol{\phi}^{(\alpha)}$ could in general take distinct values along Γ_I, we desire that the domains $\Omega^{(1)}$ and $\Omega^{(2)}$ remain compatible and equilibrated with respect to each other for all time such that the image of the body $\Omega = \Omega^{(1)} \bigcup \Omega^{(2)}$ remains contiguous. Namely, as shown in Figure 3.1 (c), while the interface may deform and translate, these motions are subject to the constraint that the mapped portions of the boundary $\boldsymbol{\phi}^{(\alpha)}(\Gamma^{(\alpha)} \bigcap \Gamma_I)$ must coincide and conform within this zone. Thus, the equilibrium equation and boundary conditions for each region $\Omega^{(\alpha)}$ are combined with the statements of deformation continuity and balance of tractions along Γ_I to yield the

following system of equations for the composite domain Ω:

$$\text{DIV}\,\boldsymbol{P}^{(\alpha)}\left(\boldsymbol{F}^{(\alpha)}\right)+\rho_o^{(\alpha)}\boldsymbol{B}^{(\alpha)}=\boldsymbol{0} \qquad \text{in} \quad \Omega^{(\alpha)},\ \alpha=1,2 \tag{3-2}$$

$$\boldsymbol{\phi}^{(\alpha)}=\boldsymbol{X}^{(\alpha)} \qquad \text{on}\ \ \Gamma^{(\alpha)}\setminus\Gamma_{\text{I}},\ \alpha=1,2 \tag{3-3}$$

$$\boldsymbol{\phi}^{(1)}-\boldsymbol{\phi}^{(2)}=\boldsymbol{0} \qquad \text{on}\ \ \Gamma_{\text{I}} \tag{3-4}$$

$$\boldsymbol{P}^{(1)}\cdot\boldsymbol{N}^{(1)}+\boldsymbol{P}^{(2)}\cdot\boldsymbol{N}^{(2)}=\boldsymbol{0} \qquad \text{on}\ \ \Gamma_{\text{I}} \tag{3-5}$$

where $\boldsymbol{B}^{(\alpha)}$ is the mass-specific body force, $\rho_o^{(\alpha)}$ is the referential mass density, $\text{DIV}\left(\bullet\right)=\text{tr}\left[\text{GRAD}\left(\bullet\right)\right]$ is the material divergence operator, and $\boldsymbol{N}^{(\alpha)}$ is the unit outward normal on the region boundary $\Gamma^{(\alpha)}$. The first Piola-Kirchhoff stress tensor is denoted by $\boldsymbol{P}^{(\alpha)}$, and we restrict our current focus to hyperelastic materials such that $\boldsymbol{P}^{(\alpha)}$ is derived from an associated strain energy density function $W^{(\alpha)}\left(\boldsymbol{F}^{(\alpha)};\boldsymbol{X}\right)$:

$$\boldsymbol{P}^{(\alpha)}=\frac{\partial W^{(\alpha)}}{\partial\boldsymbol{F}^{(\alpha)}} \tag{3-6}$$

We assume for simplicity that $W^{(\alpha)}$ is spatially homogeneous, i.e. $W^{(\alpha)}=W^{(\alpha)}\left(\boldsymbol{F}^{(\alpha)}\right)$; however, we in general allow distinct material models such that $W^{(1)}\left(\boldsymbol{F}\right)\neq W^{(2)}\left(\boldsymbol{F}\right)$. Additionally, we have prescribed homogeneous Dirichlet conditions on the external boundaries in order to focus on the interfacial contributions in the following developments; the results are easily extended to treat nonhomogeneous boundary conditions or Neumann (traction) conditions.

Two classical techniques exist for weakly imposing the interface conditions (3-4) to (3-5): the penalty method and the Lagrange multiplier method. While the penalty method is conceptually simple and easy to implement, it suffers from the inconsistent enforcement of the traction balance (3-5) which is resolved only in the limit as the penalty parameter approaches infinity. Also, overly large values of the penalty parameter yield ill-conditioning in the global stiffness matrix, which can be detrimental to the stability of the nonlinear solution procedure [52,21] or of the iterative linear equation solver [31]. In contrast, the Lagrange multiplier technique consistently enforces (3-4) to (3-5) through the incorporation of an auxiliary unknown field $\boldsymbol{\lambda}$ at the interface. Thus, we adopt this technique as the starting point for developing our proposed formulation. The associated

weak form is stated as: Find $\left\{\boldsymbol{\phi}^{(1)},\boldsymbol{\phi}^{(2)},\boldsymbol{\lambda}\right\}\in\mathcal{S}^{(1)}\times\mathcal{S}^{(2)}\times\mathcal{Q}$ such that for all $\left\{\boldsymbol{\eta}_o^{(1)},\boldsymbol{\eta}_o^{(2)}\right\}\in\mathcal{V}^{(1)}\times\mathcal{V}^{(2)}\times\mathcal{Q}$:

$$\sum_{\alpha=1}^{2}\int_{\Omega^{(\alpha)}}\text{GRAD}\,\boldsymbol{\eta}_o^{(\alpha)}:\boldsymbol{P}^{(\alpha)}\,\mathrm{d}V-\sum_{\alpha=1}^{2}\int_{\Omega^{(\alpha)}}\rho_o^{(\alpha)}\boldsymbol{B}^{(\alpha)}\cdot\boldsymbol{\eta}_o^{(\alpha)}\,\mathrm{d}V-\int_{\Gamma_{\mathrm{I}}}\boldsymbol{\lambda}\cdot[\![\boldsymbol{\eta}_o]\!]\,\mathrm{d}A=0 \tag{3-7}$$

$$-\int_{\Gamma_{\mathrm{I}}}\boldsymbol{\mu}\cdot[\![\boldsymbol{\phi}]\!]\,\mathrm{d}A=0 \tag{3-8}$$

Herein, the Lagrange multiplier field $\boldsymbol{\lambda}$ has the connotation of the traction field on Γ_{I} derived from region $\Omega^{(1)}$. Also, we have introduced the jump operator $[\![\bullet]\!]=(\bullet)^{(1)}-(\bullet)^{(2)}$ defined for vector-valued fields on interface Γ_{I}. Although this definition depends on the ordering of the domains as in [162], the final weak form obtained at the completion of the derivations is independent of the ordering. We specify the functional spaces contained in (3-7)-(3-8) as:

$$\mathcal{S}^{(\alpha)}=\left\{\boldsymbol{\phi}^{(\alpha)}\,\middle|\,\boldsymbol{\phi}^{(\alpha)}\in\left[H^1\left(\Omega^{(\alpha)}\right)\right]^{n_{\mathrm{sd}}},\ \det\left(\boldsymbol{F}^{(\alpha)}\left(\boldsymbol{\phi}^{(\alpha)}\right)\right)>0,\ \ \boldsymbol{\phi}^{(\alpha)}\big|_{\Gamma^{(\alpha)}\setminus\Gamma_{\mathrm{I}}}=\boldsymbol{X}^{(\alpha)}\right\} \tag{3-9}$$

$$\mathcal{V}^{(\alpha)}=\left\{\boldsymbol{\eta}_o^{(\alpha)}\,\middle|\,\boldsymbol{\eta}_o^{(\alpha)}\in\left[H_o^1\left(\Omega^{(\alpha)}\right)\right]^{n_{\mathrm{sd}}},\ \boldsymbol{\eta}_o^{(\alpha)}\big|_{\Gamma^{(\alpha)}\setminus\Gamma_{\mathrm{I}}}=\boldsymbol{0}\right\} \tag{3-10}$$

$$\mathcal{Q}=\left\{\boldsymbol{\lambda}\,\middle|\,\boldsymbol{\lambda}\in\left[H^{-\frac{1}{2}}\left(\Gamma_{\mathrm{I}}\right)\right]^{n_{\mathrm{sd}}}\right\} \tag{3-11}$$

An alternate viewpoint for obtaining expressions (3-7)-(3-8) is through finding the saddle point $\left\{\boldsymbol{\phi}^{(1)},\boldsymbol{\phi}^{(2)},\boldsymbol{\lambda}\right\}$ of the following interface potential functional (see e.g. [79]):

$$\Pi\left(\boldsymbol{\phi}^{(1)},\boldsymbol{\phi}^{(2)},\boldsymbol{\lambda}\right)=\sum_{\alpha=1}^{2}\left[\int_{\Omega^{(\alpha)}}W^{(\alpha)}\left(\boldsymbol{F}^{(\alpha)}\right)\mathrm{d}V-\int_{\Omega^{(\alpha)}}\rho_o^{(\alpha)}\boldsymbol{B}^{(\alpha)}\cdot\boldsymbol{\phi}^{(\alpha)}\,\mathrm{d}V\right]-\int_{\Gamma_I}\boldsymbol{\lambda}\cdot[\![\boldsymbol{\phi}^{(\alpha)}]\!]\,\mathrm{d}A \tag{3-12}$$

This expression, which clearly possesses an underlying variational structure, will serve as the point of departure for the developments in the following sections. Preserving the characteristics of this structure will be an important concern through the derivations that follow.

3.3 Multiscale Decomposition

Our objective at this point is to convert the preceding Lagrange multiplier formulation into a stabilized pure-displacement method reminiscent of the standard Discontinuous Galerkin method. By doing so, we can avoid the two main shortcomings of the Lagrange multiplier method, namely the inclusion of additional unknowns to solve for and the stability issues associated with the mixed

field problems. While the mixed weak form (3-7)-(3-8) is well-posed in the continuum setting for most classes of deformations, the question of stability is more delicate for the discrete counterpart. Specifically, the choice of approximation for the deformation and multiplier spaces must satisfy the inf-sup condition, commonly termed as the Babuška–Brezzi (BB) condition [28], the analysis of which can be difficult in the nonlinear setting [63,121]. Additional complications for selecting appropriate multipliers spaces arise when the discretizations of regions $\Omega^{(1)}$ and $\Omega^{(2)}$ are nonconforming. To avoid these issues, we employ the general framework of Masud and Scovazzi [97] for mathematically non-smooth problems and consistently combine the stabilized linear Discontinuous Galerkin methods presented by Truster and Masud [162] with the stabilized finite deformation formulation of Masud and Truster [101] to derive a stabilized finite strain interface method. The underlying philosophy common to each of these works is the Variational Multiscale (VMS) method [69], which has served as a platform for developing methods with enhanced stability across solid mechanics [99,100, 101, 102] and fluid mechanics [18, 92,94].

The key idea of the VMS philosophy is that the solution field is decomposed into coarse scales, often associated with the discrete function space, and fine scales, associated with the features of the solution unresolved by the discrete space. Presently, we follow [101] and assume an overlapping decomposition of the deformation map $\boldsymbol{\phi}^{(\alpha)}$ in each region $\Omega^{(\alpha)}$ consisting of a fine-scale deformation $\tilde{\boldsymbol{\phi}}^{(\alpha)}$ superimposed upon a coarse-scale deformation $\hat{\boldsymbol{\phi}}^{(\alpha)}$. This deformation can be expressed in terms of the multiscale displacement field as follows:

$$\boldsymbol{\phi} = \tilde{\boldsymbol{\phi}} \circ \hat{\boldsymbol{\phi}} = \boldsymbol{X} + \hat{\boldsymbol{u}} + \tilde{\boldsymbol{u}} \tag{3-13}$$

$$\hat{\boldsymbol{\phi}}\left(\boldsymbol{X}\right) = \boldsymbol{X} + \hat{\boldsymbol{u}}\left(\boldsymbol{X}\right) \equiv \hat{\boldsymbol{x}} \tag{3-14}$$

$$\tilde{\boldsymbol{\phi}}\left(\hat{\boldsymbol{x}}\right) = \hat{\boldsymbol{x}} + \tilde{\boldsymbol{u}}\left(\hat{\boldsymbol{x}}\right) \tag{3-15}$$

An illustrative example of the decomposed deformation is presented in Figure 3.2 for region $\Omega^{(1)}$. As highlighted in [101], a multiplicative decomposition of the deformation gradient $\boldsymbol{F}^{(\alpha)}$ follows from substituting (3-13) into (3-1):

$$\boldsymbol{F}\left(\boldsymbol{X}\right) = \frac{\partial \boldsymbol{x}}{\partial \boldsymbol{X}} = \frac{\partial \boldsymbol{x}}{\partial \hat{\boldsymbol{x}}} \cdot \frac{\partial \hat{\boldsymbol{x}}}{\partial \boldsymbol{X}} = \left[\boldsymbol{1} + \frac{\partial \tilde{\boldsymbol{u}}}{\partial \hat{\boldsymbol{x}}}\right] \cdot \left[\boldsymbol{1} + \frac{\partial \hat{\boldsymbol{u}}}{\partial \boldsymbol{X}}\right] \equiv \tilde{\boldsymbol{F}} \cdot \hat{\boldsymbol{F}} \tag{3-16}$$

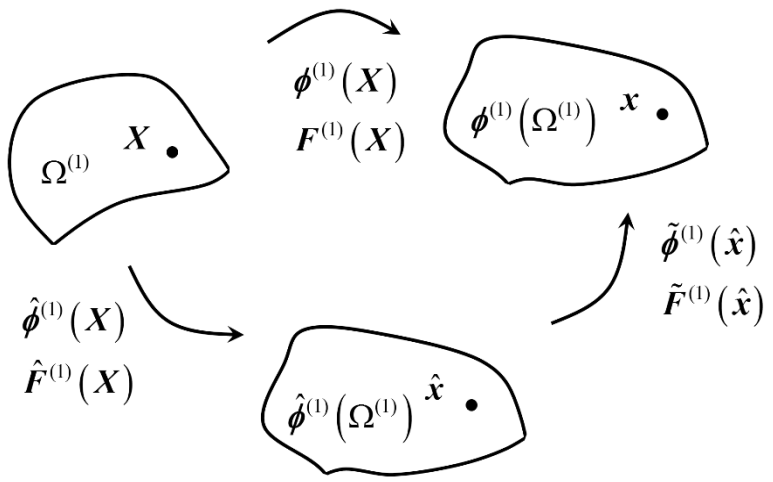

Figure 3.2. Multiscale composition of mappings $\tilde{\boldsymbol{\phi}}^{(1)} \circ \hat{\boldsymbol{\phi}}^{(1)}$ for region $\Omega^{(1)}$.

Remark: *In the context of small deformations, an additive split of the displacement field is commonly employed, see e.g. [102,99]. However in the finite deformation case, the composition of mappings properly defines the total finite displacement [94]. Consequently, the gradient of this composite mapping leads to a multiplicative split of the deformation gradient. Similar ideas are discussed in the context of enhanced strain formulations by Simo and Armero [145].*

In our developments, we elect to represent the coarse-scale field $\hat{\boldsymbol{\phi}}^{(\alpha)}$ using piecewise continuous finite element functions in each region $\Omega^{(\alpha)}$. The fine-scale field $\tilde{\boldsymbol{\phi}}^{(\alpha)}$ is treated as being local to the interface in a manner similar to [162]; the specific functional form is discussed in the following section. For concreteness, we summarize the notation pertaining to the finite element partitions as follows. Let $\left\{\Omega_e^{(\alpha)}\right\}_{e=1}^{n_{umel}^{(\alpha)}}$ be a collection of nonoverlapping open subdomains $\Omega_e^{(\alpha)}$ called elements that cover region $\Omega^{(\alpha)}$: $\bigcup_{e=1}^{n_{umel}^{(\alpha)}} \overline{\Omega}_e^{(\alpha)} = \overline{\Omega}^{(\alpha)}$. Each element $\Omega_e^{(\alpha)}$ has an associated boundary $\Gamma_e^{(\alpha)}$, and we denote the union of all element interiors and boundaries by $\tilde{\Omega}^{(\alpha)}$ and $\tilde{\Gamma}^{(\alpha)}$, respectively. Also, we use the symbol $\Gamma_{\mathrm{I},e}^{(\alpha)}$ to indicate the intersection of an element boundary with the interface Γ_{I}, and the union of all such elements boundaries is denoted by $\tilde{\Gamma}_{\mathrm{I}}^{(\alpha)}$. We remark that conformity of the partitions along Γ_{I} is not assumed, namely an element boundary $\Gamma_{\mathrm{I},e}^{(1)}$ may not exist that coincides precisely with $\Gamma_{\mathrm{I},e}^{(2)}$ on the other side of the interface, or vice versa.

With this notation in hand, the spaces of trial coarse-scale maps $\hat{\mathcal{S}}^{(\alpha)}$ and fine-scale maps $\tilde{\mathcal{S}}^{(\alpha)}$ take the following explicit form:

$$\hat{\mathcal{S}}^{(\alpha)} = \left\{ \hat{\boldsymbol{\phi}}^{(\alpha)} \,\middle|\, \hat{\boldsymbol{\phi}}^{(\alpha)} \in C^o\left(\Omega^{(\alpha)}\right) \bigcap \mathcal{S}^{(\alpha)},\ \hat{\boldsymbol{\phi}}^{(\alpha)}\big|_{\Omega_e^{(\alpha)}} \in \mathcal{P}^k\left(\Omega_e^{(\alpha)}\right) \text{ for } e = 1,\ldots,n_{umel}^{(\alpha)} \right\} \tag{3-17}$$

$$\tilde{\mathcal{S}}^{(\alpha)} = \left\{ \tilde{\boldsymbol{\phi}}^{(\alpha)} \,\middle|\, \tilde{\boldsymbol{\phi}}^{(\alpha)} = \boldsymbol{\phi}^{(\alpha)} \circ \hat{\boldsymbol{\phi}}^{-1(\alpha)} \in \mathcal{S}^{(\alpha)} \setminus \hat{\mathcal{S}}^{(\alpha)} \right\} \tag{3-18}$$

where $\mathcal{P}^k\left(\Omega_e^{(\alpha)}\right)$ is the space of complete Lagrange polynomials of order k spanning element $\Omega_e^{(\alpha)}$. These definitions ensure a unique decomposition of the component mapping functions. Following [162], we retain $\mathcal{Q}$ from (3-11) as the space of trial and test functions for the multiplier field until later in the derivation.

Returning to the interface potential functional (3-12) and substituting the multiscale decomposition (3-13), we obtain the multiscale interface potential functional:

$$\begin{aligned} \Pi\left(\hat{\boldsymbol{\phi}}^{(\alpha)}, \tilde{\boldsymbol{\phi}}^{(\alpha)}, \boldsymbol{\lambda}\right) &= -\int_{\Gamma_I} \boldsymbol{\lambda} \cdot \left[\!\left[\tilde{\boldsymbol{\phi}}^{(\alpha)} \circ \hat{\boldsymbol{\phi}}^{(\alpha)} \right]\!\right] \mathrm{d}A \\ &+ \sum_{\alpha=1}^{2} \left[\int_{\Omega^{(\alpha)}} W^{(\alpha)}\left(\boldsymbol{F}^{(\alpha)}\left(\tilde{\boldsymbol{\phi}}^{(\alpha)} \circ \hat{\boldsymbol{\phi}}^{(\alpha)} \right) \right) \mathrm{d}V - \int_{\Omega^{(\alpha)}} \rho_o^{(\alpha)} \boldsymbol{B}^{(\alpha)} \cdot \left(\tilde{\boldsymbol{\phi}}^{(\alpha)} \circ \hat{\boldsymbol{\phi}}^{(\alpha)} \right) \mathrm{d}V \right] \end{aligned} \tag{3-19}$$

The corresponding multiscale weak form is obtained by taking the variation with respect to both the coarse-scale arguments $\hat{\boldsymbol{\phi}}^{(\alpha)}$ and $\boldsymbol{\lambda}$ along with the fine-scale arguments $\tilde{\boldsymbol{\phi}}^{(\alpha)}$. To facilitate this step, we record the following intermediate results from [101]:

$$\mathrm{D}_{\hat{\phi}}\left(\tilde{\boldsymbol{\phi}} \circ \hat{\boldsymbol{\phi}} \right) \cdot \hat{\boldsymbol{\eta}}_o = \tilde{\boldsymbol{\phi}} \circ \hat{\boldsymbol{\eta}}_o \equiv \hat{\boldsymbol{\eta}}_{\tilde{\phi}}; \qquad \mathrm{D}_{\tilde{\phi}}\left(\tilde{\boldsymbol{\phi}} \circ \hat{\boldsymbol{\phi}} \right) \cdot \tilde{\boldsymbol{\eta}}_o = \tilde{\boldsymbol{\eta}}_o \circ \hat{\boldsymbol{\phi}} \equiv \tilde{\boldsymbol{\eta}}_{\hat{\phi}} \tag{3-20}$$

$$\mathrm{D}_{\hat{\phi}} \boldsymbol{F} \cdot \hat{\boldsymbol{\eta}}_o = \tilde{\boldsymbol{F}} \cdot \mathrm{GRAD}\, \hat{\boldsymbol{\eta}}_o - \mathrm{GRAD}\, \tilde{\boldsymbol{u}} \cdot \hat{\boldsymbol{F}}^{-1} \cdot \mathrm{GRAD}\, \hat{\boldsymbol{\eta}}_o = \mathrm{GRAD}\, \hat{\boldsymbol{\eta}}_o \tag{3-21}$$

$$\mathrm{D}_{\tilde{\phi}} \boldsymbol{F} \cdot \tilde{\boldsymbol{\eta}}_o = \left(\widehat{\mathrm{GRAD}}\, \tilde{\boldsymbol{\eta}}_o \right) \cdot \hat{\boldsymbol{F}} = \left(\mathrm{GRAD}\, \tilde{\boldsymbol{\eta}}_o \right) \cdot \hat{\boldsymbol{F}}^{-1} \cdot \hat{\boldsymbol{F}} = \mathrm{GRAD}\, \tilde{\boldsymbol{\eta}}_o \tag{3-22}$$

where the coarse-scale and fine-scale variations in each region are denoted $\hat{\boldsymbol{\eta}}_o^{(\alpha)}$ and $\tilde{\boldsymbol{\eta}}_o^{(\alpha)}$, respectively, and the variational (Gateaux) derivative is defined as $\mathrm{D}_{\phi}\boldsymbol{G} \cdot \boldsymbol{\eta}_o = \left. \dfrac{\partial}{\partial \varepsilon} \right|_{\varepsilon=0} \boldsymbol{G}\left(\boldsymbol{\phi} + \varepsilon \boldsymbol{\eta}_o \right)$ (see [101]). Note that a simplified expression (3-21) is obtained for the coarse-scale variation of $\boldsymbol{F}$ compared to the expression in [101] by accounting for the dependence of $\tilde{\boldsymbol{F}}$ on coarse-scale map $\hat{\boldsymbol{\phi}}$.

Applying the variational derivative to (3-19) and incorporating (3-20)–(3-22) leads to the following multiscale interface problem:

Coarse-Scale Problem $\mathcal{C}$

$$\begin{aligned}
\mathrm{D}_{\hat{\boldsymbol{\phi}}^{(\alpha)}}\left[\Pi\left(\hat{\boldsymbol{\phi}}^{(\alpha)},\tilde{\boldsymbol{\phi}}^{(\alpha)},\boldsymbol{\lambda}\right)\right]\cdot\hat{\boldsymbol{\eta}}_o^{(\alpha)} &\equiv R_\phi\left(\hat{\boldsymbol{\eta}}_o^{(\alpha)};\hat{\boldsymbol{\phi}}^{(\alpha)},\tilde{\boldsymbol{\phi}}^{(\alpha)},\boldsymbol{\lambda}\right)\\
&= \sum_{\alpha=1}^{2}\int_{\Omega^{(\alpha)}}\left[\mathrm{GRAD}\,\hat{\boldsymbol{\eta}}_o^{(\alpha)}:\boldsymbol{P}^{(\alpha)}-\hat{\boldsymbol{\eta}}_o^{(\alpha)}\cdot\rho_o^{(\alpha)}\boldsymbol{B}^{(\alpha)}\right]\mathrm{d}V \qquad (3\text{-}23)\\
&\quad -\int_{\Gamma_{\mathrm{I}}}\boldsymbol{\lambda}\cdot[\![\hat{\boldsymbol{\eta}}_o]\!]\,\mathrm{d}A=0\\
\mathrm{D}_{\lambda}\left[\Pi\left(\hat{\boldsymbol{\phi}}^{(\alpha)},\tilde{\boldsymbol{\phi}}^{(\alpha)},\boldsymbol{\lambda}\right)\right]\cdot\boldsymbol{\mu} &\equiv R_\lambda\left(\boldsymbol{\mu},\hat{\boldsymbol{\phi}}^{(\alpha)},\tilde{\boldsymbol{\phi}}^{(\alpha)}\right)=-\int_{\Gamma_{\mathrm{I}}}\boldsymbol{\mu}\cdot[\![\tilde{\boldsymbol{\phi}}\circ\hat{\boldsymbol{\phi}}]\!]\,\mathrm{d}A=0 \qquad (3\text{-}24)
\end{aligned}$$

Fine-Scale Problem $\mathcal{F}$

$$\begin{aligned}
\mathrm{D}_{\tilde{\boldsymbol{\phi}}^{(\alpha)}}\left[\Pi\left(\hat{\boldsymbol{\phi}}^{(\alpha)},\tilde{\boldsymbol{\phi}}^{(\alpha)},\boldsymbol{\lambda}\right)\right]\cdot\tilde{\boldsymbol{\eta}}_o^{(\alpha)} &= R_\phi\left(\tilde{\boldsymbol{\eta}}_o^{(\alpha)};\hat{\boldsymbol{\phi}}^{(\alpha)},\tilde{\boldsymbol{\phi}}^{(\alpha)},\boldsymbol{\lambda}\right)\\
&= \sum_{\alpha=1}^{2}\int_{\Omega^{(\alpha)}}\left[\mathrm{GRAD}\,\tilde{\boldsymbol{\eta}}_o^{(\alpha)}:\boldsymbol{P}^{(\alpha)}-\tilde{\boldsymbol{\eta}}_o^{(\alpha)}\cdot\rho_o^{(\alpha)}\boldsymbol{B}^{(\alpha)}\right]\mathrm{d}V \qquad (3\text{-}25)\\
&\quad -\int_{\Gamma_{\mathrm{I}}}\boldsymbol{\lambda}\cdot[\![\tilde{\boldsymbol{\eta}}_o]\!]\,\mathrm{d}A=0
\end{aligned}$$

We would now like to adapt the fine-scale modeling procedure presented in [162] to convert the system (3-23) – (3-25) into a primal formulation in which $\hat{\boldsymbol{\phi}}^{(\alpha)}$ is the sole unknown. This objective is achieved through a three stage modeling process. First, the fine-scale equation (3-25) is localized to the vicinity of the interface Γ_{I} and subsequently linearized to obtain a closed-form expression for $\tilde{\boldsymbol{\phi}}^{(\alpha)}$ in terms of $\hat{\boldsymbol{\phi}}^{(\alpha)}$ and $\boldsymbol{\lambda}$. Second, this fine-scale model is substituted into (3-24) to yield a point-wise expression for $\boldsymbol{\lambda}$ in terms of $\hat{\boldsymbol{\phi}}^{(\alpha)}$. Finally, these models for $\boldsymbol{\lambda}$ and $\tilde{\boldsymbol{\phi}}^{(\alpha)}$ are consistently embedded into (3-23) to remove their explicit appearance while retaining their effects.

Remark: *These derivations result in additional interface terms that have a form analogous to numerical flux and penalty terms found in standard Nitsche or DG formulations [140,8,100,9]. However, the specific form of these terms is usually selected by the user based on the long history of the method, and multiple options have been proposed within the context of nonlinear solid mechanics [53,107,84,141,51,132]. Herein, these terms arise naturally through the modeling of fine scales within a Lagrange multiplier interface formulation, thereby providing a rational basis for their origin.*

3.3.1 Modeling of fine scales

The first modeling step is to localize the fine-scale problem (3-28) around the interface Γ_{I}. This is a reasonable assumption because the boundary layer effects are invariably localized in a narrow band around the interface and domain boundaries; in solid mechanics, this effect is known as Saint-Venant's principle. In the present problem, these effects are produced because of mesh nonconformity and the introduction of discrete Lagrange multipliers at the interface.

Accordingly, the effects of $\tilde{\boldsymbol{\phi}}^{(\alpha)}$ are assumed to vanish outside of a small neighborhood of the interface Γ_{I}. Herein, we adopt an explicit representation of the fine-scale fields according to the procedure described in [162], which we summarize herein for clarity. Recalling the finite element discretization the regions $\Omega^{(1)}$ and $\Omega^{(2)}$, define a partition of the interface Γ_{I} into disjoint segments γ_s such that $\bigcup_{s=1}^{n_{seg}} \overline{\gamma}_s = \overline{\Gamma}_{\mathrm{I}}$, where n_{seg} is the number of segments. Each segment is generated such that it is bordered by only a single element from each region $\Omega^{(\alpha)}$, namely $\gamma_s \subseteq \Gamma_{\mathrm{I},e}^{(\alpha)}$ for some element $\Omega_e^{(\alpha)}$ and $\gamma_s \bigcap \Gamma_{\mathrm{I},j}^{(\alpha)}$ for all $j \neq e$. Next, on both sides of segment γ_s, we associate a sector $\omega_s^{(\alpha)}$ that is a subset of the adjoining element $\Omega_e^{(\alpha)}$ such that one portion of the boundary $\partial\omega_s^{(\alpha)}$ corresponds to the segment: $\partial\omega_s^{(\alpha)} \bigcap \Gamma_{\mathrm{I}} = \gamma_s$. An example partition is shown for a small interface in Figure 3.3; we also refer the reader to [162] for further elaboration on these definitions. Finally, we elect to represent the fine scales as edge bubble functions $b_s^{(\alpha)}$ spanning these sectors adjoining the interface:

$$\tilde{\boldsymbol{\phi}}^{(\alpha)}\Big|_{\omega_s^{(\alpha)}} = \boldsymbol{\beta}_s^{(\alpha)} b_s^{(\alpha)}\left(\boldsymbol{X}\right), \qquad \tilde{\boldsymbol{\eta}}_o^{(\alpha)}\Big|_{\omega_s^{(\alpha)}} = \boldsymbol{\gamma}_s^{(\alpha)} b_s^{(\alpha)}\left(\boldsymbol{X}\right) \tag{3-26}$$

where the bubble functions are nonzero on segment γ_s and vanish along the remainder of the sector boundary $\partial\omega_s^{(\alpha)}$.

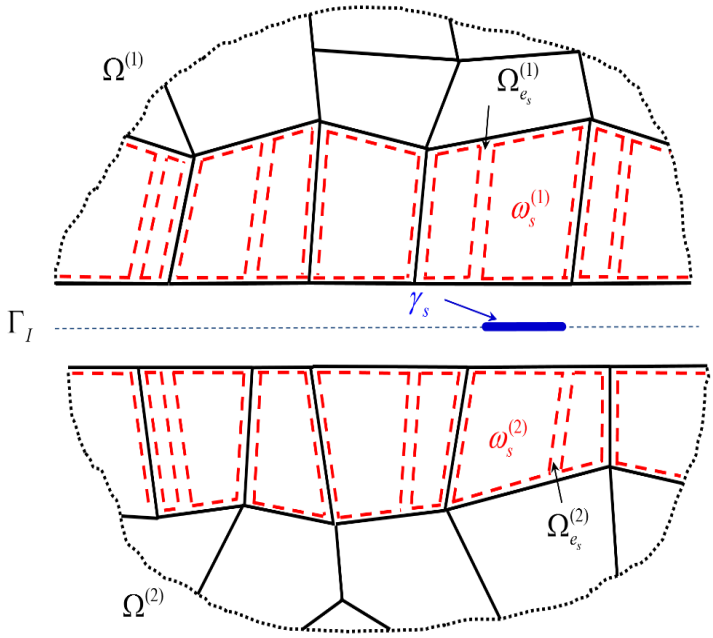

Figure 3.3. Interface partition into segments γ_s and sectors $\omega_s^{(\alpha)}$.

As a result of the localized representation of the fine scales (3-26), the fine-scale problem (3-28) can be segregated into a series of local problems defined over pairs of sectors along the interface:

$$\begin{aligned}\tilde{R}_s\left(\hat{\boldsymbol{\eta}}_o^{(\alpha)};\hat{\boldsymbol{\phi}}^{(\alpha)},\tilde{\boldsymbol{\phi}}^{(\alpha)},\boldsymbol{\lambda}\right)=&\sum_{\alpha=1}^{2}\int_{\omega_s^{(\alpha)}}\left[\mathrm{GRAD}\,\tilde{\boldsymbol{\eta}}_o^{(\alpha)}:\boldsymbol{P}^{(\alpha)}-\tilde{\boldsymbol{\eta}}_o^{(\alpha)}\cdot\rho_o^{(\alpha)}\boldsymbol{B}^{(\alpha)}\right]\mathrm{d}V\\&-\int_{\gamma_s}\boldsymbol{\lambda}\cdot[\![\tilde{\boldsymbol{\eta}}_o]\!]\,\mathrm{d}A=0\quad\text{for } s=1,\ldots,n_{seg}\end{aligned}\tag{3-27}$$

The next important step to enable a closed-form solution of the fine-scale problem (3-27) is to perform linearization along the lines of [101]. Since the fine-scale field has been localized, the effects of this further modeling approximation are also confined to the interface. Thus, fine scales are treated as an incremental displacement $\Delta\tilde{\boldsymbol{u}}^{(\alpha)}$ of the coarse-scale deformation $\hat{\boldsymbol{\phi}}^{(\alpha)}$:

$$\sum_{\alpha=1}^{2}\int_{\Omega^{(\alpha)}}\mathrm{GRAD}\,\tilde{\boldsymbol{\eta}}_o^{(\alpha)}:\mathbf{A}^{(\alpha)}\left(\boldsymbol{F}^{(\alpha)}\right):\mathrm{GRAD}\,\Delta\tilde{\boldsymbol{u}}^{(\alpha)}\,\mathrm{d}V=-\tilde{R}_s\left(\hat{\boldsymbol{\eta}}_o^{(\alpha)};\hat{\boldsymbol{\phi}}^{(\alpha)},\mathbf{0},\boldsymbol{\lambda}\right)\tag{3-28}$$

where the acoustic tensor of material moduli $\mathbf{A}^{(\alpha)}\left(\boldsymbol{F}^{(\alpha)}\right)$ is defined as:

$$\mathbf{A}^{(\alpha)}\left(\boldsymbol{F}^{(\alpha)}\right)=\frac{\partial^2 W^{(\alpha)}}{\partial\boldsymbol{F}\partial\boldsymbol{F}}\tag{3-29}$$

Due to this incremental approximation, the fine scales do not contribute significantly to the

deformation gradient such that:

$$\boldsymbol{F}^{(\alpha)} = \left(\boldsymbol{1} + \boldsymbol{0}\right) \cdot \hat{\boldsymbol{F}}^{(\alpha)} = \hat{\boldsymbol{F}}^{(\alpha)} \tag{3-30}$$

Remark: *In the reference [97], the linearized fine-scale problem was expressed in terms of the second Piola-Kirchhoff stress tensor* $\boldsymbol{S} = \partial W / \partial \boldsymbol{E}$ *and the material tangent tensor* $\mathbf{C} = \partial^2 W / \partial \boldsymbol{E}^2$, *where* $\boldsymbol{E}$ *is the Green-Lagrange strain tensor. While that presentation makes explicit the effects of geometric and material nonlinearity, herein we have employed derivations in terms of* $\mathbf{A}$ *to yield more compact expressions. There is a one-to-one correspondence between these tensors, presented e.g. in [21,148] as well as in Appendix A.*

Next, we substitute the explicit form of the fine scales (3-26) into (3-28), replacing $\boldsymbol{\beta}_s^{(\alpha)}$ by $\Delta \boldsymbol{\beta}_s^{(\alpha)}$, to obtain:

$$\begin{aligned}
&\sum_{\alpha=1}^{2} \boldsymbol{\gamma}_s^{(\alpha)} \cdot \left[\int_{\omega_s^{(\alpha)}} \text{GRAD}\, \boldsymbol{b}_s^{(\alpha)} : \mathbf{A}^{(\alpha)} : \text{GRAD}\, \boldsymbol{b}_s^{(\alpha)}\, \text{d}V \right] \cdot \Delta \boldsymbol{\beta}_s^{(\alpha)} = \\
&\sum_{\alpha=1}^{2} \boldsymbol{\gamma}_s^{(\alpha)} \cdot \left[\int_{\omega_s^{(\alpha)}} \boldsymbol{b}_s^{(\alpha)} \cdot \left(\text{DIV}\, \boldsymbol{P}^{(\alpha)} + \rho_o^{(\alpha)} \boldsymbol{B}^{(\alpha)} \right) \text{d}V \right] \\
&+ \boldsymbol{\gamma}_s^{(1)} \cdot \left[\int_{\gamma_s} \boldsymbol{b}_s^{(1)} \cdot \left(-\boldsymbol{\lambda} - \boldsymbol{P}^{(1)} \cdot \boldsymbol{N}^{(1)} \right) \text{d}A \right] + \boldsymbol{\gamma}_s^{(2)} \cdot \left[\int_{\gamma_s} \boldsymbol{b}_s^{(2)} \cdot \left(\boldsymbol{\lambda} - \boldsymbol{P}^{(2)} \cdot \boldsymbol{N}^{(2)} \right) \text{d}A \right]
\end{aligned} \tag{3-31}$$

where $\boldsymbol{b}_s^{(\alpha)} = \sum_{J=1}^{n_{\text{sd}}} b_s^{(\alpha)} \boldsymbol{E}_J$ is a vector-valued bubble function and $\boldsymbol{E}_J$ are the basis vectors in the reference configuration. Note that integration by parts has been applied to the coarse-scale stress terms and the terms involving $\boldsymbol{\lambda}$ have been separated using the linearity of the jump operator. Solving for the fine-scale coefficients $\Delta \boldsymbol{\beta}_s^{(\alpha)}$ in terms of the coarse-scale fields $\hat{\boldsymbol{\phi}}^{(\alpha)}$ and $\boldsymbol{\lambda}$ yields the following expression:

$$\Delta \boldsymbol{\beta}_s^{(\alpha)} = \tilde{\boldsymbol{\tau}}_s^{(\alpha)} \left[\int_{\omega_s^{(\alpha)}} \boldsymbol{b}_s^{(\alpha)} \cdot \left(\text{DIV}\, \boldsymbol{P}^{(\alpha)} + \rho_o^{(\alpha)} \boldsymbol{B}^{(\alpha)} \right) \text{d}V + \int_{\gamma_s} \boldsymbol{b}_s^{(\alpha)} \cdot \left[(-1)^{\alpha - 1} \boldsymbol{\lambda} - \boldsymbol{P}^{(\alpha)} \cdot \boldsymbol{N}^{(\alpha)} \right] \text{d}A \right] \tag{3-32}$$

where the stability tensor $\tilde{\boldsymbol{\tau}}^{(\alpha)}$ is expressed in terms of the fine-scale bubble function and the material tangent tensor as follows:

$$\tilde{\boldsymbol{\tau}}_s^{(\alpha)} = \left[\int_{\omega_s^{(\alpha)}} \text{GRAD}\, \boldsymbol{b}_s^{(\alpha)} : \mathbf{A}^{(\alpha)} : \text{GRAD}\, \boldsymbol{b}_s^{(\alpha)}\, \text{d}V \right]^{-1} \tag{3-33}$$

We observe that the fine scales are driven by the residual of the equilibrium equation (3-2) and traction balance equation (3-5) incorporating the multiplier field $\boldsymbol{\lambda}$.

Three additional simplifying assumptions are now applied to further simplify (3-32) with a direct analogy to [162]. Firstly, the interior residual term is neglected, which is equivalent to assuming the fine-scale bubble function is orthogonal to the coarse-scale residual, such as employed by residual-free bubble methods [45,27]. While this orthogonality condition will not be strictly enforced, larger contributions to the fine-scale model are expected from the boundary term. Secondly, the mean-value theorem is applied to extract the traction boundary residual outside of the integral, which converts (3-32) from a nonlocal to a local expression in terms of $\tilde{\boldsymbol{u}}^{(\alpha)}$ and $\boldsymbol{\lambda}$. This step is a commonly employed technique in stabilized methods [102,94]. Thirdly, the average value of the bubble function is employed in expression (3-26) for $\tilde{\boldsymbol{\phi}}^{(\alpha)}$. Applying these modeling assumption to (3-32) leads to an expression for $\Delta\tilde{\boldsymbol{u}}^{(\alpha)}$ that is analogous to stabilized methods:

$$\Delta\tilde{\boldsymbol{u}}^{(\alpha)} = \boldsymbol{\tau}_s^{(\alpha)} \cdot \left[\left(-1\right)^{\alpha-1} \boldsymbol{\lambda} - \boldsymbol{P}^{(\alpha)} \cdot \boldsymbol{N}^{(\alpha)} \right] \tag{3-34}$$

where:

$$\boldsymbol{\tau}_s^{(\alpha)} = \left[\operatorname{meas}\left(\gamma_s\right) \right]^{-1} \left(\int_{\gamma_s} b_s^{(\alpha)} \, \mathrm{d}A \right)^2 \tilde{\boldsymbol{\tau}}_s^{(\alpha)} \tag{3-35}$$

Remark: *The definition for the stability tensor $\boldsymbol{\tau}_s^{(\alpha)}$ accounts for the interface-local finite element length scale through the dependence of the integrals on the segment γ_s, sector $\omega_s^{(\alpha)}$, and fine-scale bubble function $b_s^{(\alpha)}$. Also, the effects of evolving geometric and material nonlinearity on either side of the interface are encapsulated through the appearance of the acoustic tensor $\mathbf{A}^{(\alpha)}$. These dependencies will play a key role in the properties of the numerical flux and penalty parameter derived in the following section.*

3.3.2 Variational embedding in the coarse-scale problem

The analytical model for the fine scales at the interface (3-34) will now be incorporated into the coarse-scale problem. We first concentrate on the contributions to the continuity equation (3-24) in order to obtain an expression for the Lagrange multiplier field $\boldsymbol{\lambda}$ and subsequently return to the equilibrium equation. This equation is nonlinear in $\boldsymbol{\phi}^{(\alpha)}$ due to the multiscale decomposition (3-13). Therefore, we linearize the jump operator as $\left[\!\left[\tilde{\boldsymbol{\phi}} \circ \hat{\boldsymbol{\phi}} \right]\!\right] \simeq \left[\!\left[\hat{\boldsymbol{\phi}} \right]\!\right] + \left[\!\left[\Delta\tilde{\boldsymbol{u}} \right]\!\right]$, which is a valid approximation when the fine scales are small and localized as in the preceding section. Incorporating this result and expression (3-34) for the fine-scale increment $\Delta\tilde{\boldsymbol{u}}^{(\alpha)}$ into (3-24) leads

to the following:

$$-\int_{\Gamma_I} \boldsymbol{\mu} \cdot \left[\left[\!\left[\hat{\boldsymbol{\phi}} \right]\!\right] - \boldsymbol{\tau}_s^{(1)} \cdot \left(\boldsymbol{\lambda} - \boldsymbol{P}^{(1)} \cdot \boldsymbol{N}^{(1)} \right) + \boldsymbol{\tau}_s^{(2)} \cdot \left(-\boldsymbol{\lambda} - \boldsymbol{P}^{(2)} \cdot \boldsymbol{N}^{(2)} \right) \right] \mathrm{d}A = 0 \tag{3-36}$$

Next, proceeding according to [162], we employ a piecewise L^2 functional form for the Lagrange multipliers $\boldsymbol{\lambda}$ and $\boldsymbol{\mu}$, which is admissible due to the enhanced stability afforded by the fine-scale model. By requiring that (3-36) holds for all variations $\boldsymbol{\mu}$, the quantity in square brackets must vanish almost everywhere, in the notion of the L^2 projection. Therefore, the following expression must hold point-wise on each segment:

$$\boldsymbol{\tau}_s^{(1)} \cdot \boldsymbol{\lambda} + \boldsymbol{\tau}_s^{(2)} \cdot \boldsymbol{\lambda} = \boldsymbol{\tau}_s^{(1)} \cdot \boldsymbol{P}^{(1)} \cdot \boldsymbol{N}^{(1)} - \boldsymbol{\tau}_s^{(2)} \cdot \boldsymbol{P}^{(2)} \cdot \boldsymbol{N}^{(2)} - \left[\!\left[\hat{\boldsymbol{\phi}} \right]\!\right] \quad \text{for } s = 1, ..., n_{seg} \tag{3-37}$$

where we have segregated the coarse-scale displacement terms from the multiplier terms. Solving this expression for $\boldsymbol{\lambda}$, we obtain:

$$\boldsymbol{\lambda} = \left[\boldsymbol{\delta}_s^{(1)} \cdot \boldsymbol{P}^{(1)} \cdot \boldsymbol{N}^{(1)} - \boldsymbol{\delta}_s^{(2)} \cdot \boldsymbol{P}^{(2)} \cdot \boldsymbol{N}^{(2)} \right] - \boldsymbol{\tau}_s \cdot \left[\!\left[\hat{\boldsymbol{\phi}} \right]\!\right] \tag{3-38}$$

The flux weighting tensors $\boldsymbol{\delta}_s^{(\alpha)}$ and stability tensor $\boldsymbol{\tau}_s$ are defined in terms of $\boldsymbol{\tau}_s^{(\alpha)}$ with direct analogy to [162]:

$$\boldsymbol{\tau}_s = \left(\boldsymbol{\tau}_s^{(1)} + \boldsymbol{\tau}_s^{(2)} \right)^{-1}, \qquad \boldsymbol{\delta}_s^{(\alpha)} = \boldsymbol{\tau}_s \cdot \boldsymbol{\tau}_s^{(\alpha)} \tag{3-39}$$

With this explicit form for $\boldsymbol{\lambda}$, a simplified expression for the fine scales results from substitution in (3-34):

$$\Delta \tilde{\boldsymbol{u}}^{(1)} = -\boldsymbol{\delta}_s \left[\boldsymbol{P}^{(1)} \cdot \boldsymbol{N}^{(1)} + \boldsymbol{P}^{(2)} \cdot \boldsymbol{N}^{(2)} \right] - \boldsymbol{\delta}_s^{(1)T} \cdot \left[\!\left[\hat{\boldsymbol{\phi}} \right]\!\right] \tag{3-40}$$

$$\Delta \tilde{\boldsymbol{u}}^{(2)} = -\boldsymbol{\delta}_s \left[\boldsymbol{P}^{(1)} \cdot \boldsymbol{N}^{(1)} + \boldsymbol{P}^{(2)} \cdot \boldsymbol{N}^{(2)} \right] + \boldsymbol{\delta}_s^{(2)T} \cdot \left[\!\left[\hat{\boldsymbol{\phi}} \right]\!\right] \tag{3-41}$$

where we have employed the symmetry of the tensors $\boldsymbol{\tau}_s^{(\alpha)}$ and $\boldsymbol{\tau}_s$ (derived from (3-33)) to enable the substitution $\boldsymbol{\delta}_s^{(\alpha)T} = \boldsymbol{\tau}_s^{(\alpha)} \cdot \boldsymbol{\tau}_s$. Also, the additional stability tensor $\boldsymbol{\delta}_s$ arises during the substitution and is defined as:

$$\boldsymbol{\delta}_s = \boldsymbol{\tau}_s^{(1)} \cdot \boldsymbol{\delta}_s^{(2)} = \boldsymbol{\tau}_s^{(2)} \cdot \boldsymbol{\delta}_s^{(1)} = \left[\left(\boldsymbol{\tau}_s^{(1)} \right)^{-1} + \left(\boldsymbol{\tau}_s^{(2)} \right)^{-1} \right]^{-1} \tag{3-42}$$

Remark: *Note that in general $\boldsymbol{\delta}_s^{(\alpha)T} \neq \boldsymbol{\delta}_s^{(\alpha)}$ according to (3-39). Therefore, proper care must be taken during the following derivations and subsequent implementation to maintain the consistency and variational structure of the method.*

We return to the weak form (3-23) and embed the representation of the fine scales (3-40) – (3-41) and the multiplier $\boldsymbol{\lambda}$ (3-38) to obtain a formulation that is only a function of the coarse scales $\hat{\boldsymbol{u}}^{(\alpha)}$. First, the stress term is linearized with respect to the fine scales:

$$\mathrm{D}_{\tilde{\phi}^{(\alpha)}}\left[\int_{\Omega^{(\alpha)}} \mathrm{GRAD}\,\hat{\boldsymbol{\eta}}_o^{(\alpha)} : \boldsymbol{P}^{(\alpha)}\,\mathrm{d}V\right]\cdot\Delta\tilde{\boldsymbol{u}}^{(\alpha)} = \int_{\Omega^{(\alpha)}} \mathrm{GRAD}\,\hat{\boldsymbol{\eta}}_o^{(\alpha)} : \mathbf{A}^{(\alpha)} : \mathrm{GRAD}\,\Delta\tilde{\boldsymbol{u}}^{(\alpha)}\,\mathrm{d}V \tag{3-43}$$

Next, we integrate this term by parts, taking into account the representation for the fine scales (3-26) that vanish on element boundaries that do not intersect the interface:

$$\begin{aligned}&\int_{\Omega^{(\alpha)}} \mathrm{GRAD}\,\hat{\boldsymbol{\eta}}_o^{(\alpha)} : \mathbf{A}^{(\alpha)} : \mathrm{GRAD}\,\Delta\tilde{\boldsymbol{u}}^{(\alpha)}\,\mathrm{d}V = -\int_{\Omega^{(\alpha)}} \mathrm{DIV}\left[\mathrm{GRAD}\,\hat{\boldsymbol{\eta}}_o^{(\alpha)} : \mathbf{A}^{(\alpha)}\right]\cdot\Delta\tilde{\boldsymbol{u}}^{(\alpha)}\,\mathrm{d}V \\ &+\int_{\Gamma_I}\left[\left(\mathrm{GRAD}\,\hat{\boldsymbol{\eta}}_o^{(\alpha)} : \mathbf{A}^{(\alpha)}\right)\cdot\boldsymbol{N}^{(\alpha)}\right]\cdot\Delta\tilde{\boldsymbol{u}}^{(\alpha)}\,\mathrm{d}A\end{aligned} \tag{3-44}$$

Herein, we assume that the contribution of the domain interior term from the right-hand side of (3-44) is negligible as was adopted in [162], which simplifies the resulting formulation and enables the direct substitution of the interface fine-scale model (3-34). Incorporating the expressions for $\boldsymbol{\lambda}$ (3-38) and the fine-scale fields $\Delta\tilde{\boldsymbol{u}}^{(\alpha)}$ (3-40) – (3-41) along with (3-44) into the coarse-scale problem (3-23) yields the following stabilized interface formulation for finite deformations:

$$\begin{aligned}&\sum_{\alpha=1}^{2}\int_{\Omega^{(\alpha)}}\left[\mathrm{GRAD}\,\hat{\boldsymbol{\eta}}_o^{(\alpha)} : \boldsymbol{P}^{(\alpha)} - \hat{\boldsymbol{\eta}}_o^{(\alpha)}\cdot\rho_o^{(\alpha)}\boldsymbol{B}^{(\alpha)}\right]\mathrm{d}V \\ &-\int_{\Gamma_I}[\![\hat{\boldsymbol{\eta}}_o]\!]\cdot\left(\boldsymbol{\delta}_s^{(1)}\cdot\boldsymbol{P}^{(1)}\cdot\boldsymbol{N}^{(1)} - \boldsymbol{\delta}_s^{(2)}\cdot\boldsymbol{P}^{(2)}\cdot\boldsymbol{N}^{(2)}\right)\mathrm{d}A \\ &+\int_{\Gamma_I}[\![\hat{\boldsymbol{\eta}}_o]\!]\cdot\boldsymbol{\tau}_s\cdot[\![\hat{\boldsymbol{\phi}}]\!]\,\mathrm{d}A \\ &-\int_{\Gamma_I}\left[\left(\mathrm{GRAD}\,\hat{\boldsymbol{\eta}}_o^{(1)} : \mathbf{A}^{(1)}\right)\cdot\boldsymbol{N}^{(1)}\right]\cdot\boldsymbol{\delta}_s^{(1)T}\cdot[\![\hat{\boldsymbol{\phi}}]\!]\,\mathrm{d}A \\ &+\int_{\Gamma_I}\left[\left(\mathrm{GRAD}\,\hat{\boldsymbol{\eta}}_o^{(2)} : \mathbf{A}^{(2)}\right)\cdot\boldsymbol{N}^{(2)}\right]\cdot\boldsymbol{\delta}_s^{(2)T}\cdot[\![\hat{\boldsymbol{\phi}}]\!]\,\mathrm{d}A \\ &-\int_{\Gamma_I}\left[\left(\mathrm{GRAD}\,\hat{\boldsymbol{\eta}}_o^{(1)} : \mathbf{A}^{(1)}\right)\cdot\boldsymbol{N}^{(1)}\right]\cdot\boldsymbol{\delta}_s\left[\boldsymbol{P}^{(1)}\cdot\boldsymbol{N}^{(1)} + \boldsymbol{P}^{(2)}\cdot\boldsymbol{N}^{(2)}\right]\mathrm{d}A \\ &-\int_{\Gamma_I}\left[\left(\mathrm{GRAD}\,\hat{\boldsymbol{\eta}}_o^{(2)} : \mathbf{A}^{(2)}\right)\cdot\boldsymbol{N}^{(2)}\right]\cdot\boldsymbol{\delta}_s\left[\boldsymbol{P}^{(1)}\cdot\boldsymbol{N}^{(1)} + \boldsymbol{P}^{(2)}\cdot\boldsymbol{N}^{(2)}\right]\mathrm{d}A = 0\end{aligned} \tag{3-45}$$

To cast (3-45) in a more compact form, we introduce the following notation for the so-called weighted average flux operators:

$$\left\{\boldsymbol{P}\cdot\boldsymbol{N}\right\} = \boldsymbol{\delta}_s^{(1)}\cdot\boldsymbol{P}^{(1)}\cdot\boldsymbol{N}^{(1)} - \boldsymbol{\delta}_s^{(2)}\cdot\boldsymbol{P}^{(2)}\cdot\boldsymbol{N}^{(2)} \tag{3-46}$$

$$\begin{aligned}\left\{\left(\text{GRAD}\,\hat{\boldsymbol{\eta}}_o:\mathbf{A}\right)\cdot\boldsymbol{N}\right\} &= \boldsymbol{\delta}_s^{(1)}\cdot\left[\left(\text{GRAD}\,\hat{\boldsymbol{\eta}}_o^{(1)}:\mathbf{A}^{(1)}\right)\cdot\boldsymbol{N}^{(1)}\right] \\ &\quad -\boldsymbol{\delta}_s^{(2)}\cdot\left[\left(\text{GRAD}\,\hat{\boldsymbol{\eta}}_o^{(2)}:\mathbf{A}^{(2)}\right)\cdot\boldsymbol{N}^{(2)}\right]\end{aligned} \tag{3-47}$$

Also, herein we choose to neglect the contribution from the stress jump term, which is the last two terms in (3-45), in order to improve the computational expediency of the method. Namely, fewer terms would need to be calculated for the residual force vector and stiffness matrix, as discussed in section 3.3.3. Also, this term and its counterpart in the linear context [162] are not commonly employed in interface methods (see e.g. [5,9,51,140,141]). However, these terms may provide additional stability in the presence of highly nonlinear material response. Adopting these conventions in (3-45) and removing the superimposed hats for clarity, we arrive at the final form of the stabilized finite strain interface formulation:

$$\begin{aligned}&R\left(\boldsymbol{\eta}_o^{(\alpha)},\boldsymbol{\phi}^{(\alpha)}\right)=\sum_{\alpha=1}^{2}\int_{\Omega^{(\alpha)}}\left[\text{GRAD}\,\boldsymbol{\eta}_o^{(\alpha)}:\boldsymbol{P}^{(\alpha)}-\boldsymbol{\eta}_o^{(\alpha)}\cdot\rho_o^{(\alpha)}\boldsymbol{B}^{(\alpha)}\right]\text{d}V \\ &-\int_{\Gamma_\text{I}}[\![\boldsymbol{\eta}_o]\!]\cdot\left\{\boldsymbol{P}\cdot\boldsymbol{N}\right\}\text{d}A-\int_{\Gamma_\text{I}}\left\{\left(\text{GRAD}\,\boldsymbol{\eta}_o:\mathbf{A}\right)\cdot\boldsymbol{N}\right\}\cdot[\![\boldsymbol{\phi}]\!]\,\text{d}A \\ &+\int_{\Gamma_\text{I}}[\![\boldsymbol{\eta}_o]\!]\cdot\boldsymbol{\tau}_s\cdot[\![\boldsymbol{\phi}]\!]\,\text{d}A=0\end{aligned} \tag{3-48}$$

A remarkable similarity is apparent between the formulation (3-48) and both linear [140,100,9] and nonlinear [53,51,107,122,170] Discontinuous Galerkin and Nitsche interface methods. However, the key distinction is that the definitions for the numerical flux (3-46) – (3-47) and the penalty parameter (3-39) are derived with recourse to the modeling of fine scales to stabilize a Lagrange multiplier interface formulation. In particular, (3-48) is free from user-defined parameters. Due to the close analogy of the present derivations to those in the linear context [162], many of the salient features from that method carry over to the proposed formulation (3-48). For example, the definition for the flux weighting tensors delta exhibit features of area-weighting approaches [58] and stiffness-weighting approaches [140]. The reader is referred to section 2.3.2 of [162] for additional remarks.

Remark: *We emphasize the key feature unique to the present nonlinear context whereby the penalty tensor* $\boldsymbol{\tau}_s$ *evolves with the nonlinear deformations according to the stability tensors* $\boldsymbol{\tau}_s^{(\alpha)}$. *The evolution of these parameters leads to a robust formulation for highly nonlinear problems.*

Remark: *The provision for the evolution of these stability parameters as a function of the evolving nonlinear fields is similar to the adaptive schemes proposed in [52,51]. In the former, a heuristic*

approach wherein the penalty term is scaled locally by the minimum eigenvalue of the acoustic tensor is advocated based on a mathematical analysis of linearized stress-free elasticity. Rigorous bounds on stability are proved in the latter for a DG method containing non-standard stabilizing terms that are valid for a general nonlinear hyperelastic material response. In both cases, the numerical flux is defined through lifting operators and employs the simple average of the fields across the interface. Our derivation presented in this Chapter instead adopts the VMS philosophy for developing stabilized methods along the lines of [162,101].

3.3.3 Consistent linearization

To complete the derivation in the preceding sections, we carry out the consistent linearization of the stabilized interface formulation (3-48) to provide the tangent stiffness matrix required for the Newton-Raphson nonlinear solution scheme. These derivations also highlight that the variational structure of the formulation which originated from (3-19) has been preserved through the consistent fine-scale modeling procedure and condensation of the multiplier fields. Throughout, we will neglect the dependence of $\boldsymbol{\tau}_s$ and $\boldsymbol{\delta}_s^{(\alpha)}$ on the displacement field.

Since the penalty term is linear in the deformation fields $\boldsymbol{\phi}^{(\alpha)}$ and the treatment of the domain terms can be found elsewhere (see e.g. [21]), we focus on the contributions emanating from the interface flux terms. These contributions are highlighted in the following expression:

$$
\begin{aligned}
&K\left(\boldsymbol{\eta}_o^{(\alpha)}, \Delta\boldsymbol{u}^{(\alpha)}; \boldsymbol{\phi}^{(\alpha)}\right) = \mathrm{D}_{\boldsymbol{\phi}^{(\alpha)}}\left[R\left(\boldsymbol{\eta}_o^{(\alpha)}, \boldsymbol{\phi}^{(\alpha)}\right)\right]\cdot\Delta\boldsymbol{u}^{(\alpha)} \\
&= \sum_{\alpha=1}^{2}\int_{\Omega^{(\alpha)}} \mathrm{GRAD}\,\boldsymbol{\eta}_o^{(\alpha)} : \mathbf{A}^{(\alpha)} : \mathrm{GRAD}\,\Delta\boldsymbol{u}^{(\alpha)}\,\mathrm{d}V + \sum_{\alpha=1}^{2}\int_{\Gamma_\mathrm{I}} [\![\boldsymbol{\eta}_o]\!]\cdot\boldsymbol{\tau}_s\cdot\mathrm{D}_{\boldsymbol{\phi}^{(\alpha)}}\left[[\![\boldsymbol{\phi}]\!]\right]\cdot\Delta\boldsymbol{u}^{(\alpha)}\,\mathrm{d}A \\
&-\sum_{\alpha=1}^{2}\int_{\Gamma_\mathrm{I}} [\![\boldsymbol{\eta}_o]\!]\cdot\mathrm{D}_{\boldsymbol{\phi}^{(\alpha)}}\left[\{\boldsymbol{P}\cdot\boldsymbol{N}\}\right]\cdot\Delta\boldsymbol{u}^{(\alpha)}\,\mathrm{d}A \\
&-\sum_{\alpha=1}^{2}\int_{\Gamma_\mathrm{I}} \left\{\left(\mathrm{GRAD}\,\boldsymbol{\eta}_o : \mathbf{A}\right)\cdot\boldsymbol{N}\right\}\cdot\mathrm{D}_{\boldsymbol{\phi}^{(\alpha)}}\left[[\![\boldsymbol{\phi}]\!]\right]\cdot\Delta\boldsymbol{u}^{(\alpha)}\,\mathrm{d}A \\
&-\sum_{\alpha=1}^{2}\int_{\Gamma_\mathrm{I}} \left\{\left(\mathrm{GRAD}\,\boldsymbol{\eta}_o : \left(\mathrm{D}_{\boldsymbol{\phi}^{(\alpha)}}\left[\mathbf{A}\right]\cdot\Delta\boldsymbol{u}^{(\alpha)}\right)\right)\cdot\boldsymbol{N}\right\}\cdot[\![\boldsymbol{\phi}]\!]\,\mathrm{d}A
\end{aligned}
\tag{3-49}
$$

The first interface term in (3-49) involving the first Piola-Kirchhoff stress follows similarly to the linearization of the fine-scale field presented in (3-43) by treating each component of the flux separately:

$$\sum_{\alpha=1}^{2} \mathrm{D}_{\phi^{(\alpha)}} \left[\{ \boldsymbol{P} \cdot \boldsymbol{N} \} \right] = \boldsymbol{\delta}_s^{(1)} \cdot \left(\mathrm{D}_{\phi^{(1)}} \left[\boldsymbol{P}^{(1)} \right] \cdot \Delta \boldsymbol{u}^{(1)} \right) \cdot \boldsymbol{N}^{(1)} - \boldsymbol{\delta}_s^{(2)} \cdot \left(\mathrm{D}_{\phi^{(2)}} \left[\boldsymbol{P}^{(2)} \right] \cdot \Delta \boldsymbol{u}^{(2)} \right) \cdot \boldsymbol{N}^{(2)}$$
$$= \left\{ \left(\mathbf{A} : \mathrm{GRAD}\, \Delta \boldsymbol{u} \right) \cdot \boldsymbol{N} \right\} \tag{3-50}$$

Also, the second flux term is obtained trivially along with the penalty term through the linearity of the jump operator:

$$\sum_{\alpha=1}^{2} \mathrm{D}_{\phi^{(\alpha)}} \left[\left[\!\left[\boldsymbol{\phi} \right]\!\right] \right] \cdot \Delta \boldsymbol{u}^{(\alpha)} = \Delta \boldsymbol{u}^{(1)} - \Delta \boldsymbol{u}^{(2)} = \left[\!\left[\Delta \boldsymbol{u} \right]\!\right] \tag{3-51}$$

However, the last term gives rise to a nonstandard contribution due to the dependence of the acoustic tensor $\mathbf{A}$ on the deformation gradient $\boldsymbol{F}$. The result, similar to the term appearing in the interface method of Mergheim et al. [107], is expressed as follows:

$$\mathrm{D}_{\phi^{(\alpha)}} \left[\mathbf{A}^{(\alpha)} \right] \cdot \Delta \boldsymbol{u}^{(\alpha)} = \boldsymbol{\Xi}^{(\alpha)} : \mathrm{GRAD}\, \Delta \boldsymbol{u}^{(\alpha)} \tag{3-52}$$

where $\boldsymbol{\Xi}^{(\alpha)} \left(\boldsymbol{F}^{(\alpha)} \right)$ is a sixth-order tensor of material moduli defined as:

$$\boldsymbol{\Xi}^{(\alpha)} \left(\boldsymbol{F}^{(\alpha)} \right) = \frac{\partial^3 W^{(\alpha)}}{\partial \boldsymbol{F}\, \partial \boldsymbol{F}\, \partial \boldsymbol{F}} \tag{3-53}$$

The contraction of the tensors in (3-52) is handled through the extension of the double-contraction operator ‘ : ’ to higher-order tensors in a similar manner as presented in section 3.3.2 of [101].

Substituting (3-50) – (3-53) into (3-49) leads to the final linearized form:

$$\begin{aligned} K\left(\boldsymbol{\eta}_o^{(\alpha)}, \Delta \boldsymbol{u}^{(\alpha)}; \boldsymbol{\phi}^{(\alpha)} \right) &= \sum_{\alpha=1}^{2} \int_{\Omega^{(\alpha)}} \mathrm{GRAD}\, \boldsymbol{\eta}_o^{(\alpha)} : \mathbf{A}^{(\alpha)} : \mathrm{GRAD}\, \Delta \boldsymbol{u}^{(\alpha)}\, \mathrm{d}V \\ &+ \int_{\Gamma_{\mathrm{I}}} \left[\!\left[\boldsymbol{\eta}_o \right]\!\right] \cdot \boldsymbol{\tau}_s \cdot \left[\!\left[\Delta \boldsymbol{u} \right]\!\right] \mathrm{d}A - \int_{\Gamma_{\mathrm{I}}} \left[\!\left[\boldsymbol{\eta}_o \right]\!\right] \cdot \left\{ \left(\mathbf{A} : \mathrm{GRAD}\, \Delta \boldsymbol{u} \right) \cdot \boldsymbol{N} \right\} \mathrm{d}A \\ &- \int_{\Gamma_{\mathrm{I}}} \left\{ \left(\mathrm{GRAD}\, \boldsymbol{\eta}_o : \mathbf{A} \right) \cdot \boldsymbol{N} \right\} \cdot \left[\!\left[\Delta \boldsymbol{u} \right]\!\right] \mathrm{d}A \\ &- \int_{\Gamma_{\mathrm{I}}} \left\{ \left(\mathrm{GRAD}\, \boldsymbol{\eta}_o : \boldsymbol{\Xi} : \mathrm{GRAD}\, \Delta \boldsymbol{u} \right) \cdot \boldsymbol{N} \right\} \cdot \left[\!\left[\boldsymbol{\phi} \right]\!\right] \mathrm{d}A \end{aligned} \tag{3-54}$$

We observe that (3-54) is symmetric with respect to the variations $\boldsymbol{\eta}_o^{(\alpha)}$ and the incremental displacement $\Delta \boldsymbol{u}^{(\alpha)}$. Therefore, the underlying variational structure associated with the mixed interface problem (3-12) has been preserved throughout the fine-scale modeling procedure. The fact that the stiffness matrix is symmetric also makes this formulation amenable for incorporation into standard pure-displacement finite element codes. Additionally, once an explicit form of the material model $W^{(\alpha)}$ is chosen for each region $\Omega^{(\alpha)}$, all of the terms in the weak form (3-48) and

the incremental form (3-54) can be directly evaluated through the constitutive equations (3-6), (3-29), and (3-53).

Remark: *The higher-order derivatives involved in the definition of* $\boldsymbol{\Xi}^{(\alpha)}$ *may be difficult to derive and subsequently expensive to evaluate within an element subroutine for complex material models. However, the term involving this sixth-order material moduli tensor in (3-54) is driven by the interface residual, namely the discrete interface gap* $[\![\boldsymbol{\phi}]\!]$*. When the value of this residual is small within a finite element simulation, the contribution from this term becomes less significant. Also, this term does not appear in (3-48), and thus it only contributes to the stiffness matrix. The effect of neglecting these terms will be considered in future work.*

Remark: *While the derivations in section 3.3 have been carried out in the reference configuration, the resulting expressions may be pushed forward to the spatial configuration, which may be easier to implement in the finite element context. We provide the spatial counterpart of the significant equations in Appendix B.1.*

3.4 Extension to Multiple Interfaces and Fully Discontinuous Approximations

The preceding derivations can be readily extended to domains containing multiple interfaces and ultimately lead to a formulation analogous to the classical DG interior penalty method. To expand upon this point, consider the weak form (3-7) involving the Lagrange multiplier at the interface Γ_{I}. We apply the integration by parts and the divergence theorem in each domain $\Omega^{(\alpha)}$ to obtain the Euler-Lagrange equations through the weighted-residual form:

$$\begin{aligned}&-\sum_{\alpha=1}^{2}\int_{\Omega^{(\alpha)}}\boldsymbol{\eta}_o^{(\alpha)}\cdot\left(\mathrm{DIV}\,\boldsymbol{P}^{(\alpha)}+\rho_o^{(\alpha)}\boldsymbol{B}^{(\alpha)}\right)\mathrm{d}V+\sum_{\alpha=1}^{2}\int_{\Gamma^{(\alpha)}\setminus\Gamma_{\mathrm{I}}}\left(\boldsymbol{P}^{(\alpha)}\cdot\boldsymbol{N}^{(\alpha)}\right)\cdot\boldsymbol{\eta}_o^{(\alpha)}\,\mathrm{d}A\\&+\int_{\Gamma_{\mathrm{I}}}\left(\boldsymbol{P}^{(1)}\cdot\boldsymbol{N}^{(1)}-\boldsymbol{\lambda}\right)\cdot\boldsymbol{\eta}_o^{(1)}\,\mathrm{d}A+\int_{\Gamma_{\mathrm{I}}}\left(\boldsymbol{P}^{(2)}\cdot\boldsymbol{N}^{(2)}+\boldsymbol{\lambda}\right)\cdot\boldsymbol{\eta}_o^{(2)}\,\mathrm{d}A=0\end{aligned}\tag{3-55}$$

Here, the traction boundary integral $\partial\Omega^{(\alpha)}=\Gamma^{(\alpha)}$ has been split into a portion adjoining the interface and the remainder of the boundary. The terms on $\Gamma^{(\alpha)}\setminus\Gamma_{\mathrm{I}}$ vanish because $\boldsymbol{\eta}_o^{(\alpha)}=\mathbf{0}$ according to the functional space $\mathcal{V}^{(\alpha)}$ in (3-10). Therefore, upon invoking the fundamental theorem of the calculus of variations, we arrive at the equilibrium equation in each region $\Omega^{(\alpha)}$ as in (3-2) along with traction equilibrium on Γ_{I} as in (3-5) imposed through $\boldsymbol{\lambda}$.

Now suppose that multiple interfaces are present in domain Ω. The continuity conditions on each

interface can be imposed weakly by incorporating independent Lagrange multiplier fields $\boldsymbol{\lambda}_{(\alpha)}$ over each unique pair of adjacent region boundaries. The corresponding weak form would be the generalization of the integrals in (3-5) to summations over all domain regions and over all region boundary pairs constituting interfaces. However, by assuming that the fine-scale fields are localized to the vicinity of the interfaces, the fine-scale problem corresponding to (3-25) may again be separated into a series of smaller problems posed over individual interfaces and furthermore over discrete interface segments as in (3-27). Thereafter, the remainder of the derivations applies identically to each specific interface, allowing a condensation of each $\boldsymbol{\lambda}_{(\alpha)}$ analogous to (3-38) and resulting in a global problem expressed entirely in terms of the coarse scale $\hat{\boldsymbol{\phi}}^{(\alpha)}$ across all regions.

Taking this argument further, let the domain Ω be discretized into a set of finite elements $\left\{\Omega_e\right\}_{e=1}^{n_{umel}}$. Within the context of the preceding discussion, we now treat each interelement boundary as an interface and each element as a region. By weakly imposing continuity across each pair of adjacent elements, we arrive at a fully discontinuous approximation of the solution field $\boldsymbol{\phi}$, where the integrals in (3-48) are evaluated over all element interiors $\tilde{\Omega}$ and element interfaces $\tilde{\Gamma}$. The resulting formulation appears quite similar to the classical interior penalty Discontinuous Galerkin method [8,107,9,122]. Note that in these methods, the numerical flux is almost invariably defined as the arithmetic average of tractions and the penalty parameter is obtained via dimensional and scaling arguments. In contrast, we emphasize that the penalty parameter contained herein has been consistently derived and the numerical flux is obtained as a weighted average according to (3-46).

Remark: *A strong point of the present framework is that it naturally accommodates a spectrum of problems from domains with a single interface to domains with multiple interfaces and to fully discontinuous approximations across finite element boundaries. The inherent stability enabling this range of problem classes derives from the stability afforded by the evolving fine-scale models for* $\boldsymbol{\tau}_s^{(\alpha)}$.

Remark: *As is the case amongst almost all Discontinuous Galerkin methods, the fully discontinuous approximation case is more computationally expensive than the corresponding continuous Galerkin approximation for the same number of elements because of the increased*

number of degrees of freedom in the global stiffness matrix. This cost is greatly reduced for domains with specific nonconforming interfaces wherein continuous approximations are employed in the region interiors. For such problems, the cost of the present method is lower than the comparable mortar methods because the Lagrange multiplier field is not solved as an added unknown in the discrete problem. The only relative increase in element-level calculations compared to existing DG methods [122] and Nitsche methods [58] is the evaluation of the stability tensors, which represents the crucial benefit of the proposed method. A remark on the relative cost increase at the interface element level is contained in section 3.6.3.

Remark: *Special care must be taken when localizing the fine scales within elements in the context of the fully discontinuous approximation. For example, consider a triangular element* Ω_e *which has individual interface segments* $\gamma_s^{(\beta)}$ *corresponding to each of its three edges. Each segment is assigned a sector* $\omega_s^{(\beta)} \subseteq \Omega_e$ *over which a portion of the fine-scale field* $\tilde{\boldsymbol{\phi}}$ *is supported as in (3-26). Strictly speaking, to ensure that the fine-scale problems (3-27) for each interface segment/sector pair remain independent, the sectors* $\omega_s^{(\beta)}$ *within the common element* Ω_e *must not overlap, namely* $\omega_s^{(1)} \bigcap \omega_s^{(2)} = \varnothing$, $\omega_s^{(2)} \bigcap \omega_s^{(3)} = \varnothing$, *and* $\omega_s^{(3)} \bigcap \omega_s^{(1)} = \varnothing$. *This issue is discussed further in section 3.5.*

3.5 Aspects of Implementation: Fine-Scale Sectors and Bubble Functions

In this section, we elaborate on key aspects of our implementation of the proposed method. As noted in [162], the choice of the fine-scale bubble functions $b_s^{(\alpha)}$ has an important impact on the accuracy of the computed results. One possible representation considered in other interface methods [45] is the use of residual-free bubbles, which are designed to be orthogonal to the space of the coarse-scale equilibrium residual, implying $\int_{\omega_s^{(\alpha)}} \boldsymbol{b}_s^{(\alpha)} \cdot \left(\mathrm{DIV}\, \boldsymbol{P}^{(\alpha)} + \rho_o^{(\alpha)} \boldsymbol{B}^{(\alpha)} \right) \mathrm{d}V = 0$. Although these functions satisfy the assumption that was employed to simplify the fine-scale solution (3-32), they are obtained by solving a local boundary-value problem and are therefore quite expensive. As an alternative, simple polynomial bubble functions were analyzed in [162] for two-dimensional linear elasticity problems and found to provide robust performance across various element types and mesh distortion. Therefore, we elect to use these edge bubble functions for the present nonlinear formulation, which are summarized in Table 3.1; note that the letter and number

designate the element shape and number of nodes, respectively. For three-dimensional domains, the authors proposed in [162] to partition the interface into triangular segments in order to accommodate general nonconforming meshes. The corresponding sectors for tetrahedral and hexahedral elements take the form of smaller tetrahedral and wedge-shaped regions, respectively. Polynomial bubble functions which are nonzero within the base of these sectors are listed in Table 3.2. To simplify these tables, the reference sector coordinate system (ξ,η) or (ξ,η,ζ) is assumed to be oriented such that the interface segment corresponds to the bottom of the sector. The reader is referred to [162] for several figures illustrating the definitions of the sectors along with further discussion on the bubble functions. The contour plots of the edge bubble functions in Table 3.1 for element type Q4 and Q9 are given in Figure 3.4.

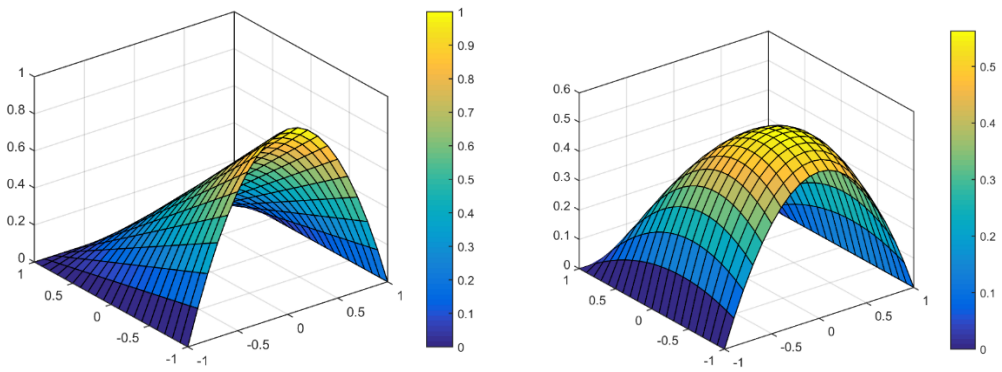

(a) (b)

Figure 3.4.Contour plots for the edge bubble functions: (a) Q4 element; (b) Q9 element.

Table 3.1. Edge bubble functions employed for fine-scale fields, two dimensions.

Element	Bubble Function
T3	$4\xi(1-\xi-\eta)$
Q4	$\frac{1}{2}(1-\xi^2)(1-\eta)$
T6	$4\xi^2(1-\xi-\eta)^2$
Q9	$\frac{1}{4}(1-\xi^4)(1-\eta)^2+\frac{1}{4}(1-\xi^2)(1-\eta)$

Table 3.2. Face bubble functions employed for fine-scale fields, three dimensions.

Element	Bubble Function
T4	$27\xi\eta\left(1-\xi-\eta-\zeta\right)$
B8	$\frac{27}{2}\xi\eta\left(1-\xi-\eta\right)\left(1-\zeta\right)$

Another key factor in the fine-scale modeling procedure is the definition of the interface sectors $\omega_s^{(\alpha)} \subseteq \Omega_e$ over which the localized fine-scale equation (3-27) is solved. An obvious convention is to define a tributary sector that extends from the interface segment through the entire depth of the element, as illustrated in Figure 3.3. However, previous investigations [162] determined that the bubble functions in Table 3.1 remain non-zero over a significant portion of their domain of support. For elements with high aspect ratios, namely a large depth compared to width along the interface, taking their domain of support $\omega_s^{(\alpha)}$ to extend through the entire depth of the element produces exceedingly large values of the penalty parameter in the context of linear elasticity. In comparison, the residual free bubble remains locally supported in the zone of the interface and produces a smaller value for the penalty parameter. Therefore, the authors advocated in [162] to employ truncated definitions of the interface sectors for elements with large aspect ratios, whereby the maximum extension of the sector into the element is approximately limited to the size of the segment γ_s. This procedure contained in Boxes 1 through 4 of [162] is entirely geometrical in nature and is therefore readily extendable to the present nonlinear formulation, and we adopt it for the numerical studies in section 3.6. Note that the integrals in the fine-scale model (3-27) are performed in the reference configuration; as such, we treat the image of the interface sectors in the reference configuration to be fixed throughout the course of the numerical simulations.

Remark: *A further rationale for limiting the support of the bubble functions is that the interfacial effects which they model are localized according to Saint-Venant's principle, mentioned previously in section 3.3.2. While other functions could be proposed that decay exponentially with distance from the interface, the bubble functions presented here have the advantages of being simple in form and easily integrated by numerical quadrature.*

As remarked at the end of section 3.4, instances may arise in which an element has multiple edges serving as interfaces, particularly in the case when fully discontinuous approximations are

employed. Each of the sectors that are assigned to these edges should be taken as disjoint regions of the element such that the localized fine-scale problems (3-27) remain independent. A possible definition for the sectors of a quadrilateral element with all four edges identified as interface segments is illustrated in Figure 3.5. However, the definition of such regions is not directly compatible with the procedure summarized in the preceding paragraphs, which is adapted from [162]. Previously, the sectors were assumed to be freely extendable across the entire depth of the element in the direction orthogonal to the interface segment without conflict from neighboring sectors. In order to keep the implementation of the method simple, we adopt the following heuristic approach. For each edge serving as an interface segment, we define the sector according to the appropriate Box from [162] without considering the presence of other segments. Then the value of the stabilizing tensor $\boldsymbol{\tau}_s^{(\alpha)}$ for each sector is computed using (3-35). Finally, each tensor is scaled down by the number of edges e_s: $\overline{\boldsymbol{\tau}}_s^{(\alpha)} = \left(e_s\right)^{-1} \boldsymbol{\tau}_s^{(\alpha)}$ to approximately account for the overlap of the sectors. For example, notice that in Figure 3.5 that the area of each sector $\omega_s^{(\alpha)}$ is one-fourth the area of Ω_e. The values of $\overline{\boldsymbol{\tau}}_s^{(\alpha)} = \left(e_s\right)^{-1} \boldsymbol{\tau}_s^{(\alpha)}$ are then substituted into definition (3-39) for the numerical flux weights $\boldsymbol{\delta}_s^{(\alpha)}$ and the penalty parameter $\boldsymbol{\tau}_s$. Combining the definitions of the bubble functions $\boldsymbol{b}_s^{(\alpha)}$ from Table 3.1 and Table 3.2 with the above definitions for the sectors $\omega_s^{(\alpha)}$ completes the description of the fine-scale models employed in this study.

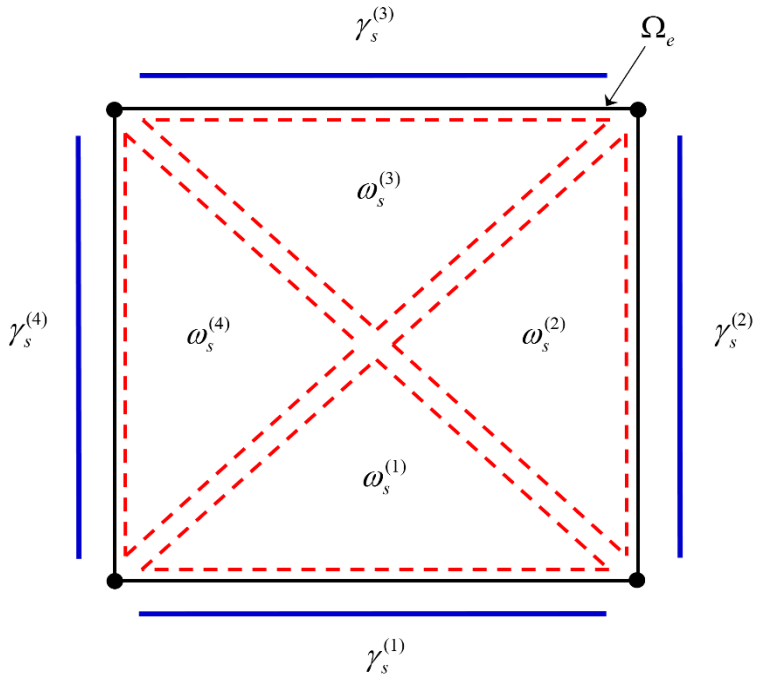

Figure 3.5. Disjoint sectors within a quadrilateral element possessing multiple interface segments.

Remark: *Notice from definition (3-39) that when the stability tensors* $\boldsymbol{\tau}_s^{(1)} \approx \boldsymbol{\tau}_s^{(2)}$ *across a segment, the weights* $\boldsymbol{\delta}_s^{(\alpha)}$ *are not significantly affected by this heuristic modification of* $\boldsymbol{\tau}_s^{(\alpha)}$. *In contrast, the value of the stability parameter* $\boldsymbol{\tau}_s$ *is increased proportionally to* e_s. *This small increase tends to enhance the stability of the method without inducing ill-conditioning of the stiffness matrix (3-54).*

3.6 Numerical Results

We investigate the performance of the proposed interface method across a range of deformation modes. Standard Lagrange polynomials are employed within the finite elements of either linear or quadratic degree, and both two- and three-dimensional problems are considered. A common neo-Hookean material model is employed for each of the problems, with a strain energy density function as follows:

$$W(\boldsymbol{F}) = \frac{1}{2}\mu\left(\mathrm{tr}\left(\boldsymbol{F}^T\boldsymbol{F}\right)-3\right) - \mu \ln J + \frac{1}{2}\lambda(J-1)^2 \tag{3-56}$$

Expressions for the corresponding constitutive tensors $\boldsymbol{P}$, $\mathbf{A}$, and $\boldsymbol{\Xi}$ are provided in the Appendix B.2. All integral expressions over surfaces and volumes are evaluated using Gauss quadrature rules of sufficient degree. Results are presented first for meshes with specific interfaces where continuity is weakly imposed, which corresponds with the formulation derived in sections 3.2 and 3.3. Additional numerical tests are performed using fully discontinuous approximations across all elements as illustrations of the multiple interface formulation discussed in section 3.4. To distinguish these cases, we refer to the former case by the name stabilized Nitsche interface method while the latter case is termed as the stabilized DG method.

Remark: *The integration of the material contribution to $\boldsymbol{\tau}_s^{(\alpha)}$ according to (3-33) is performed over the interface sector $\omega_s^{(\alpha)}$ which is typically a subset of the element Ω_e. However, the acoustic tensor $\mathbf{A}^{(\alpha)}$ is evaluated in terms of the deformation gradient $\boldsymbol{F}$, which is a function of the coarse-scale deformation $\hat{\boldsymbol{\phi}}$ defined over the entire element. Thus, evaluating these integrals requires a transformation of coordinates between the sector and the parent element, which is not encountered for homogeneous materials in the linear setting [162].*

Remark: *Since the fine-scale tensors $\boldsymbol{\tau}_s^{(\alpha)}$ are a function of the deformation, three value evolves during each iteration of the Newton-Raphson solution procedure. However, this effect is not accounted for in the linearization provided in section 3.3.3, as remarked at that point. Similar to observations in the context of a VMS formulation for nonlinear incompressible elasticity [101], neglecting these effects leads to a reduced convergence rate of the out-of-balance force vector. To restore the quadratic rate of iterative convergence, the value of $\boldsymbol{\tau}_s^{(\alpha)}$ can be frozen for each interface segment after a specified number of iterations and held constant over the remainder of the load step. Herein, the value is frozen after three iterations.*

3.6.1 Tensile patch test

We begin by solving a simple patch test to verify the consistency of the interface formulation. A rectangular bar of 1 mm × 1 mm is separated into two rectangular regions by a nonconforming interface over which the proposed stabilized Nitsche interface method is employed, as shown in Figure 3.6. The material properties within the neo-Hookean model (3-56) are taken as $E = 100$ MPa and $\nu = 0.25$. A uniform traction of 20 MPa is applied to the right edge of the

domain and boundary conditions are assigned on the left face in order to create a state of uniform tensile stress throughout the specimen. Under these conditions, the exact value for the tip elongation is $\delta = 0.2110\,\text{mm}$.

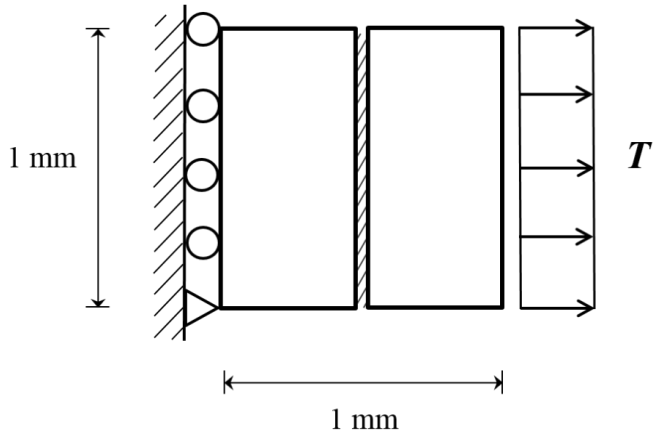

Figure 3.6. Patch test problem description.

Two meshes are considered that contain linear triangular and quadrilateral elements, respectively, as shown in Figure 3.7. Each region contains four quadrilateral elements; the triangular mesh is obtained by bisecting the quadrilateral elements. In the left region, the elements are rectangles 0.25×0.5; in the right region, the line of nodes in the center is dropped downward to the coordinate $Y = 0.4$ to make the interface nonconforming. The traction field is applied in a single load step to produce the numerical solutions in Figure 3.7. The solution field from both meshes is smooth and reproduces the exact value of the tip displacement, with the displacement gap between the regions correctly resolved as identically zero.

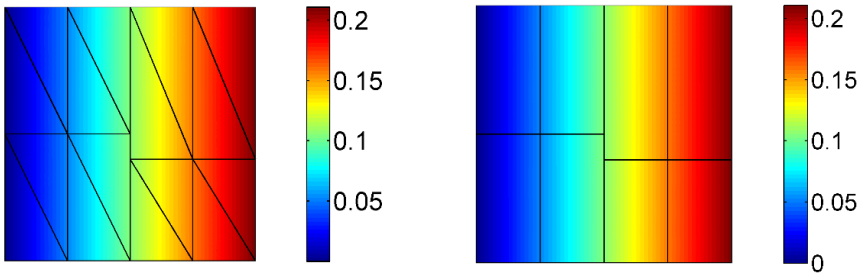

(a) (b)

Figure 3.7. Displacement u_x contour on nonconforming meshes: (a) triangular mesh; (b) quadrilateral mesh.

In Table 3.3, we record the Euclidean norm of the out-of-balance force vector computed at each iteration during the Newton-Raphson solution procedure. The observed quadratic convergence rate numerically confirms of the consistent linearization and tangent matrix provided in section 3.3.3.

Table 3.3. Evolution of residual l^2 norm for nonconforming meshes.

Iteration Number	Residual Norm	
	T3 Elements	Q4 Elements
1	5.6094580×10^{-2}	5.6094580×10^{-2}
2	2.9576726×10^{-5}	2.9576726×10^{-5}
3	8.1814644×10^{-12}	8.1870099×10^{-12}
4	3.0798871×10^{-14}	2.2733456×10^{-14}

3.6.2 Trapezoidal deformation problem

As further verification of consistency and stability, we consider another problem with an exact solution that was originally proposed in [101]. The geometry consists of a square domain which is subsequently deformed into a trapezoid by raising the upper right-hand corner. A single pure-displacement quadrilateral element is capable of representing this deformation mode, as shown in Figure 3.8.

The analytical solution is reproduced below in Cartesian coordinates in terms of the vertical displacement δ of the corner node:

$$x = X, \qquad y = \delta XY + Y, \qquad z = Z \tag{3-57}$$

The deformation gradient and Jacobian are given as:

$$\boldsymbol{F} = \begin{bmatrix} 1 & 0 & 0 \\ \delta Y & \delta X + 1 & 0 \\ 0 & 0 & 1 \end{bmatrix}, \qquad J = \delta X + 1 \tag{3-58}$$

Considering the stored elastic strain energy function given by (3-56), the first Piola-Kirchhoff stress tensor follows as:

$$\boldsymbol{P} = \begin{bmatrix} \delta\lambda JX & \delta\mu Y/J - \delta^2\lambda XY & 0 \\ \delta\mu Y & \left[\delta X\left(\lambda J + \mu + \mu J\right)\right]/J & 0 \\ 0 & 0 & \delta\lambda JX \end{bmatrix} \tag{3-59}$$

Substituting (3-59) into (3-2) leads to an expression for the body force term below:

$$\rho_o \boldsymbol{B} = -\text{DIV}\ \boldsymbol{P} = \left[-\left(\delta\mu/J + \delta\lambda J\right) \quad 0 \quad 0\right]^T \tag{3-60}$$

The material parameters are taken as $\lambda = \mu = 40$ and the load parameter as $\delta = 1.01$. To investigate this problem in the numerical setting, we apply fixed boundary conditions on the lower edge and apply the analytical tractions arising from (3-59) on the other edges, as depicted in Figure 3.8 (a). Due to the appearance of $J = \delta X + 1$ in the denominator of (3-59) and (3-60), the integrands within the finite element residual vector and the tangent matrix will contain rational polynomials that are not precisely evaluated through low-order Gauss quadrature. In order to obtain the exact solution to numerical precision, we employ higher-order rules using 10 × 10 quadrature points for element-interior integrals and 10 points for boundary or interface integrals.

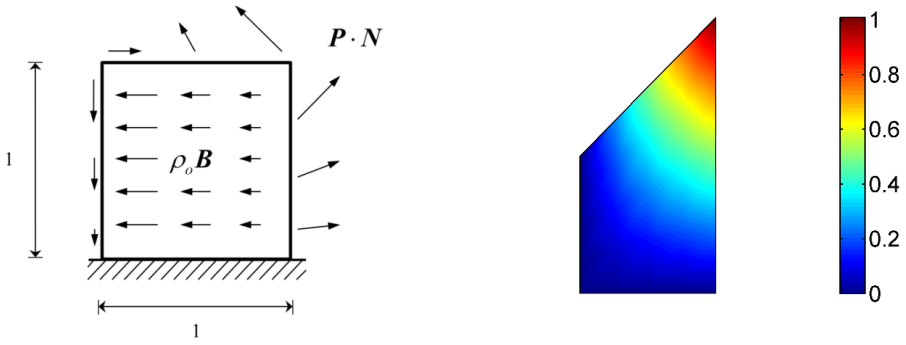

(a) (b)

Figure 3.8. Trapezoidal deformation problem: (a) problem domain; (b) exact vertical displacement on deformed configuration.

Two discretizations of the domain are considered, as shown in Figure 3.9. The first mesh consists of two regions of four bilinear quadrilateral elements separated by an initially horizontal stabilized Nitsche interface. In the second mesh, the lower region is represented using two quadratic triangular elements in the lower-left and one biquadratic element in the lower-right; the upper region contains three bilinear quadrilaterals such that the interface is nonconforming. Note that linear triangular elements cannot reproduce the exact solution except in the limit of mesh refinement [101] and thus are not employed in this study. Also, the mid-side nodes of the quadratic elements must be located at the midpoint of the associated element edge in order for the finite element shape functions to reproduce the exact solution. Using this problem, we investigate the performance of the interface method for higher-order elements and for an interface that undergoes

rotation during the loading.

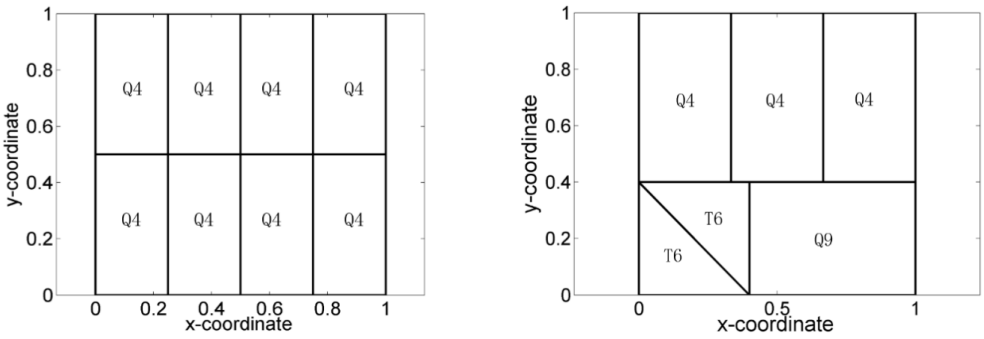

(a) (b)

Figure 3.9. Nonconforming meshes: (a) bilinear quadrilaterals; (b) linear and quadratic elements.

The body force and tractions (3-59) – (3-60) are applied in four equal load steps to reach the deformed configurations presented in Figure 3.10. For both meshes, the displacement field matches precisely with the solution contour in Figure 3.8 (b), confirming the consistency of the formulation. No gaps or distortion of the interface is evident in the discrete response. Thus, the proposed interface method is capable of tying meshes with different element types across interfaces undergoing finite deformations.

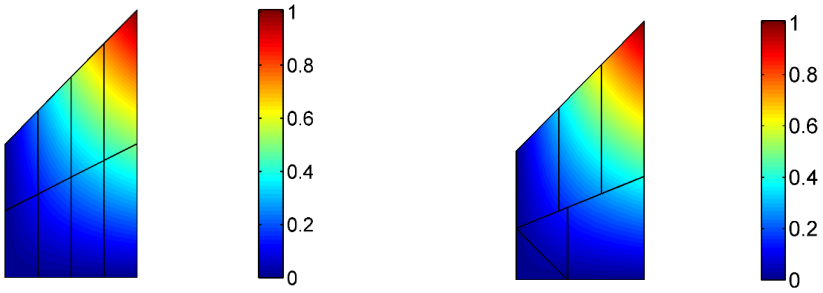

(a) (b)

Figure 3.10. Vertical displacement contours on deformed configuration: (a) bilinear quadrilaterals (b) mixture of linear and quadratic elements.

In Table 3.4, we again show the Euclidean norm of the out-of-balance force vector computed at each iteration during the Newton-Raphson solution procedure. The quadratic convergence rate is achieved.

Table 3.4. Evolution of residual l^2 norm for two different mesh types.

Iteration Number	Residual Norm	
	Q4 Elements	Q4-T6-Q9 Elements
1	6.1686067×10^{-1}	1.0397659×10^{0}
2	2.6368099×10^{-2}	1.8790396×10^{-2}
3	2.0567903×10^{-6}	5.0704490×10^{-6}
4	4.0519883×10^{-14}	4.0763657×10^{-13}

Remark: *The number of quadrature points is increased solely for this numerical example in order to resolve the analytical solution to numerical precision. For low-order rules, the slight errors in the discrete solution are directly attributed to the quadrature error. Note that since the stress tensor (3-59) involves rational polynomials, the computation of the internal force vector associated with (3-48) also requires higher-order quadrature. As an alternative, quadrature rules for integrating rational functions could be employed.*

3.6.3 Parabolic indentation of a square block

In this problem, we investigate the ability of the fine-scale models to providing varying levels of stabilization across a domain in accordance with the evolving geometric and material nonlinearity. The domain consists of a bi-unit square with fixed boundary conditions on the lower edge and traction-free vertical edges. The top surface of the block is indented by an applied displacement which maps it into a parabola according to the following:

$$u_2\left(X_1, X_2 = 1.0\right) = a\left(X_1 - 0.25\right)\left(X_1 - 0.75\right) \tag{3-61}$$

where a is a proportional loading parameter and the horizontal displacement component is left free. This problem was originally studied by Ten Eyck and Lew [52]; the distinguishing feature is that the acoustic tensor $\mathbf{A}$ becomes indefinite in the vicinity of the bowl of the parabola for values of $a > 0.1$. The resulting negative eigenvalues are an indicator of localized material instability. When a DG method with a spatially-uniform value for the stabilization parameter was employed, spurious oscillations in the inter-element displacement field jumps were manifested in this region of the domain. This observation prompted the adaptive stabilization strategy in [52] where the stability parameter along each element edge was scaled by the magnitude of the largest negative eigenvalue of $\mathbf{A}$ along that same edge. This strategy led to stable discrete response whereby the jump discontinuities were controlled throughout the domain.

Presently, we employ a DG approximation using linear triangular elements within the interface

method proposed herein. The key idea is to determine whether the consistent definitions for the numerical flux and penalty parameter (3-39) are able to accommodate the local material instability naturally. Three levels of mesh resolution are selected to coincide with the meshes from [52]. However, the Dirichlet boundary conditions are strongly rather than weakly imposed, which leads to slight discrepancies in the computed results compared to the reference. The indentation is applied in ten equal load steps $\Delta a = 0.25$ up to the maximum value $a = 2.5$.

Deformed configurations obtained at two load levels are shown in Figure 3.11 for the mesh with $h = 1/9$. As the indentation is increased, larger inter-element discontinuities appear in the upper-left portion of the domain, which can be attributed to the strongly imposed boundary conditions and the coarseness of the mesh. However, the global response is quite stable and in close agreement with the stable results presented in [52].

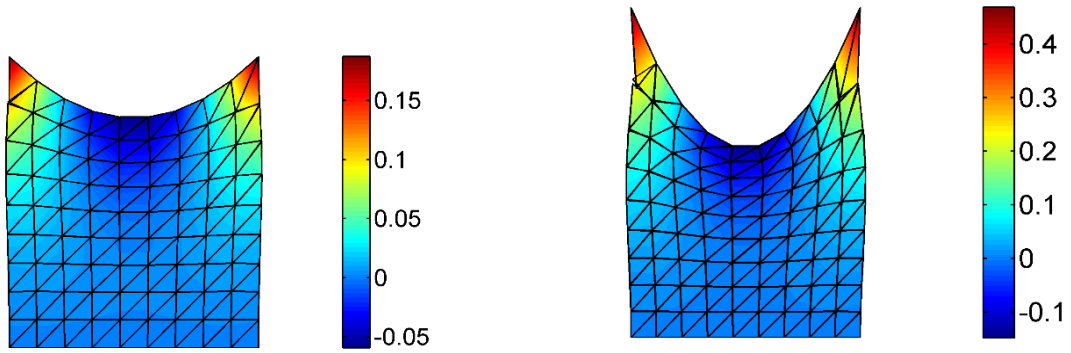

(a) (b)

Figure 3.11. Vertical displacement u_2 superimposed on deformed configuration, mesh $h = 1/9$: (a) $a = 1.0$; (b) $a = 2.5$.

We also compare the final deformed configurations obtained on the three mesh resolutions in Figure 3.12. On the coarse mesh in Figure 3.12 (a), discontinuities are reasonably significant throughout the domain. A key attribute of DG methods as advocated in [52] is that coarse-mesh solutions can be obtained with improved accuracy in the gradient fields compared to continuous Galerkin approximations by relaxing inter-element continuity. Our results in Figure 3.12 agree qualitatively with that assessment, and the discontinuities steadily diminish as the mesh is refined.

Additionally, across all meshes, the proposed formulation yields stable results free from spurious oscillations in the displacement jumps.

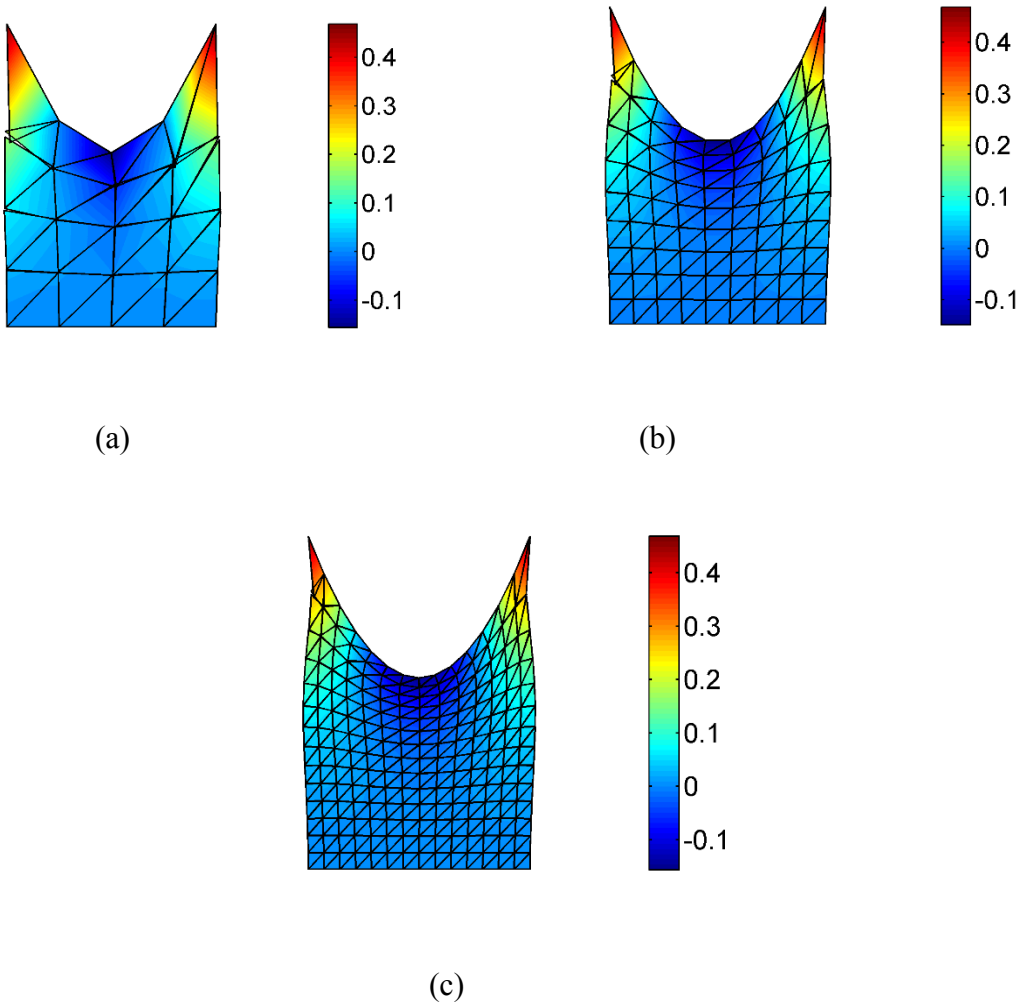

Figure 3.12. Vertical displacement u_2 superimposed on deformed configuration at load level $a = 2.5$: (a) $h = 1/4$; (b) $h = 1/9$; (c) $h = 1/14$.

In order to examine the stabilization afforded by the fine-scale models, in Figure 3.13 we plot the norm of the penalty parameter $\|\boldsymbol{\tau}_s\| = \sqrt{\boldsymbol{\tau}_s : \boldsymbol{\tau}_s}$ computed according to (3-39) along each element interface at the final indentation level. The colors of the element edges in the mesh correspond to the magnitude of the parameter as denoted by the color-bar. Clearly, significant spatial variability is present in the stabilization parameters. Firstly, the magnitude of the parameters increases uniformly with mesh refinement while the distributions remain fairly consistent, indicating proper scaling with the element length scale [9,51,52]. Thus, the remarks that follow apply equally to each

of Figure 3.13 (a) – (c). Another common trend is that the values for diagonal edges are larger than for edges aligned with the coordinate axes. Namely, the fine scales are attuned to the anisotropy induced in the discrete problem by isosceles triangular elements. More importantly, the values near the bowl of the parabola are about 5-10 times higher than the values observed throughout the rest of the domain. This results in more stabilization being applied in regions coinciding with the indefinite acoustic tensor, which agrees closely with the adaptive strategy considered in [52]. However, we emphasize that the trends presented here arise automatically from the fine-scale models (3-34) without any external calibration or monitoring.

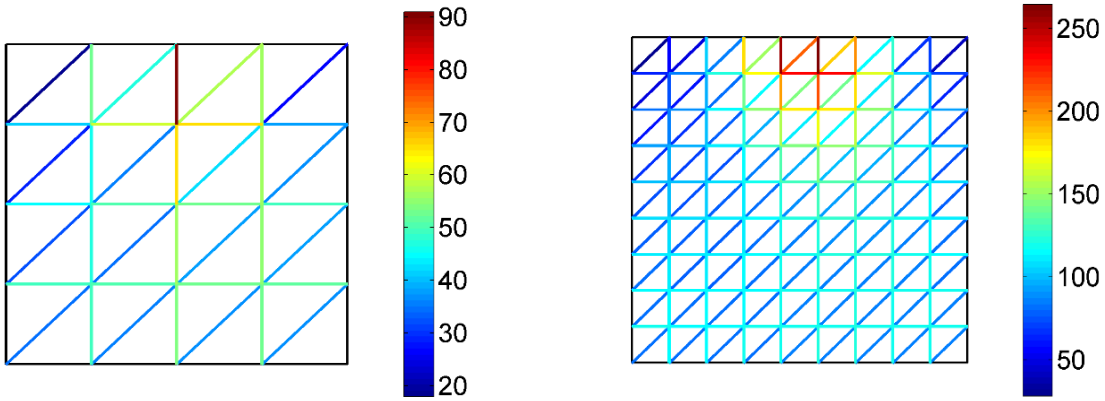

(a) (b)

Figure 3.13. Wire-frame contour of stabilization tensor $\|\boldsymbol{\tau}_s\|$ along element edges: (a) $h = 1/4$; (b) $h = 1/9$; (c) $h = 1/14$.

Figure 3.13 continued.

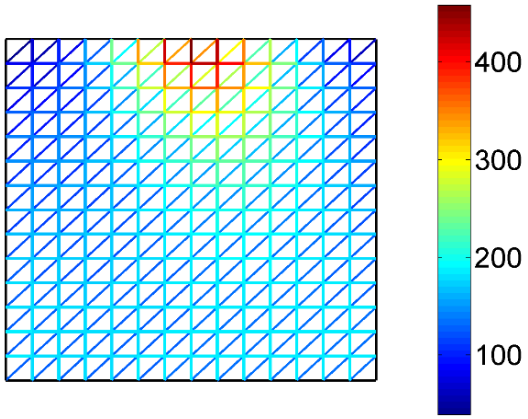

(c)

Remark: *Similar spatial variation in the stabilization tensors was observed in the context of a VMS-stabilized method for finite mixed hyperelasticity [101], whereby the magnitude of the tensors was larger in regions corresponding to larger stresses. Therein, the stabilization tensors are also derived in terms of fine-scale bubble functions and incorporate the constitutive material tensors. Thus, the strong link between the fine scales and the evolving coarse-scale deformations is shared with the present method.*

Remark: *From the perspective of the cost of computation of the element-level quantities, the computation of the stability tensors* $\boldsymbol{\tau}_s^{(\alpha)}$, $\boldsymbol{\tau}_s$, *and* $\boldsymbol{\delta}_s^{(\alpha)}$ *add approximately one-third additional computational cost relative to the cost of evaluation of the residual vector and stiffness matrix associated with the interface terms as compared to using constant values for the parameters. In the opinion of the authors, this cost is offset by the benefits of having robust, nonlinearly evolving definitions of the parameters that require no calibration by the end-user. This enables the confident application of the method to problems containing non-matching meshes, different element types, and heterogeneous material properties in the context of finite strains.*

3.6.4 Finite deformation pure bending

In the fourth example problem, we investigate the performance of the proposed DG method under significant bending deformation. The domain of interest is a rectangular bar that is bent into an arc

subtending an angle 2ψ, as illustrated in Figure 3.14. The solution for this plane strain problem is presented in Ogden [124] for an incompressible neo-Hookean material model, for which the deformation map $\boldsymbol{x} = \boldsymbol{\phi}(\boldsymbol{X})$ takes the following form:

$$\boldsymbol{x} = \begin{bmatrix} r\cos\theta \\ r\sin\theta \\ Z \end{bmatrix}, \qquad r(X) = \sqrt{\frac{2LX}{\psi} + R_o^2 - \frac{LH}{\psi}}, \qquad \theta(Y) = \frac{Y\psi}{L} \tag{3-62}$$

where R_0 and R_i are the outer and inner radii, respectively, of the beam in the deformed configuration.

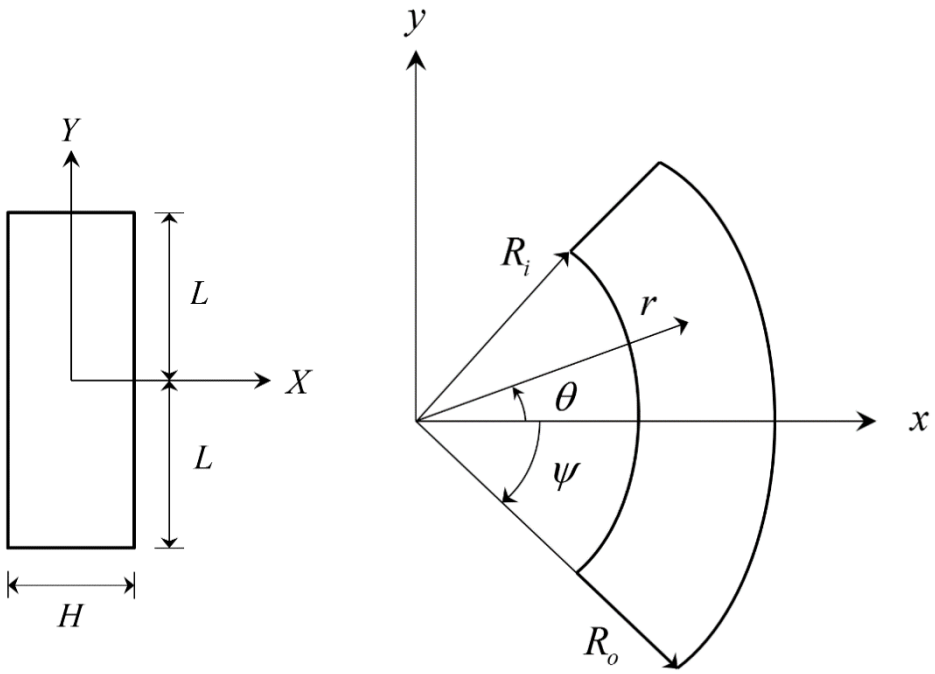

(a) (b)

Figure 3.14. Pure bending of a rectangular beam: (a) undeformed configuration; (b) deformed configuration.

Notice that each longitudinal fiber of the beam originally parallel to the Y-axis is mapped into an arc of radius r, although this radius is not directly proportional to the original depth X of the fiber in the reference configuration. Additionally, the radius r and angle θ are separable functions of the reference coordinates X and Y, respectively. Therefore, the deformation gradient $\boldsymbol{F}$ can be expressed in the following simple form:

$$\boldsymbol{F}=\begin{bmatrix}\left(L/\psi r\right)\cos\theta & -\left(\psi r/L\right)\sin\theta & 0\\ \left(L/\psi r\right)\sin\theta & \left(\psi r/L\right)\cos\theta & 0\\ 0 & 0 & 1\end{bmatrix} \tag{3-63}$$

It can be seen that the deformation represents pure bending since the off-diagonal components of the Green deformation tensor $\boldsymbol{C}=\boldsymbol{F}^T\boldsymbol{F}$ are identically zero and is also isochoric since $J=\det\left(\boldsymbol{F}\right)=1$. To ensure a globally incompressible response, the deformed and undeformed areas of the beam must be equal:

$$2HL=\psi\left(R_o^2-R_i^2\right) \tag{3-64}$$

Furthermore, a second condition on the radii is obtained from the equilibrium equation [124] such that the tractions on the inner and outer surfaces vanish for an incompressible material:

$$\left(L/\psi\right)^2=R_oR_i \tag{3-65}$$

For a given value of the bend angle ψ, the system of equations (3-64) – (3-65) can be solved simultaneously to determine relationships for R_i and R_0 in order to express the deformed radius r solely in terms ψ (These rather lengthy expressions are not reported here). While this solution was originally derived for an ideal incompressible material, the deformation remains valid for a compressible material. Employing (3-63) within the constitutive law (3-56) results in the following expressions for the stress tensor and consistent body force for equilibrium:

$$\boldsymbol{P}=\left(\mu\left(L^2-\psi^2r^2\right)\Big/\psi Lr\right)\begin{bmatrix}\cos\theta & \sin\theta & 0\\ \sin\theta & -\cos\theta & 0\\ 0 & 0 & 0\end{bmatrix} \tag{3-66}$$

$$\rho_o\boldsymbol{B}=\frac{\mu\kappa}{\psi^2L^2r^3}\begin{bmatrix}\cos\theta\\ \sin\theta\\ 0\end{bmatrix},\qquad \kappa=R_o^2\psi^4\left(2r^2-R_o^2\right)+L^2\left(L^2+\psi^2\left(H-2X\right)^2\right) \tag{3-67}$$

Using this exact solution, we conduct a numerical convergence analysis on a sequence of uniformly refined meshes. Only the top half of the beam is modeled, and symmetry boundary conditions are applied to the mid-plane of the beam $Y=0$. The traction field resulting from (3-66) is applied to all surfaces of the beam (including the mid-plane) along with the body force (3-67) throughout the domain. Although the surfaces $X=\pm W/2$ are traction free for an incompressible material due to the volumetric pressure field, this condition is lost for the compressible case.

Uniform discretizations with quadrilateral and triangular elements are employed with fully discontinuous function spaces, where the coarsest quadrilateral mesh is 2×16 elements. Their performance will be benchmarked against the results from continuous finite element approximations on the same meshes. During the simulations, the bend angle ψ is increased up to a maximum value of π in increments $\Delta\psi = \pi/16$. We remark that since the applied forces from (3-66) – (3-67) are nonlinear functions of ψ, the consistent external nodal loads for the finite element mesh must be recomputed at each load step rather than proportionally incremented.

The bending stress $\sigma_{\theta\theta}$ plot for the 4×32 element mesh is illustrated on the deformed configuration of the beam for two load levels $\psi = \pi/2$ and $\psi = \pi$ in Figure 3.15. At the first load level, the discretized beam is almost bent into a quarter of a circular arc. Since the load level is controlled through force-type boundary conditions rather than prescribed displacement, the bend angle observed in the computed results will be less than the actual value. Furthermore, the finite element method typically produces approximations that are stiffer than the actual structure. Nonetheless, the deformed configuration in Figure 3.15 (b) is approaching a half-circular arc and is fairly accurate for a coarse approximation.

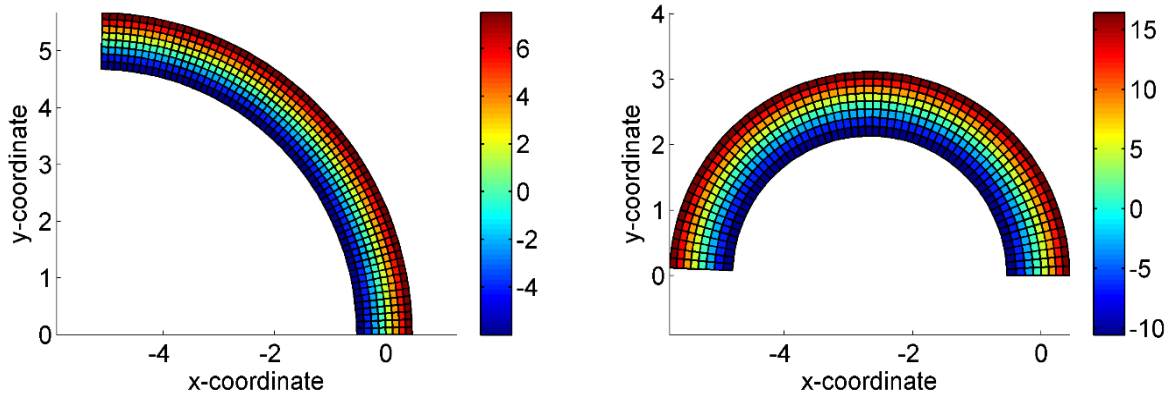

(a) (b)

Figure 3.15. Stress $\sigma_{\theta\theta}$ on deformed configuration under pure bending of 4×32 quadrilateral mesh: (a) $\psi = \pi/2$; (b) $\psi = \pi$.

To quantify the accuracy of the results, we compute the error in the displacement field $\boldsymbol{e} = \boldsymbol{u} - \boldsymbol{u}^h$ obtained at each level of mesh refinement and record the value of the L^2 and H^1 norm in Figure

3.16. The error norms are evaluated at the load level $\psi = 3\pi/16$. For nonlinear field theories, proving the theoretical convergence rate for the finite element method can be quite involved. However, the optimal rate of convergence for linear-interpolation elements from the linear field theory is a rate of 2.0 in the L^2 norm and 1.0 in the H^1 norm. We observe rates close to this optimal limit for the present analysis. Also, the triangular meshes contain a higher level of absolute error compared to the quadrilateral meshes, indicating that these elements are rather stiff, which is a common observation amongst discrete approximations with triangles [21]. However, the DG approximation does provide a slightly more accurate solution compared to CG for the same number of elements. This response indicates that the displacement jumps increase the flexibility of the discrete domain. The results for the DG and CG quadrilateral meshes are nearly identical.

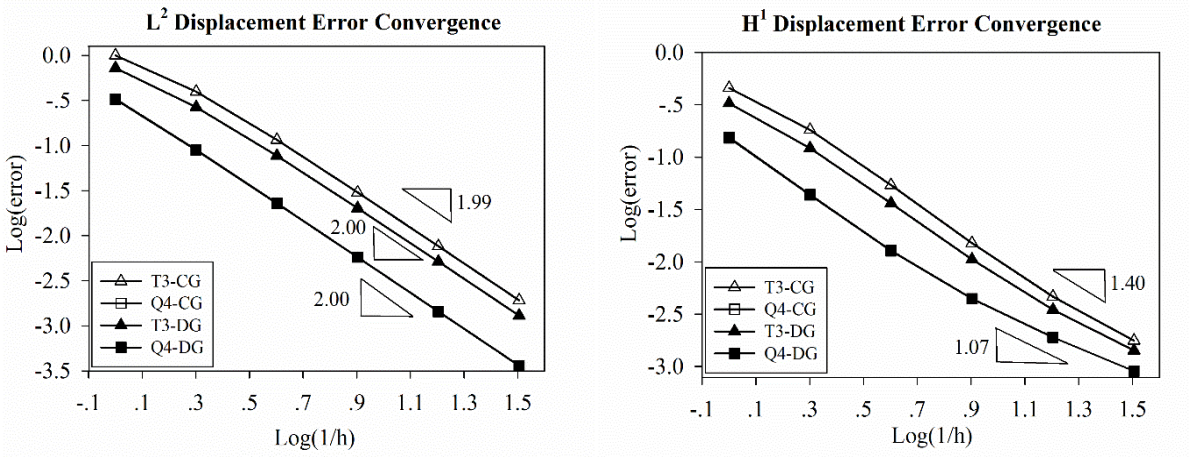

(a) (b)

Figure 3.16. Convergence rate of displacement error norm for pure bending at bend angle $\psi = 3\pi/16$: (a) L^2 norm; (b) H^1 seminorm.

As a final result, we determine the discrete angle ψ^h from the computed solution at each load level for comparison against the prescribed angle ψ and present the values in Figure 3.17. Since the deformation of the beam is driven by the applied tractions in terms of ψ, the actual deflection of the beam becomes a derived quantity for measuring the accuracy. We illustrate a consistent procedure for determining the angle ψ^h in Figure 3.17 (a). First, a line segment is drawn connecting the endpoints A and B of the beam. Next, a perpendicular bisector CD is constructed, where the point D is located at the intersection with the horizontal axis. Finally, the angle ψ^h

between line segments AD and BD is calculated using the law of cosines. This angle is determined for four of the quadrilateral DG meshes and plotted in Figure 3.17 (b); the angle is measured in radians, and n indicates the number of elements through the thickness of the beam. Clearly the exact curve is $\psi^h = \psi$, a line with a slope of one. We observe that as the mesh is refined, the values from the quadrilateral DG meshes converge to the correct result. Similar trends were obtained for the CG method and the triangular meshes.

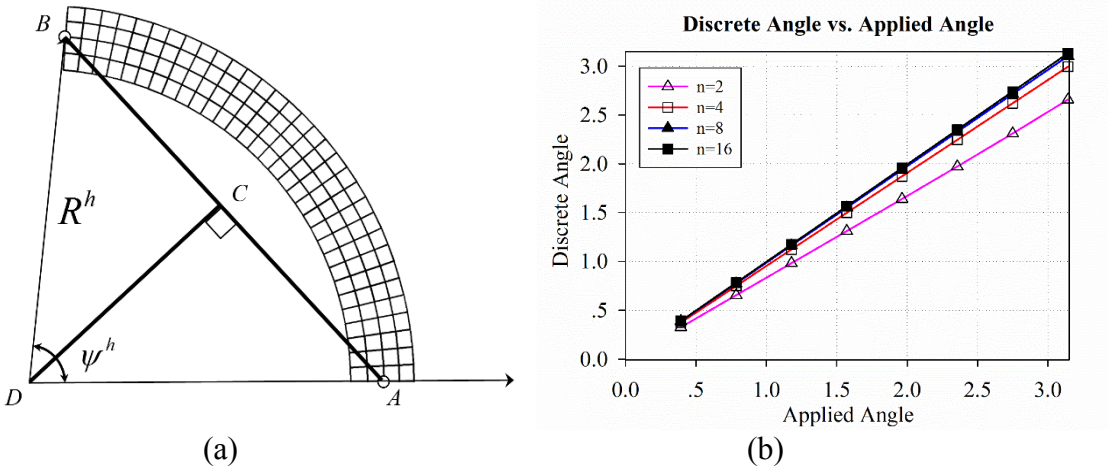

(a) (b)

Figure 3.17. Discrete angle ψ^h for pure bending: (a) determination from computed results; (b) discrete angle ψ^h versus prescribed angle ψ for DG method.

3.6.5 Torsion at finite strains

For the final numerical problem, we consider a rectangular bar subjected to torsion, as shown in Figure 3.18. A deformation map that induces longitudinal twist to the bar can be expressed as follows:

$$\boldsymbol{x} = \boldsymbol{R}(\theta)\cdot\boldsymbol{X}, \qquad \boldsymbol{R}(\theta) = \begin{bmatrix} \cos\theta & -\sin\theta & 0 \\ \sin\theta & \cos\theta & 0 \\ 0 & 0 & 1 \end{bmatrix}, \qquad \theta(Z) = \frac{2\pi Z\psi}{L} \tag{3-68}$$

where L is the length of the bar and the parameter ψ represents the number of complete revolutions of the top face of the bar with respect to the bottom face. This deformation mode is described in [124], where the expressions have been converted from cylindrical to Cartesian components by using the trigonometric identity concerning the summation of angles. Similar to the problems in sections 3.6.2 and 3.6.4, equation (3-68) is taken as the exact solution, and the

surface tractions and body force required for equilibrium are derived and applied within the computational model. The resulting expressions for $\boldsymbol{F}$, $\boldsymbol{P}$, and $\boldsymbol{B}$ are given by:

$$\boldsymbol{F} = \begin{bmatrix} \cos\theta & -\sin\theta & 2\pi(\psi/L)(-Y\cos\theta - X\sin\theta) \\ \sin\theta & \cos\theta & 2\pi(\psi/L)(X\cos\theta - Y\sin\theta) \\ 0 & 0 & 1 \end{bmatrix} \tag{3-69}$$

$$\boldsymbol{P} = 2\pi\mu(\psi/L)\begin{bmatrix} 0 & 0 & -Y\cos\theta - X\sin\theta \\ 0 & 0 & X\cos\theta - Y\sin\theta \\ -Y & X & 0 \end{bmatrix} \tag{3-70}$$

$$\rho_o\boldsymbol{B} = \mu\left[2\pi(\psi/L)\right]^2\begin{bmatrix} X\cos\theta - Y\sin\theta \\ Y\cos\theta + X\sin\theta \\ 0 \end{bmatrix} \tag{3-71}$$

where $\mu = E/2(1+\nu)$ again is the shear modulus. Note that the deformation induces pure shear and is thus isochoric, namely $J = 1$. Therefore, this problem will be used to test the performance of the DG method for large shearing and rotational effects.

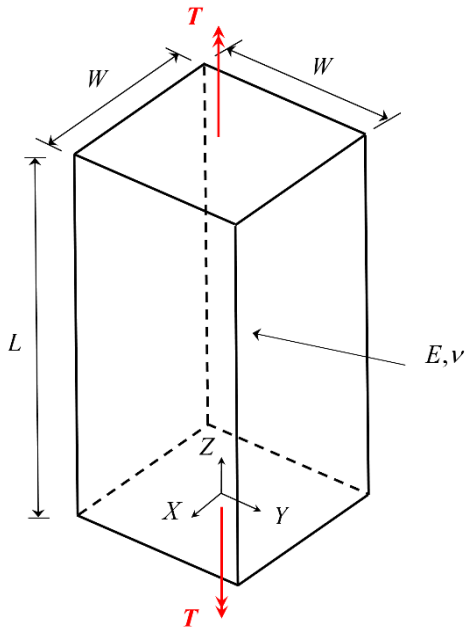

Figure 3.18. Rectangular bar under longitudinal torsion.

In the benchmark study herein, the dimensions of the bar are taken as $L = 4$ and $W = 2$ along with the material properties $E = 100$ and $\nu = 0.25$. Uniform meshes of linear tetrahedral elements and

trilinear hexahedral elements are employed with fully discontinuous approximations between each element. The coarsest mesh consists of $2\times2\times8$ hexahedral elements, and the tetrahedral meshes are formed by subdividing each hexahedral element into six tetrahedra, similar to [101]. Again, continuous finite element approximations will serve as a reference. The bottom face of the bar is held fixed in the *Z*-direction and prevented from rigid-body rotation by restraining the middle node along each edge. Surface tractions according to $\boldsymbol{T} = \boldsymbol{P} \cdot \boldsymbol{N}$ from (3-70) are applied to all faces of the bar; in particular, the vertical faces have non-zero tractions because the cross-section is not circular.

For a series of uniformly refined meshes, simulations were conducted in which the bar was twisted to a maximum revolution of $\psi = 2$ at equal intervals of $\Delta\psi = 0.125$. Representative deformed configurations of the bar are shown in Figure 3.19 for two load levels on the crudest 2×2×8 element mesh and a refined mesh. The superimposed contour plot represents the value of the torsional Cauchy stress $\sigma_{z\theta}$ computed at the center of each element from the DG approximations. For planes of elements parallel to the *X*-*Y* plane, we observe a constant value of the torsional stress for elements that are equidistant from the longitudinal axis, which agrees with the intuition from the classical mechanics of materials. Namely, as the mesh is refined, the computed solution more closely captures the linearly varying torsional stress in the radial direction. This is evidenced by the similar magnitude but increased resolution provided between Figure 3.19 (a) and (c) at load level $\psi = 0.125$ and similarly for Figure 3.19 (b) and (d) at load level $\psi = 0.5$. Moreover, the level of stress remains constant along the length of the bar in the computed results and does not show any decay or spurious features. Note that these stresses are computed in the rotated coordinate system obtained from the deformed configuration of the mesh. The uniformity of the results obtained both in the longitudinal and transverse directions is a testimony to the accuracy of the results. In particular, significant deformations are present at the load level $\psi = 0.5$ as evidenced in Figure 3.19 (b) and (d).

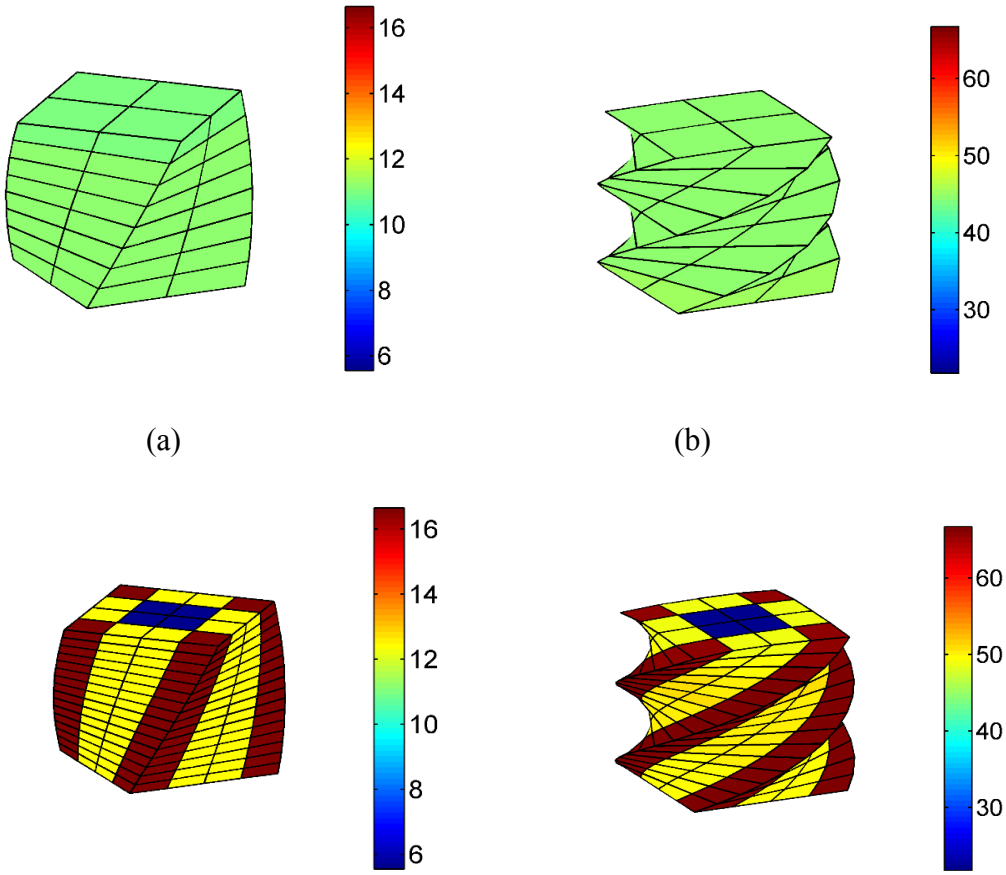

Figure 3.19. Stress $\sigma_{z\theta}$ on deformed configuration at two load levels: (a) $h=2;\ \psi=0.125$; (b) $h=2;\ \psi=0.5$; (c) $h=4;\ \psi=0.125$; (d) $h=4;\ \psi=0.5$.

Since this problem has an exact solution, we compute the displacement discretization error obtained on each mesh and plot the value of the L^2 norm and H^1 seminorm in Figure 3.20 (a) and (b), respectively, at the loading stage $\psi=0.125$. For this problem, the DG approximation significantly outperforms the CG approximation for hexahedral elements in both error measures. Also, the optimal convergence rate of 1.0 in the H^1 seminorm is obtained by each of the element types. These smooth trends are a strong indicator of the stability of the results. The convergence rates in the L^2 norm are fairly optimal for the tetrahedral elements. The hexahedral meshes also exhibit slightly suboptimal performance in the field norm upon mesh refinement; however, the convergent results of the gradients indicate that these elements are stable nonetheless.

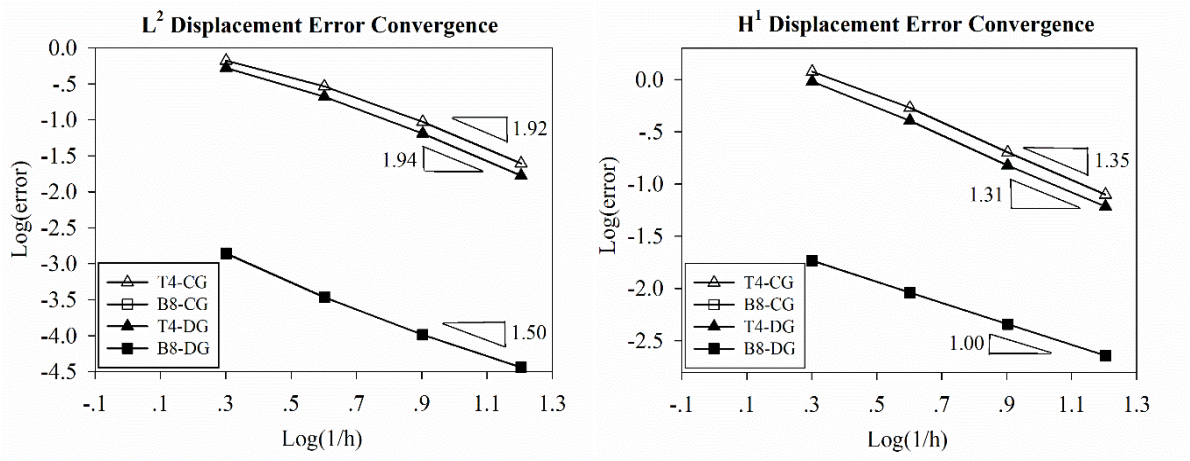

(a) (b)

Figure 3.20. Convergence rates of displacement error for longitudinal torsion at load level $\psi = 0.125$: (a) L^2 norm; (b) H^1 seminorm.

By inspecting the deformation map (3-68) as well as considering the response of the bar in Figure 3.19, we observe that the response is somewhat periodic. Namely, the response of a bar with length nL could be obtained by simulating one bar of length L and appending n copies of the response end-to-end, with appropriate rigid rotations applied to match the bases from each section. Furthermore, the traction field on cross-sections parallel to the $X-Y$ plane (with normal $\boldsymbol{N} = \boldsymbol{E}_3$ take the following simple form according to (3-70):

$$\begin{aligned} \boldsymbol{P}\cdot\boldsymbol{E}_3 &= 2\pi\mu\left(\psi/L\right)\left[-Y\cos\theta - X\sin\theta \quad X\cos\theta - Y\sin\theta \quad 0\right]^T \\ &= 2\pi\mu\left(\psi/L\right)\boldsymbol{R}^{\perp}\left(\theta\right)\cdot\left(\boldsymbol{X} - Z\boldsymbol{E}_3\right) \equiv 2\pi\mu\left(\psi/L\right)\boldsymbol{R}^{\perp}\left(\theta\right)\cdot\boldsymbol{X}_{12} \end{aligned} \tag{3-72}$$

where $\boldsymbol{R}^{\perp}$ is the tensor that produces rotations which are orthogonal to $\boldsymbol{R}$, such that $\left(\boldsymbol{R}\cdot\boldsymbol{X}_{12}\right)\cdot\left(\boldsymbol{R}^{\perp}\cdot\boldsymbol{X}_{12}\right) = \boldsymbol{0}$. This traction vector clearly lies in the plane of the cross-section, is perpendicular to the twisted radial vector $\boldsymbol{R}\cdot\boldsymbol{X}_{12}$, and has a magnitude equal to $2\pi\mu\left(\psi/L\right)$ when normalized by the radial distance. An example of these vectors is provided in Figure 3.21 (a).

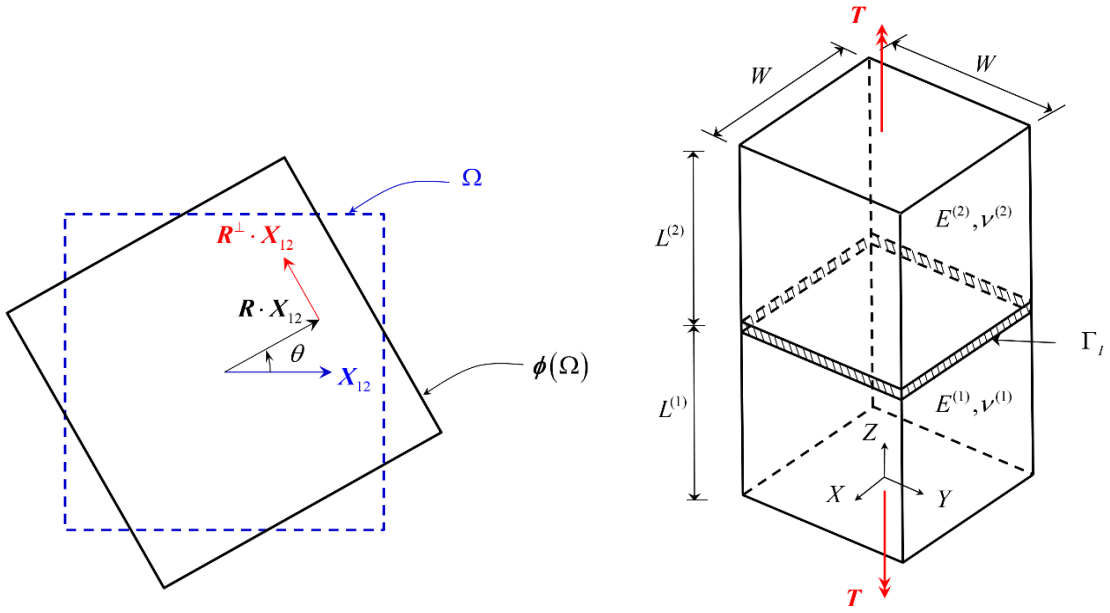

(a) (b)

Figure 3.21. Enhanced torsion problem: (a) traction vector on twisted cross-section; (b) bi-material rectangular bar.

Now suppose that two different bars undergo torsion such that $\mu^{(1)}\left(\psi^{(1)}/L^{(1)}\right)=\mu^{(2)}\left(\psi^{(2)}/L^{(2)}\right)=C$. According to (3-72), the cross-sections of each bar would experience the same traction field. This thought experiment suggests a possible sophistication of the previous problem to a bar consisting of two materials, which is illustrated in Figure 3.21 (b). In light of the above discussion, we obtain the solution for the deformed shape of the upper portion of the bar simply by rotating and translating the general expressions (3-68) – (3-71):

$$\boldsymbol{x}'=\boldsymbol{Q}_\theta\cdot\boldsymbol{x}\left(\boldsymbol{X}'\right),\qquad \boldsymbol{T}'=\boldsymbol{Q}_\theta\cdot\boldsymbol{P}\left(\boldsymbol{X}'\right)\cdot\boldsymbol{N},\qquad \boldsymbol{B}'=\boldsymbol{Q}_\theta\cdot\boldsymbol{B}\left(\boldsymbol{X}'\right) \tag{3-73}$$

where the translated coordinate is $\boldsymbol{X}'=\boldsymbol{X}-L^{(1)}\boldsymbol{E}_3$ and the rotation tensor $\boldsymbol{Q}_\theta=\boldsymbol{R}\left(2\pi\psi^{(1)}\right)$ reorients the bases of the bars to match at the interface. The expressions in (3-73) are evaluated in terms of the properties $\mu^{(2)},\psi^{(2)},L^{(2)}$ for the second portion of the bar. These results align with classical strength of materials: when a composite rod is subjected to torsion, the twist experienced by each component is inversely proportional to its shear modulus while the torque in each component remains constant.

For the numerical tests that follow, we adopt the geometric and material properties $L^{(1)} = L^{(2)} = 2$, $W = 2$, $E^{(1)} = 100$, $E^{(2)} = 400$, and $\nu^{(1)} = \nu^{(2)} = 0.25$. Also, to make this test more stringent, the portions of the bar are discretized in a biased fashion to create a nonconforming mesh in the zone of the material interface. Plan views of the coarse meshes for the top and bottom portion of the bar are shown in Figure 3.22; subsequent meshes are obtained by bisecting this discretization. Within the remainder of the bar, continuous finite element approximations are employed. This problem is a good test case for a unified CG-DG method under large rotational effects wherein potential weak discontinuities from material mismatch can evolve into strong discontinuities such as debonding. Therefore, it serves as a test bed for mathematically nonsmooth problems under evolving finite rotations.

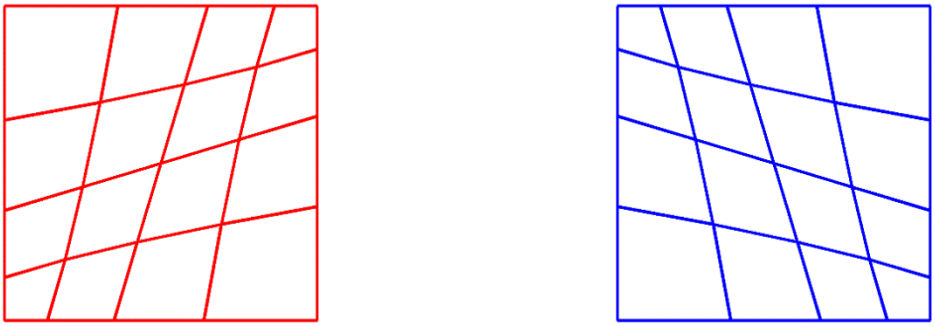

(a) (b)

Figure 3.22. Plan view of nonconforming coarse mesh: (a) bottom region; (b) top region.

The response of the bar is simulated on the coarse mesh by increasing the twist angle $\psi^{(1)}$ in increments $\Delta\psi^{(1)} = 0.125$ and computing applied tractions and body forces on both regions, with $\psi^{(2)} = \psi^{(1)}/4$. The deformed configuration of the domain is shown in Figure 3.23 for two representative load levels. We highlight that the top half of the bar indeed twists less than the lower portion. However, both the displacement field and tractions are continuous at the interface. Spurious gaps have not opened up between the nonconforming meshes, and the discrete solution is quite smooth. Thus, the stabilized interface formulation provides very accurate results for this challenging problem.

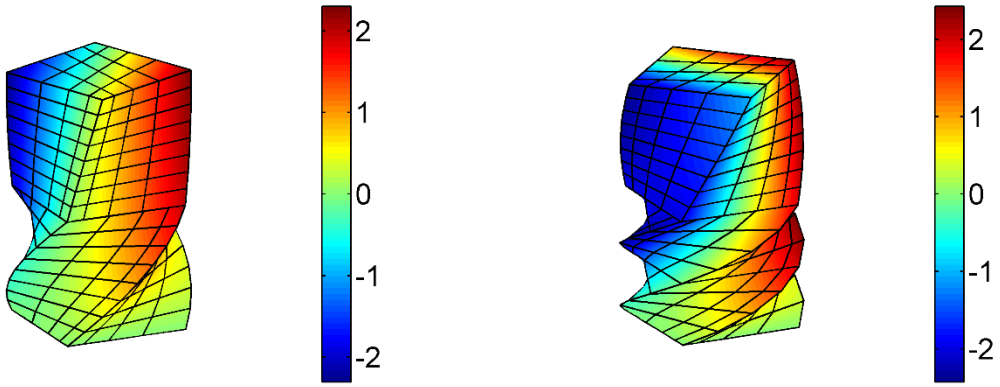

(a) (b)

Figure 3.23. Displacement u_x contour plot on the deformed shape for the bi-material torsion problem: (a) load level $\psi^{(1)} = 0.25$; (a) load level $\psi^{(1)} = 0.5$.

To further investigate the properties at the nonconforming interface, we compute some quantities of interest such as the magnitude of discrete interface gap $[\![\boldsymbol{\phi}]\!]$ and average traction vector normal to the interface, which are shown in Figure 3.24. The contour of the interface gap $[\![\boldsymbol{\phi}]\!]$ is not symmetric because of the differing bias in the top and bottom meshes along with the fact that the loading and deformed configuration in Figure 3.23 does not display symmetry. However, the jump is three orders of magnitude smaller than the displacement field, indicating that the discontinuities are well-controlled. Also, the traction field at the interface appears quite smooth in Figure 3.24 (b), where the edge-lines have been removed for clarity. Note that the total numerical flux $\boldsymbol{\lambda} = \{\boldsymbol{P} \cdot \boldsymbol{N}\} - \boldsymbol{\tau}_s \cdot [\![\boldsymbol{\phi}]\!]$ as given by (3-38) containing both the average traction and the penalty term is plotted in the figure, which is traditionally the defining measure of interface stress [5,162]. Slight over-predictions of the numerical flux, indicated by the red color contour, are present in the extremely small triangular interface segments formed from slightly mismatched nodes in the upper and lower portions of the bar. These artifacts are generated by the over-prediction of the penalty tensor $\boldsymbol{\tau}_s$ in these segments, which is an issue similar to that encountered in embedded mesh techniques in the presence of vanishingly small cut elements [5]. Nonetheless, the accuracy of the computed stresses compared to the exact stress in Figure 3.24 (c) is a testament to the quality of the stability tensors derived from the fine-scale models (3-35) in the presence of significant

geometric and material mismatch.

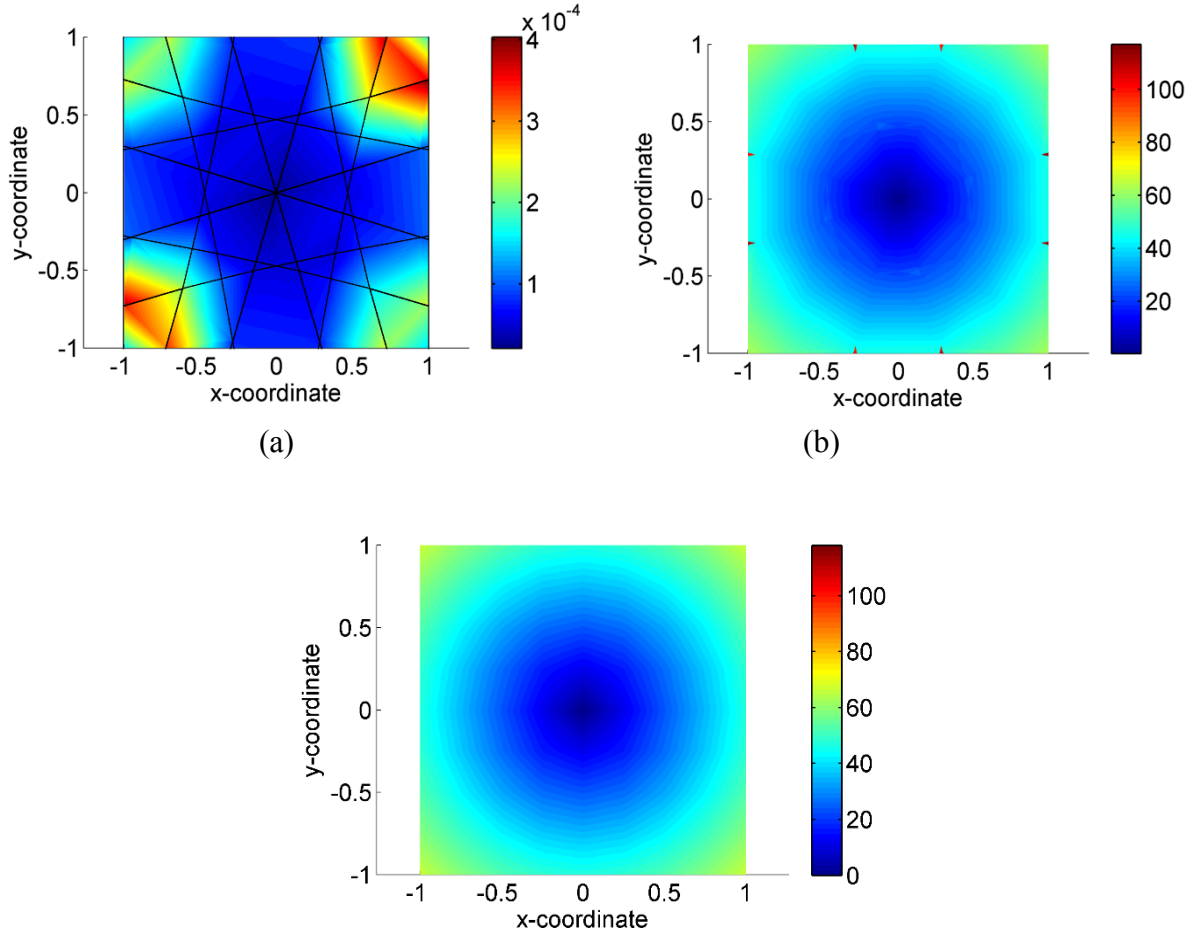

(a) (b)

(c)

Figure 3.24. Contour plots at material interface for twist $\psi^{(1)} = 0.375$: (a) magnitude of discrete interface gap $[\![\phi]\!]$; (b) magnitude of numerical flux vector; (c) exact interface stress $\sigma_{z\theta}$.

3.7 Conclusions

In this work, we derive a Discontinuous Galerkin (DG) interface formulation for finite strain kinematics by extending the developments for linear elasticity contained in the general framework of [162]. A Lagrange multiplier treatment of the interface continuity constraints serves as the starting point for the derivation, and this mixed field problem is stabilized by invoking concepts from the Variational Multiscale method. Herein, a distinguishing feature is that the localized fine-scale problems at the interface are consistently linearized in order to develop analytical models for the fine-scale displacement field. By embedding these fine-scale models into the coarse-scale

problem, enhanced stability is obtained that subsequently enables the Lagrange multipliers to be condensed from the formulation, leading to a primal weak form analogous to the DG method. Through the fine-scale stabilization process, closed-form expressions are obtained for the numerical flux and penalty parameter that vary from element to element based on the material properties and local mesh topology at the interface. Unique to the present nonlinear context, these fine-scale models evolve with the local material and geometric nonlinearity of the bulk domain in the vicinity of the interface. By accounting for the complete spectrum of the constitutive material model, element geometry and length scale, and nonlinear effects, the robust definitions for the numerical flux and penalty parameter herein adaptively compensate for instabilities that may arise under increasing deformations.

To facilitate implementation of the method, we represent the fine-scale fields using simple polynomial bubble functions, similar to those previously investigated in the context of small strains [162]. While the method was originally developed for imposing continuity weakly over nonconforming meshes within a domain, a natural extension of the ideas yields a formulation accommodating fully discontinuous approximations over the discretized domain. Both versions of the method, enforcing continuity across nonconforming interfaces or across inter-element boundaries, are investigated through a series of two- and three-dimensional test problems that cover a range of deformation modes. Particular emphasis is placed on problems incorporating significant bending and torsional effects to verify that the fine-scale models remain objective and provide stability under large strains. In all cases, accurate results were obtained from the method by using the form of the stability parameters derived herein without additional calibration. Strong performance is exhibited by both triangular and quadrilateral elements along with their higher-dimensional counterparts for problems with material mismatch and significant mesh nonconformity. Error convergence analyses were conducted for problems with analytical solutions, and the convergence of the discretization error confirmed the stability of the proposed interface method. The next logical steps for extending this formulation which we plan to pursue are the treatment of history-dependent material response as well as the treatment of evolving strong discontinuities such as delamination.

CHAPTER 4: INTERFACIAL STABILIZATION AT FINITE STRAINS FOR INTERFACIAL DAMAGE IN MULTI-CONSTITUENT MATERIALS[2]

4.1 Introduction

Accurate modeling of interfacial debonding that leads to local failure in natural and engineered material systems constitutes an essential building block for high fidelity computational material modeling frameworks. A common classical approach for this class of problems that involve local failure and separation is the use of intrinsic cohesive elements or springs along the bimaterial interfaces; see e.g. [2,25,59,82,103,140]. It is however well documented in the literature that these formulations typically introduce an additional elastic stiffness at the interface that upsets the consistency of the discrete formulation, thereby resulting in inaccurately representation of the multi-material interfacial configuration. Numerical tests show that loss of consistency can result in serious degradation in the accuracy of the simulations [31]. As an alternative approach that avoids artificial compliance, the extrinsic cohesive zone method [30,85,107,175] adaptively inserts interface elements into contiguous meshes when a fracture criterion is met in the neighboring solid elements. Later developments [169] using the extended finite element method (XFEM) enable the failure surface to grow through elements. However, the insertion of cohesive elements adds degrees of freedom to the global stiffness matrix, requiring special data structures for adaptivity in the finite element software.

On the other hand, kinematic treatment of embedded interfaces has been carried out in the context of Lagrange multiplier methods [61,85], as well as Nitsche type methods [2,5,53,51,52, 60,140] that can be categorized as a class of primal methods [31]. Lagrange multiplier based methods, though general, and applicable to linear as well as nonlinear material systems, render the resulting method a mixed-field method. Numerical schemes for mixed-field methods require stabilized methods if arbitrary combinations of interpolation functions are to be employed for the underlying

2 This Chapter has been adapted from "P. Chen, T.J. Truster, A. Masud, Interfacial stabilization at finite strains for weak and strong discontinuities in multi-constituent materials, Computer Methods in Applied Mechanics and Engineering. 328 (2018) 717–751." The copyright owner has provided written permission to reprint the work.

fields. Nitsche type methods on the other hand do not introduce an additional field to be approximated, but they require specification of interfacial continuity parameters which are not always easy to define especially in the general nonlinear regime [53].

A third approach for the treatment of the failure models is based on the hybrid DG method [106,119,142] which has also been employed in fracture mechanics [129,172]. In this approach, discontinuous Galerkin (DG) method is used in the pre-failure regime together with a standard cohesive zone approximation to perform the post-failure process. In this particular method, the stiffness matrix and the underlying mathematical formulation changes when switching from the pre-failure to post-failure regime. Yet another approach by Belytschko and coworkers [153,174], employs Cohesive Zone Method (CZM) embedded in the XFEM method to model transition between perfectly adhered to fully debonded regimes via some properly chosen enrichment functions. This approach requires carefully selected point-wise consistency conditions for the initiation of the new degree of freedom [172].

With the objective of developing a general framework for local failure at material interfaces, we derived a Lagrange multiplier method, in the context of small strains, for continuity of fields across embedded interfaces [161]. In this method Lagrange multipliers manifested interfacial traction field. This idea was further enhanced in [160] wherein interfacial Lagrange multiplier as well as the penalty parameters were fully derived via sub-scale modeling concept facilitated by the VMS ideas [69,99,159]. In an allied effort a finite strain interface formulation for multi-material interfaces in the finite strain regime was developed by us in Chapter 3. However local failure in the form of strong discontinuity was not considered. Numerical tests with primal interfacial formulation in Chapter 3 revealed that the success of the method in the finite strain regime relied heavily on the consistent evolution of the interfacial stabilization parameters, and consequently, the variational structure of the sub-grid scale modeling problem was crucial to the derivation presented. This Chapter builds on Lagrange multiplier enforcement of continuity and derivation of Nitsche parameters in [161] with variationally consistent derivation of interfacial stabilization parameters in Chapter 3 for local interfacial failure and appearance of strong discontinuities. A crucial component of this derivation is the modeling of fine scales in the neighborhood of element interfaces. These ideas have similarities with certain aspects of Weak Galerkin methods by Wang and co-workers [112-114,168]. Weak Galerkin method makes use of discontinuous functions that endows WG-FEMs with great flexibility to deal with geometric complexities and boundary

conditions. These methods have been applied to interface problems [113] wherein flexibility of using discontinuous functions gives rise to robustness in the enforcement of interface jump conditions and therefore has been used to develop methods for handling discontinuous approximation functions. However, while the edge restricted functions that are used in Weak Galerkin appear similar to the fine scale field in the present formulation, the derived solution of the fine scale problem depends on the interior support of the fine-scale field.

To keep the discussion self-contained, we first present the synopsis of the stabilized formulation for finite strain interface without damage]. We then introduce the notion of inelastic residual gap $\boldsymbol{\zeta}$ in the formulation to restrict the continuity along the interface. The key underlying idea is that the residual gap or separation along the interface is treated as an irrecoverable or inelastic strain-like variable which evolves with the debonding process. We then present a thermodynamically consistent formulation analogous to the variational constructs for bulk domain inelasticity discussed in [146] wherein the residual gap $\boldsymbol{\zeta}$ is conjugate to the interface traction $\boldsymbol{T}$, thereby incorporating hardening/softening variables. This methodology is a slight departure from the method of [161] and enables the treatment of interface constitutive behavior through yield functions and flow rules that are inspired by the literature from plasticity. In the present method the combination of damage and friction along the debonding surfaces is easily accommodated by borrowing concepts from multi-surface plasticity [146]. Also, rate dependency and other advanced phenomena can be easily treated in the new framework. Specially, the proposed method avoids using cohesive elements that can introduce artificial elastic interface stiffness that affects the consistency and therefore the stability of the method. With the fine-scale models evolving with the material and geometric nonlinearity exhibited in the vicinity of the interface, the algorithmic interface parameters are updated continuously through the evolution of the nonlinear problem. Furthermore, the proposed method provides a general framework to incorporate friction, rate-dependency, and softening, as desired.

An outline of the Chapter is as follows. In section 4.2, we begin with the governing equations of finite strain elasticity with internal variable $\boldsymbol{\zeta}$ associated with damage. Next, in section 4.3 we derive the stabilized weak form for interfacial debonding in multi-constituent materials by employing the sub-grid scale modeling concept facilitated by the VMS method, but restricted to narrow zone across the bimaterial interfaces. In section 4.4, the appearance of the gap function in

the expression for the Lagrange multiplier and therefore in the evolving finite-scales provides a natural mechanism to embed physics based models [100, 161] as well as phenomenological models [163] and Chapter 3 for progressive failure under various loading scenarios [2,161]. In section 4.5, specifically, tension debonding and evolution of normal gap, and compressive frictional sliding are presented and algorithmic generalizations are developed. Corresponding return mapping algorithms that are motivated by the literature on computational inelasticity [146] are discussed. An essential ingredient for a robust numerical method for finite deformation kinematics in the finite strain regime is the derivation of the consistent tangent that can yield quadratic convergence when employed in conjunction with the Newton-Raphson scheme. Therefore, section 4.6 presents consistent linearization of the stabilized method. Finally, section 4.7 presents a series of numerical test cases that validate the method and show its range of applicability with the concluding remarks in section 4.8.

4.2 Governing Equations and Mixed Interfacial Weak Form

Evolving interfaces between elements in the finite deformation context, where interfaces not only undergo finite deformation but can also develop interfacial gaps, are shown in Figure 4.1. Our earlier work in Chapter 3 presents the equilibrium equations at finite strains, but with no openings or gaps. Further extensions to frictional interface dynamics are presented in [163]. Interested readers are referred to Chapter 3 and [163] for detailed discussions. In this Chapter, an open bounded region $\Omega \subset \mathbb{R}^{n_{sd}}$ is cut into two disjoint regions $\Omega^{(1)}$ and $\Omega^{(2)}$ by an interface Γ_I. Points in the reference configuration are denoted by $\boldsymbol{X} \in \Omega^{(1)} \bigcup \Omega^{(2)}$ and their corresponding images in the current configuration by $\boldsymbol{x}$. Herein, the superscript (α) denotes quantities appearing in both regions 1 and 2. The two bodies deform according to the motion $\boldsymbol{\phi}^{(\alpha)}(\boldsymbol{X},t)$ that maps the reference configuration onto the current configuration, $\boldsymbol{x} = \boldsymbol{\phi}^{(\alpha)}(\boldsymbol{X},t)$.

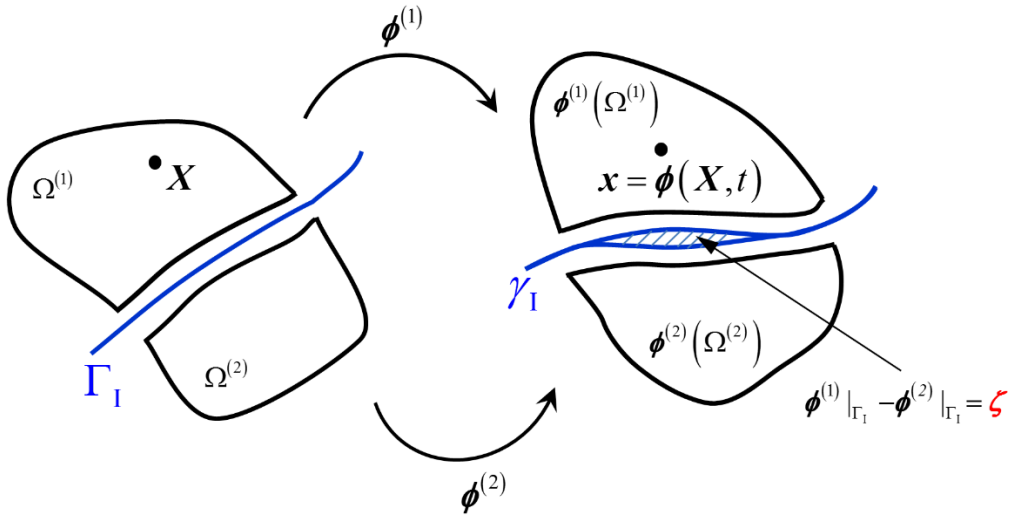

(a) (b)

Figure 4.1. Domain Ω with interface Γ_{I}. The deformed configurations are given by $\boldsymbol{\phi}^{(1)}$ and $\boldsymbol{\phi}^{(2)}$: (a) Reference configuration; (b) Current configuration.

We allow the deformations $\boldsymbol{\phi}^{(\alpha)}$ to be distinct along the interface Γ_{I} to accommodate the existence of the interface gap or debonding $\boldsymbol{\zeta}$ and the Lagrange multiplier $\boldsymbol{\lambda}$. as illustrated in Figure 4.1 (b). The interior domains $\Omega^{(1)}$ and $\Omega^{(2)}$ remain self-compatible and self-equilibrated within each sub-region. Equilibrium equations and boundary conditions for each sub-region $\Omega^{(\alpha)}$ are supplemented with the discontinuity evolution equation and the traction conditions along Γ_{I} via the Lagrange multiplier field $\boldsymbol{\lambda}$, thereby resulting in the following system of equations for the composite domain Ω.

$$\mathrm{DIV}\,\boldsymbol{P}^{(\alpha)}\left(\boldsymbol{F}^{(\alpha)}\right)+\rho_o^{(\alpha)}\boldsymbol{B}^{(\alpha)}=\boldsymbol{0} \quad \text{in} \quad \Omega^{(\alpha)},\ \alpha=1,2 \tag{4-1}$$

$$\boldsymbol{\phi}^{(\alpha)}=\boldsymbol{X}^{(\alpha)} \quad \text{on} \quad \Gamma^{(\alpha)}\setminus\Gamma_{\mathrm{I}},\ \alpha=1,2 \tag{4-2}$$

$$\boldsymbol{\phi}^{(1)}-\boldsymbol{\phi}^{(2)}=\boldsymbol{\zeta} \quad \text{on} \quad \Gamma_{\mathrm{I}} \tag{4-3}$$

$$\boldsymbol{\lambda}-\boldsymbol{P}^{(1)}\cdot\boldsymbol{N}^{(1)}=\boldsymbol{0} \quad \text{on} \quad \Gamma_{\mathrm{I}} \tag{4-4}$$

$$-\boldsymbol{P}^{(2)}\cdot\boldsymbol{N}^{(2)}-\boldsymbol{\lambda}=\boldsymbol{0} \quad \text{on} \quad \Gamma_{\mathrm{I}} \tag{4-5}$$

Equation (4-3) facilitates non-conforming evolution of the interfaces that are subject to impenetrability constraint and phenomenological and/or physics based interfacial kinematics. In

(4-1) to (4-5), $\boldsymbol{P}^{(\alpha)}$ is the first Piola-Kirchhoff stress tensor, $\boldsymbol{B}^{(\alpha)}$ is the body force vector, $\rho_o^{(\alpha)}$ is the mass density, and $\boldsymbol{N}^{(\alpha)}$ is the unit outward normal vector at the region boundary Γ_{I}. Homogeneous Dirichlet boundary conditions are applied for simplicity of presentation but they can be easily generalized in Chapter 3. Lagrange multiplier $\boldsymbol{\lambda}$ is introduced to enforce the equilibrium of tractions (4-4) - (4-5) while the two subdomains are fully or partially bonded; the multipliers vanish identically upon complete debonding. The case of multiple interfaces can be accommodated by a straightforward generalization.

Multiplying equilibrium equations (4-1) to (4-5) by weighting function $\boldsymbol{\eta}_o^{(\alpha)}$ and applying the divergence theorem, the associated weak form is expressed as follows: Find $\left\{\boldsymbol{\phi}^{(1)}, \boldsymbol{\phi}^{(2)}, \boldsymbol{\lambda}\right\} \in \mathcal{S}^{(1)} \times \mathcal{S}^{(2)} \times \mathcal{Q}$ such that for all $\left\{\boldsymbol{\eta}_o^{(1)}, \boldsymbol{\eta}_o^{(2)}, \mu\right\} \in \mathcal{V}^{(1)} \times \mathcal{V}^{(2)} \times \mathcal{Q}$:

$$\sum_{\alpha=1}^{2} \int_{\Omega^{(\alpha)}} \mathrm{GRAD}\, \boldsymbol{\eta}_o^{(\alpha)} : \boldsymbol{P}^{(\alpha)}\, \mathrm{d}V - \sum_{\alpha=1}^{2} \int_{\Omega^{(\alpha)}} \rho_o^{(\alpha)} \boldsymbol{B}^{(\alpha)} \cdot \boldsymbol{\eta}_o^{(\alpha)}\, \mathrm{d}V - \int_{\Gamma_{\mathrm{I}}} \boldsymbol{\lambda} \cdot [\![\boldsymbol{\eta}_o]\!]\, \mathrm{d}A = 0 \tag{4-6}$$

$$-\int_{\Gamma_{\mathrm{I}}} \boldsymbol{\mu} \cdot \left([\![\boldsymbol{\phi}]\!] - \boldsymbol{\zeta} \right) \mathrm{d}A = 0 \tag{4-7}$$

As mentioned earlier in Chapter 3, the Lagrange multiplier field $\boldsymbol{\lambda}$ in (4-6) has the connotation of the traction field on Γ_{I}. Eqn.(4-7) weakly enforces the jump continuity where $[\![\bullet]\!] = (\bullet)^{(1)} - (\bullet)^{(2)}$ is the jump operator defined for vector-valued fields at interface Γ_{I}. The inelastic gap function or debonding function $\boldsymbol{\zeta}$ is set to lie in the $\left[L_2\left(\Gamma_{\mathrm{I}}\right)\right]^{n_{\mathrm{sd}}}$ space. The appropriate function spaces contained in the weak forms (4-6) and (4-7) are given as:

$$\mathcal{S}^{(\alpha)} = \left\{ \boldsymbol{\phi}^{(\alpha)} \,\middle|\, \boldsymbol{\phi}^{(\alpha)} \in \left[H^1\left(\Omega^{(\alpha)}\right) \right]^{n_{\mathrm{sd}}},\ \det\left(\boldsymbol{F}^{(\alpha)}\left(\boldsymbol{\phi}^{(\alpha)}\right) \right) > 0,\ \left. \boldsymbol{\phi}^{(\alpha)} \right|_{\Gamma^{(\alpha)} \setminus \Gamma_{\mathrm{I}}} = \boldsymbol{X}^{(\alpha)} \right\} \tag{4-8}$$

$$\mathcal{V}^{(\alpha)} = \left\{ \boldsymbol{\eta}_o^{(\alpha)} \,\middle|\, \boldsymbol{\eta}_o^{(\alpha)} \in \left[H_o^1\left(\Omega^{(\alpha)}\right) \right]^{n_{\mathrm{sd}}},\ \left. \boldsymbol{\eta}_o^{(\alpha)} \right|_{\Gamma^{(\alpha)} \setminus \Gamma_{\mathrm{I}}} = \boldsymbol{0} \right\} \tag{4-9}$$

$$\mathcal{Q} = \left\{ \boldsymbol{\lambda} \,\middle|\, \boldsymbol{\lambda} \in \left[H^{-\frac{1}{2}}\left(\Gamma_{\mathrm{I}}\right) \right]^{n_{\mathrm{sd}}} \right\} \tag{4-10}$$

4.3 Multiscale Decomposition

Our objective at this point is to convert the preceding Lagrange multiplier formulation (4-6) and (4-7) into a stabilized single-field formulation for the evolution of interfacial debonding in the finite deformation context. Interested reader is referred to Chapter 3 for details of the primal

interface formulation without damage and for the advantages of the single field formulation in the context of the inf-sup stability conditions. For the sake of completeness, we highlight the significant steps to variationally derive the method for evolving gaps and debonding.

Following the work in [101] and Chapter 3, we decompose the solution field into coarse-scale and fine-scale fields. We assume an overlapping decomposition of the deformation map $\boldsymbol{\phi}^{(\alpha)}$ in each region $\Omega^{(\alpha)}$ consisting of a fine-scale deformation $\tilde{\boldsymbol{\phi}}^{(\alpha)}$ superimposed upon a coarse-scale deformation $\hat{\boldsymbol{\phi}}^{(\alpha)}$. This deformation can be expressed in terms of the multiscale displacement field as follows:

$$\hat{\boldsymbol{x}} = \hat{\boldsymbol{\phi}}\left(\boldsymbol{X}\right) = \boldsymbol{X} + \hat{\boldsymbol{u}} \tag{4-11}$$

$$\tilde{\boldsymbol{\phi}}\left(\hat{\boldsymbol{x}}, t\right) = \hat{\boldsymbol{x}} + \tilde{\boldsymbol{u}} = \boldsymbol{\phi}\left(\boldsymbol{X}, t\right) = \boldsymbol{X} + \boldsymbol{u} = \boldsymbol{x} \tag{4-12}$$

From (4-11) and (4-12), we arrive at a relation between the total displacement and its coarse and fine-scale displacement components as follows:

$$\boldsymbol{u} \;=\; \hat{\boldsymbol{u}} \;+\; \tilde{\boldsymbol{u}} \tag{4-13}$$

As in our recent developments [100], the coarse-scale field $\hat{\boldsymbol{\phi}}^{(\alpha)}$ is represented using piecewise continuous finite element functions in each region $\Omega^{(\alpha)}$, and the fine-scale field $\tilde{\boldsymbol{\phi}}^{(\alpha)}$ is represented locally at the interfaces via functions of compact support.

Although the displacement field is assumed additively decomposed, and in the nonlinear regime this decomposition is to be viewed in the sense of mappings, the Lagrange multiplier fields are not decomposed. Therefore, weak enforcement of jump continuity only contributes to the coarse-scale model. Accordingly, the weak forms (4-6) and (4-7) can be separated into the following multiscale interface sub-problems:

Coarse-Scale Problem $\mathcal{C}$

$$\begin{aligned}\hat{R}\left(\hat{\boldsymbol{\eta}}_o^{(\alpha)}; \hat{\boldsymbol{\phi}}^{(\alpha)}, \tilde{\boldsymbol{\phi}}^{(\alpha)}, \boldsymbol{\lambda}\right) = \sum_{\alpha=1}^{2} \int_{\Omega^{(\alpha)}} \left[\operatorname{GRAD} \hat{\boldsymbol{\eta}}_o^{(\alpha)} : \boldsymbol{P}^{(\alpha)} - \hat{\boldsymbol{\eta}}_o^{(\alpha)} \cdot \rho_o^{(\alpha)} \boldsymbol{B}^{(\alpha)}\right] \mathrm{d}V \\ - \int_{\Gamma_{\mathrm{I}}} \boldsymbol{\lambda} \cdot [\![\hat{\boldsymbol{\eta}}_o]\!] \, \mathrm{d}A = 0\end{aligned} \tag{4-14}$$

$$\hat{R}_{\mu}\left(\boldsymbol{\mu}, \hat{\boldsymbol{\phi}}^{(\alpha)}, \tilde{\boldsymbol{\phi}}^{(\alpha)}, \boldsymbol{\zeta}\right) = -\int_{\Gamma_{\mathrm{I}}} \boldsymbol{\mu} \cdot \left([\![\tilde{\boldsymbol{\phi}} \circ \hat{\boldsymbol{\phi}}]\!] - \boldsymbol{\zeta}\right) \mathrm{d}A = 0 \tag{4-15}$$

Fine-Scale Problem $\mathcal{F}$

$$\tilde{R}\left(\tilde{\boldsymbol{\eta}}_o^{(\alpha)};\hat{\boldsymbol{\phi}}^{(\alpha)},\tilde{\boldsymbol{\phi}}^{(\alpha)},\boldsymbol{\lambda}\right)=\sum_{\alpha=1}^{2}\int_{\Omega^{(\alpha)}}\left[\text{GRAD}\,\tilde{\boldsymbol{\eta}}_o^{(\alpha)}:\boldsymbol{P}^{(\alpha)}-\tilde{\boldsymbol{\eta}}_o^{(\alpha)}\cdot\rho_o^{(\alpha)}\boldsymbol{B}^{(\alpha)}\right]\mathrm{d}V \\ -\int_{\Gamma_1}\boldsymbol{\lambda}\cdot[\![\tilde{\boldsymbol{\eta}}_o]\!]\,\mathrm{d}A=0 \tag{4-16}$$

As discussed in Chapter 3, our objective at this point is to derive an analytical expression for Lagrange multipliers in terms of the coarse-scale deformation map $\hat{\boldsymbol{\phi}}^{(\alpha)}$ and the inelastic gap $\boldsymbol{\zeta}$ as the two unknown fields. The detailed procedure is provided in Chapter 3, which is comprised of three step modeling process. In the following sections we outline the main steps of the modeling process.

4.3.1 Modeling of fine scales

We localize the fine-scale problem (4-16) to the vicinity of the interface and approximate the fine scales using edge bubble functions that are only supported within the sectors next to the interface segments. We express fine scales via edge bubble functions as follows:

$$\tilde{\boldsymbol{\phi}}^{(\alpha)}=\boldsymbol{\beta}_s^{(\alpha)}b_s^{(\alpha)},\qquad\qquad \tilde{\boldsymbol{\eta}}_o^{(\alpha)}=\boldsymbol{\gamma}_s^{(\alpha)}b_s^{(\alpha)} \tag{4-17}$$

In the interest of brevity, the reader is referred to Chapter 3 for the details on the localization procedure. The method proposed in Chapter 3 is general and therefore applicable to nonconforming meshes as well. However, our present work on evolving debonding is particular to conforming meshes, so the segments are simply the intersecting/adjacent element boundaries.

The next step is the linearization of (4-16) with respect to the fine scales $\tilde{\boldsymbol{\phi}}^{(\alpha)}$. Because the fine scales are localized to the interface, after the linearization of (4-16), the fine-scale field is treated as an incremental displacement $\Delta\tilde{\boldsymbol{u}}^{(\alpha)}$ field about the coarse-scale deformation $\hat{\boldsymbol{\phi}}^{(\alpha)}$ along the interface:

$$\sum_{\alpha=1}^{2}\int_{\omega^{(\alpha)}}\text{GRAD}\,\tilde{\boldsymbol{\eta}}_o^{(\alpha)}:\mathbf{A}^{(\alpha)}\left(\boldsymbol{F}^{(\alpha)}\right):\text{GRAD}\,\Delta\tilde{\boldsymbol{u}}^{(\alpha)}\,\mathrm{d}V=-\tilde{R}_s\left(\hat{\boldsymbol{\eta}}_o^{(\alpha)};\hat{\boldsymbol{\phi}}^{(\alpha)},\mathbf{0},\boldsymbol{\lambda}\right) \tag{4-18}$$

where the acoustic tensor of material moduli $\mathbf{A}^{(\alpha)}\left(\boldsymbol{F}^{(\alpha)}\right)$ is defined as:

$$\mathbf{A}^{(\alpha)}\left(\boldsymbol{F}^{(\alpha)}\right)=\frac{\partial^2 W^{(\alpha)}}{\partial\boldsymbol{F}\partial\boldsymbol{F}} \tag{4-19}$$

We solve (4-18) by substituting the expression for fine scales (4-17). The detailed procedures for solving the fine-scale solution are provided in Chapter 3. A key property of the method is that the expression for the fine-scale solution $\Delta\tilde{\boldsymbol{u}}^{(\alpha)}$ remains unchanged when compared with Chapter 3:

$$\Delta\tilde{\boldsymbol{u}}^{(\alpha)} = \boldsymbol{\tau}_s^{(\alpha)} \cdot \left[\left(-1\right)^{\alpha-1} \boldsymbol{\lambda} - \boldsymbol{P}^{(\alpha)} \cdot \boldsymbol{N}^{(\alpha)} \right] \tag{4-20}$$

where:

$$\boldsymbol{\tau}_s^{(\alpha)} = \left[\text{meas}\left(\gamma_s\right) \right]^{-1} \left(\int_{\gamma_s} b_s^{(\alpha)} \, \text{d}A \right)^2 \tilde{\boldsymbol{\tau}}_s^{(\alpha)} \tag{4-21}$$

$$\tilde{\boldsymbol{\tau}}_s^{(\alpha)} = \left[\int_{\omega_s^{(\alpha)}} \text{GRAD}\, \boldsymbol{b}_s^{(\alpha)} : \mathbf{A}^{(\alpha)} : \text{GRAD}\, \boldsymbol{b}_s^{(\alpha)} \, \text{d}V \right]^{-1} \tag{4-22}$$

An important point to note is that the residual based fine-scale solution incorporates the effects of evolving geometric and material nonlinearity on either side of the interface via the acoustic tensor $\mathbf{A}^{(\alpha)}\left(\boldsymbol{F}^{(\alpha)}\right)$ that appears in the expression for the stability tensors $\tilde{\boldsymbol{\tau}}_s^{(\alpha)}$, as presented in Chapter 3. These dependencies play a key role in the properties of the numerical flux derived below.

***Remark**: The fine-scale derivation is based on a two-step process: localization and then linearization, as in Chapter 3 and [160] in the finite strain regime. One can also refer to [162] for evolution of the fine scales for different PDEs. The distinction emerges in the derived form of the Lagrange multipliers that account for the gap function* $\boldsymbol{\zeta}$ *.*

4.3.2 Variational embedding in the coarse-scale problem

We now focus on the continuity equation (4-15) in order to obtain an expression for the Lagrange multiplier field $\boldsymbol{\lambda}$. Following [163] and Chapter 3, we substitute the fine-scale model (4-17) and the multiscale decomposition (4-11) – (4-13) into (4-15). Assuring $\boldsymbol{\lambda}$ projection of $\boldsymbol{\lambda}$ and locally satisfying the resulting equation for all values of the multiplier μ, an explicit form is obtained for the interfacial traction $\boldsymbol{\lambda}$:

$$\boldsymbol{\lambda} = \left[\boldsymbol{\delta}_s^{(1)} \cdot \boldsymbol{P}^{(1)} \cdot \boldsymbol{N}^{(1)} - \boldsymbol{\delta}_s^{(2)} \cdot \boldsymbol{P}^{(2)} \cdot \boldsymbol{N}^{(2)} \right] - \boldsymbol{\tau}_s \cdot \left(\left[\!\left[\hat{\boldsymbol{\phi}} \right]\!\right] - \boldsymbol{\zeta} \right) \tag{4-23}$$

where $\boldsymbol{\delta}_s^{(\alpha)} = \boldsymbol{\tau}_s \cdot \boldsymbol{\tau}_s^{(\alpha)}$ is the flux weighting tensor consisting of the stabilization tensor from both subdomains, and $\boldsymbol{\tau}_s = \left(\boldsymbol{\tau}_s^{(1)} + \boldsymbol{\tau}_s^{(2)} \right)^{-1}$.

By substituting $\boldsymbol{\lambda}$ into (4-20), a simplified expression for the fine scales results is as follows:

$$\Delta\tilde{\boldsymbol{u}}^{(\alpha)} = -\boldsymbol{\delta}_s \left[\boldsymbol{P}^{(1)} \cdot \boldsymbol{N}^{(1)} + \boldsymbol{P}^{(2)} \cdot \boldsymbol{N}^{(2)} \right] + \left(-1\right)^{\alpha} \boldsymbol{\delta}_s^{(\alpha)T} \cdot \left(\left[\!\left[\hat{\boldsymbol{\phi}} \right]\!\right] - \boldsymbol{\zeta} \right) \tag{4-24}$$

where the last term contains the inelastic gap term, which is a significantly distinct feature as compared to the expression for the fine-scale field in Chapter 3. Furthermore, the symmetry of the tensors $\boldsymbol{\tau}_s^{(\alpha)}$ and $\boldsymbol{\tau}_s$ has been employed to enable the substitution $\boldsymbol{\delta}_s^{(\alpha)T} = \boldsymbol{\tau}_s^{(\alpha)} \cdot \boldsymbol{\tau}_s$. Also, the additional stability tensor $\boldsymbol{\delta}_s$ in (4-24) is form identical to the one in Chapter 3:

$$\boldsymbol{\delta}_s = \boldsymbol{\tau}_s^{(1)} \cdot \boldsymbol{\delta}_s^{(2)} = \boldsymbol{\tau}_s^{(2)} \cdot \boldsymbol{\delta}_s^{(1)} \tag{4-25}$$

It is important to note that the expression for Lagrange multiplier $\boldsymbol{\lambda}$ naturally accommodates the gap function $\boldsymbol{\zeta}$. Since evolution of gap function is governed by kinematic constraint conditions in addition to evolution models dictating the evolution of $\boldsymbol{\zeta}$, the micromechanical physics manifested via these models is fully embedded in expression (4-23) for $\boldsymbol{\lambda}$. This is a significant contribution of the present Chapter and sets it apart from any numerical methods that have been proposed for interfacial kinematics of finitely deforming embedded interfaces with evolving gaps and discontinuities. Namely, the consistently derived numerical flux $\boldsymbol{\lambda}$ contains a-priori the ability to represent strong discontinuities, rather than methods which transition to debonding by adaptively inserting interface elements as in extrinsic methods or by changing algorithmic parameters from 0 to 1 as in hybrid methods. We wish to emphasize that the proposed consistent derivation that variationally embeds the interfacial kinematic models is crucial to the derivation of consistent tangent tensors that are fundamental to obtaining quadratic convergence rates when employed in the Newton Raphson method.

***Remark**: Note that by adding the inelastic gap $\boldsymbol{\zeta}$ function in (4-3), the first term in (4-24) which is the average traction term does not change with respect to the form presented in Chapter 3. Furthermore, the structural form of the stability tensor $\boldsymbol{\tau}_s$ and the fine-scale stabilization tensor $\boldsymbol{\tau}_s^{(\alpha)}$ are not altered by the introduction of the $\boldsymbol{\zeta}$ term. Short of the strong discontinuity capturing term $\boldsymbol{\zeta}$, the structure of the interface stabilizing terms can be traced through the VMS derivation back to the Galerkin least-squares inspired methods in the linear field context [14,50].*

Incorporating the expressions for $\boldsymbol{\lambda}$ (4-23) and the fine-scale fields $\Delta\tilde{\boldsymbol{u}}^{(\alpha)}$ (4-24) in the linearized coarse-scale problem (4-14) yields the following stabilized interface formulation for finite

deformations:

$$
\begin{aligned}
&R\left(\boldsymbol{\eta}_o^{(\alpha)},\boldsymbol{\phi}^{(\alpha)}\right)=\sum_{\alpha=1}^{2}\int_{\Omega^{(\alpha)}}\left[\text{GRAD}\,\boldsymbol{\eta}_o^{(\alpha)}:\boldsymbol{P}^{(\alpha)}-\boldsymbol{\eta}_o^{(\alpha)}\cdot\rho_o^{(\alpha)}\boldsymbol{B}^{(\alpha)}\right]\mathrm{d}V\\
&-\int_{\Gamma_I}[\![\boldsymbol{\eta}_o]\!]\cdot\{\boldsymbol{P}\cdot\boldsymbol{N}\}\,\mathrm{d}A-\int_{\Gamma_I}\left\{\left(\text{GRAD}\,\boldsymbol{\eta}_o:\mathbf{A}\right)\cdot\boldsymbol{N}\right\}\cdot\left([\![\boldsymbol{\phi}]\!]-\boldsymbol{\zeta}\right)\mathrm{d}A\\
&+\int_{\Gamma_I}[\![\boldsymbol{\eta}_o]\!]\cdot\boldsymbol{\tau}_s\cdot\left([\![\boldsymbol{\phi}]\!]-\boldsymbol{\zeta}\right)\mathrm{d}A-\int_{\Gamma_I}[\![\left(\text{GRAD}\,\boldsymbol{\eta}_o:\mathbf{A}\right)\cdot\boldsymbol{N}]\!]\cdot\boldsymbol{\delta}_s\cdot[\![\boldsymbol{P}\cdot\boldsymbol{N}]\!]\mathrm{d}A=0
\end{aligned}
\tag{4-26}
$$

where $\boldsymbol{\delta}_s=\left[\left(\boldsymbol{\tau}_s^{(1)}\right)^{-1}+\left(\boldsymbol{\tau}_s^{(2)}\right)^{-1}\right]^{-1}$ is the derived stability tensor for the traction jump term, $\{(\bullet)\cdot\boldsymbol{N}\}=(\bullet)^{(1)}\cdot\boldsymbol{N}^{(1)}-(\bullet)^{(2)}\cdot\boldsymbol{N}^{(2)}$ is the defined as the weighted average flux operator, and $[\![(\bullet)\cdot\boldsymbol{N}]\!]=(\bullet)^{(1)}\cdot\boldsymbol{N}^{(1)}+(\bullet)^{(2)}\cdot\boldsymbol{N}^{(2)}$ is defined as the jump operator. The traction jump term, which emerges also in previous derivations for small strain [162,163] and large strain in Chapter 3, is a distinguishing feature with respect to Nitsche and interior penalty Discontinuous Galerkin formulations for small [5,9,140] and large [116] strains. We remark that this term is most significant when the traction jump $[\![\boldsymbol{P}\cdot\boldsymbol{N}]\!]$ is large, such as models with large material mismatch or element size changes across an interface. However, we choose to simplify the formulation by neglecting this term as in [163] and in Chapter 3, leading to a formulation structurally similar to typical DG methods with all parameters consistently derived:

$$
\begin{aligned}
&R\left(\boldsymbol{\eta}_o^{(\alpha)},\boldsymbol{\phi}^{(\alpha)}\right)=\sum_{\alpha=1}^{2}\int_{\Omega^{(\alpha)}}\left[\text{GRAD}\,\boldsymbol{\eta}_o^{(\alpha)}:\boldsymbol{P}^{(\alpha)}-\boldsymbol{\eta}_o^{(\alpha)}\cdot\rho_o^{(\alpha)}\boldsymbol{B}^{(\alpha)}\right]\mathrm{d}V\\
&-\int_{\Gamma_I}[\![\boldsymbol{\eta}_o]\!]\cdot\{\boldsymbol{P}\cdot\boldsymbol{N}\}\,\mathrm{d}A-\int_{\Gamma_I}\left\{\left(\text{GRAD}\,\boldsymbol{\eta}_o:\mathbf{A}\right)\cdot\boldsymbol{N}\right\}\cdot\left([\![\boldsymbol{\phi}]\!]-\boldsymbol{\zeta}\right)\mathrm{d}A\\
&+\int_{\Gamma_I}[\![\boldsymbol{\eta}_o]\!]\cdot\boldsymbol{\tau}_s\cdot\left([\![\boldsymbol{\phi}]\!]-\boldsymbol{\zeta}\right)\mathrm{d}A=0
\end{aligned}
\tag{4-27}
$$

The stabilized residual form (4-27) has the inelastic gap $\boldsymbol{\zeta}$ term inside the integral expression which plays a key role in the evolution of interfacial damage. Variationally consistent updating of these stabilization tensors results in a stabilized formulation that leads to a robust numerical method as shown via numerical test cases in section 4.7.

***Remark**: The interface formulation presented in (4-27) is symmetric. For further simplification of the residual form (4-27), the interested reader is referred to [160] which suggests several generalizations along with insights into the efficiency of such modifications.*

***Remark**: The present derivations are restricted to hyperelastic material response in each solid domain $\Omega^{(\alpha)}$. Material inelasticity can be accommodated by extending the developments in [157] for a symmetric, small strain, elastoplastic DG method.*

***Remark**: As seen in (4-27) the numerical flux contains a priori the ability to represent strong discontinuities which sets it apart from other interface numerical methods.*

4.4 Constitutive Models for Progressive Debonding Along the Interface

With the variational structure of the edge-stabilized finite-strain interfacial model in hand, we now concentrate on the kinematic models for the interfacial damage phenomenon under various loading conditions. These models are based on the notion of irreversible damage evolution and consequently are inspired by the internal variable formalism employed in computational inelasticity literature [146]. We develop evolution equations for the gap function that model interfacial separation and/or sliding, via Kuhn-Tucker complementary conditions from constrained optimization theory. Specifically, the discrete damage evolution or flow rule for the residual gap $\boldsymbol{\zeta}$ and the material softening/hardening parameter $\boldsymbol{Q}$ are derived in a manner analogous to the variational treatment of elastoplasticity as presented in [146,161]. In contrast to cohesive element method [2,59,106,129,161], we use an incremental approach to develop the evolution equation or flow rule for each internal variable [98,155]. Accordingly, the total free energy of the multi-constituent material domain at time $t \in \mathcal{T} =]0,T[$ incorporating both bulk material and interfacial energies can be expressed as:

$$\begin{aligned}\mathcal{P}_t\left(\boldsymbol{\phi}_t^{(1)},\boldsymbol{\phi}_t^{(2)},\boldsymbol{\zeta}_t,\boldsymbol{Q}_t\right) = &\left[\sum_{\alpha=1}^{2}\int_{\Omega^{(\alpha)}} W^{(\alpha)}\left(\boldsymbol{F}_t^{(\alpha)}\right)\,dV + \mathcal{P}_{ext}\left(\boldsymbol{\phi}_t^{(\alpha)}\right)\right] \\ &- \int_{\Gamma_I}\boldsymbol{\lambda}\cdot\left(\left[\!\left[\boldsymbol{\phi}_t\right]\!\right]-\boldsymbol{\zeta}_t\right) - \frac{1}{2}\boldsymbol{Q}_t\cdot\boldsymbol{D}^{-1}\cdot\boldsymbol{Q}_t\,dA\end{aligned} \tag{4-28}$$

where the potential energy of external forces $P_{ext}\left(\boldsymbol{\phi}_t^{(\alpha)}\right)$ contains the contributions from the body forces:

$$\mathcal{P}_{ext}\left(\boldsymbol{\phi}_t^{(\alpha)}\right) = -\int_{\Omega^{(\alpha)}}\rho_0\boldsymbol{B}^{(\alpha)}\cdot\boldsymbol{\phi}_t^{(\alpha)}\,dV \tag{4-29}$$

The present approach is based on the notion of incremental updating of the nonlinearly evolving internal variables while in our earlier work on interfacial mechanics we had employed a potential function approach with embedded $\boldsymbol{\zeta}$, thereby facilitating the evolution of total $\boldsymbol{\zeta}$ at any instant

in time. It is to be noted that frictional model incorporated in the present developments for damage in comparison gets activated only due to the tangential component of the interface traction that triggers local shearing and, in the present context of finite deformation framework, local rotational effects. Rotational effects necessitate objective update of the stress and the stress-like quantities which is readily facilitated via the variationally consistent pull-back and push-forward operations embedded in the derivation of these quantities. However, introduction of friction renders the damage evolution flow rule non-associative and therefore requires a rate form for the enforcement of normality condition in the evolution of frictional damage.

Recall the derivation of the expression for the Lagrange multiplier in (4-18). Substituting (4-18) into (4-28), we arrive at an expression for the potential energy for multi-constituent material, accounting for the interfacial energy, however without explicit appearance of the Lagrange multiplier $\boldsymbol{\lambda}$:

$$\begin{aligned}\mathcal{P}_t\left(\boldsymbol{\phi}_t^{(1)},\boldsymbol{\phi}_t^{(2)},\boldsymbol{\zeta}_t,\boldsymbol{Q}_t\right)=&\left[\sum_{\alpha=1}^{2}\int_{\Omega^{(\alpha)}}W^{(\alpha)}\left(\boldsymbol{F}^{(1)},\boldsymbol{F}^{(2)}\right)dV+\mathcal{P}_{ext}\left(\boldsymbol{\phi}_t^{(\alpha)}\right)\right]\\&-\int_{\Gamma_I}\left(\left\{\boldsymbol{P}\cdot\boldsymbol{N}\right\}+\boldsymbol{\tau}_s\cdot\frac{1}{2}\left(\left[\!\left[\boldsymbol{\phi}_t\right]\!\right]-\boldsymbol{\zeta}\right)\right)\cdot\left(\left[\!\left[\boldsymbol{\phi}_t\right]\!\right]-\boldsymbol{\zeta}_t\right)-\frac{1}{2}\boldsymbol{Q}_t\cdot\mathbf{D}^{-1}\cdot\boldsymbol{Q}_t\,dA\end{aligned}\tag{4-30}$$

where W is the stored-energy function, $\mathcal{P}_{ext}$ is the external energy function, $\mathbf{D}^{-1}$ is the hardening/softening tangent compliance tensor, and $\boldsymbol{Q}_t$ is the hardening/softening parameter. The last term in (4-30) appears due to the hardening function $\mathcal{H}$ [146] and for simplicity, we have assumed $\mathcal{H}$ to be quadratic.

***Remark**: The potential energy provided in (4-30) is obtained by substituting the expression of the Lagrange multiplier. An important point to note is that explicit appearance of Lagrange multiplier $\boldsymbol{\lambda}$ which would have been an additional unknown in the system has been substituted by consistently derived interface coupling terms that eliminate the additional unknown. In addition, equation (4-30) leads to the stabilized formulation (4-27) by taking the variational derivative with respect to $\boldsymbol{\phi}^{(1)}$ and $\boldsymbol{\phi}^{(2)}$. Another example of having a potential energy function for elastoplasticity is given in [157].*

***Remark**: In our previous work [161], we used potential energy based approach along with solving local nonlinear problem to calculate the total residual gap, and this method is being termed as the*

total approach. The incremental approach proposed here has several advantages compared to the total approach in [161]. The proposed approach being incrementally objective accommodates friction together with other debonding cases in a unified manner. This results in improved numerical behavior in the finite strain range than the total approach.

As illustrated in [133], taking variational derivative of (4-30) with respect to the inelastic gap term $\boldsymbol{\zeta}$, we arrive at the interface traction term that is analogous to the term derived in [161] and is defined as:

$$\boldsymbol{T} := \{\boldsymbol{P}\cdot\boldsymbol{N}\} + \|\boldsymbol{\tau}^s\|\left(\llbracket\boldsymbol{\phi}\rrbracket - \boldsymbol{\zeta}\right) \tag{4-31}$$

Note that in the definition of the interface traction term, we use the norm of the stability tensor $\boldsymbol{\tau}^s$ to maintain the direction of the discontinuity term $\left(\llbracket\boldsymbol{\phi}\rrbracket - \boldsymbol{\zeta}\right)$. This is a simplification that enables radial return algorithm for debonding constitutive models that we use in the next section.

Following the ideas from [146], we now use the interface traction (4-31) to define the damage energy dissipation at time $\xi \in \mathcal{T}$ as:

$$\mathcal{D}_\xi^P := \dot{\boldsymbol{\zeta}}_\xi \cdot \left[\left\{\boldsymbol{P}\left(\boldsymbol{F}_\xi^{(\alpha)}\right)\boldsymbol{N}\right\} + \|\boldsymbol{\tau}^s\|\left(\llbracket\boldsymbol{\phi}_\xi\rrbracket - \boldsymbol{\zeta}_\xi\right)\right] - \dot{\boldsymbol{Q}}_\xi \cdot \mathbf{D}^{-1}\cdot\boldsymbol{Q}_\xi \geq 0 \tag{4-32}$$

where $\left\{\boldsymbol{\phi}_\xi^{(\alpha)}, \boldsymbol{\zeta}_\xi, \boldsymbol{Q}_\xi\right\}$ must lie within the elastic domain. We emphasize that for any admissible deformation map $\boldsymbol{\phi}_\xi^{(\alpha)}$, the yield surface associated with the yield condition $f\left(\boldsymbol{T}, \boldsymbol{Q}_\xi\right) \leq 0$ is:

$$\mathbb{E} := \left\{\left(\boldsymbol{T}, \boldsymbol{Q}_\xi\right) \in \left(\mathbb{L}_2\right)^3 \times \mathbb{R}^m \mid f\left(\boldsymbol{T}, \boldsymbol{Q}_\xi\right) \leq 0\right\} \tag{4-33}$$

Note that the damage yield condition $f\left(\boldsymbol{T}, \boldsymbol{Q}_\xi\right)$ is a function of both the interface traction $\boldsymbol{T}$ and the hardening/softening parameter $\boldsymbol{Q}_\xi$. We now develop the formulation of total dissipation by combining the damage dissipation $\mathcal{D}_\xi^P$ with the damage yield condition $f\left(\boldsymbol{T}, \boldsymbol{Q}_\xi\right)$. Thus, the total dissipation up to time t can be evaluated by integrating over the entire interface and for the total elapsed time:

$$\mathcal{L}_t^P = \int_0^t \int_{\Gamma_1} \left\{\mathcal{D}_\xi^P - \gamma_\xi f\left[\left\{\boldsymbol{P}\left(\boldsymbol{F}_\xi^{(\alpha)}\right)\boldsymbol{N}\right\} + \|\boldsymbol{\tau}^s\|\left(\llbracket\boldsymbol{\phi}_\xi\rrbracket - \boldsymbol{\zeta}_\xi\right), \boldsymbol{Q}_\xi\right]\right\} dA\, d\xi \tag{4-34}$$

Here, γ_ξ is considered the damage consistency parameter, which enforces the admissibility

constraint (4-33) at the instant ξ in time and is taken to lie in the positive cone $\mathbb{K}^P$ defined as:

$$\mathbb{K}^P := \left\{ \gamma_\xi \,|\, \gamma_\xi \in L_2\left(\Gamma_{\mathrm{I}}\right) \right\} \tag{4-35}$$

Now we consider the time-discrete counterpart of functional (4-34). Taking $t = t_{n+1} = t_n + \Delta t$ as the current time level, where $t = t_n$ is the previous time level, we can rewrite the time discrete form of (4-34) along with (4-32) as follows:

$$\begin{aligned} \mathcal{L}^P_{n+1} = \mathcal{L}^P_n + \int_{t_n}^{t_{n+1}} \int_{\Gamma_{\mathrm{I}}} \left\{ \dot{\boldsymbol{\zeta}}_\xi \cdot \left[\left\{ \boldsymbol{P}\left(\boldsymbol{F}^{(\alpha)}_\xi\right) \boldsymbol{N} \right\} + \left\| \boldsymbol{\tau}^s \right\| \left(\left[\!\left[\boldsymbol{\phi}_\xi \right]\!\right] - \boldsymbol{\zeta}_\xi \right) \right] - \dot{\boldsymbol{Q}}_\xi \cdot \mathbf{D}^{-1} \cdot \boldsymbol{Q}_\xi \right\} dA\, d\xi \\ - \int_{t_n}^{t_{n+1}} \int_{\Gamma_{\mathrm{I}}} \left\{ \gamma_\xi f \left[\left\{ \boldsymbol{P}\left(\boldsymbol{F}^{(\alpha)}_\xi\right) \boldsymbol{N} \right\} + \left\| \boldsymbol{\tau}^s \right\| \left(\left[\!\left[\boldsymbol{\phi}_\xi \right]\!\right] - \boldsymbol{\zeta}_\xi \right), \boldsymbol{Q}_\xi \right] \right\} dA\, d\xi \end{aligned} \tag{4-36}$$

The history of the state variables at the interface over the interval $\left[0, t_n\right]$ is assumed to be known, while the unknown variables at time t_{n+1} along with the yield function are denoted as:

$$\boldsymbol{\chi}_{n+1} := \left\{ \boldsymbol{\phi}^{(1)}_{n+1}, \boldsymbol{\phi}^{(2)}_{n+1}, \boldsymbol{\zeta}_{n+1}, \boldsymbol{Q}_{n+1}, \Delta\gamma \right\} \tag{4-37}$$

$$f_{n+1} := f\left[\left\{ \boldsymbol{P}\left(\boldsymbol{F}^{(\alpha)}_{n+1}\right) \boldsymbol{N} \right\} + \left\| \boldsymbol{\tau}^s \right\| \left(\left[\!\left[\boldsymbol{\phi}_{n+1} \right]\!\right] - \boldsymbol{\zeta}_{n+1} \right), \boldsymbol{Q}_{n+1} \right] \tag{4-38}$$

Applying the backward Euler difference scheme to (4-36) results in the following expressions:

$$\begin{aligned} \mathcal{L}^P_{n+1}\left(\boldsymbol{\chi}_{n+1}\right) := \mathcal{L}^P_n + \int_{\Gamma_{\mathrm{I}}} \left\{ \left(\boldsymbol{\zeta}_{n+1} - \boldsymbol{\zeta}_n \right) \cdot \left[\left\{ \boldsymbol{P}\left(\boldsymbol{F}_{n+1}\right) \boldsymbol{N} \right\} + \left\| \boldsymbol{\tau}^s \right\| \left(\left[\!\left[\boldsymbol{\phi}_{n+1} \right]\!\right] - \boldsymbol{\zeta}_{n+1} \right) \right] \right\} dA \\ - \int_{\Gamma_{\mathrm{I}}} \left\{ \Delta\gamma f_{n+1} + \boldsymbol{Q}_{n+1} \cdot \mathbf{D}^{-1} \cdot \left(\boldsymbol{Q}_{n+1} - \boldsymbol{Q}_n \right) \right\} dA \end{aligned} \tag{4-39}$$

where $\Delta\gamma := \gamma \Delta t$ is the incremental consistency parameter.

We now return to the potential functional (4-30) and define a discrete variational form for interface damage as the total free energy available at time t_n expressed in terms of the total free energy at time t_{n+1} along with the dissipation during the interval $\left[t_n, t_{n+1}\right]$:

$$\hat{\mathcal{P}}_n\left(\boldsymbol{\chi}_{n+1}\right) := \mathcal{P}_{n+1}\left(\boldsymbol{\chi}_{n+1}\right) + \left(\mathcal{L}^P_{n+1}\left(\boldsymbol{\chi}_{n+1}\right) - \mathcal{L}^P_n \right) \tag{4-40}$$

Substituting (4-30) and (4-39) in (4-40) and rearranging, we arrive at the following expression wherein all the interface contribution is accumulated in the term $\hat{\mathcal{L}}_n\left(\boldsymbol{\chi}_{n+1}\right)$.

$$\hat{\mathcal{P}}_n\left(\boldsymbol{\chi}_{n+1}\right) := \left[\sum_{\alpha=1}^{2} \int_{\Omega^{(\alpha)}} W^{(\alpha)}\left(\boldsymbol{\phi}^{(\alpha)}_{n+1}, \boldsymbol{\zeta}_{n+1} \right) dV + P_{ext}\left(\boldsymbol{\phi}^{(\alpha)}_{n+1} \right) \right] + \hat{\mathcal{L}}_n\left(\boldsymbol{\chi}_{n+1}\right) \tag{4-41}$$

$$\begin{aligned}\hat{\mathcal{L}}_n\left(\boldsymbol{\chi}_{n+1}\right)=&\int_{\Gamma_I}\left[\left\{\boldsymbol{P}\left(\boldsymbol{F}_{n+1}\right)\boldsymbol{N}\right\}+\frac{\left\|\boldsymbol{\tau}^s\right\|}{2}\left(\left[\!\left[\boldsymbol{\phi}_{n+1}\right]\!\right]-\boldsymbol{\zeta}_{n+1}\right)\right]\cdot\left(\left[\!\left[\boldsymbol{\phi}_{n+1}\right]\!\right]-\boldsymbol{\zeta}_{n+1}\right)dA\\&+\int_{\Gamma_I}\left(\boldsymbol{\zeta}_{n+1}-\boldsymbol{\zeta}_n\right)\cdot\left[\left\{\boldsymbol{P}\left(\boldsymbol{F}_{n+1}\right)\boldsymbol{N}\right\}+\left\|\boldsymbol{\tau}^s\right\|\left(\left[\!\left[\boldsymbol{\phi}_{n+1}\right]\!\right]-\boldsymbol{\zeta}_{n+1}\right)\right]dA\\&-\int_{\Gamma_I}\left\{\Delta\gamma f_{n+1}+\boldsymbol{Q}_{n+1}\cdot\mathbf{D}^{-1}\cdot\left(\boldsymbol{Q}_{n+1}-\boldsymbol{Q}_n\right)\right\}+\frac{1}{2}\boldsymbol{Q}_{n+1}\cdot\boldsymbol{D}^{-1}\cdot\boldsymbol{Q}_{n+1}\,dA\end{aligned}\tag{4-42}$$

To show that (4-41) has an underlying variational structure, the next crucial step is to verify that the stationary conditions of (4-41) furnish the weak form of the governing equations for interfacial damage. We utilize this weak form in our finite element formulation. Accordingly, we first specify the spaces of trial functions for the fields:

$$\mathcal{S}^{(\alpha)}=\left\{\boldsymbol{\phi}^{(\alpha)}\,\middle|\,\boldsymbol{\phi}^{(\alpha)}\in\left[H^1\left(\Omega^{(\alpha)}\right)\right]^{n_{\text{sd}}},\ \det\left(\boldsymbol{F}^{(\alpha)}\left(\boldsymbol{\phi}^{(\alpha)}\right)\right)>0,\ \ \boldsymbol{\phi}^{(\alpha)}\big|_{\Gamma^{(\alpha)}\setminus\Gamma_I}=\boldsymbol{X}^{(\alpha)}\right\}\tag{4-43}$$

$$\mathcal{X}_\zeta=\left\{\boldsymbol{\zeta}\,\middle|\,\boldsymbol{\zeta}\in\left[L_2\left(\Gamma_I\right)\right]^{n_{\text{sd}}}\right\}\tag{4-44}$$

$$\mathcal{X}_Q=\left\{\boldsymbol{Q}\,\middle|\,\boldsymbol{Q}\in\left[L_2\left(\Gamma_I\right)\right]^{n_{\text{sd}}}\right\}\tag{4-45}$$

Then, taking variational derivative [146] of (4-41) we obtain the following weak forms of the governing equations:

$$\begin{aligned}\delta\widehat{\mathcal{P}}_n\left(\boldsymbol{\chi}_{n+1},\boldsymbol{\eta}_0\right)=&\sum_{\alpha=1}^{2}\int_{\Omega^{(\alpha)}}\left[\text{GRAD}\,\boldsymbol{\eta}_0^{(\alpha)}:\boldsymbol{P}^{(\alpha)}-\boldsymbol{\eta}_0^{(\alpha)}\cdot\rho_0^{(\alpha)}\boldsymbol{B}^{(\alpha)}\right]\text{dV}\\&+\int_{\Gamma_I}\left[\left\{\boldsymbol{P}\cdot\boldsymbol{N}\right\}+\left\|\boldsymbol{\tau}^s\right\|\left(\left[\!\left[\boldsymbol{\phi}_{n+1}\right]\!\right]-\boldsymbol{\zeta}_n\right)-\Delta\gamma\left\|\boldsymbol{\tau}^s\right\|\partial_{\boldsymbol{T}}f_{n+1}\right]\cdot\left[\!\left[\boldsymbol{\eta}_0\right]\!\right]\text{d}A\\&+\int_{\Gamma_I}\left[\left(\left[\!\left[\boldsymbol{\phi}_{n+1}\right]\!\right]-\boldsymbol{\zeta}_n\right)-\Delta\gamma\partial_{\boldsymbol{T}}f_{n+1}\right]\cdot\left\{\left(\text{GRAD}\,\boldsymbol{\eta}_o:\mathbf{A}\right)\cdot\boldsymbol{N}\right\}\text{d}A\end{aligned}\tag{4-46}$$

$$\delta\widehat{\mathcal{P}}_n\left(\boldsymbol{\chi}_{n+1},\boldsymbol{\beta}\right)=\int_{\Gamma_I}\left(\boldsymbol{\zeta}_{n+1}-\boldsymbol{\zeta}_n-\Delta\gamma\partial_{\boldsymbol{T}}f_{n+1}\right)\cdot\left(-\left\|\boldsymbol{\tau}^s\right\|\boldsymbol{\beta}\right)\text{d}A=0\tag{4-47}$$

$$\delta\widehat{\mathcal{P}}_n\left(\boldsymbol{\chi}_{n+1},\boldsymbol{p}\right)=\int_{\Gamma_I}\left[\mathbf{D}^{-1}\cdot\left(\boldsymbol{Q}_{n+1}-\boldsymbol{Q}_n\right)+\Delta\gamma\partial_{\boldsymbol{Q}}f_{n+1}\right]\cdot\left(-\boldsymbol{p}\right)\text{d}A=0\tag{4-48}$$

$$\delta\widehat{\mathcal{P}}_n\left(\boldsymbol{\chi}_{n+1},\lambda\right)=\int_{\Gamma_I}\lambda f_{n+1}\,\text{d}A=0\tag{4-49}$$

that hold for arbitrary displacement variations $\boldsymbol{\eta}_0\in\mathcal{V}$, residual gap variations $\boldsymbol{\beta}\in\mathcal{X}_\zeta$, hardening variations $\boldsymbol{p}\in\mathcal{X}_Q$, and variations $\lambda\in\mathbb{K}^p$. We summarize the Euler-Lagrange equations for interfacial damage in Box 4.1.

Box 4.1. Euler-Lagrange equations for interfacial damage.

- Equilibrium in the bulk domain, and at the traction boundary:

$$\text{DIV}\, \boldsymbol{P}^{(\alpha)}\left(\boldsymbol{F}^{(\alpha)}\right)+\rho_o^{(\alpha)}\boldsymbol{B}^{(\alpha)}=\boldsymbol{0} \qquad \text{in} \quad \Omega^{(\alpha)},\ \alpha=1,2 \tag{4-50}$$

- Interface traction equilibrium:

$$\boldsymbol{P}^{(1)}\cdot\boldsymbol{N}^{(1)}+\boldsymbol{P}^{(2)}\cdot\boldsymbol{N}^{(2)}=\boldsymbol{0} \qquad \text{on}\ \ \Gamma_I \tag{4-51}$$

- Interface gap constraint:

$$\left[\!\left[\boldsymbol{\phi}_{n+1}\right]\!\right]-\left(\boldsymbol{\zeta}_n+\Delta\gamma\,\partial_{\boldsymbol{T}} f_{n+1}\right)=0 \tag{4-52}$$

- Interface damage flow rule:

$$\boldsymbol{\zeta}_{n+1}=\boldsymbol{\zeta}_n+\Delta\gamma\,\partial_{\boldsymbol{T}} f_{n+1} \tag{4-53}$$

- Interface hardening law:

$$\boldsymbol{Q}_{n+1}=\boldsymbol{Q}_n+\mathbf{D}\Delta\gamma\,\partial_Q f_{n+1} \tag{4-54}$$

- Kuhn-Tucker consistency condition:

$$f_{n+1}\le 0, \qquad \Delta\gamma\ge 0, \qquad f_{n+1}\Delta\gamma=0 \tag{4-55}$$

To make the discussion precise we now specify damage yield conditions and softening models to develop traction-gap relations. In section 4.5, we specify the evolution of the internal variables by separating the constitutive behavior into two regimes: tension and compression. The tension branch is presented in section 4.5.1. For the compression case, only the tangential component of the interface traction contributes to the debonding of the material. Consequently, we further separate compression case into compression damage and compression friction as presented in section 4.5.2.

4.5 Interfacial Constitutive Models and Corresponding Return Mapping Algorithms

In the finite element implementation of constitutive models that are based on internal variable formulism, the equilibrium equation (4-46) is enforced weakly. However, the constitutive model is considered local and therefore enforced pointwise. Consequently, we strongly enforce the yield condition, damage evolution flow rule, and consistency condition at the Gauss points along the interface wherein the residual gap $\boldsymbol{\zeta}$ and hardening variable Q are treated as internal variables and are evolved point-wise from t_n to t_{n+1}. This results in a displacement-driven algorithm that is similar to the strain-driven treatment of computational elastoplasticity problems [146]. Assuming isotropy, we have adopted the classical return mapping approach to solve for $\left(\boldsymbol{\phi}_{n+1},\boldsymbol{\zeta}_{n+1},Q_{n+1}\right)$ in a

coupled manner. Details of the return mapping algorithm for the case of both tension and compression are described below.

4.5.1 The Tension Model

The yield criterion in tension is defined via the following isotropic linear softening model:

$$f\left(\boldsymbol{T},Q\right)=\left\|\boldsymbol{T}\right\|-\left(P_c-Q\right) \tag{4-56}$$

where P_c is the critical stress at which debonding initiates, and Q is the softening stress. The relation between the tensile stress and the inelastic gap is shown in Figure 4.2. The interfacial traction $\boldsymbol{T}$ defined in (4-31) is as follows:

$$\boldsymbol{T}:=\left\{\boldsymbol{PN}\right\}+\left\|\boldsymbol{\tau}^s\right\|\left(\left[\!\left[\boldsymbol{\phi}\right]\!\right]-\boldsymbol{\zeta}\right) \tag{4-57}$$

The flow rule and hardening law under the assumption of isotropy are derived as follows:

$$\dot{\boldsymbol{\zeta}}=\dot{\gamma}\underbrace{\left(\partial f/\partial\boldsymbol{T}\right)}_{\text{Normality}},\qquad \dot{Q}=H_c\,\dot{\gamma} \tag{4-58}$$

where the normality condition $\partial f/\partial\boldsymbol{T}=\boldsymbol{n}=\boldsymbol{T}/\left\|\boldsymbol{T}\right\|$ defines the unit vector in the direction of the interface traction, $H_c:=P_c/\zeta_c$ is the negative slope of the softening curve shown in Figure 4.2, and ζ_c is the critical residual gap. From (4-58), we find that $\dot{\gamma}:=\left\|\dot{\boldsymbol{\zeta}}\right\|$ which implies $\dot{Q}=H_c\,\dot{\gamma}=\left(P_c/\zeta_c\right)\left\|\dot{\boldsymbol{\zeta}}\right\|$, namely that Q increases proportional to the rate of increase in the magnitude of the residual gap. Combining the yield function f with the Kuhn-Tucker form results in the constitutive framework [171].

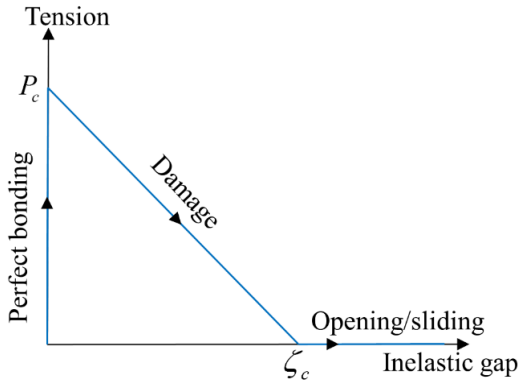

Figure 4.2. Constitutive behavior in tension.

4.5.1.1 Return mapping for damage under tensile loading

To develop the return mapping algorithm, let us focus at a Gauss point along interface Γ_{int}. We assume that the current iterated values of displacements fields in $\Omega^{(1)}$ and $\Omega^{(2)}$, denoted by $\boldsymbol{\phi}_{n+1}^{(i),1}$ and $\boldsymbol{\phi}_{n+1}^{(i),2}$ respectively, are known, along with the previous converged state variables $\left(\boldsymbol{\phi}_n, \boldsymbol{\zeta}_n, Q_n\right)$. The objective is to compute the variables $\boldsymbol{\zeta}_{n+1}$ and Q_{n+1} such that the damage yield criterion is satisfied subject to the constraint imposed by the Kuhn-Tucker consistency conditions. Accordingly, we focus on the expression for the interface traction and by plugging in the interface damage flow rule (4-53), we rewrite the interface traction as:

$$\boldsymbol{T} = \{\boldsymbol{PN}\} + \left\|\boldsymbol{\tau}^s\right\|\left(\left[\!\left[\boldsymbol{\phi}\right]\!\right] - \boldsymbol{\zeta}_{n+1}\right) = \{\boldsymbol{PN}\} + \left\|\boldsymbol{\tau}^s\right\|\left(\left[\!\left[\boldsymbol{\phi}\right]\!\right] - \boldsymbol{\zeta}_n\right) - \left\|\boldsymbol{\tau}^s\right\|\Delta\gamma\,\partial_{\boldsymbol{T}} f_{n+1} \tag{4-59}$$

From the flow rule evaluated at time t_{n+1} we have:

$$\partial_{\boldsymbol{T}} f_{n+1} = \frac{\partial\left\|\boldsymbol{T}_{n+1}\right\|}{\partial \boldsymbol{T}_{n+1}} = \frac{\boldsymbol{T}_{n+1}}{\left\|\boldsymbol{T}_{n+1}\right\|} = \boldsymbol{n}_{n+1} \tag{4-60}$$

Substituting into (4-59), we make the following observations on the magnitude and direction of the trial and resultant interface tractions:

$$\left\|\boldsymbol{T}_{n+1}\right\| = \left\|\boldsymbol{T}_{n+1}^{tr}\right\| - \left\|\boldsymbol{\tau}^s\right\|\Delta\gamma \tag{4-61}$$

where $\boldsymbol{T}_{n+1}^{tr} = \{\boldsymbol{PN}\} + \left\|\boldsymbol{\tau}^s\right\|\left(\left[\!\left[\boldsymbol{\phi}\right]\!\right] - \boldsymbol{\zeta}_n\right)$ is based on the last converged value of the gap function.

Next, define the trial unit vector $\boldsymbol{n}_{n+1}^{tr}$ in the direction of $\boldsymbol{T}_{n+1}^{tr}$ and the trial yield criterion f_{n+1}^{tr} as:

$$\boldsymbol{n}_{n+1}^{tr} = \boldsymbol{n}_{n+1} = \frac{\boldsymbol{T}_{n+1}^{tr}}{\left\|\boldsymbol{T}_{n+1}^{tr}\right\|} \tag{4-62}$$

$$f_{n+1}^{tr} = \left\|\boldsymbol{T}_{n+1}^{tr}\right\| - \left(P_c - Q_n\right) \tag{4-63}$$

According to the consistency condition, if $f_{n+1}^{tr} \le 0$, there is no further damage, namely, $\Delta\gamma = 0$. However, if $f_{n+1}^{tr} > 0$, we can compute $\Delta\gamma$ by satisfying the consistency condition. Substituting Eqn. (4-54), (4-61) and (4-63) in (4-56), we arrive at the equation for $\Delta\gamma$.

$$
\begin{aligned}
0 = f_{n+1} &= \left\| \boldsymbol{T}_{n+1} \right\| - \left(P_c - Q_{n+1} \right) \\
&= \left\| \boldsymbol{T}_{n+1}^{tr} \right\| - \left\| \boldsymbol{\tau}^s \right\| \Delta\gamma - \left(P_c - Q_n \right) + H_c \, \Delta\gamma \\
&= f_{n+1}^{\mathrm{tr}} - \left(\left\| \boldsymbol{\tau}^s \right\| - H_c \right) \Delta\gamma
\end{aligned}
\tag{4-64}
$$

Solving (4-64) for $\Delta\gamma$ yields:

$$
\Delta\gamma = \frac{f_{n+1}^{\mathrm{tr}}}{\left(\left\| \boldsymbol{\tau}^s \right\| - H_c \right)} \tag{4-65}
$$

Substituting (4-65) in (4-53), (4-54), and (4-59), we obtain the updated values for ζ_{n+1}, Q_{n+1} and $\boldsymbol{T}_{n+1}$, respectively. This procedure for updating the internal variables is summarized in Box 4.2, where $\boldsymbol{x}^{\mathrm{int}}$ represents the integration point belonging to the interface segment set $\mathcal{B}$.

Box 4.2. Return mapping algorithm for damage evolution under tensile loading.

- STEP 1: Database at $\boldsymbol{x}^{\mathrm{int}} \in \mathcal{B}$: $\left\{ \zeta_n, Q_n \right\}$.
- STEP 2: Given the stress and displacement jump at $\boldsymbol{x}^{\mathrm{int}} \in \mathcal{B}$: $\left\{ \left\{ \boldsymbol{PN} \right\}, \left[\!\left[\boldsymbol{\phi} \right]\!\right] \right\}$
- STEP 3: Compute the trial stress and test for inelastic damage evolution

$$
\boldsymbol{T}_{n+1}^{tr} = \left\{ \boldsymbol{PN} \right\} + \left\| \boldsymbol{\tau}^s \right\| \left(\left[\!\left[\boldsymbol{\phi} \right]\!\right] - \boldsymbol{\zeta}_n \right) \tag{4-66}
$$

$$
f_{n+1}^{tr} = \left\| \boldsymbol{T}_{n+1}^{tr} \right\| - \left(P_c - Q_n \right) \tag{4-67}
$$

IF $f_{n+1}^{tr} \le 0$ THEN

Elastic step: Set $\left(\bullet \right)_{n+1} = \left(\bullet \right)_{n+1}^{tr}$ & EXIT

ELSE

Damage evolution step: Proceed to STEP 4.

ENDIF

- STEP 4: Return mapping

$$
\Delta\gamma = \frac{f_{n+1}^{\mathrm{tr}}}{\left(\left\| \boldsymbol{\tau}^s \right\| - H_c \right)} > 0 \tag{4-68}
$$

$$
\boldsymbol{\zeta}_{n+1} = \boldsymbol{\zeta}_n + \Delta\gamma \, \boldsymbol{n}_{n+1} \tag{4-69}
$$

$$
Q_{n+1} = Q_n + H_c \Delta\gamma \, \partial_Q f_{n+1} \tag{4-70}
$$

Box 4.2 continued.

$$\boldsymbol{T}_{n+1} = \boldsymbol{T}^{tr}_{n+1} - \left\| \boldsymbol{\tau}^{s} \right\| \Delta\gamma \boldsymbol{n}_{n+1} \tag{4-71}$$

4.5.2 The compression model

In order to model contact under compression, the residual gap is not permitted to grow in the direction normal to the interface. Consequently, the residual gap $[\![\boldsymbol{\phi}]\!] \cdot \boldsymbol{N} = 0$, where $\boldsymbol{N} = \boldsymbol{N}^{(2)}$ is the normal vector to the interface. The yield condition is modified as follows:

$$f\left(\boldsymbol{T}, Q\right) = \left\| \boldsymbol{T}_T \right\| - \left(P_c - Q\right) \tag{4-72}$$

where $\boldsymbol{T}_T = \left(\boldsymbol{I} - \boldsymbol{N} \otimes \boldsymbol{N}\right)\boldsymbol{T}$ is the shearing traction at the interface. The corresponding flow rules are defined as:

$$\dot{\boldsymbol{\zeta}} = \dot{\gamma} \underbrace{\left(\partial f / \partial \boldsymbol{T}_T\right)}_{\text{Normality}}, \qquad \dot{Q} = H_c \dot{\gamma} \tag{4-73}$$

where $\partial f / \partial \boldsymbol{T}_T = \boldsymbol{n}_T = \boldsymbol{T}_T / \left\| \boldsymbol{T}_T \right\|$. When debonding occurs under compressive loading, the effects of friction have been found to be significant [2]. Therefore, we enhance the yield model by incorporating a yield condition for friction that takes the form [147,171]:

$$f\left(\boldsymbol{T}\right) = \left\| \boldsymbol{T}_T \right\| + \mu_f T_N \tag{4-74}$$

where $T_N = \boldsymbol{T} \cdot \boldsymbol{N}$ is the contact pressure (positive in tension) and μ_f is the coefficient of friction.

One can combine (4-72) and (4-74) into a comprehensive model by employing ideas from multi-surface plasticity [146]. Following the computational inelasticity literature, we determine the damage/softening or friction criteria that is active, by selecting the one that leads to the smallest change in $\boldsymbol{\zeta}$ for the given or the current level of traction. Detailed return mapping algorithm for the compression loading case is given in Box 4.3.

***Remark**: The flow rule (4-73) is non-associative when combined with the friction yield condition (4-74) because slip is only allowed in the tangential direction. However, in the present work we employ a return mapping strategy that serves as a predictor/corrector algorithm which is widely used in the theory of plasticity [146,147].*

4.5.2.1 Return mapping for frictional constraint under compressive loading

In compressive loading, the normal traction does not play any role in damage evolution or in sliding, and therefore shearing traction is the only component that needs to be considered. In this section we only provide the algorithmic treatment for the friction part of compressive loading since the damage in compression is form identical to that in the tension case.

Employing interfacial traction as in (4-59) and considering only the shearing traction component, the definitions for the trial quantities and the consistency parameter are summarized in Box 4.3.

Box 4.3. Return mapping algorithm for friction under compressive loading.

- STEP 1: Database at $\boldsymbol{x}^{\text{int}} \in \mathcal{B}$: $\{\zeta_n, Q_n\}$.
- STEP 2: Given the stress and displacement jump at $\boldsymbol{x}^{\text{int}} \in \mathcal{B}$: $\{\{\boldsymbol{PN}\}, [\![\boldsymbol{\phi}]\!]\}$
- STEP 3: Compute the trial stress and test for damage evolution

$$\boldsymbol{T}_{T,n+1}^{tr} = (\boldsymbol{I} - \boldsymbol{N} \otimes \boldsymbol{N})\left[\{\boldsymbol{PN}\} + \|\boldsymbol{\tau}^s\|([\![\boldsymbol{\phi}]\!] - \zeta_n)\right] \tag{4-75}$$

$$T_{N,n+1} = \boldsymbol{N} \cdot \left[\{\boldsymbol{PN}\} + \|\boldsymbol{\tau}^s\|[\![\boldsymbol{\phi}]\!]\right] \tag{4-76}$$

$$f_{n+1}^{tr,\mu_f} = \|\boldsymbol{T}_{T,n+1}^{tr}\| + \mu_f T_{N,n+1} \tag{4-77}$$

$$f_{n+1}^{tr,P_c} = \|\boldsymbol{T}_{T,n+1}^{tr}\| - (P_c - Q) \tag{4-78}$$

IF $f_{n+1}^{tr} \le 0$ THEN

Elastic step: Set $(\bullet)_{n+1} = (\bullet)_{n+1}^{tr}$ & EXIT

ELSE

Damage evolution step: Proceed to STEP 4.

ENDIF

- STEP 4: Return mapping

Calculate incremental consistency parameter $\Delta\gamma$

$$\Delta\gamma = \frac{f_{n+1}^{\text{tr},\mu_f}}{\|\boldsymbol{\tau}^s\|} > 0 \tag{4-79}$$

$$\Delta\gamma = \frac{f_{n+1}^{\text{tr},P_c}}{\left(\|\boldsymbol{\tau}^s\| - H_c\right)} > 0 \tag{4-80}$$

Box 4.3 continued.

Compare (4-79) and (4-80), and select the smaller $\Delta\gamma$ and plug into (4-81):

$$\zeta_{n+1} = \zeta_n + \Delta\gamma \chi_{n+1} \tag{4-81}$$

$$Q_{n+1} = Q_n + H_c \Delta\gamma \partial_Q f_{n+1} \tag{4-82}$$

$$\boldsymbol{T}_{T,n+1} = \boldsymbol{T}^{tr}_{T,n+1} - \left\| \boldsymbol{\tau}^s \right\| \Delta\gamma \boldsymbol{n}_{n+1} \tag{4-83}$$

The flowchart of the algorithm for different interfacial constitutive models including tension damage, compression damage, and compression friction is shown in Figure 4.3.

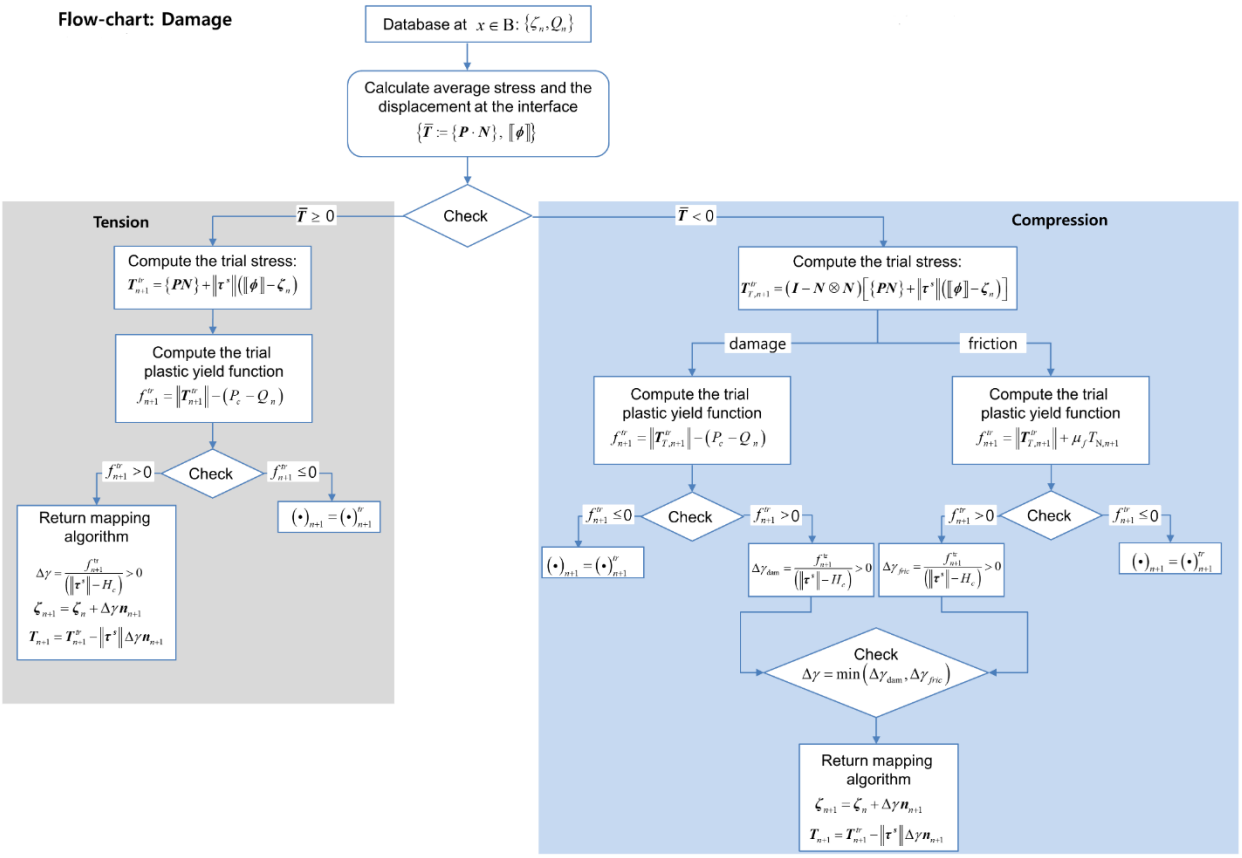

Figure 4.3. Flowchart of the interfacial constitutive models and the return mapping algorithms.

4.6 Consistent Linearization

Due to the nonlinear interface constitutive models, we need to solve the weak form (4-27) in an iterative fashion using the Newton-Raphson algorithm. The linearization of the bulk material terms

and the standard DG terms is given in Chapter 3 and Appendix B. In the following we primarily focus on the linearization of the term related to the interface damage part.

$$
\begin{aligned}
&K_{\text{damage}}\left(\boldsymbol{\eta}_o^{(\alpha)},\boldsymbol{\phi}^{(\alpha)},\boldsymbol{\zeta}\right)\\
&=-\int_{\Gamma_I}\left[\left\{\left(\text{GRAD}\,\boldsymbol{\eta}_o:\mathbf{A}\right)\cdot\boldsymbol{N}\right\}+\left[\!\left[\boldsymbol{\eta}_o\right]\!\right]\cdot\left\|\boldsymbol{\tau}_s\right\|\right]\cdot\left(\frac{\partial}{\partial u}\Delta\gamma\partial_{\boldsymbol{T}}f_{n+1}\cdot\Delta\boldsymbol{u}\right)\mathrm{d}A\\
&=-\int_{\Gamma_I}\tilde{\boldsymbol{T}}\left(\boldsymbol{\eta}_o\right)\cdot\left[\frac{\partial}{\partial\boldsymbol{T}}\left(\Delta\gamma\boldsymbol{n}\right)\cdot\tilde{\boldsymbol{T}}\left(\Delta\boldsymbol{u}\right)\right]dA
\end{aligned}
\tag{4-84}
$$

where $\tilde{\boldsymbol{T}}\left(\bullet\right)=\left[\left\{\left(\text{GRAD}\left(\bullet\right):\mathbf{A}\right)\cdot\boldsymbol{N}\right\}+\left[\!\left[\bullet\right]\!\right]\cdot\left\|\boldsymbol{\tau}_s\right\|\right]$ is the numerical interface flux. The discussion for the linearized tensor expression $\frac{\partial}{\partial\boldsymbol{T}}\left(\Delta\gamma\boldsymbol{n}\right)=\frac{\partial\Delta\gamma}{\partial\boldsymbol{T}}\otimes\boldsymbol{n}+\gamma\frac{\partial\boldsymbol{n}}{\partial\boldsymbol{T}}$, which depends on different interfacial constitutive models is presented in Appendix C.1. Along with the standard DG linearization terms presented in Chapter 3, the final tangent stiffness matrix is shown as follows:

$$
\begin{aligned}
&K\left(\boldsymbol{\eta}_o^{(\alpha)},\Delta\boldsymbol{u}^{(\alpha)};\boldsymbol{\phi}^{(\alpha)}\right)=\sum_{\alpha=1}^{2}\int_{\Omega^{(\alpha)}}\text{GRAD}\,\boldsymbol{\eta}_o^{(\alpha)}:\mathbf{A}^{(\alpha)}:\text{GRAD}\,\Delta\boldsymbol{u}^{(\alpha)}\,\mathrm{d}V\\
&+\int_{\Gamma_I}\left[\!\left[\boldsymbol{\eta}_o\right]\!\right]\cdot\boldsymbol{\tau}_s\cdot\left[\!\left[\Delta\boldsymbol{u}\right]\!\right]\mathrm{d}A+\int_{\Gamma_I}\left[\!\left[\boldsymbol{\eta}_o\right]\!\right]\cdot\left\{\left(\mathbf{A}:\text{GRAD}\,\Delta\boldsymbol{u}\right)\cdot\boldsymbol{N}\right\}\mathrm{d}A\\
&+\int_{\Gamma_I}\left\{\left(\text{GRAD}\,\boldsymbol{\eta}_o:\mathbf{A}\right)\cdot\boldsymbol{N}\right\}\cdot\left[\!\left[\Delta\boldsymbol{u}\right]\!\right]\mathrm{d}A\\
&+\int_{\Gamma_I}\left\{\left(\text{GRAD}\,\boldsymbol{\eta}_o:\boldsymbol{\Xi}:\text{GRAD}\,\Delta\boldsymbol{u}\right)\cdot\boldsymbol{N}\right\}\cdot\left(\left[\left(\left[\!\left[\boldsymbol{\phi}\right]\!\right]-\boldsymbol{\zeta}_n\right)-\Delta\gamma\boldsymbol{n}\right]\right)\mathrm{d}A\\
&-\int_{\Gamma_I}\tilde{\boldsymbol{T}}\left(\boldsymbol{\eta}_o\right)\cdot\left[\frac{\partial}{\partial\boldsymbol{T}}\left(\Delta\gamma\boldsymbol{n}\right)\cdot\tilde{\boldsymbol{T}}\left(\Delta\boldsymbol{u}\right)\right]dA
\end{aligned}
\tag{4-85}
$$

The first four terms on the right hand side of (4-85) constitute the linearized form of the standard interface DG method present in Chapter 3. The last two terms are related to the residual gap $\boldsymbol{\zeta}$. Comparing (4-85) with our previous work in [161], the structural form of the last term is similar. However, the key difference is that we use return mapping algorithm to calculate the incremental value of $\boldsymbol{\zeta}$ at integration points as given in Box 4.2 and 4.3.

Remark: *The tangent stiffness matrix (4-85) remains symmetric if the loading scenarios only induce tensile and/or compressive debondings. For compressive frictional case, it is not symmetric thereby necessitating an incrementally imposed normality* $\left(\partial f/\partial\boldsymbol{T}_T\right)$ *condition in the yield function* $f\left(\boldsymbol{T},Q\right)$.

4.7 Numerical Results

This section investigates the performance of the proposed interface method across a range of deformation modes. We have employed standard linear Lagrange polynomials and two and three-dimensional test problems are considered. All integral expressions over surfaces and volumes are evaluated using quadrature rules of sufficiently high order. A common neo-Hookean material model is employed, and the strain energy density function is given as follows:

$$W\left(\boldsymbol{F}\right)=\frac{1}{2}\mu\left(\mathrm{tr}\left(\boldsymbol{F}^{T}\boldsymbol{F}\right)-3\right)-\mu\ln J+\frac{1}{2}\lambda\left(J-1\right)^{2} \tag{4-86}$$

We first present results for test cases wherein continuity is weakly enforced at specific bi-material interfaces with the gap ζ and this corresponds to the formulation derived in sections 4.2 and 4.3. The treatment of the evolution for ζ is discussed in sections 4.4 and 4.5.

***Remark**: In the numerical tests presented below, we indicate the interfaces across which the weakly imposed continuity conditions are imposed. For discussion on the algorithmic treatment of generating interfaces within finite element meshes, reader is referred to [158].*

4.7.1 Patch Test

4.7.1.1 Interfacial debonding under tension

We begin with a simple patch test to verify variational consistency of the interface damage formulation. Two blocks of 1 mm^3 modeled via one brick element each are separated by an interface along which the proposed stabilized interface method is employed, as shown in Figure 4.4. The material properties used in the neo-Hookean model (4-86) are $E=5$ GPa and $\nu=0.25$. Prescribed tip displacement $\delta=0.4\,\mathrm{mm}$ is applied at all the nodes at the right surface of the domain. Boundary conditions applied on to the left face create a state of uniform tensile stress throughout the domain. Symmetric roller boundary condition is applied on the top surface to prevent rigid body motion. For the evolution of damage, we set the critical stress $P_{\mathrm{c}}=100\,\mathrm{MPa}$ and critical inelastic gap $\zeta_c=0.2\,\mathrm{mm}$.

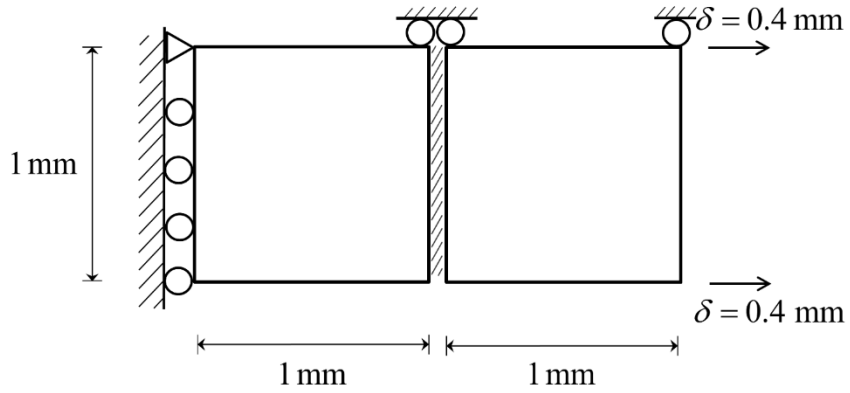

Figure 4.4. Description of the patch test problem.

The relation between the tension at the right surface and the opening at the interface is shown in Figure 4.5, which matches exactly the behavior shown in Figure 4.2 for the softening response. As the magnitude of the applied displacement at the right end is increased, the induced traction increases up to the critical stress $P_c = 100\,\text{MPa}$ and at that point the interfacial debonding gets activated, giving rise to a softening response under progressive debonding.

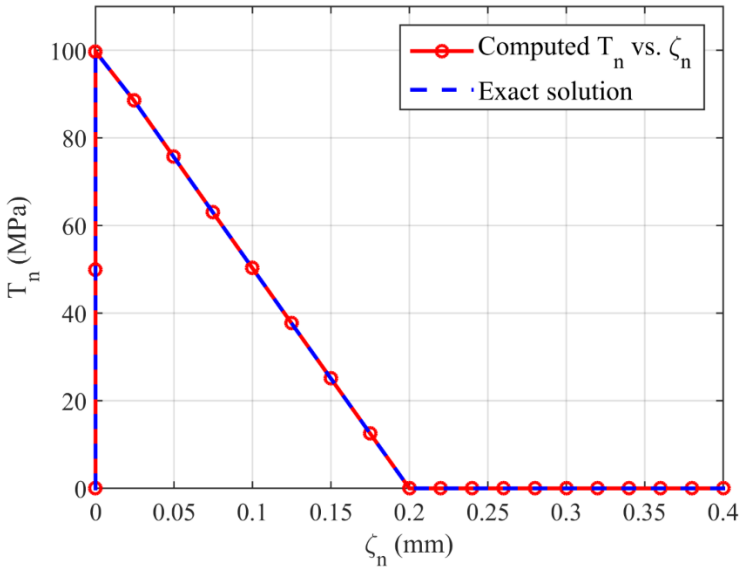

Figure 4.5. Traction-gap relation between induced traction T_n and the residual gap ζ_n.

Figure 4.6 represents contour plots of the axial stress for various load levels that is overlaid on the corresponding deformed configurations. Because of isotropic material properties and due to the applied BCs that produce uniform axial deformation, the axial stress field is constant over the

domain. In Figure 4.6 (a), the stress in the elements has not yet reached the critical stress, thus the two blocks are perfectly bonded together. In Figure 4.6 (b), the displacement gap at the interface is significant enough to be noticed for this large deformation test, and the traction is smaller as compared to that in Figure 4.6 (a) due to the damage softening effects. Once the gap between these two blocks exceeds the critical inelastic gap ζ_c, which is shown in Figure 4.6 (c), the two blocks are independent and no longer interact with each other. At this stage the two blocks are completely unloaded and there is no traction between them.

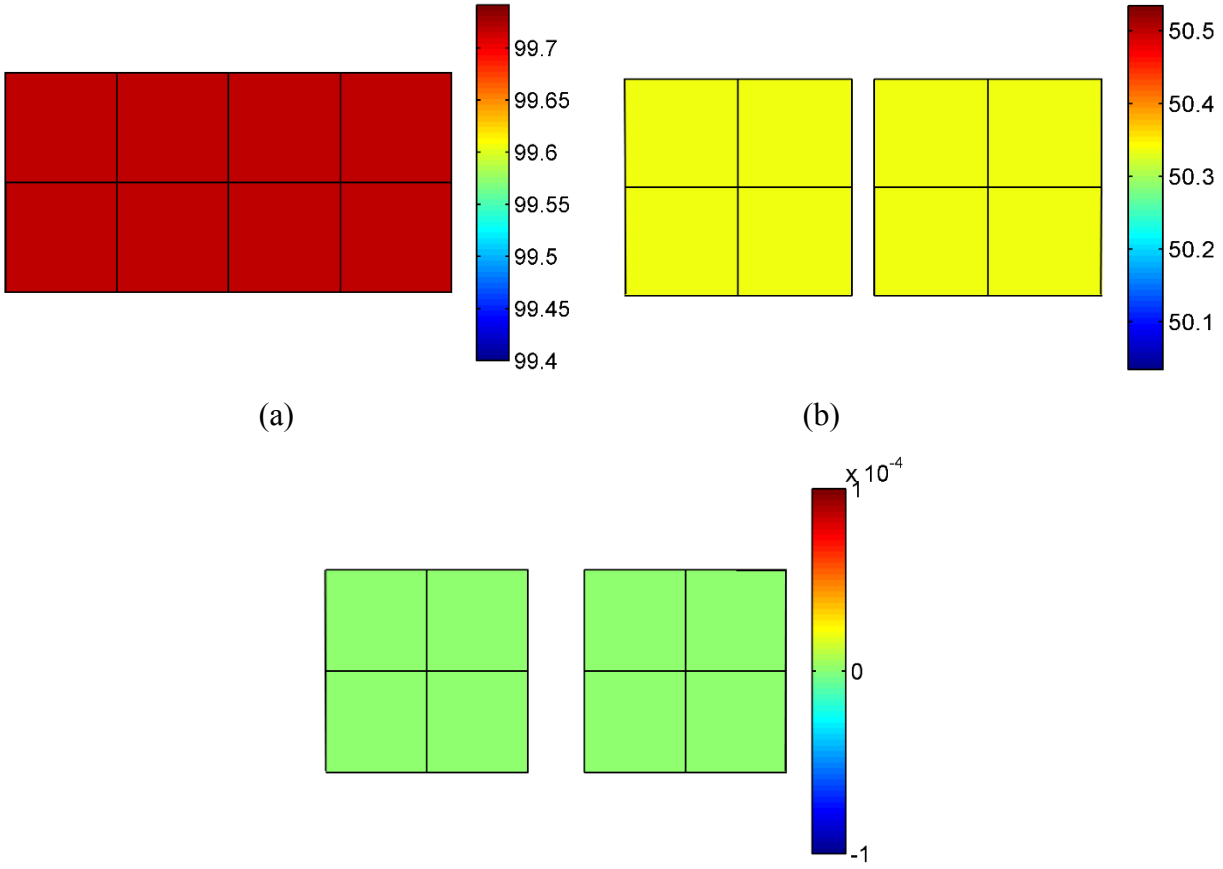

Figure 4.6. Contour plots of the traction T_n at three different steps: (a) $\zeta = 0\,\text{mm}$;(b) $\zeta = 0.0998\,\text{mm}$; (c) $\zeta = 0.26\,\text{mm}$.

Table 4.1 presents the Euclidean norm of the out-of-balance force vector computed at each iteration during the Newton-Raphson solution procedure in step 6 when $\zeta = 0.0747\,\text{mm}$. The observed quadratic rate of convergence numerically confirms consistent linearization and the derivation of the consistent tangent presented in section 4.6.

Table 4.1. Evolution of residual l^2 norm for the patch test.

Iteration Number	Residual Norm
1	2.8833671×10^{1}
2	2.9488081×10^{-1}
3	2.5465645×10^{-5}
4	7.6179649×10^{-13}

For the same tensile problem with the same material properties, we also tested by using nonconforming meshes shown in Figure 4.11. At the interface between two blocks, there is no node on node contact.

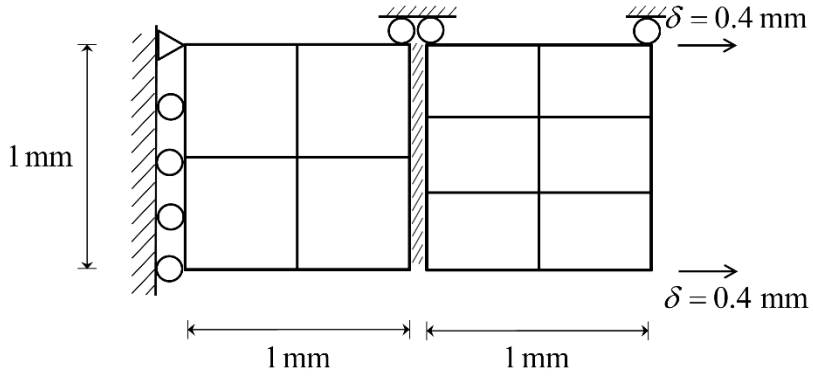

Figure 4.7. Description of the nonconforming mesh.

The contour plot of axial stress σ_{11} for three different load steps are given in Figure 4.8 with the line plot of the interface traction T_n versus the normal gap ζ_n plot in Figure 4.9. As compared with Figure 4.6 and Figure 4.5, the results generated with nonconforming mesh match exactly well with the conforming mesh.

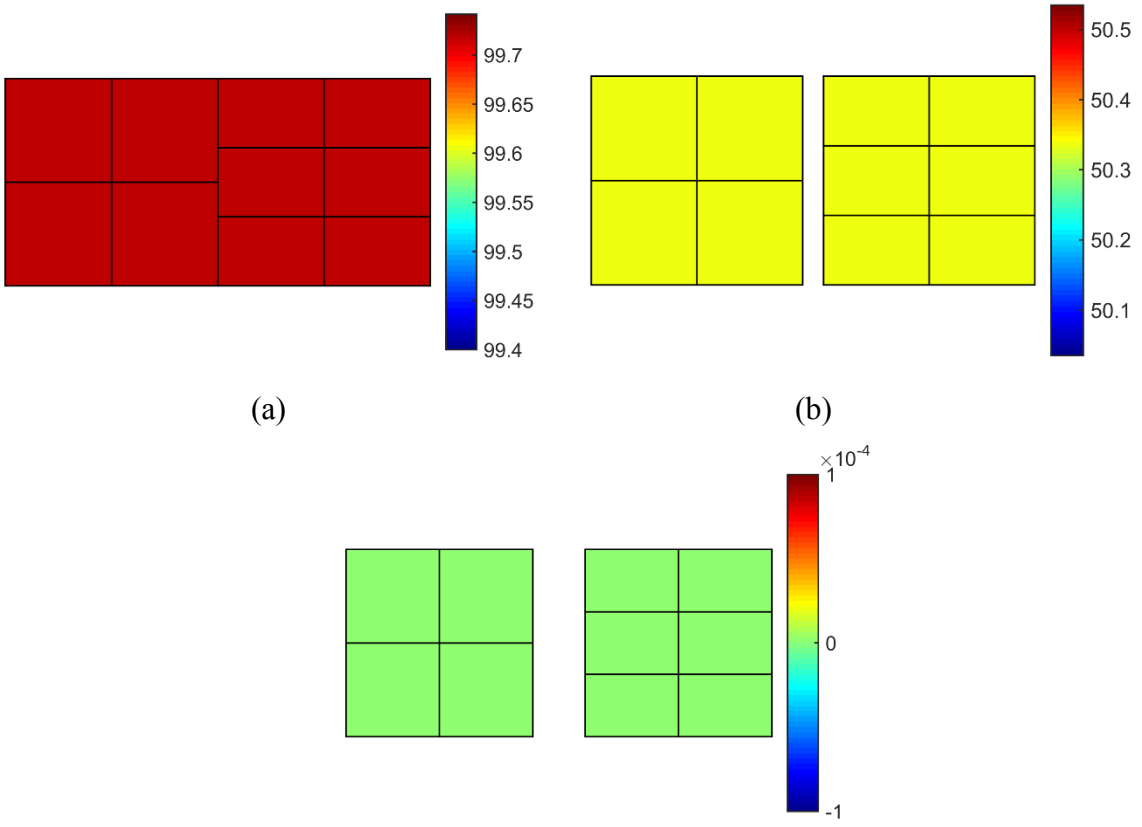

Figure 4.8. Contour plots of the traction T_n at three different steps (Nonconforming mesh): (a) $\zeta = 0\,\text{mm}$;(b) $\zeta = 0.0998\,\text{mm}$; (c) $\zeta = 0.26\,\text{mm}$.

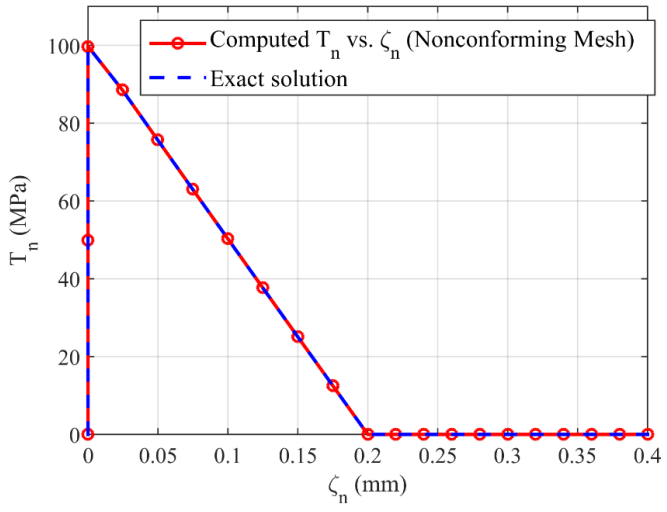

Figure 4.9. Traction-gap relation between induced traction T_n and the residual gap ζ_n (Nonconforming mesh).

In Figure 4.10, the norm of the stability tensor $\boldsymbol{\tau}_s$ is plotted across the interfaces for this nonconforming mesh test problem. As shown in Figure 4.10 (b), The norm of the stability tensor is different for different interface element size, which indicates the impact of the geometry on the stability tensor, namely, the area-weighting.

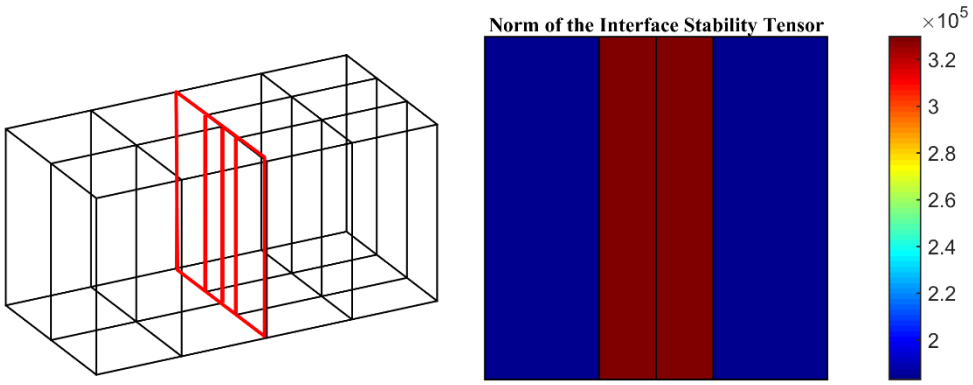

(a) (b)

Figure 4.10. (a) Location of the interfaces with nonconforming meshes; (b) Norm of the stability tensor $\|\boldsymbol{\tau}_s\|$ plot at interfaces.

4.7.1.2 Debonding under compressive shear

The second patch test is comprised of two blocks with an inclined interface as shown in Figure 4.11. The material properties are same as in the previous section, with the prescribed displacement $\delta = -0.2$ mm applied at all the nodes at the right surface to induce a compression load on the right block.

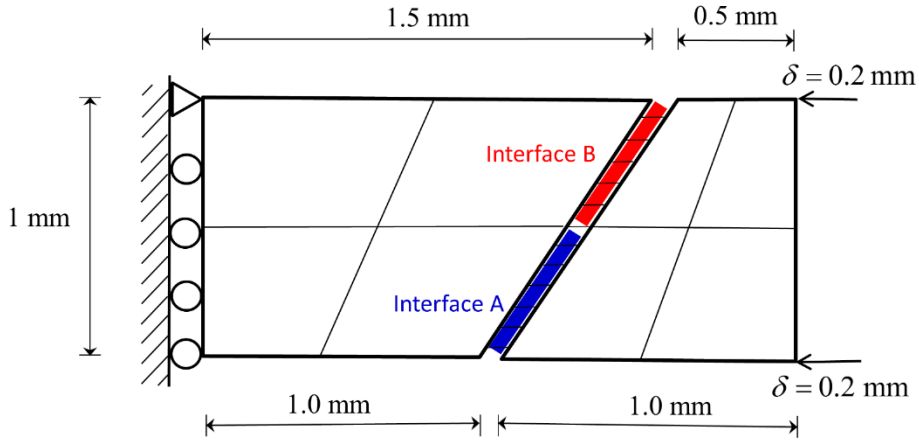

Figure 4.11. Geometry for patch test with inclined interface.

Figure 4.12 shows the axial stress contour plots for three load steps. At the inclined interface, the tangential component of traction increases up to the critical value due to the applied compressive displacement as shown in Figure 4.12 (a) and thereafter triggers the compression damage process which leads to the sliding of the right block as shown in Figure 4.12 (b). At the final step, the right block slides down after the tangential shear overcomes the frictional resistance and the stress reduces to zero as shown in Figure 4.12 (c).

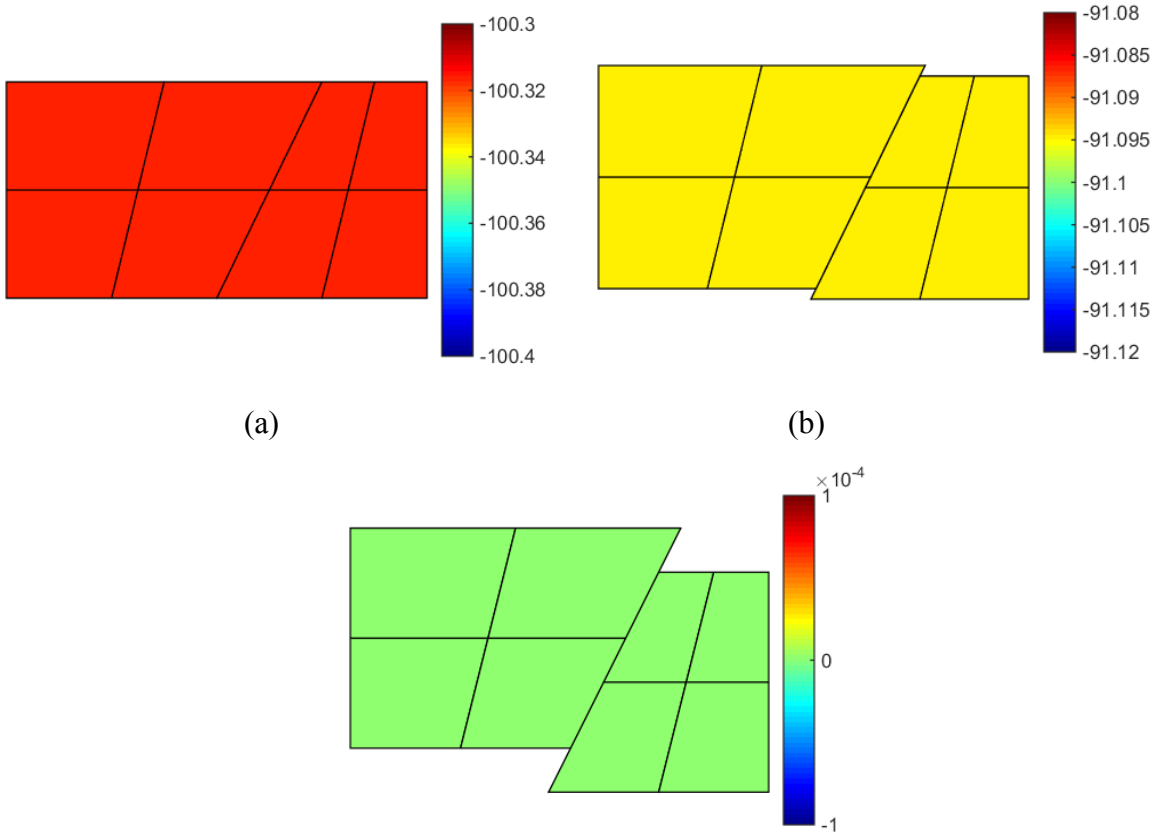

Figure 4.12. Contour plot of the axial stress σ_{11} at three different steps: (a) $d = -0.08\text{mm}$; (b) $d = -0.12\text{mm}$; (c) $\delta = -0.2\ \text{mm}$.

Table 4.2. Stability parameter $\|\boldsymbol{\tau}_s\|$ for different load steps.

Load step	Interface A	Interface B
1	1.3182×10^5	1.2769×10^5
2	1.3207×10^5	1.2801×10^5
3	1.3234×10^5	1.2836×10^5
4	1.3229×10^5	1.2829×10^5
5	1.3182×10^5	1.2769×10^5

Table 4.2 shows the evolution of the stability parameter $\|\boldsymbol{\tau}_s\|$ for different load steps. The stability value drops for both interfaces at last step because of switching from compression damage branch to the friction branch. Since the derived $\boldsymbol{\tau}_s$ embeds the concepts of area averaging and stress averaging, due to the difference in the element size, the computed values show slight variability that is however within 1%, thus validating the consistent derivation of this stability parameter as a function of the evolving geometric and material nonlinearity.

4.7.2 Fiber matrix debonding under transverse loading

This test case is for fiber-matrix debonding under transverse axial loading. The bulk material parameters for the fiber and matrix are: $E_f = 40\text{GPa}, \nu_f = 0.4$ and $E_m = 10\text{GPa}, \nu_m = 0.33$, respectively. As shown in [82], due to the damage at the interface, there is stress concentration in the matrix near the interface. Therefore, we assume that debonding, once initiated at the fiber-matrix interface, can trigger failure inside the matrix as well. Conversely, material failure via fracture can also get initiated in the matrix which can then trigger bimaterial debonding. Since the fiber is invariably much stronger than the matrix material, it is assumed that fiber remains intact during damage evolution. In addition, crack in the matrix is assumed to propagate along the element edges, and in the current implementation, crack propagation through the elements is not considered [119].

The interface properties for debonding are as follows: critical stress $P_{\text{c}}^{\text{f}} = 10\,\text{MPa}$ for fiber-matrix interfaces, and $P_{\text{c}}^{\text{m}} = 30\,\text{MPa}$ for inter-element debonding within the matrix. The critical inelastic gap $\zeta_c = 0.2\,\text{mm}$. Boundary conditions are shown in Figure 4.13 (a); plane strain conditions are

applied for the z direction. We apply a displacement increment $\bar{u} = 10^{-4}$ mm at both left and right surfaces at each step. The cross section of the unstructured mesh that is comprised of brick elements is shown in Figure 4.13 (b),

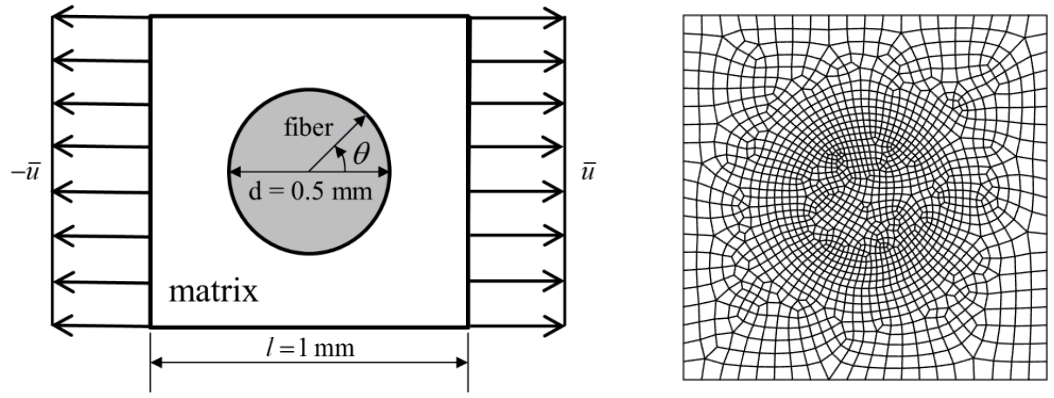

(a) (b)

Figure 4.13. Fiber-matrix debonding problem: a) Problem description; b) Hexahedral element mesh.

Figure 4.14 shows stress versus strain plot in the direction of the applied loading. The stress is obtained by summing up stresses from all the elements within edges coincident with the left and right surfaces. Since only small deformations are induced, engineering strain is chosen for expressing the results, which is evaluated as the displacement divided by the original length. One can see the four critical stages as a function of the evolution of interfacial debonding and matrix cracking. The contour plots corresponding to these four stages are shown in Figure 4.15 where displacement field is magnified twenty times to clearly show the process of debonding. The fracture process starts from a state of perfectly bonded fiber and matrix interface and debonding initiates when interfacial stress reaches the critical stress level as shown in Figure 4.15. Then through stage 2 to stage 3, the cracks start to kink into the matrix and grow orthogonal to the direction of principal stress until they reach the edges as shown in Figure 4.15 (b) and Figure 4.15 (c). Finally, multiple cracks initiate inside the matrix that triggers failure of the material as illustrated in Figure 4.15 (d). The overall behavior is consistent with the response reported in [119].

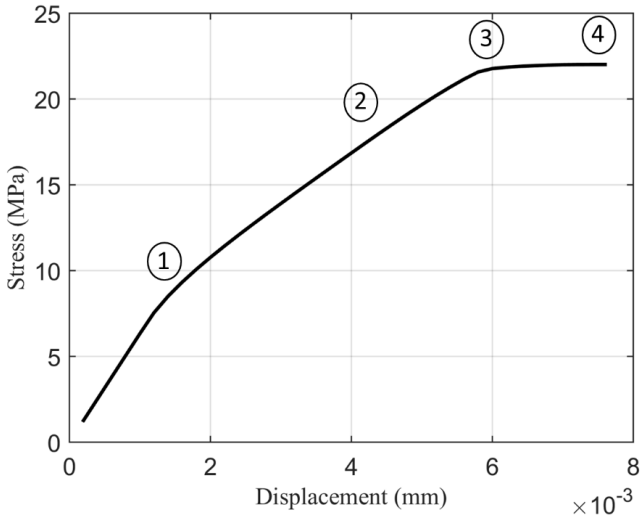

Figure 4.14. Force-displacement curve for the various stages of the material interface evolution.

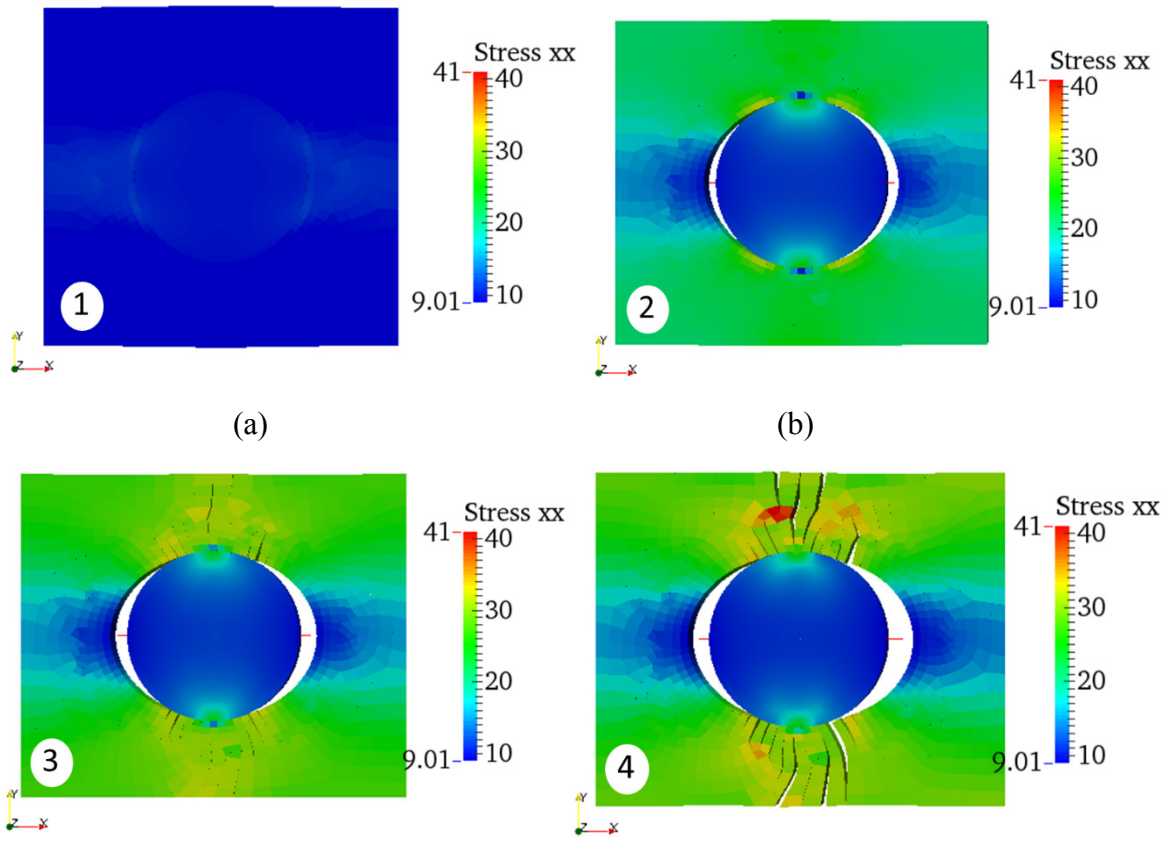

(a) (b)

(c) (d)

Figure 4.15. Contour plots of the stress σ_{xx} at four different stages: (a) Initiation of fiber-matrix interfacial debonding; (b) Crack kinking into the matrix; (c) Crack propagation orthogonal to the principal stresses; (d) Multiple cracking and material failure.

Figure 4.16 shows the plot of the normal component of the displacement gap at interface between the fiber and the matrix. The angle θ is measured as shown in Figure 4.13 (a). A comparison of stress versus applied displacement plot with results presented in Nguyen [119] is shown in Figure 4.17, and a good comparison during the four steps of the evolution of the problem is attained.

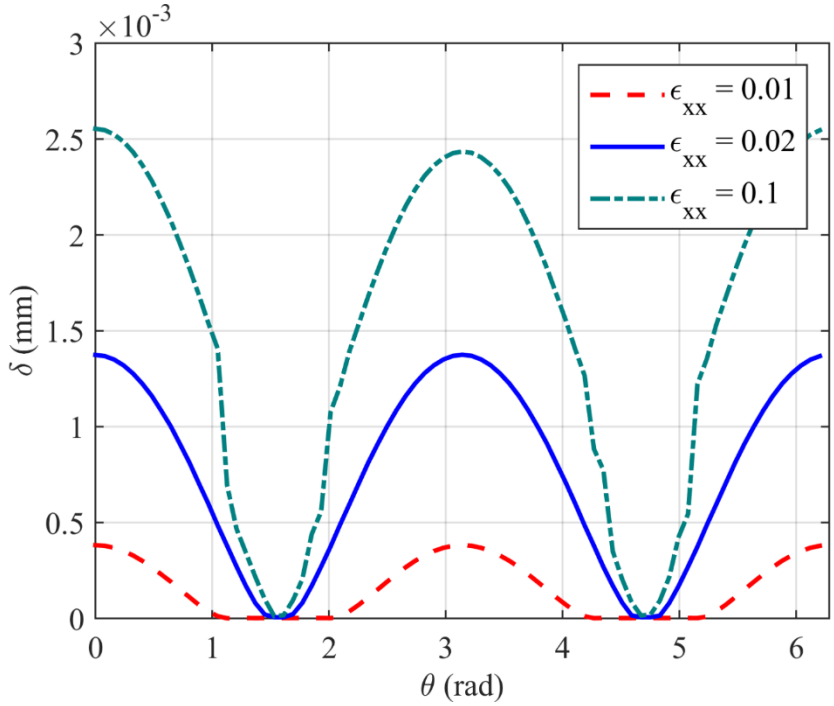

Figure 4.16. Normal gap between fiber and matrix around the interface.

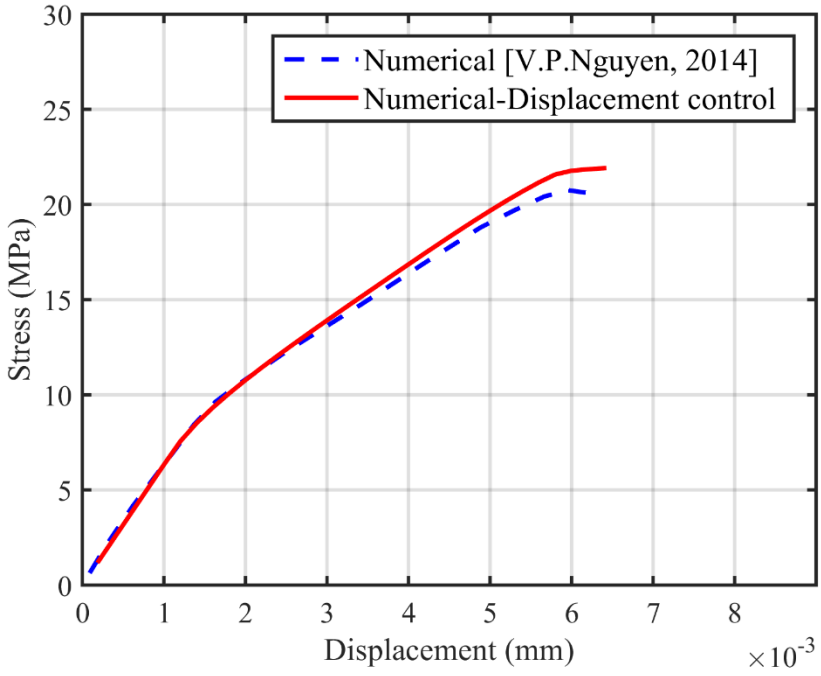

Figure 4.17. Stress vs. applied displacement plot.

4.7.3 Tearing of bimaterial interfaces

This test case presents tearing of bimaterial interface between a soft and hard material. This problem is inspired by the stretching of a cracked plate in finite elasticity [149, 101], and due to large difference in mechanical material properties it serves as a model problem for tearing of tendons from the bone under excessive mechanical stresses. In this test case, the two plates have an existing partial crack along the interface. Spatial dimensions and boundary conditions are shown in Figure 4.18. The bottom plate that is comprised of the softer material has same dimensions as in [101] and the proposed interface formulation is employed along the bimaterial interface between the hard and soft material. A given displacement field is applied at the bottom surface of the lower plate that produces 100% strains as shown in Figure 4.18.

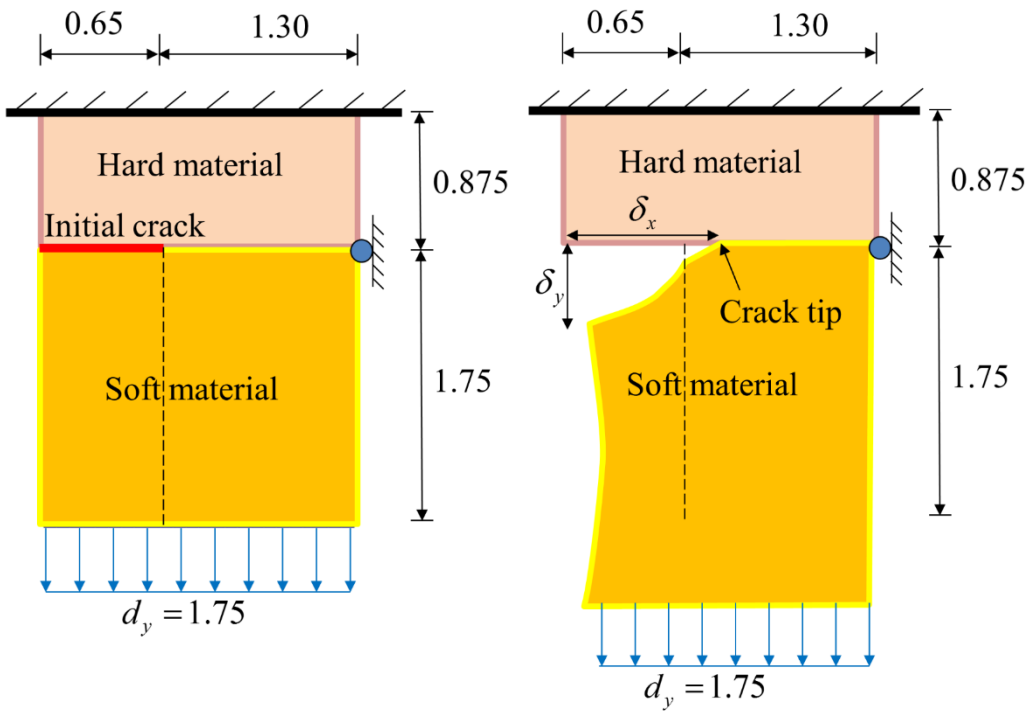

(a) (b)

Figure 4.18. Tearing along soft and hard material interface: (a) original state; (b) deformed state.

We have employed two different material types to study the effects of the material on interfacial debonding evolution: (a) the standard Neo-Hookean material as in (4-86) for both the plates, and (b) Ogden-type material in (4-87)-(4-88) for the bottom plate. In the latter case the top plate is still modeled with the Neo-Hookean material.

The material properties are listed in Table 4.3. Young's modulus for the top plate is four times larger than that for the bottom plate to simulate the stiff and soft material response. We have employed three meshes with successive refinements to test the robustness of the method. For the coarse discretization, mesh size is 24×20 for the bottom plate, while for the top plate the mesh discretization is 24×10. For the medium mesh, discretization size is 48×40 for the bottom plate and 48×20 for the top plate. For the fine mesh, discretization is 96×80 for the bottom plate and 96×40 for the top plate. We want to point out that the objective in this problem is to test the stability of the numerical method for coarse meshes, and we note that this solution may not accurately resolve the crack tip stresses and the crack velocity.

Table 4.3. Coefficients for the two materials.

Neo-Hookean Material			
Top plate	Properties	Bottom plate	Properties
$E_m\,(\mathrm{N/mm^2})$	16000	$E_f\,(\mathrm{N/mm^2})$	4000
ν_m	0.44	ν_f	0.44
Damage properties	$\mathrm{P}_c\,(\mathrm{MPa})$	$\zeta_c\,(\mathrm{mm})$	
	200	0.2	
Ogden-type Material	Bottom plate		
c_α / m_α	6.3	0.012	–0.010
m_α	1.3	5.0	–2.0
Damage properties	$\mathrm{P}_c\,(\mathrm{MPa})$	$\zeta_c\,(\mathrm{mm})$	
	20	0.2	

In Figure 4.19 and Figure 4.20, we plot the contours of σ_{yy} at different steps during the evolution of the problem for different mesh refinements. These figures exhibit the process of tearing of the soft material from the hard material, where the problem is run with an applied displacement at the bottom. The pattern of the tearing process for coarse and fine mesh is almost identical, which numerically verifies the robustness of the proposed method. For plotting purpose, the range of stress is kept the same in order to obtain an objective comparison between the various frames. Figure 4.19 (a) shows initiation of the tearing process at around 4% applied strain. Figure 4.19 (b) shows stress concentration at the crack tip at 10% strain. The process of tearing along bimaterial interface evolves with an increase in applied strain and finally the two plates are almost separated as shown in Figure 4.19 (d). We can also see that there is a jump in the value of stress across the interface, while the stress is continuous within each of the two subdomains.

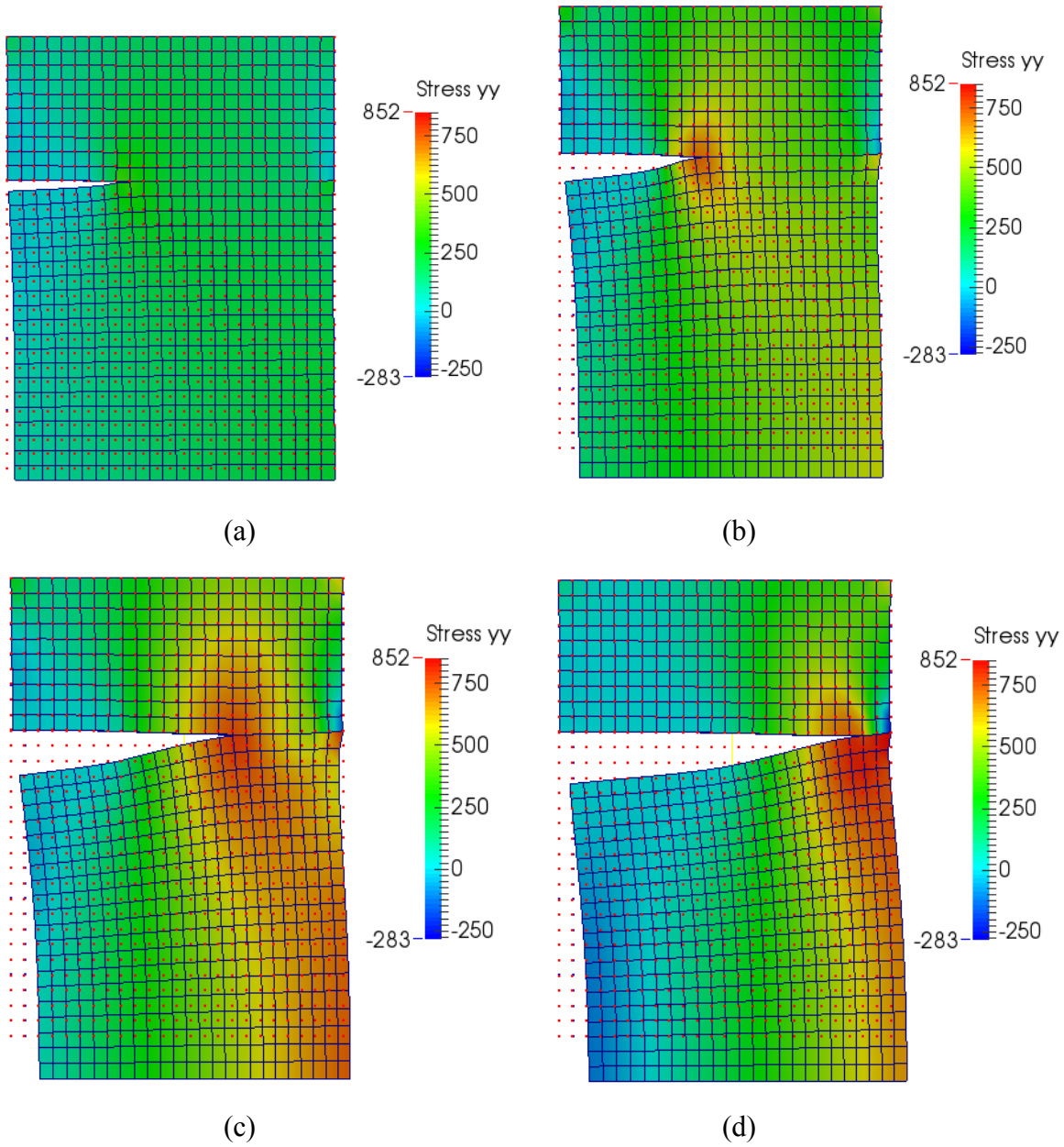

Figure 4.19. σ_{yy} contour plots for different load steps in the tearing of bimaterial interface (Neo-Hookean material; Coarse mesh): (a) $\varepsilon = 4\%$; (b) $\varepsilon = 10\%$; (c) $\varepsilon = 14\%$; (d) $\varepsilon = 14.8\%$ (last step).

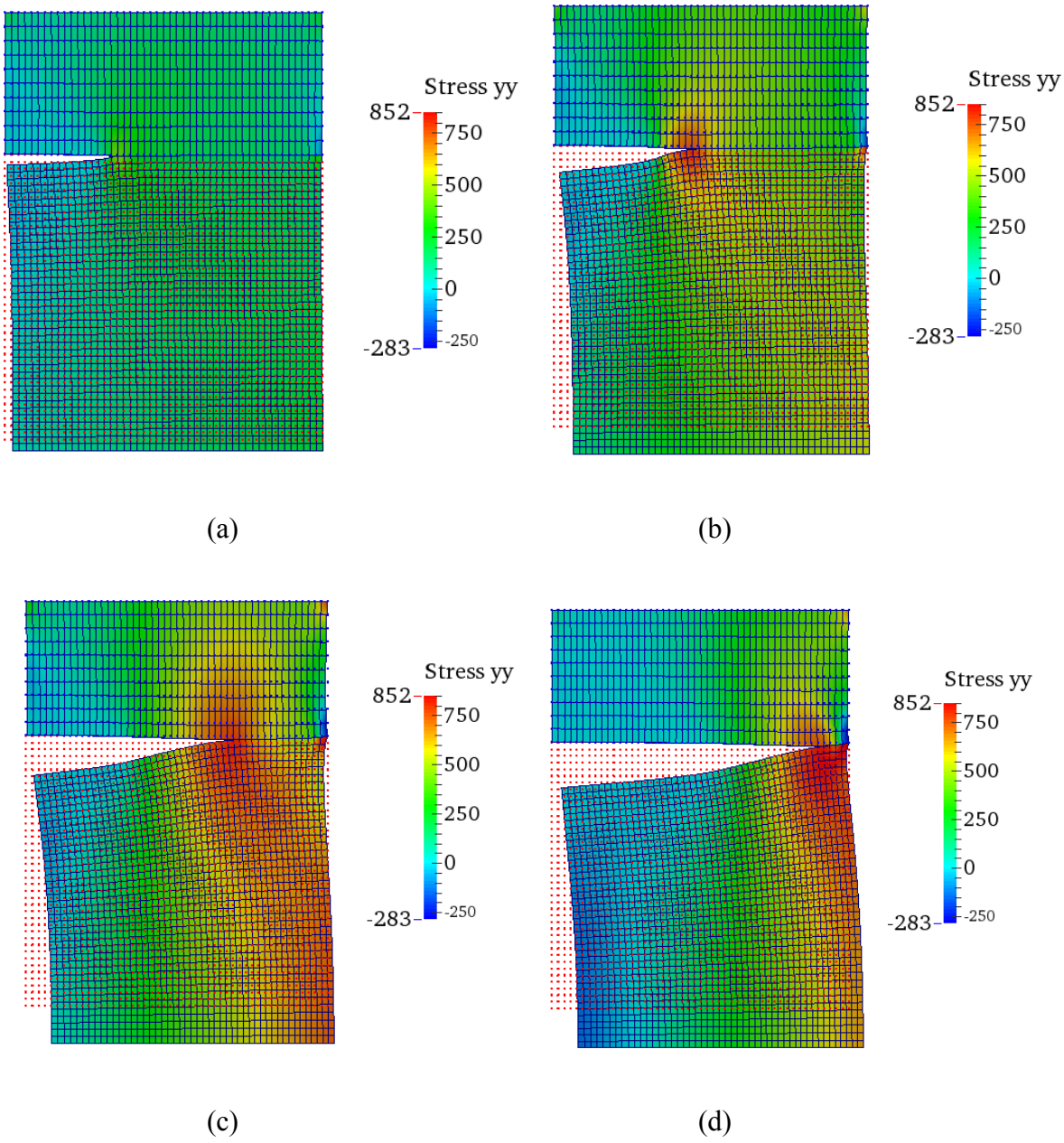

Figure 4.20. σ_{yy} contour plots for different load steps in the tearing of bimaterial interface (Neo-Hookean material; Medium mesh): (a) $\varepsilon = 4\%$; (b) $\varepsilon = 10\%$; (c) $\varepsilon = 14\%$; (d) $\varepsilon = 14.8\%$ (last step).

The plot of the gap/opening at the bimaterial interface for various load steps is given in Figure 4.21 with three different mesh refinement levels. With reference to the increasing distance of the crack tip from the left end, the opening gradually increases due to the stretch applied at the bottom. The computed results from the coarse and the fine mesh match which is a numerical manifestation

of the robustness of the method for relatively cruder discretizations.

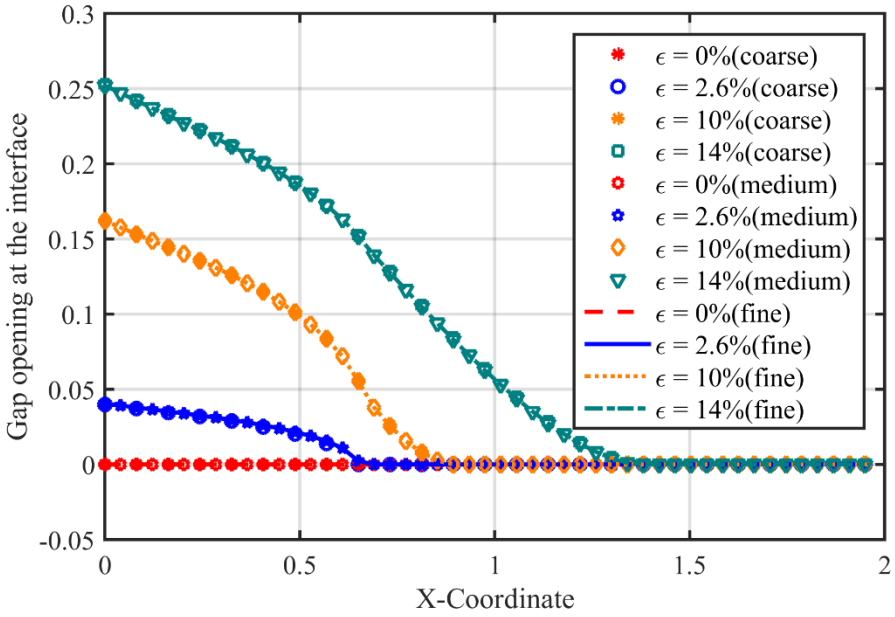

Figure 4.21. Gap/opening evolution plots for different load steps in the tearing of bimaterial interface (Neo-Hookean material; coarse, medium and fine mesh): (a) $\varepsilon = 0\%$; (b) $\varepsilon = 2.6\%$; (c) $\varepsilon = 10\%$; (d) $\varepsilon = 14\%$.

In Figure 4.22, we plot the normal component of interfacial stress and the vertical gap measured at the location point of the original crack tip. The stress plot follows the traction gap relation which is shown in Figure 4.2.

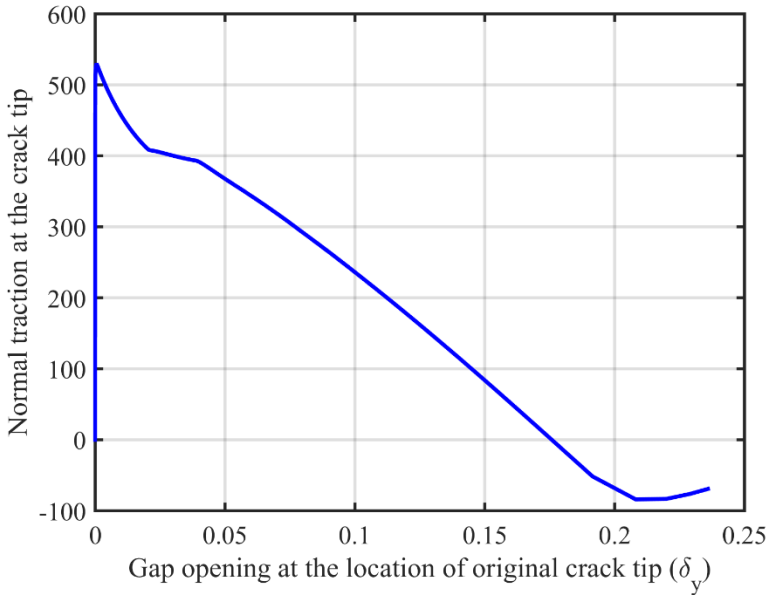

Figure 4.22. Normal traction at the interface vs. δ_y plot.

Figure 4.23 shows the spatial distribution of the fine scales along the interface during the loading process. The absolute value of the fine scales is not significant, while around the separation zone the magnitude of the fine scales is relatively high which indicates that the contribution from the fine scale model is higher in this zone. As presented in [100], these post computed fine scales also serve as a measure of local error in the solution, and the magnitude of the fine-scale error is a measure of the accuracy of the solution at the interface.

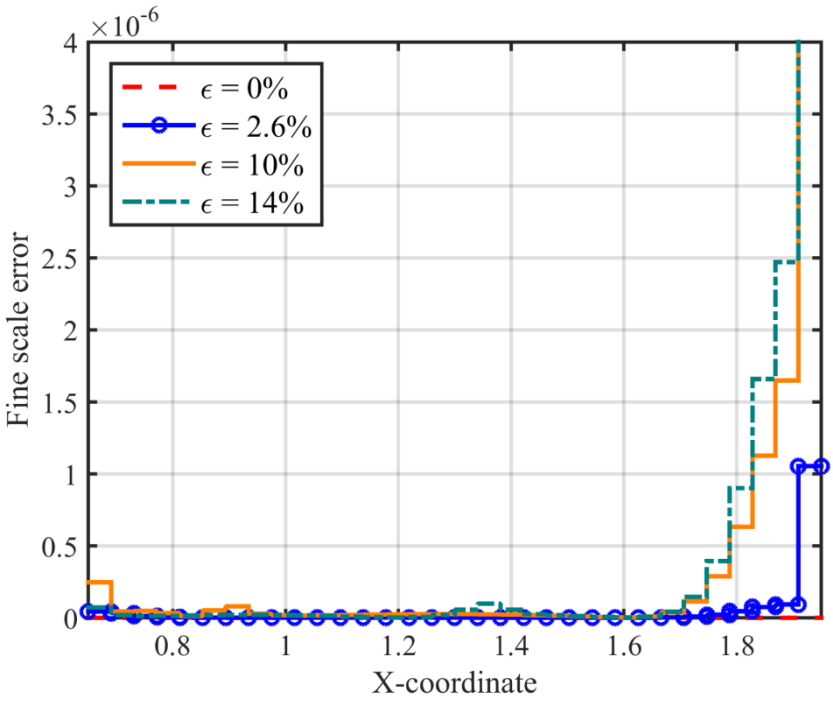

Figure 4.23. Fine scale error along the interface plot.

For this problem, nonconforming meshes without node on node contact are also considered. The mesh is generated as shown in Figure 4.24, which a very coarse mesh for the hard material on the top, and a finer mesh for the soft material on the bottom. At the material interfaces, on every three elements on the bottom and every two elements on the top, there is a node matching.

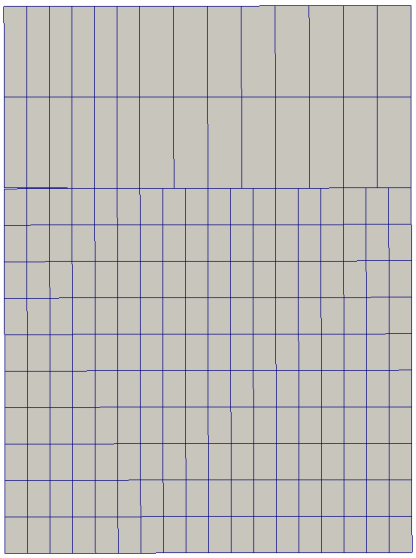

Figure 4.24. Spatial mesh generation of the nonconforming mesh.

The σ_{yy} stress contour plots for different load steps are plotted in Figure 4.25. When compared with the results for conforming mesh plots in Figure 4.19 and Figure 4.20, the nonconforming mesh captures the physics very well. The line plot of the opening of the top and bottom surface across the interfaces are given in Figure 4.26 which shows the comparison of the nonconforming meshes with three different mesh refinements and conforming. Thus, unlike the CZM method where the mesh needs to be uniform and conform at the interface [174], the proposed method is capable of capturing material mismatch and mesh mismatch.

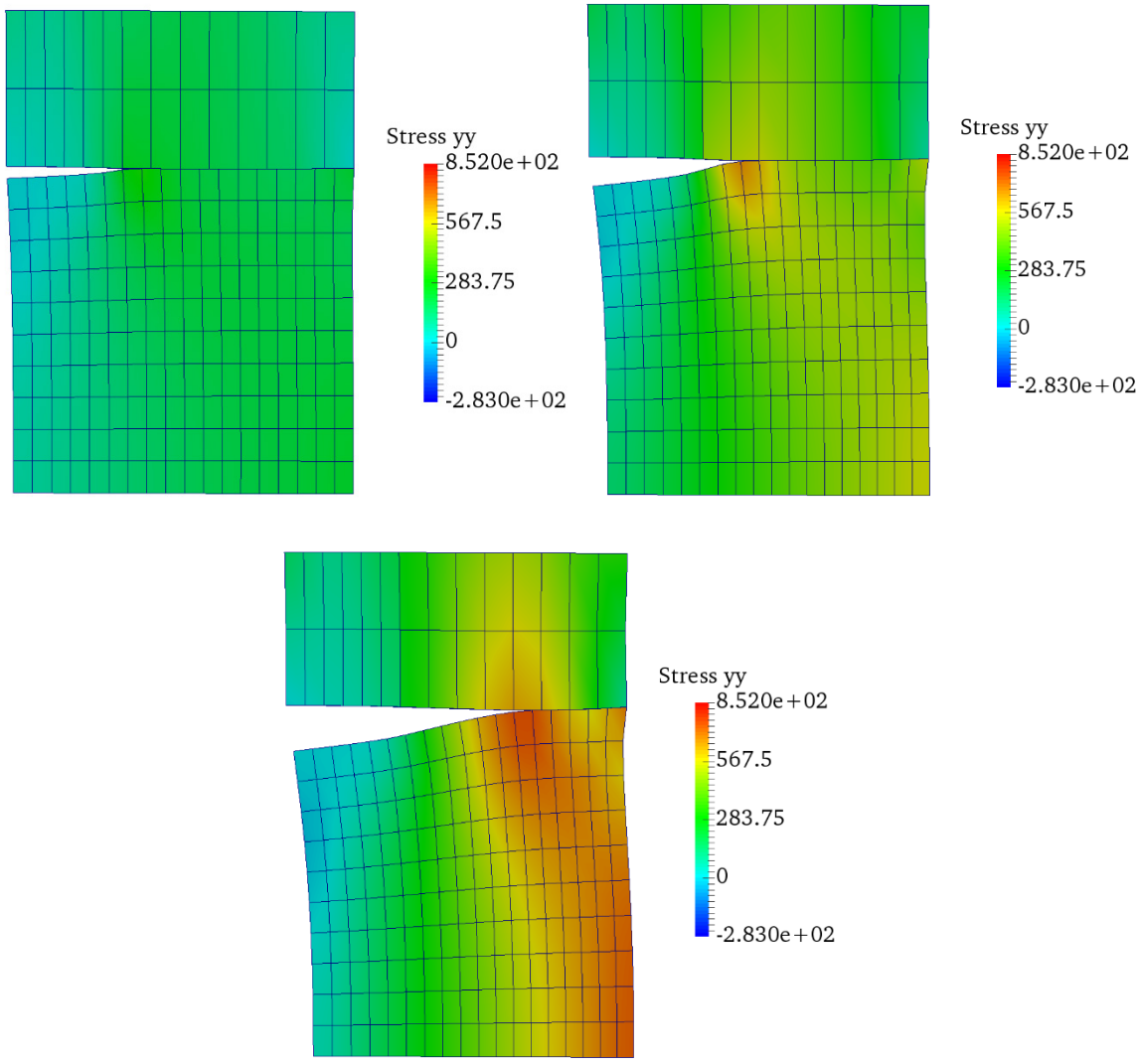

Figure 4.25. σ_{yy} contour plots for different load steps in the tearing of bimaterial interface (Neo-Hookean material: Nonconforming mesh): (a) $\varepsilon = 4\%$; (b) $\varepsilon = 10\%$; (c) $\varepsilon = 14\%$.

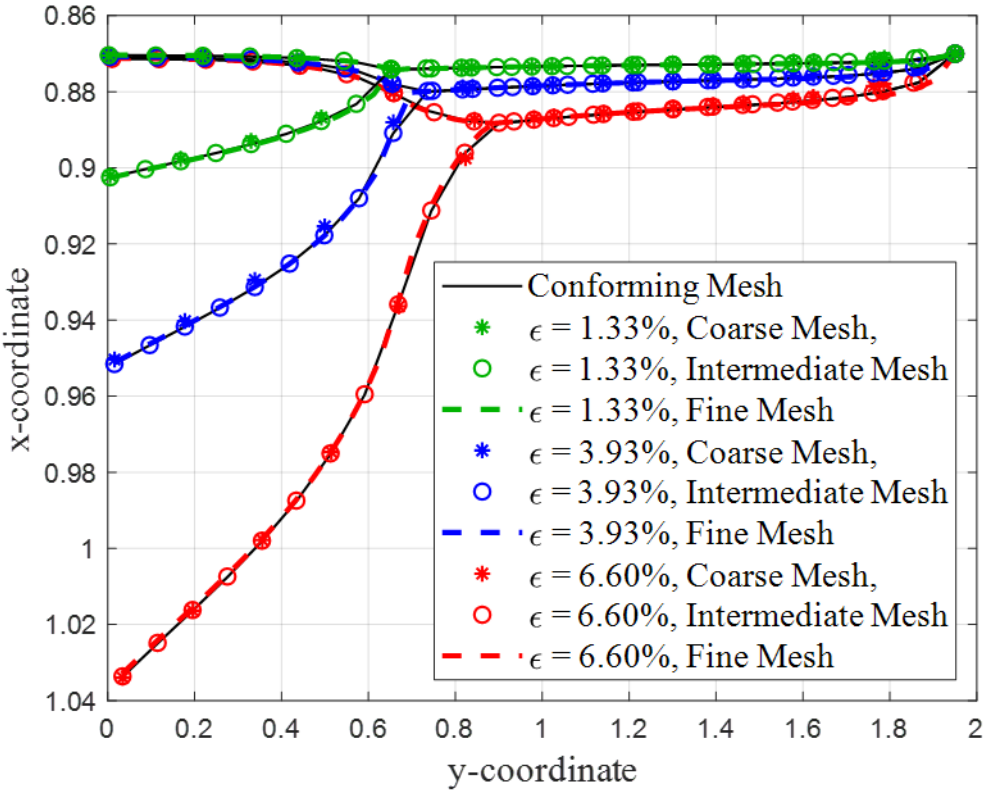

Figure 4.26. Comparison of the opening on the interface (Nonconforming mesh).

We repeat the problem where, instead of using the standard Neo-Hookean material for both stiff and soft plates, for the lower plate we use a three-term Ogden-type material that matches the material response of rubber type material [101]. The strain energy function for the Ogden-type material is:

$$W(C)=\sum_{\alpha=1}^{3}\left[\frac{c_\alpha}{m_\alpha^2}\left(\tilde{\lambda}_1^{m_\alpha}+\tilde{\lambda}_2^{m_\alpha}+\tilde{\lambda}_3^{m_\alpha}-3\right)\right]+\kappa U(J) \tag{4-87}$$

$$U(J)=\frac{1}{2}\left[\frac{1}{2}\left(J^2-1\right)-\ln J\right] \tag{4-88}$$

where $\tilde{\lambda}_\alpha$ is the deviatoric principal stretch. The material constants c_α and m_α, and elastic modulus and Poisson ratio which are used to compute the Bulk modulus κ are given in Table 4.3.

The contour plots for stress evolution and the corresponding process of tearing of bimaterial interface are shown in Figure 4.27 and Figure 4.28. It can be seen that as compared to the behavior of the standard Neo-Hookean material given in Figure 4.19, Ogden type material is easily

stretchable that results in crack blunting and therefore prevents the crack from propagating as shown in Figure 4.27. Stress concentration at the crack tip and discontinuous stress field around the interface are shown in Figure 4.27, and these can be contrasted with the neo-Hookean material present in Figure 4.19.

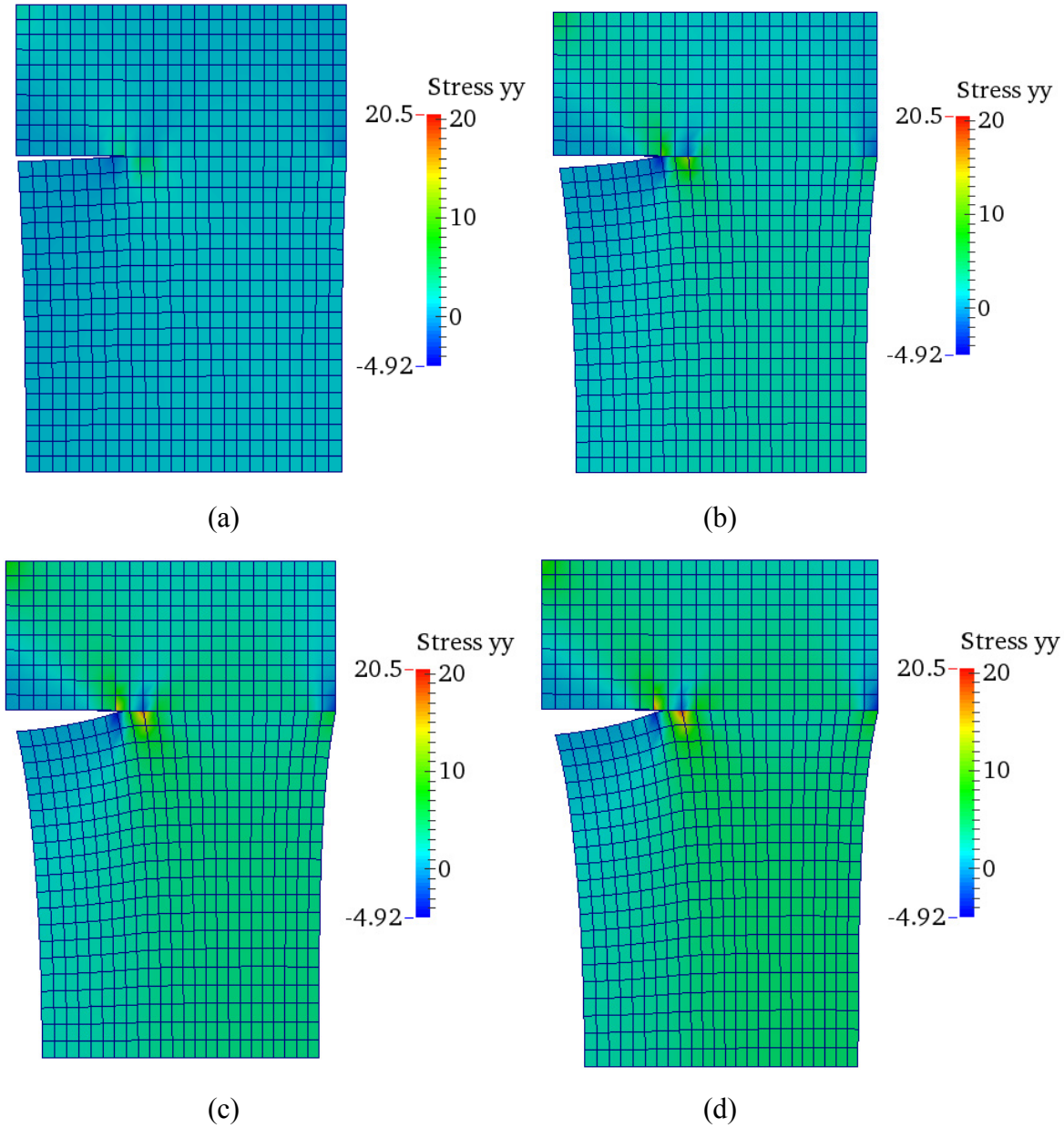

Figure 4.27. σ_{yy} contour plots for tearing of bimaterial interface for Ogden-type material (Coarse mesh): (a) $\varepsilon = 4\%$; (b) $\varepsilon = 10\%$; (c) $\varepsilon = 16\%$; (d) $\varepsilon = 19\%$ (last step).

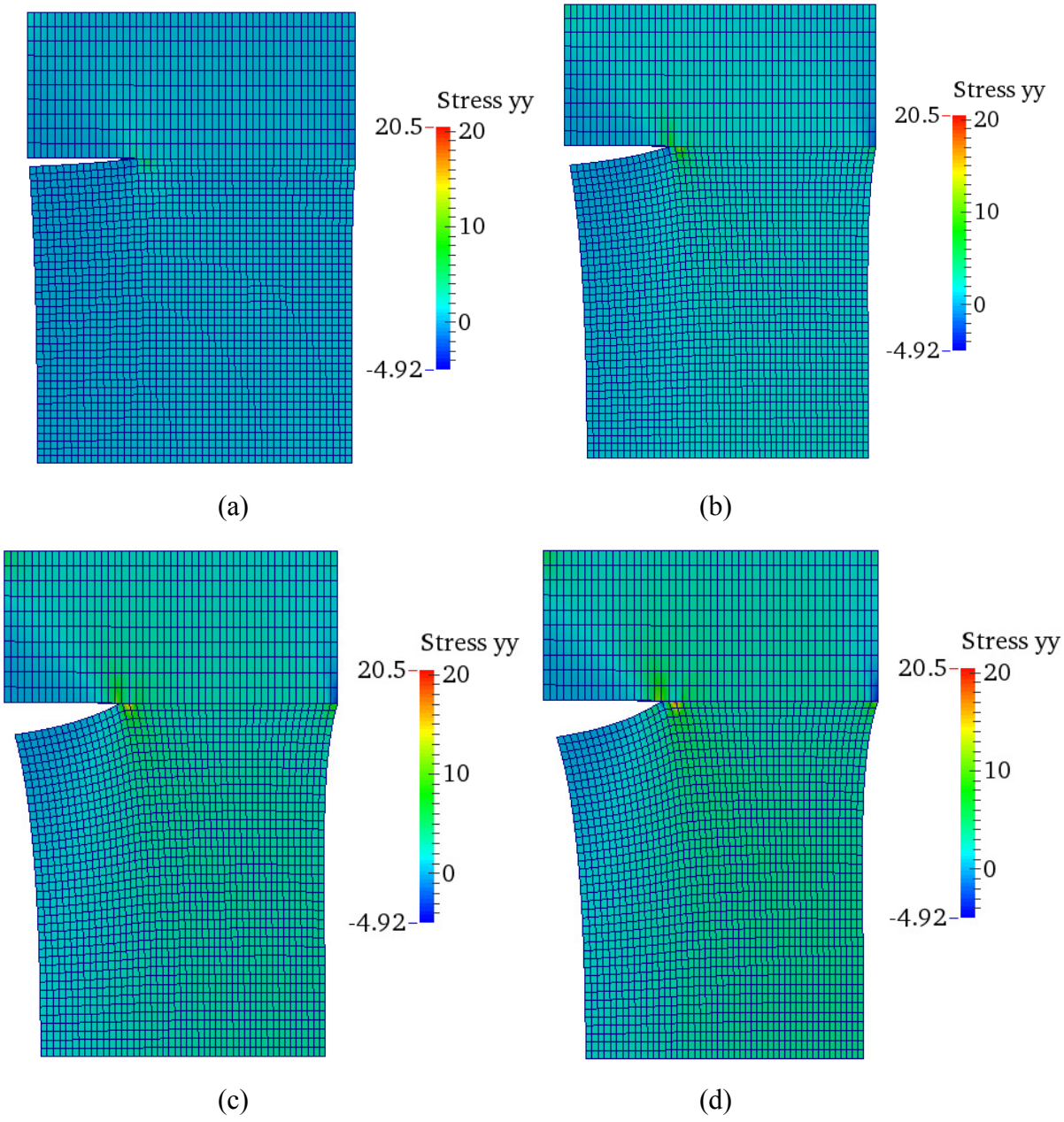

Figure 4.28. σ_{yy} contour plots for tearing of bimaterial interface for Ogden-type material (Medium mesh): (a) $\varepsilon = 4\%$; (b) $\varepsilon = 10\%$; (c) $\varepsilon = 16\%$; (d) $\varepsilon = 19\%$ (last step).

Unlike the behavior of Neo-Hookean material shown in Figure 4.21, Ogden type material easily undergoes large stretching. This reduces the stresses intensity at the tip of the propagating crack, and therefore triggers crack arrest. Results from the three different levels of mesh refinement are plotted, and they all converge to the response for the fine mesh, as shown in Figure 4.29.

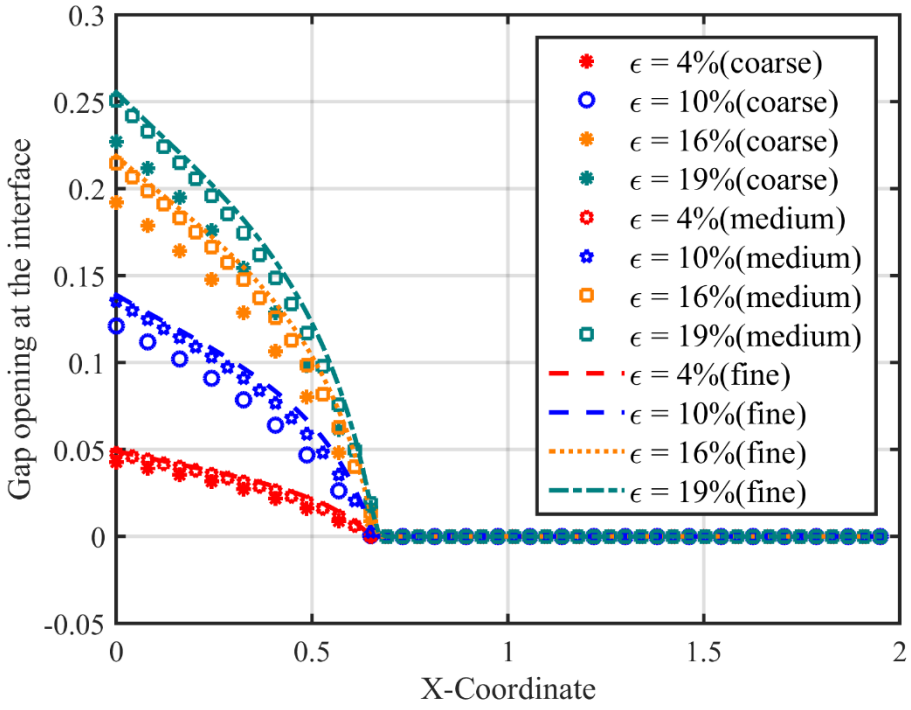

Figure 4.29. Gap/opening plot for tearing of bimaterial interface for Ogden-type material (Coarse, Medium and Fine mesh): (a) $\varepsilon = 4\%$; (b) $\varepsilon = 10\%$; (c) $\varepsilon = 19\%$.

Figure 4.30 presents the interfacial fine scales along the bimaterial interface for various applied strains, which also highlights the high accuracy of the computed solution and manifests the precise enforcement of the interfacial conditions.

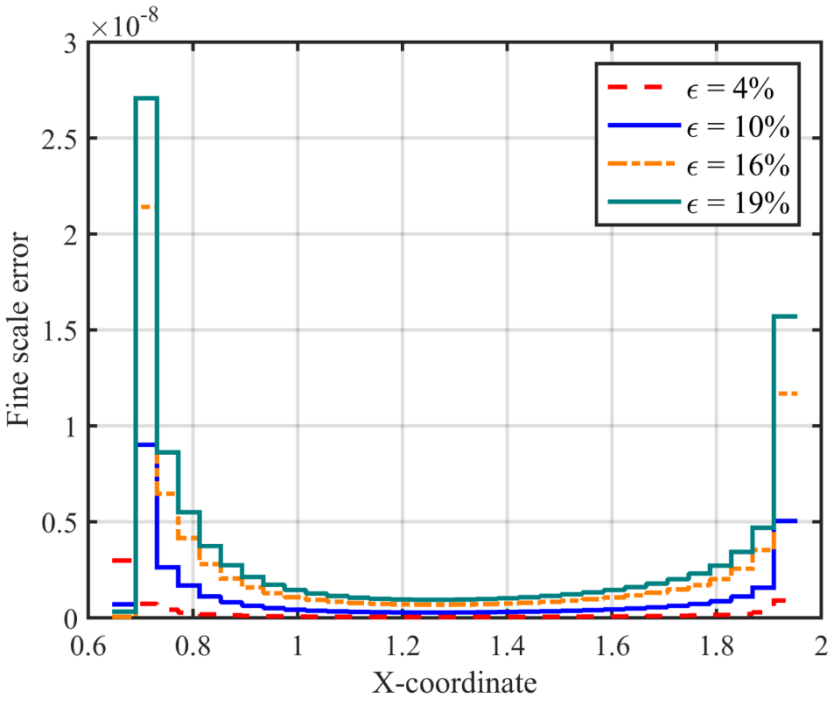

Figure 4.30. Fine scale error along the interface plot.

4.7.4 Fiber push-out test

The last test case is a comprehensive problem that involves all three kinematic modes arising in interfacial debonding, i.e., damage in tension, damage in compression, and frictional sliding in compression. Matrix is comprised of EPON 828/DETA epoxy material and we provide a comparison of the computed solution with the numerical and experimental data presented in Bechel and Sottos [19].

Pushout tests are carried out to determine the strength of the bonded interfaces under shear stresses [19]. Consequently, this is a problem of practical interest to model fiber-matrix interface and to quantify the evolving interfacial debonding and therefore the strength and integrity of fibrous composites at microscopic level [83]. In the experimental setup, a single fiber embedded in the matrix is pressed by a punch until it is pushed out of the composite. The force-displacement history of the punch is recorded and thereafter is used to compute interface properties such as fracture toughness and the coefficient of friction [83]. A schematic cross-section of the experimental setup is shown in Figure 4.31. The dimensions of the specimen as shown in Figure 4.31 are $r_f = 0.95$ mm, $r_m = 4.3$ mm, $H = 5.36$ mm, and $r_s = 1.025$ mm.

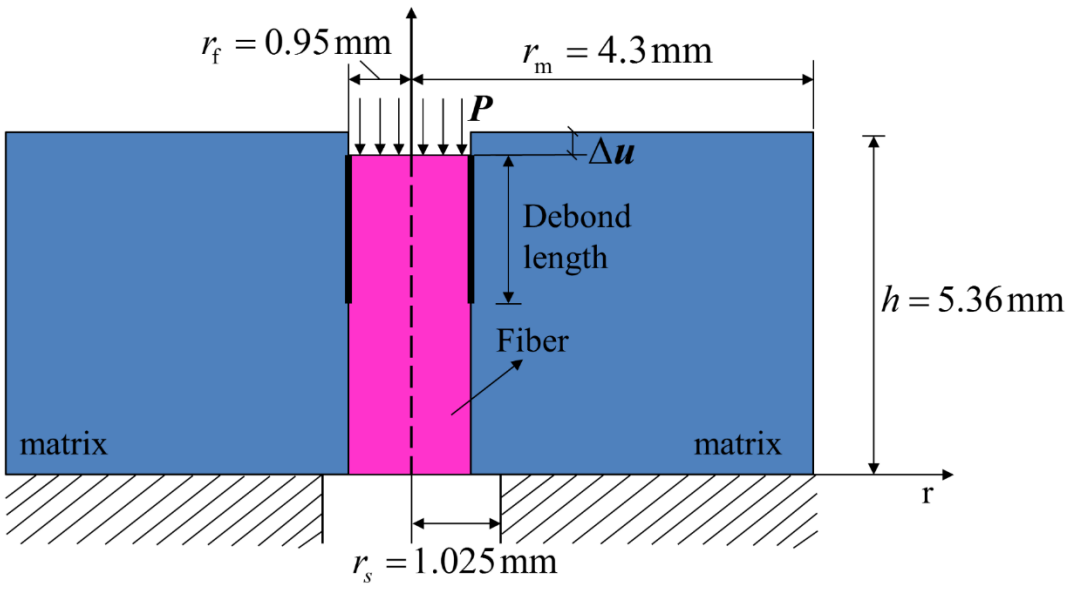

Figure 4.31. Pushout test problem description, cross-sectional view [19].

The three-dimensional finite element mesh is shown in Figure 4.32. Trilinear hexahedral elements are employed for the matrix and the fiber, and the DG method with a residual gap as an internal variable is used along the composite interface. To numerically evaluate the interfacial quantities four integration points are employed in each interface "element". A quarter of the cylindrical domain is modeled with 2,125 elements in the fiber and 9,775 elements in the matrix, with 25 elements through the height of the specimen. The material properties for the fiber and matrix are listed in Table 4.4; critical stress and critical inelastic gap which are interface properties are taken as $P_c = 22\ \text{N/mm}^2$ and $\delta_c = 0.011\ \text{mm}$, respectively, to match the study presented in [83,2,19].

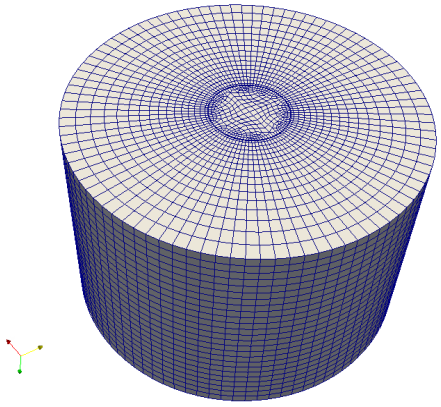

Figure 4.32. Mesh for the pushout test.

Table 4.4. Material properties of the fiber and matrix.

Material	Youngs modulus		Poisson ratio	
Matrix	E_m (N/mm^2)	4000	v_m	0.33
Fiber	E_f (N/mm^2)	2500	v_f	0.35

This simulation is performed in two steps. To model the manufacturing stage (initial stage), a constant thermal strain field equal to $\varepsilon_{\text{th}} = -0.0022$ is applied to the matrix to replicate the shrinkage effects that occur during the curing phase, and this value is an experimentally measured value reported in [19]. To model the mechanical loading stage (second stage), a prescribed displacement along the fiber axis is applied to the top surface of the fiber, representing the application of the punch load P. The maximum displacement applied is $\mathrm{u}_y = -0.174$ mm. The corresponding associated force is computed by summing the reactions computed at the nodes at the top surface of the fiber.

4.7.4.1 Evolution of stress and interfacial damage

Contour plots of the maximum principal stress and shear stress for the two loaded configurations are presented in Figure 4.33 and Figure 4.34. The initial residual stress pattern caused by the shrinkage of the matrix is shown in Figure 4.33 (a) and Figure 4.34 (a). At the initial stage, due to the thermal strain ε_{th} in the matrix, the top region of the interface is under tension, which causes the debonding under tension. As can be seen in Figure 4.33 (a) and Figure 4.34 (a), elements at the interface near the top are undergoing relatively large positive traction that validates tangential debonding near the top of the interface. The value of the shear stress in Figure 4.33 (b) is found to be closer to the critical stress, indicating that debonding gets triggered at the top. Also, the location of the maximum value of the shear stress tends to occur near the evolving front of the debonded interface. In Figure 4.33 (d) and Figure 4.34 (d) that correspond to the last step of the simulation, the computed displacement field in the fiber shows a lack of connectivity between these two constituents. Accordingly, the force also gradually reduces and at this stage, the fiber and matrix are separate from each other and any remaining interfacial interaction force is due to the frictional sliding along the bimaterial interface.

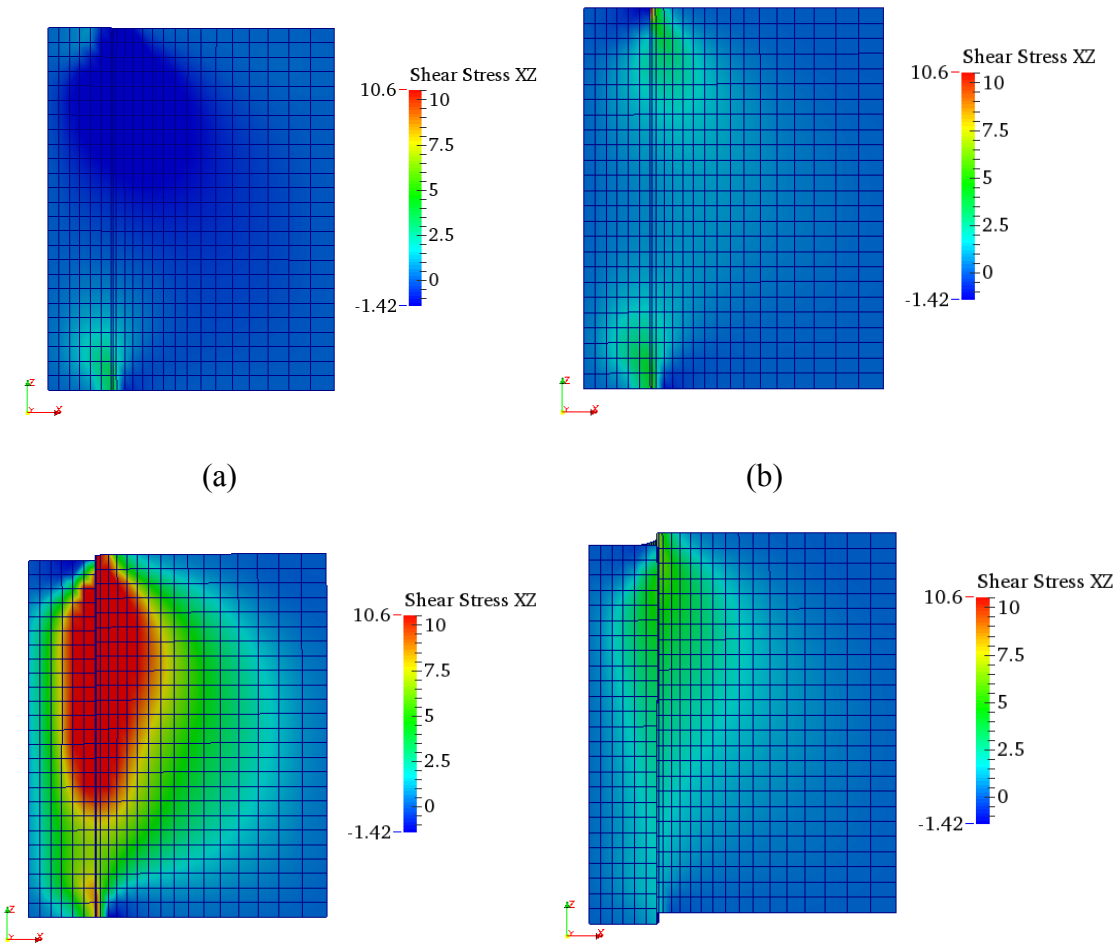

Figure 4.33. Shearing stress (MPa) contours at four load levels: (a) Initial step; (b) Initiation of debonding ($P = 98.62\,\mathrm{N}$); (c) Maximum sustained force ($P = 412.21\,\mathrm{N}$); (d) Final stage ($P = 105.52\,\mathrm{N}$).

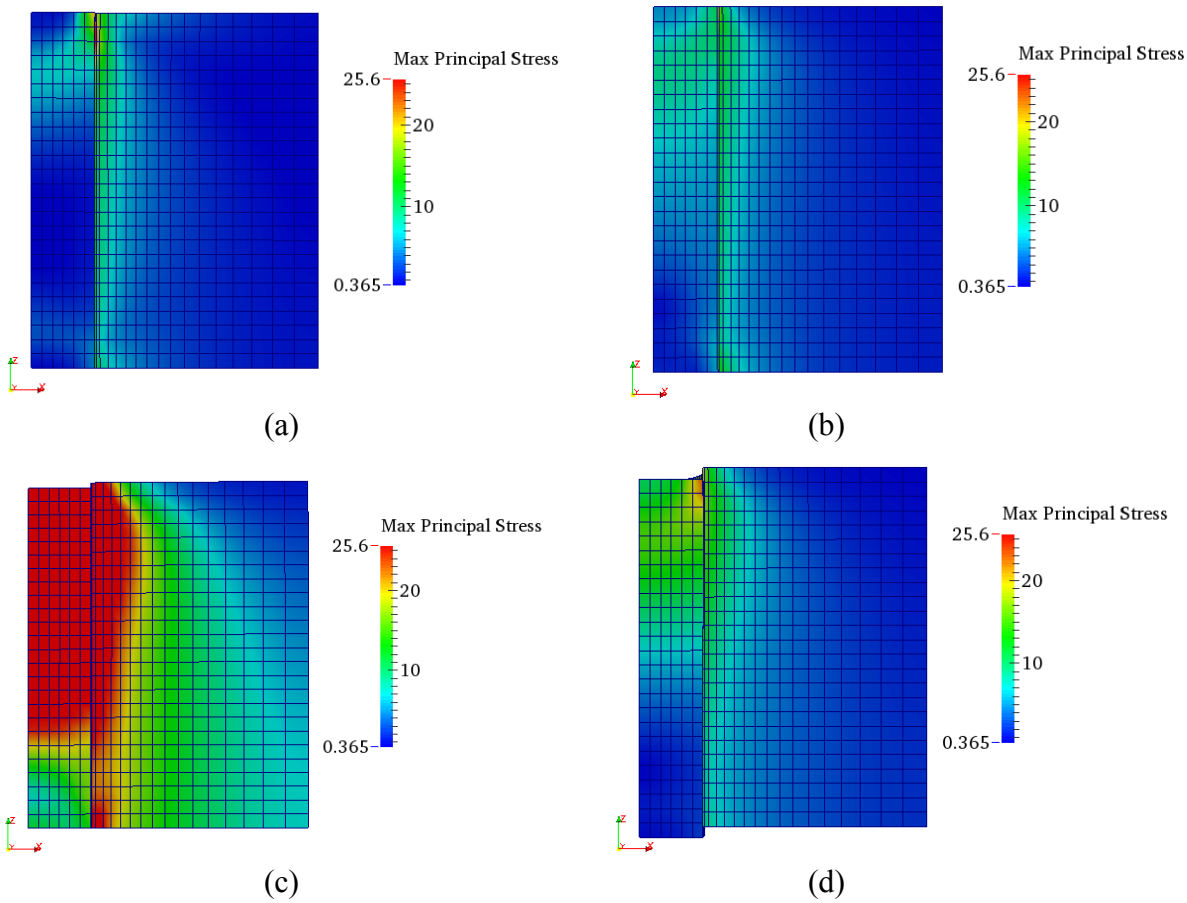

Figure 4.34. Maximum principal stress (MPa) distribution at four load levels: (a) Initial step; (b) Initiation of debonding ($P = 98.62\,\mathrm{N}$); (c) Maximum sustained force ($P = 412.21\,\mathrm{N}$); (d) Final stage ($P = 105.52\,\mathrm{N}$).

In Figure 4.35, we provide this unique property of our method that can indicate the corresponding interface kinematic model that is active for any interfacial element at the different load levels. From Figure 4.35 (a) to Figure 4.35 (d), the top elements at the interface switch from damage-tension to damage-compression and finally to the frictional sliding model, which matches exactly the loading process from the initial step to the final load step.

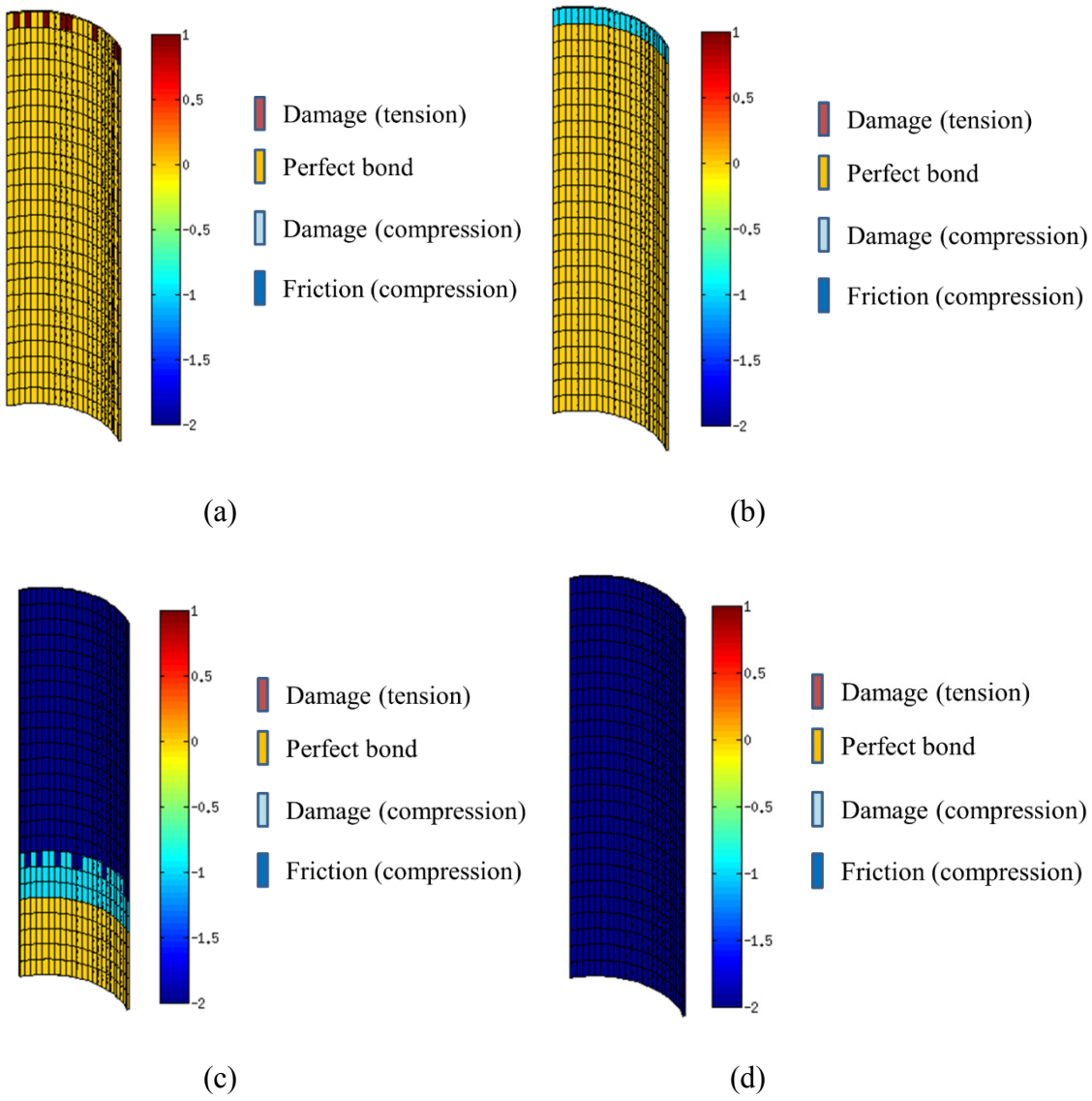

Figure 4.35. Tracking of damage propagation at four load levels: (a) Initial step; (b) Initiation of debonding ($P = 98.62\,\mathrm{N}$); (c) Maximum sustained force ($P = 412.21\,\mathrm{N}$); d) Final stage ($P = 105.52\,\mathrm{N}$).

4.7.4.2 Evolution of punch force and debond-length curve

The time-history of the applied punch force versus displacement at the top surface of the fiber is plotted as the red curve in Figure 4.36, and the results compare well with the experimental and numerical results presented in references [83,2]. The slopes of the curves in the initial loading region were computed to be approximately 8,800 N/mm. The figure shows that the proposed DG method can model debonding behavior and trace the curve successfully. As stated in Alfano [2],

when the force reaches its maximum value, debond evolution becomes unstable. Thus in [2], a secant method is used to numerically model the sudden decrease in force as observed in the experiment. Unlike the method in [2], our VMDG method can model the sudden jump in the force automatically. In our method, we have the critical inelastic gap as the variable that controls the softening process in the material. Therefore, without switching to another numerical solver such as the secant method [2], a force curve with stiff slope in the softening process is obtained as shown in Figure 4.36, which matches well the rapid drop in force as presented in Lin [83] and Alfano [2].

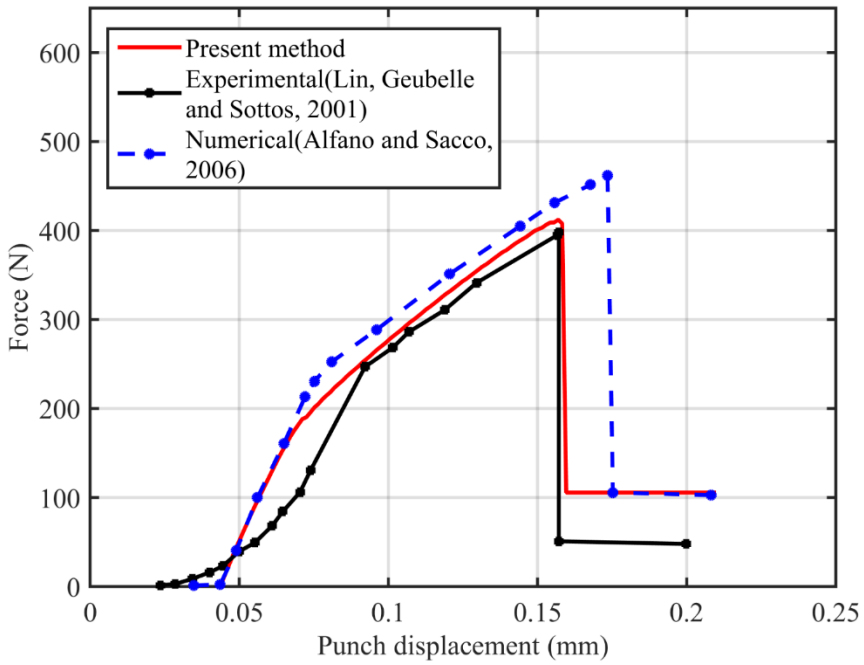

Figure 4.36. Force-displacement curves for mechanical stage.

The relation between the debond length versus the punch displacement is shown and compared with Lin [83] and Alfano [2] in Figure 4.37, and a good comparison is attained.

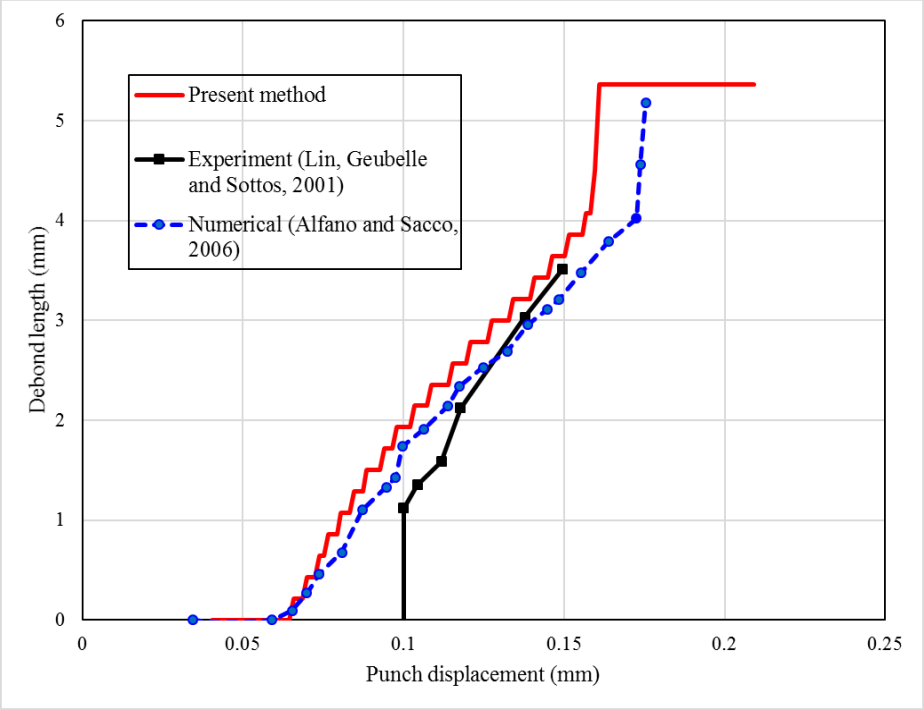

Figure 4.37. Debond length versus punch displacement.

4.7.4.3 Parametric study

As illustrated in [83], many parameters affect the overall performance of this push-out test. For further investigation of the robustness of our method, we study the effect of different E_f / E_m ratios and friction coefficients μ_f. The force-displacement curves for different Young's modulus ratio and for different friction coefficient μ_f are given in Figure 4.38 and Figure 4.39. In Figure 4.38, the maximum force attained for $E_f / E_m = 0.625$ and $E_f / E_m = 2.5$ is in the same range while for $E_f / E_m = 6$, the maximum force that the interface can sustain, drops. Likewise, the force vs. punch displacement plots for different friction coefficient are presented in Figure 4.39. As the friction coefficient μ_f represents the strength of the bonding at the interface between fiber and matrix, for a given punch displacement the interfacial force sustained at the interface increases as friction coefficient increases. Furthermore the punch displacement that leads to interfacial failure also increases, as shown in Figure 4.39.

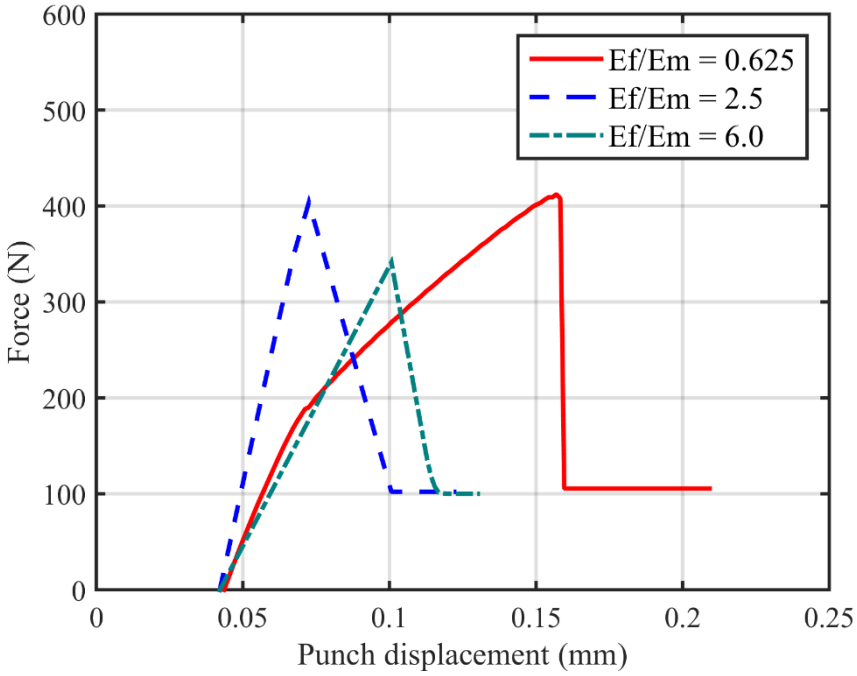

Figure 4.38. Force vs. punch displacement for various E_f / E_m ratio.

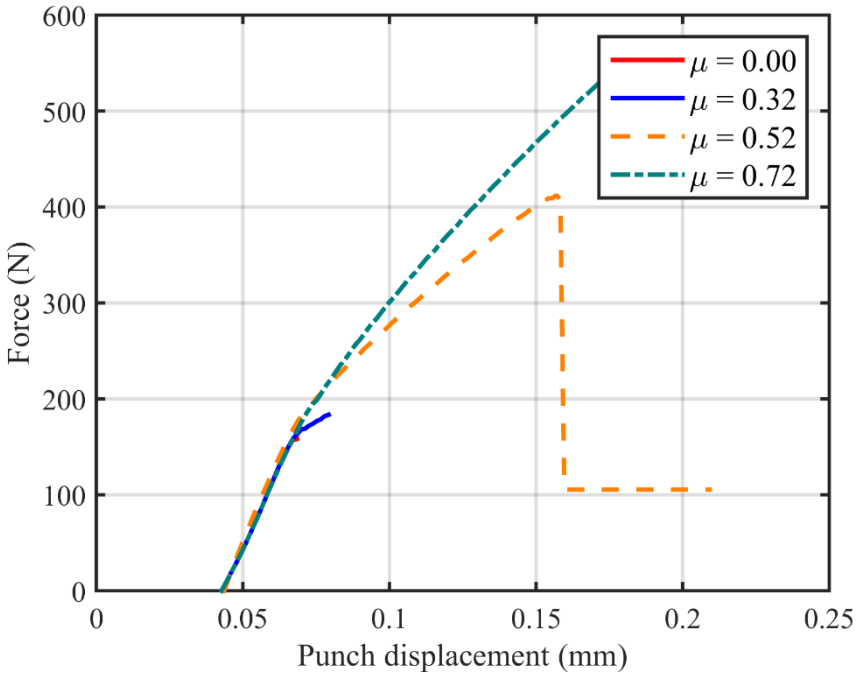

Figure 4.39. Force vs. punch displacement for various frictional coefficient μ_f.

4.8 Conclusions

We have presented a Variational Multiscale DG (VMDG) formulation for interfacial debonding in multi-constituent materials at finite strains. A significant contribution of the method is a consistently derived Lagrange multiplier field as a function of interface tractions and evolving gap function. It is weighted by the evolving stability tensor which is a function of the nonlinearly evolving material and geometric parameters, thus accommodating the notions of area averaging and stress averaging. Appearance of the gap function in the expression for the Lagrange multiplier and therefore in the evolving finite-scales provides a natural mechanism to embed physics based models as well as phenomenological models for progressive failure under various loading scenarios. This is a significant contribution of the present Chapter 4 and sets it apart from any numerical methods that have been proposed for interfacial kinematics of finitely deforming embedded interfaces with evolving gaps and discontinuities. The proposed method allows treatment of the interface constitutive behavior through yield functions and flow rules that are inspired by the literature from plasticity. In the present method the combination of damage and friction along the debonding surfaces is easily accommodated by borrowing concepts from multi-surface plasticity. Also, rate dependency and other advanced phenomena can be easily treated in the new framework. Specially, the proposed method avoids using cohesive elements that can introduce artificial elastic interface stiffness that affects the consistency and therefore the stability of the method. With the fine-scale models evolving with the material and geometric nonlinearity exhibited localized to the interface, the algorithmic interface parameters are updated continuously through the evolution of the nonlinear problem. Several interfacial kinematic modes involving tension debonding, evolution of normal gap, and compressive frictional sliding are considered and corresponding algorithmic generalizations are presented. The proposed consistent derivation that variationally embeds the interfacial kinematic models is crucial to the derivation of consistent tangent tensors that result in quadratic convergence rates when employed in the Newton Raphson method. A series of 2D and 3D benchmark problems are presented that show the numerical attributes of the method and seamlessly track the various interfacial debonding modes in the finite strain context.

CHAPTER 5: FATIGUE AND INTERFACIAL DAMAGE INITIALIZATION AND PROPAGATION PREDICTION

5.1 Introduction

Composite materials are widely used in different fields such as aerospace engineering and civil engineering. When studying the strength of composite materials, the failure of the interphase cohesion between two or more constituents, especially due to fatigue effects under cyclic loadings, is one of the major concerns.

While both experimental and numerical methods have been applied to the modeling of this effect, the most commonly used method is experimental, based on low-cycle fatigue (ductile material) and high-cycle fatigue (brittle material). However, experiments on fatigue have limitations on different aspects that can be investigated such as material types, size of equipment and require modeling of initial conditions and boundaries [126]. Therefore, researchers have pursued numerical methods for computational modeling of fatigue to account for the physics that cannot be directly accounted for in the experimental approaches. For interface modeling, Chaboche et al. [37] provided discussion and comparison of the two numerical approaches for analysis of composites. One approach considers the interphase as a volumetric entity and uses the so-called 'Continuous Damage Mechanical' (CDM) concept to study the deterioration of the material. The other approach discretizes the two materials and introduces interfaces elements to model the debonding phenomenon.

Chaboche [33] and Lemaitre [81] employed CDM which was introduced by Kachanov [77] to model fatigue effects. This theory was extended for both low-cycle fatigue [24, 77, 126] and high-cycle fatigue [127,166,47]. In this method, the damage is considered as a smooth and continuous internal variable that describes the degradation of the material properties [78]. This model is thermomechanically consistent and has a sound mathematical representation of damage growth phenomena [76]. This method is later applied to composite materials such as fiber reinforced composites [54]. However, this method is not equipped with giving detailed information on the propagation of a particular crack as well as the stress distribution around the crack tip [76].

Another possible approach is to use the cohesive element models which have been successfully applied for describing both the monotonic fracture process [115] and the cyclic loading process [129]. In this method, fatigue crack growth is modeled by an irreversible cohesive fracture law and

the unloading is assumed to linear towards to the origin. This model has been further extended to adopt the unloading-reloading hysteresis [117,143] to predict fatigue life and applied to ferroelectric materials which exhibit electronic fatigue [7]. For interface fatigue crack growth, Roe and Siegmund [136] proposed an irreversible cohesive zone model which has no predefined path. In their method, the traction stage depended on the damage variable leading to a history dependent method [136].

In the field of Additive manufacturing, with the layer-by-layer technique, fatigue and interfacial damage are essential for a wide range of scientific and industrial processes. For single material fabrication such as metal, plastics, and resins, at interphases between layers, a weak bonding which lead to delamination and breakage under stresses [22]. In the recent years, multi-material additive manufacturing technique is of great interest due to its capacity to improve the overall performance of the products by optimizing certain mechanical properties, or thermal and chemical reactions [164]. By selectively adding additional materials into the system or using specific types of material at targeted locations, newly engineered materials with more flexibility and designed properties are achieved. For multiple materials or even blends of materials processing, the failure and fatigue mechanism at interfaces is a dominant aspect of studying the behavior of the multi-material 3D printed products. A number of experimental results are conducted by many researchers including the fatigue properties analysis for Polyjet-printed elastomer [110]. Sugavaneswaran and Arumaikkannu [152] show the fracture is primarily initiated by the debonding between the randomly distributed and orientated plastic reinforcement and the elastomer matrix.

In the current work, we aim to propose another damage evolution method at finite strains to model the low-cycle fatigue effects induced at the interface. This method is based on embedding discontinuous Galerkin ideas in continuous Galerkin framework, leading to a VMS-based primal interface formulation with consistent stabilization as presented in Chapter 3. This idea was further enhanced in Chapter 4 to accommodate debonding under monotone loading [39] and treat damage and friction in a unified manner. In the current Chapter, we extend our work for modeling the low-cycle fatigue effects. A cohesive damage envelope along with the material softening behavior is embedded with the existence of the loading, unloading and reloading hysteresis. The evolution of the fatigue effects is tracked by the return mapping algorithm. The most appealing feature of the VMS based formulation is that there are no predefined parameters such as the penalty parameter for uniform and consistent enforcement of interfacial modeling, thus showing the robustness of

the proposed numerical method.

The outline of Chapter 5 is summarized as follows. In section 5.2, the standard system of governing equations and the corresponding interfacial weak form are given. In section 5.3, a stabilized interface formulation with the existence of the inelastic gap function is presented. The corresponding constitutive model for tracking the fatigue evolution is given in section 5.4. In section 5.5, a series of numerical results with damage and fatigue life prediction are presented. Conclusions are summarized in section 5.6.

5.2 Governing Equations and Interfacial Weak Form

In the context of finite strain, the domain Ω is deformable under a deformation gradient where all the points in the current configuration which are shown in Figure 5.1 (b) are a mapping of all the points in the material configuration in Figure 5.1 (a). For problems with interfaces, the domain in reference configuration is cut into two subdomains, $\Omega^{(1)}$ and $\Omega^{(2)}$ with the deformed configurations $\boldsymbol{\phi}^{(1)}$ and $\boldsymbol{\phi}^{(2)}$ as shown in Figure 5.1. At the interface Γ_I, the opening is allowed such that the deformation map $\boldsymbol{\phi}^{(1)}$ and $\boldsymbol{\phi}^{(2)}$ can be different with the gap variable $\boldsymbol{\zeta}$. At interfaces, cyclic loadings such as loading, unloading and reloading initiate based on different loading scenarios.

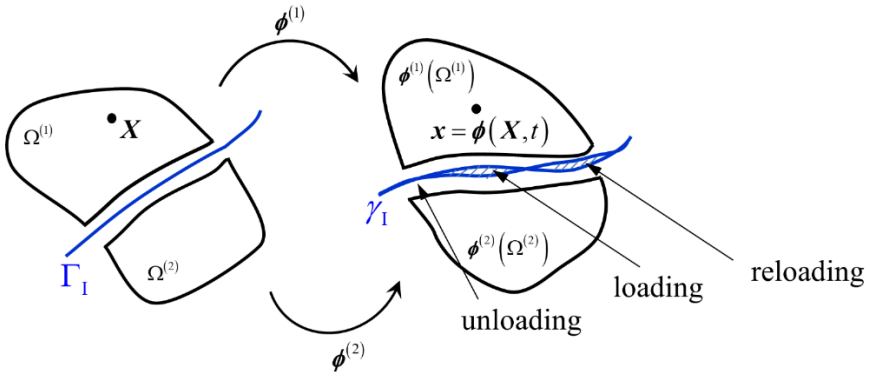

Figure 5.1. Domain Ω with interface Γ_I: a) Material configuration; b) Current configuration.

The governing system of equations can be written as follows. At the interface Γ_I, displacement and traction continuity are prescribed with the existence of $\boldsymbol{\zeta}$ and the Lagrange multiplier $\boldsymbol{\lambda}$.

$$\text{DIV}\ \boldsymbol{P}^{(\alpha)}\left(\boldsymbol{F}^{(\alpha)}\right)+\rho_o^{(\alpha)}\boldsymbol{B}^{(\alpha)}=\boldsymbol{0} \qquad \text{in} \quad \Omega^{(\alpha)},\ \alpha=1,2 \tag{5-1}$$

$$\boldsymbol{\phi}^{(\alpha)}=\boldsymbol{X}^{(\alpha)} \qquad \text{on}\ \ \Gamma^{(\alpha)}\setminus\Gamma_{\text{I}},\ \alpha=1,2 \tag{5-2}$$

$$\boldsymbol{\phi}^{(2)}-\boldsymbol{\phi}^{(1)}=\boldsymbol{\zeta} \qquad \text{on}\ \ \Gamma_{\text{I}} \tag{5-3}$$

$$\boldsymbol{P}^{(1)}\cdot\boldsymbol{N}^{(1)}-\boldsymbol{\lambda}=\boldsymbol{0} \qquad \text{on}\ \ \Gamma_{\text{I}} \tag{5-4}$$

$$\boldsymbol{P}^{(2)}\cdot\boldsymbol{N}^{(2)}+\boldsymbol{\lambda}=\boldsymbol{0} \qquad \text{on}\ \ \Gamma_{\text{I}} \tag{5-5}$$

where $\boldsymbol{P}^{(1)}$ and $\boldsymbol{P}^{(2)}$ are first P-K stress in different subdomains, $\boldsymbol{B}^{(\alpha)}$ is the body force, $\boldsymbol{N}^{(1)}$ and $\boldsymbol{N}^{(2)}$ are unit normal at interfaces for $\Omega^{(1)}$ and $\Omega^{(2)}$, $\rho_o^{(\alpha)}$ is the material density, and $\boldsymbol{F}^{(\alpha)}$ is the deformation gradient defined as $\boldsymbol{F}^{(\alpha)}=\dfrac{\partial\boldsymbol{\phi}^{(\alpha)}}{\partial\boldsymbol{X}^{(\alpha)}}$. Converting Eqn. (5-1) to (5-5) into the corresponding weak form and applying integration by part, the mixed interfacial weak formulation is derived as follows:

$$\sum_{\alpha=1}^{2}\int_{\Omega^{(\alpha)}}\text{GRAD}\,\boldsymbol{\eta}_o^{(\alpha)}:\boldsymbol{P}^{(\alpha)}\,\text{d}V-\sum_{\alpha=1}^{2}\int_{\Omega^{(\alpha)}}\rho_o^{(\alpha)}\boldsymbol{B}^{(\alpha)}\cdot\boldsymbol{\eta}_o^{(\alpha)}\,\text{d}V-\int_{\Gamma_{\text{I}}}\boldsymbol{\lambda}\cdot[\![\boldsymbol{\eta}_o]\!]\,\text{d}A=0 \tag{5-6}$$

$$-\int_{\Gamma_{\text{I}}}\boldsymbol{\mu}\cdot\left([\![\boldsymbol{\phi}]\!]-\boldsymbol{\zeta}\right)\text{d}A=0 \tag{5-7}$$

where $\boldsymbol{\lambda}$ and $\boldsymbol{\mu}$ serves as Lagrange multipliers to enforce the traction and displacement continuity, respectively.

***Remark**: Detailed descriptions and derivations from Eqn. (5-1) to (5-5) to Eqn. (5-6)-(5-7) are presented in Chapter 3 and Chapter 4. Interested readers are referred to these Chapters for more information.*

5.3 VMS-based Consistent Interfacial Coupling

In Chapter 4, we developed a consistent interface form with provision for strong discontinuity across bimaterial interfaces. We had also proposed various interface models that represented different physical behaviors. Specifically, we considered debonding in tension, debonding in compression and frictional sliding in compression in a unified way as presented in Chapter 4. In this Chapter, we extend along these lines and consider fatigue under tension.

We adopted the ideas from the Variational Multiscale Method (VMS) [68,69] and derived an analytical expression for the Lagrange multiplier field $\boldsymbol{\lambda}$ which appears as an additional unknown

field in Eqn. (5-6). Here the expression for the Lagrange multiplier λ is not a function of the gap term ζ and is backward compatible with our previous work in Chapter 4. The residual opening or gap ζ in Eqn. (5-3) is treated like a plastic strain-like field. The debonding process is modeled by introducing this internal variable ζ for which constitutive models are proposed to track the debonding evolution. As given in Chapter 4, the final stabilized Discontinuous Galerkin formulation for debonding is as follows:

$$\begin{aligned} R\left(\boldsymbol{\eta}_o^{(\alpha)}, \boldsymbol{\phi}^{(\alpha)}, \boldsymbol{\zeta}\right) = \sum_{\alpha=1}^{2} \int_{\Omega^{(\alpha)}} \left[\mathrm{GRAD}\, \boldsymbol{\eta}_o^{(\alpha)} : \boldsymbol{P}^{(\alpha)} - \boldsymbol{\eta}_o^{(\alpha)} \cdot \rho_o^{(\alpha)} \boldsymbol{B}^{(\alpha)} \right] \mathrm{d}V + \int_{\Gamma_1} [\![\boldsymbol{\eta}_o]\!] \cdot \{ \boldsymbol{P} \cdot \boldsymbol{N} \}\, \mathrm{d}A \\ + \int_{\Gamma_1} \left[\left\{ \left(\mathrm{GRAD}\, \boldsymbol{\eta}_o : \mathbf{A} \right) \cdot \boldsymbol{N} \right\} + [\![\boldsymbol{\eta}_o]\!] \cdot \left\| \boldsymbol{\tau}_s \right\| \right] \cdot \left([\![\boldsymbol{\phi}]\!] - \boldsymbol{\zeta} \right) \mathrm{d}A \end{aligned} \tag{5-8}$$

Remark: *Eqn. (5-8) is derived via VMS framework without any assumption of predefined parameters. Unlike the Lagrange multiplier method, it is a primal formulation with displacement be the only unknown variable. Since all the parameters are naturally derived, there are no user input parameters as in Penalty method. Though our proposed formulation shares the same feature with Nitsche's method, it is derived from the VMS technique and reserve the geometric and material nonlinearity inside the penalty parameter* $\left\| \boldsymbol{\tau}_s \right\|$.

Remark: *To model the debonding gap* ζ *, we propose a relationship between the traction* $\boldsymbol{T} := \{ \boldsymbol{PN} \} + \left\| \boldsymbol{\tau}^s \right\| \left([\![\boldsymbol{\phi}]\!] - \boldsymbol{\zeta} \right)$ *and the material separation. The monotonic loading case has already been given in Chapter 4 where tension damage, compression damage, and compression friction are presented in a unified way. In this Chapter, we focus on the constitutive model for cyclic loading.*

5.4 Constitutive Behavior for Interface Fatigue Effects

We start this section by describing our constitutive model for interface fatigue. For simplicity, we consider only the uniaxial tension scenario [143]. Unlike the general Cohesive zone method [136, 143], we developed a constitutive model based on the evolution of the debonding gap ζ . The idea from inelasticity has been given in Simo and Hughes [146] and further adopted in Chapter 4 and [4] for updating interface gap and traction with monotonic loading. In the case of cyclic loading, to define nucleation of the material after the fatigue cycles, we propose a cohesive envelope as an upper bound for damage as shown in blue dot line given in Figure 5.2. There are different types of

the cohesive envelopes, and we adopt the UBER relation [44,143] as given in the following:

$$\frac{P}{P_c} = e\frac{\zeta}{\zeta_{c1}}e^{-\frac{\zeta}{\zeta_{c1}}} \tag{5-9}$$

where P_c is the critical stress, and ζ_{c1} is the opening/sliding value in the cohesive envelope for $\|\boldsymbol{T}\| = P_c$.

Thus from Eqn. (5-9), the yield surface for the cohesive envelope curve can be represented as

$$f_{\text{cohesive}}(\boldsymbol{T}, \boldsymbol{\zeta}) = \|\boldsymbol{T}\| - eP_c\frac{\|\boldsymbol{\zeta}\|}{\zeta_{c1}}e^{-\frac{\|\zeta\|}{\zeta_{c1}}} \tag{5-10}$$

where $\|\boldsymbol{T}\|$ is the norm of traction $\boldsymbol{T} := \{\boldsymbol{PN}\} + \|\boldsymbol{\tau}^s\|(\llbracket\boldsymbol{\phi}\rrbracket - \boldsymbol{\zeta})$, and $\|\boldsymbol{\zeta}\|$ is the norm of the inelastic gap.

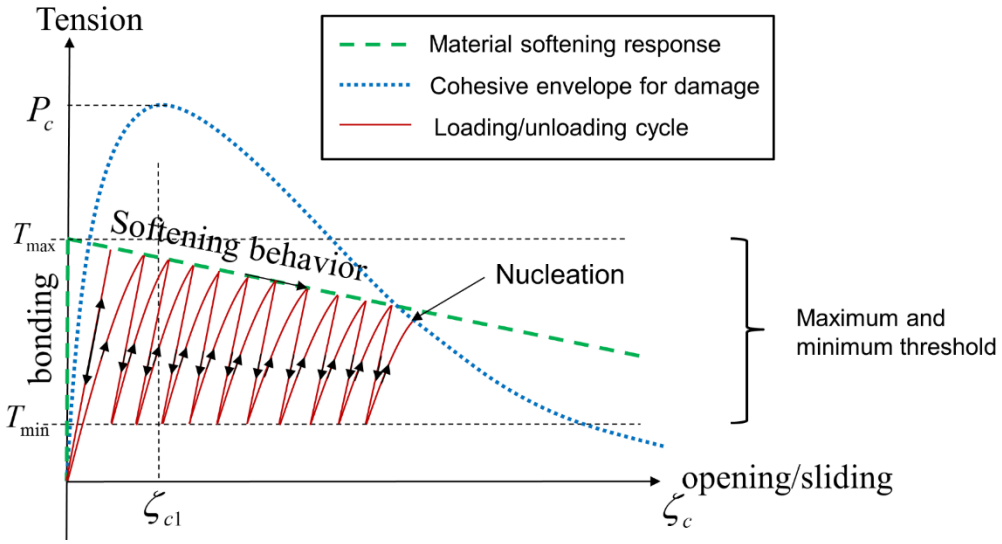

Figure 5.2. Fatigue loading/unloading curve.

As shown in the green line in Figure 5.2, the material softening response curve represents material behavior at the interface for a different gap or debonding values for monotonic loading. One of the highlights here is that the maximum capacity decreases after the loading/unloading cycle which matches the physical behavior of materials such as aluminum alloy and steel material deterioration due to the fatigue effect. With the cohesive envelope defined in Eqn. (5-9) and Eqn. (5-10), we need to specify the material softening curve shown as the green curve in Figure 5.2. Herein, as given in Chapter 4, we propose the following material softening response curve:

$$f_{\text{softening}}(\boldsymbol{T},\boldsymbol{\zeta}) = \|\boldsymbol{T}\| - \left(T_{\max} - H_c \|\boldsymbol{\zeta}\|\right) \tag{5-11}$$

where $H_c = T_{\max} / \zeta_c$ is the softening/hardening stiffness, and ζ_c is the critical inelastic gap for the softening response curve when $\|\boldsymbol{T}\| = 0$.

The lower bound yield surface can be written as

$$f_{\min}(\boldsymbol{T},\boldsymbol{\zeta}) = \|\boldsymbol{T}\| - T_{\min} \tag{5-12}$$

While the cohesive damage envelope and the material softening response curves are both assigned to present a prescribed material behavior at interfaces, the red curve in Figure 5.2 is the actual material loading and unloading cycle under a fatigue loading. The material undergoes multiple loading/unloading cycles, with a decreasing of the maximum value following the monotonic softening curve, till it reaches the cohesive envelope for damage which causes the nucleation, as shown in Figure 5.2. For materials under cyclic loading, the specification of the constitutive behavior under monotonic loading is not sufficient [143]. We adopted the similar idea in [143] and a simple phenomenological model with the assumption that the reloading stiffness changed for each step as shown in the red curve in Figure 5.2. This feature captures the hysteresis behavior for simulation of fatigue effects. The relation is stated as follows:

$$\dot{P} = \begin{cases} K_{\text{unloading}}\dot{\zeta}, K_{\text{unloading}} = K_0, \ if\ \dot{\zeta} < 0, \\ K_{\text{reloading}}\dot{\zeta}, \dot{K}_{\text{reloading}} = -K_{\text{reloading}}\dot{\zeta} / \zeta_a, \ if\ \dot{\zeta} > 0 \end{cases} \tag{5-13}$$

where $K_{\text{unloading}}$ is assumed to be equal to the initial loading stiffness K_0, K_{loading} is evolving in each step, and $\zeta_a = \zeta_{c1} N_c$ is the characteristic opening gap as given in [143]. The corresponding yield functions for loading, unloading and reloading curve are represented as follows:

$$f_{\text{loading}}(\boldsymbol{T},\boldsymbol{\zeta}) = \|\boldsymbol{T}\| - H_{c1}\|\boldsymbol{\zeta}\| \tag{5-14}$$

$$f_{\text{unloading}}(\boldsymbol{T},\boldsymbol{\zeta}) = \left(\|\boldsymbol{T}\| - \|\boldsymbol{T}_n\|\right) - H_{c1}^{-}\left(\|\boldsymbol{\zeta}\| - \|\boldsymbol{\zeta}_n\|\right) \tag{5-15}$$

$$f_{\text{reloading}}(\boldsymbol{T},\boldsymbol{\zeta}) = \left(\|\boldsymbol{T}\| - \|\boldsymbol{T}_n\|\right) - H_{c1,n+1}^{+}\left(\|\boldsymbol{\zeta}\| - \|\boldsymbol{\zeta}_n\|\right) \tag{5-16}$$

where $H_{c1} = K_0$ is the initial loading stiffness, $H_{c1}^{-} = K_0$ is the unloading stiffness, and the reloading stiffness is given as follows:

$$H_{c1,n+1}^{+}=\frac{H_{c1,n}^{+}}{\left(1+\frac{\left\|\boldsymbol{\zeta}\right\|-\left\|\boldsymbol{\zeta}_{n}\right\|}{\zeta_{a}}\right)} \tag{5-17}$$

We regard the debonding term $\boldsymbol{\zeta}$ as an internal variable at each interface and use the return mapping algorithm [4] and computational inelasticity idea [146] to solve it. The algorithm and corresponding parameters are summarized in Box 5.1.

Box 5.1. Return mapping algorithm for fatigue damage.

- STEP 1: Extract internal variables at certain integration point $\boldsymbol{x}^{\mathrm{i}}\in\Gamma_{\mathrm{int}}$ from last converging step: $\left\{\zeta_{n},Q_{n}\right\}$.
- STEP 2: Calculate the current step traction and displacement jump at $\boldsymbol{x}^{\mathrm{i}}\in\Gamma_{\mathrm{int}}$: $\left\{\left\{\boldsymbol{PN}\right\}_{\mathrm{n+1}},\left[\!\left[\boldsymbol{\phi}\right]\!\right]_{n+1}\right\}$
- STEP 3: Compute the trial stress and yield functions to check for fatigue evolution:

$$\boldsymbol{T}_{n+1}^{tr}=\left\{\boldsymbol{PN}\right\}+\left\|\boldsymbol{\tau}^{s}\right\|\left(\left[\!\left[\boldsymbol{\phi}\right]\!\right]-\boldsymbol{\zeta}_{n}\right) \tag{5-18}$$

$$f_{\mathrm{softening},n+1}^{tr}=\left\|\boldsymbol{T}_{n+1}^{tr}\right\|-\left(T_{\max}-H_{c}\left\|\boldsymbol{\zeta}_{n}\right\|\right) \tag{5-19}$$

$$f_{\min,n+1}^{tr}=\left\|\boldsymbol{T}_{n+1}^{tr}\right\|-T_{\min} \tag{5-20}$$

$$f_{\mathrm{cohesive},n+1}^{tr}=\left\|\boldsymbol{T}_{n+1}^{tr}\right\|-eP_{c}\frac{\left\|\boldsymbol{\zeta}_{n}\right\|}{\zeta_{c1}}e^{-\frac{\left\|\zeta_{n}\right\|}{\zeta_{c1}}} \tag{5-21}$$

$$f_{\mathrm{loading},n+1}^{tr}=\left\|\boldsymbol{T}_{n+1}^{tr}\right\|-H_{c1}\left\|\boldsymbol{\zeta}_{n}\right\| \tag{5-22}$$

$$f_{\mathrm{unloading/reloading},n+1}^{tr}=\left(\left\|\boldsymbol{T}_{n+1}^{tr}\right\|-\left\|\boldsymbol{T}_{n}\right\|\right) \tag{5-23}$$

- STEP 4: Check for fatigue loading/unloading/reloading:
  - Initialization: bonddbond1 = 0
  - IF $f_{\mathrm{softening},n+1}^{tr}\le 0$ and bonddbond1 = 0 THEN <u>Initial Loading</u>:

$$\Delta\gamma=\frac{f_{\mathrm{loading},n+1}^{tr}}{\left(\left\|\boldsymbol{\tau}^{s}\right\|+H_{c1}\right)}>0 \tag{5-24}$$

$$\boldsymbol{\zeta}_{n+1}=\boldsymbol{\zeta}_{n}+\Delta\gamma\boldsymbol{n}_{n+1} \tag{5-25}$$

Box 5.1 continued.

$$Q_{n+1} = Q_n + H_{c1}\Delta\gamma\,\partial_Q f_{n+1} \tag{5-26}$$

$$\boldsymbol{T}_{n+1} = \boldsymbol{T}^{tr}_{n+1} - \left\|\boldsymbol{\tau}^s\right\|\Delta\gamma\boldsymbol{n}_{n+1} \tag{5-27}$$

- ELSE IF $f^{tr}_{\text{softening},n+1} > 0$, THEN Unloading

$$\Delta\gamma = \frac{f^{tr}_{\text{unloading},n+1}}{\left(\left\|\boldsymbol{\tau}^s\right\| + H^-_{c1}\right)} > 0 \tag{5-28}$$

$$\boldsymbol{\zeta}_{n+1} = \boldsymbol{\zeta}_n + \Delta\gamma\boldsymbol{n}_{n+1} \tag{5-29}$$

$$Q_{n+1} = Q_n + H^-_{c1}\Delta\gamma\,\partial_Q f_{n+1} \tag{5-30}$$

$$\boldsymbol{T}_{n+1} = \boldsymbol{T}^{tr}_{n+1} - \left\|\boldsymbol{\tau}^s\right\|\Delta\gamma\boldsymbol{n}_{n+1} \tag{5-31}$$

bonddbond1 = 1

- ELSE IF $f^{tr}_{\text{min},n+1} < 0$ AND bonddbond1=1 or bonddbond1=2, THEN Reloading

$$\Delta\gamma = \frac{f^{tr}_{\text{reloading},n+1}}{\left(\left\|\boldsymbol{\tau}^s\right\| + H^+_{c1}\right)} > 0 \tag{5-32}$$

$$\boldsymbol{\zeta}_{n+1} = \boldsymbol{\zeta}_n + \Delta\gamma\boldsymbol{n}_{n+1} \tag{5-33}$$

$$Q_{n+1} = Q_n + H^+_{c1}\Delta\gamma\,\partial_Q f_{n+1} \tag{5-34}$$

$$\boldsymbol{T}_{n+1} = \boldsymbol{T}^{tr}_{n+1} - \left\|\boldsymbol{\tau}^s\right\|\Delta\gamma\boldsymbol{n}_{n+1} \tag{5-35}$$

$$H^+_{c1,n+1} = \frac{H^+_{c1,n}}{\left(1 + \dfrac{\left\|\boldsymbol{\zeta}_{n+1}\right\| - \left\|\boldsymbol{\zeta}_n\right\|}{\zeta_a}\right)} \tag{5-36}$$

bonddbond1 = 2

- ENDIF

5.5 Numerical Examples

5.5.1 Adhesive joints problem: Monotonic loading

For the first numerical simulation, a single lap joint (SLJ) type adhesively bonded joint problem

is studied. The problem is initially taken from Khoramishad et al. [75]. The geometric description of the problem is shown in Figure 5.3. Uniaxial boundary conditions are applied to the left surface of the top substrate and the displacement $d = 0.5$ mm is applied to the right surface of the bottom substrate. The two bonded substrates are made of aluminum alloy 2025-T3 and FM 73M OST toughened epoxy film is used as the adhesive material with the properties are given in Table 5.1.

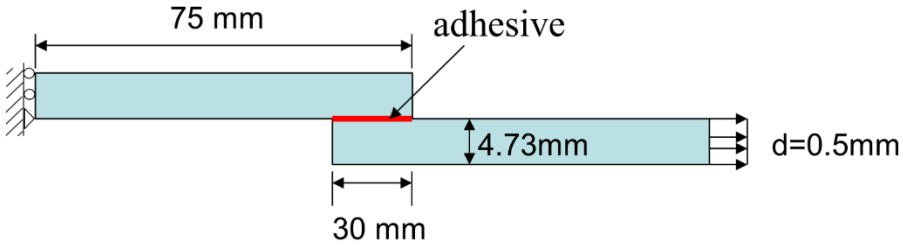

Figure 5.3. Problem geometric description of the single lap joint.

Before fatigue testing, Khoramishad et al. [75] conduct static loading testing to determine all the coefficients such as the static strength for the cohesive zone model they use in the numerical simulation. The critical traction P_c in our model is taken to be identical to the experimental value of static strength for the epoxy film adhesive given in [75].

Table 5.1. Material Coefficients for the adhesive joints problem.

Aluminum alloy 2024-T3	Young's modulus E (GPa)	Poisson's ratio v
	73	0.33
FM 73M OST toughened epoxy film adhesive	Critical traction P_c (MPa)	Critical inelastic gap ζ_c (mm)
	10	0.001

The numerical results for SLJ problem are shown in Figure 5.4 to Figure 5.8. Von Mises stresses are plotted for different load steps to show both the damage initialization and propagation. The Von Mises stress contour plots shown in Figure 5.4 to Figure 5.8 have similar trend compared with the results presented by Khoramishad et al. [75].

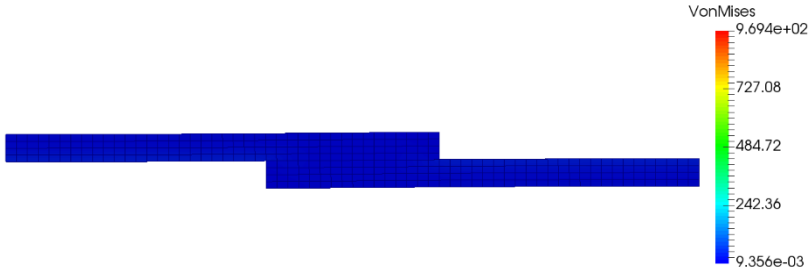

Figure 5.4. Von Mises stress plot for the adhesive joint problem (Step 1).

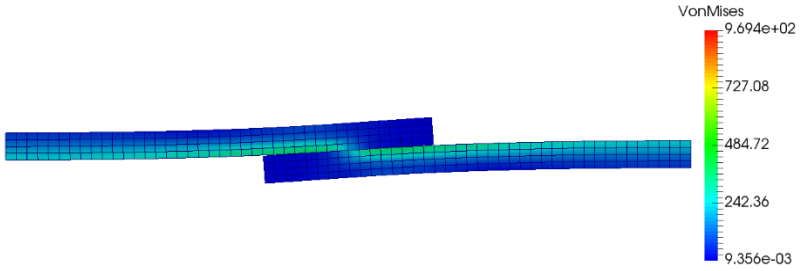

Figure 5.5. Von Mises stress plot for the adhesive joint problem (Step 10).

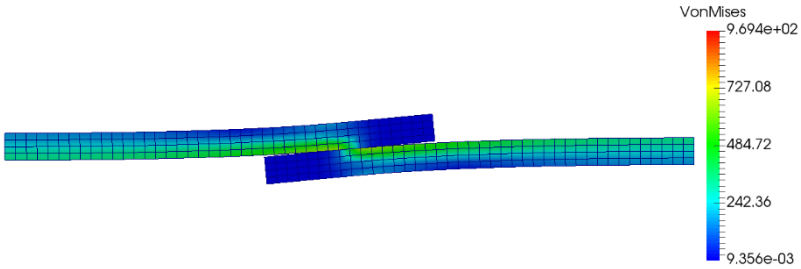

Figure 5.6. Von Mises stress plot for the adhesive joint problem (Step 15).

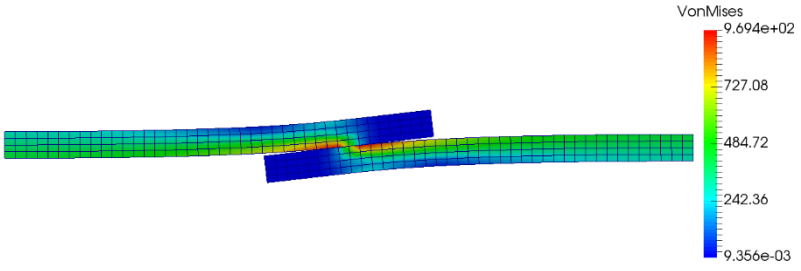

Figure 5.7. Von Mises stress plot for the adhesive joint problem (Step 20).

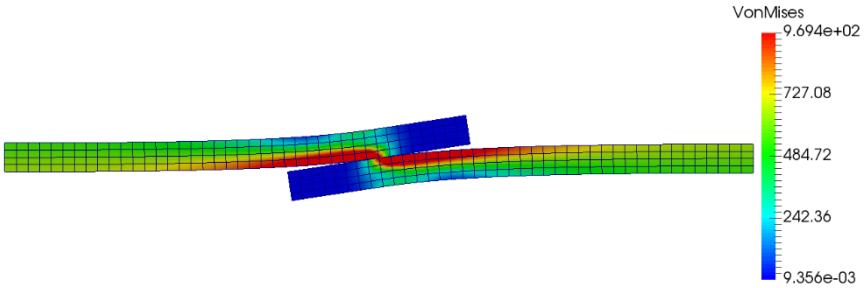

Figure 5.8. Von Mises stress plot for the adhesive joint problem (Step 31).

5.5.2 Fatigue-life prediction

In this problem, we use the proposed model to simulate the cyclic loading in tensile testing for Aluminum alloy 2048-T851. The problem description is given in Figure 5.9, with the initially applied traction $P = 700\text{MPa}$ acting on the right surface of the block. At the interface between the two blocks, the proposed interface fatigue model is applied.

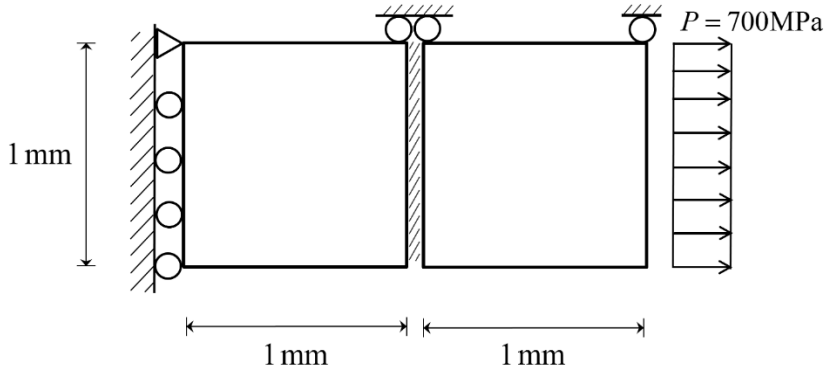

Figure 5.9. Geometry description for fatigue loading problem.

The material properties given in Table 5.2 are chosen to match the experimental data from the ASM metals handbook [130] and the numerical simulation results [143].

Table 5.2. Properties of the materials.

Material	Young's modulus E (GPa)	Poisson's ratio v	Uniaxial tensile strength P_c (MPa)
Aluminum alloy 2048-T851	70	0.33	465

The problem is set up to have different stress ranges as defined by the load ratio: $R = P_{\max} / P_{\min}$. In the simulation, two different load ratios are chosen as $R = 0.1$ and $R = 0.5$.

The results are summarized in Figure 5.10; the proposed method is compared with both numerical [143] and experimental results [130]. As shown in Figure 5.10, our method captures both the trend and the number of cycles for both load ratios.

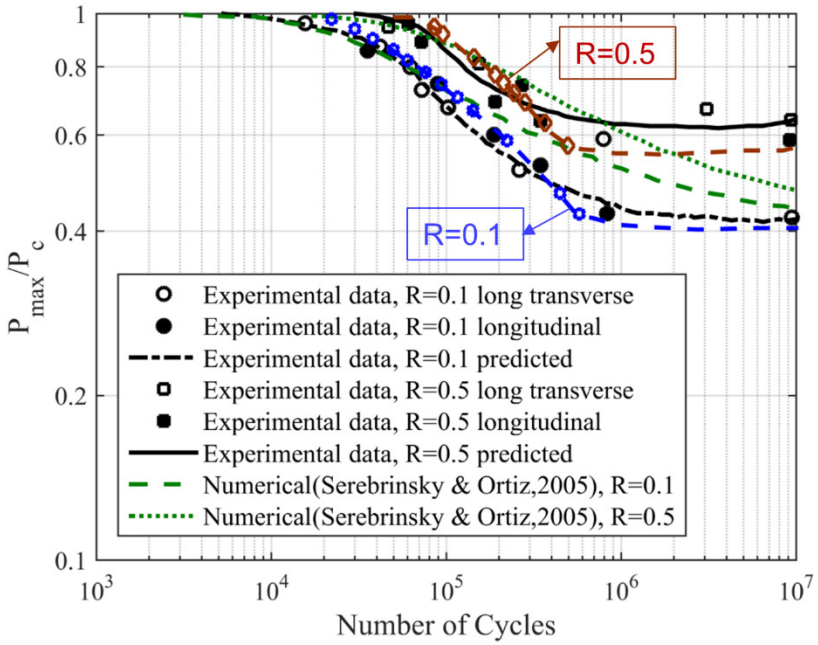

Figure 5.10. Numerical results of the S-N curves in comparison to the experimental data [130] and the line calculation [143]: Aluminum alloy 2048-T851 with $R = 0.1$ and $R = 0.5$.

5.6 Conclusions

In this work, we derived a DG stabilized interface formulation with the evolution of the damage feature at finite strains with the framework of weakly imposed interface continuity. Starting from using the Lagrange multiplier to enforce the traction equilibrium and introducing the inelastic gap ζ, the VMS method is employed for deriving a stabilized formulation which shares the same features of evolving fine-scale models through the existence of stability tensors with previous development. By giving an energy potential based on the Lagrange multiplier field derived through VMS, we recover the same stabilized formulation as derived from VMS method and the evolution equations of the debonding ζ. By introducing the return mapping algorithm, an incremental method to treat the debonding ζ locally at the integration point is developed. Multiple benchmark problems are presented to show the robustness of the method. Significant debonding along the

interface between two different constitutive materials is shown in the numerical simulation. With the above interface damage model, an extension of the framework to incorporate fatigue effects is proposed. It is a new hysteretic damage model different than the traditional cohesive zone model. We extend our work to accommodate the low-cycle fatigue effects and investigate the fatigue behavior of different types of steel materials which are used in civil infrastructures. By comparing the computational results with the experimental results, we validate the proposed framework. The next step would be bringing this work to a multi-physics regime with the changing of temperature field as well as the study of the dynamic material response.

CHAPTER 6: A DISCONTINUOUS GALERKIN FORMULATION OF THERMOELASTICITY AT FINITE STRAINS

6.1 Introduction

The modern field of additive manufacturing involves various types of processes for the deposition of the material. Depending on the timescales involved in the deposition process as compared to the intrinsic time scales of the curing of the material, the manufactured part develops embedded interfaces across which the time-lag in curing of layers creates weak discontinuities in the mechanical properties. In addition, curing processes involve chemical reactions with accompanying thermal field. Differential thermal cooling leads to interfacial residual stresses that are not there in injection wounded specimens. When these additively manufactured parts are loaded, there are loading thresholds below which the layers are uniformly connected, while beyond these thresholds, which are a function of the material properties and processing parameters, weak discontinuities grow into strong discontinuities.

Likewise, thermomechanical modeling of polycrystalline materials required approximate kinematic or kinematic condition to be applied along the crystal boundaries. Variationally embedding the interfacial phenomenological models necessitates a thermomechanical framework for interfacial mechanics. In addition, thermomechanical interfacial problems are important in a wide range of engineering applications. Hot sections in turbine engines have components with dove-tail joints with discrete interfaces that uniformly transmit mechanical and thermal fluxes across the interface in addition to satisfying the impenetrability condition in the mechanical field and the continuity of the temperature field.

Coupled thermomechanical formulations and methods have classically been developed in the context of continuous Galerkin framework. From an algorithmic perspective, emphasis has been on the staggered solution schemes that find roots in operator splitting methodologies. Although staggered algorithms are computationally economical, a series drawback is their first-order accuracy in most of the cases. Developing second order accurate staggered algorithms requires algorithmic simplification of the coupling physics, and is therefore neither easy nor straightforward. Furthermore, simplifying the coupled physics, especially in the context of highly coupled phenomena reduces the range of applicability of the resulting method. In [6], Armero and Simo developed a continuous Galerkin method, and presented fractional step solution techniques for

thermomechanical problems. Two strategies termed as (i) isothermal split, and (ii) adiabatic split were presented, and method based on adiabatic split was shown to be unconditionally stable for a range of material parameters. With a small implementation strategy that is based on local solution of the thermal equation at the integration point of the element during the mechanical evolution part, the method was shown to attain second-order accuracy. In the work of Miche [108] these methods were extended to finite strain regime. Several recent work address this important class of coupled field problems [72,135,154].

To address the class of problems with embedded interfaces that require enforcement of the continuum based conditions of continuity of the fields and their flux across the interface, methods that are based on penalty function formulation [8] and Lagrange multiplier formulation have been proposed [61,80]. Since the objective of the current Chapter is to account for the evolution of interfacial kinetics and interfacial kinematics, therefore penalty function formulation would not work because the penalty parameter, which is selected rather arbitrarily, can mask entire interfacial physics. Lagrange multiplier approach [61,80] would also not be appropriate here because, in the context of mechanical fields, Lagrange multiplier has the connotation of force type quantity, which under increasing external loads, would provide quantitative evaluation of the internal force needed to maintain the kinematic constraints, but it can not model the evolving interfacial kinematics. A third method, Nitsche method [120] that is based on motion of Discontinuous Galerkin (DG) methods [59,107,122,170] has been proposed in the literature [12,58,60,116,140]. While Nitsche method models interfacial continuity via flux based terms, it requires parameters to be selected for numerical implementation of the strategy. For linear elastic systems which discretization on either side of the interface of the same polynomial order as well as same spatial length scale ‘h’, these parameters are selected as $\delta = 1/2$ for both sides. There is substantial literature [9,122,140] shows that this selection is appropriate for (i) homogenous elastic mechanics, (ii) same element types and order and (iii) same order of material coefficients across the boundary. For problems where material coefficients are widely varied, or for cases which geometric nonlinearity, these parameters need to evolve as a function of stress averaging and area averaging. However, the techniques proposed to where these parameters evolve are neither ad hoc for which multiple options are provided to address this issue [42,52,53,107,141].

In our earlier work, we developed a framework for stabilized interface formulations that seamlessly couples scalar and vector field problems [99,101] on adjacent subdomains. Method

was applied to the modeling of joints, and to problems with incompatible spatial discretization on adjoining subdomains with a common boundary [159,162]. This method was then extended to the case of evolving interfacial damage wherein the subdomain boundaries at the common interface could evolve independently of each other, thus accommodating interfacial damage. An important feature of the developments was that the stability terms were variationally derived and were shown to be functions of the evolving material and geometric nonlinearity.

In this Chapter, we extend our framework to multi-field interfacial problems. The objectives of this Chapter are two folds. First, develop a Variational framework that accommodates the presence of embedded weak discontinuities in the field which may evolve into strong discontinuities. This requires the provision for application of interfacial kinematic or kinetic conditions or embedding of interfacial evolution models across the embedded planes of discontinuity. Secondly, in the interest of not simplifying the coupling physics a priori, we aim to develop a fully coupled solution procedure that accounts for the evolution of all the field variables concurrently, and wherein one can develop consistent tangent tensors for quadratic convergence of the nonlinear iterative solution procedure.

An outline of the Chapter is as follows. Section 6.2 presents the governing system of equations for the coupled thermomechanical system. Section 6.3 presents multiscale decomposition of the thermal and mechanical fields in the context of finite deformation kinematics. A stabilized interfacial formulation, in the context of the thermal problem, is discussed in section 6.3.1 and 6.3.2. Numerical test cases are shown in section 6.4 and conclusions are drawn in section 6.5.

6.2 Governing Equations and Coupled Interfacial Weak Forms

Evolving embedded interfaces in the finite deformation context, where interfaces not only undergo finite deformation but also produce interfacial gaps, are shown in Figure 6.1. Herein, an open bounded region $\Omega \subset \mathbb{R}^{n_{sd}}$ is cut into two disjoint regions $\Omega^{(1)}$ and $\Omega^{(2)}$ by an interface of interest Γ_I. Points in the reference configuration are donated by $\boldsymbol{X} \in \Omega^{(1)} \bigcup \Omega^{(2)}$ and their corresponding images in the current configuration by $\boldsymbol{x}$. The two bodies deform according to the motion $\boldsymbol{\phi}^{(\alpha)}\left(\boldsymbol{X},t\right)$ that maps the reference configuration to the current configuration, $\boldsymbol{x} = \boldsymbol{\phi}^{(\alpha)}\left(\boldsymbol{X},t\right)$. The displacement field associated with the deformation $\boldsymbol{\phi}^{(\alpha)}$ is defined as $\boldsymbol{u}^{(\alpha)}\left(\boldsymbol{X},t\right) = \boldsymbol{\phi}^{(\alpha)}\left(\boldsymbol{X},t\right) - \boldsymbol{X}$.

The absolute temperature field over Ω is denoted as $\theta(\boldsymbol{X},t):\bar{\Omega}\to\mathbb{R}_{+}\,(\theta>0)$. The deformation gradient $\boldsymbol{F}^{(\alpha)}$ is defined as follows:

$$\boldsymbol{F}(\boldsymbol{X},t)=\frac{\partial \boldsymbol{x}}{\partial \boldsymbol{X}}=\mathrm{GRAD}\,\boldsymbol{x} \tag{6-1}$$

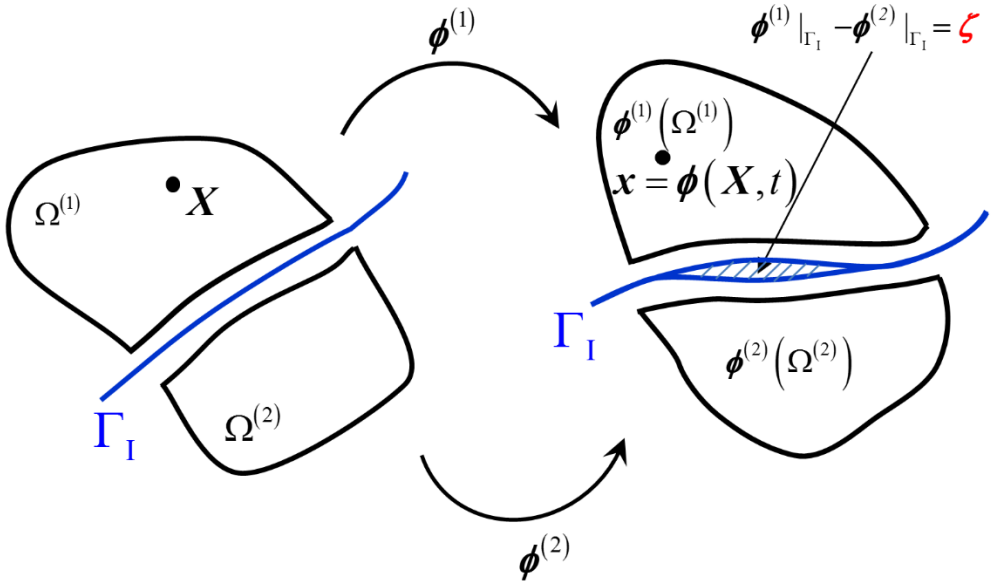

(a) (b)

Figure 6.1. Domain Ω with interface Γ_I with deformed configurations $\boldsymbol{\phi}^{(1)}$ and $\boldsymbol{\phi}^{(2)}$: (a) reference configurations; (b) current configurations.

We allow the deformations $\boldsymbol{\phi}^{(\alpha)}$ to be distinct along the interface Γ_I to accommodate the existence of the interface gap or debonding $\boldsymbol{\zeta}$ as illustrated in Figure 6.1 (b). Throughout, we denote quantities with counterparts in both regions by a superscript (α), where α takes the value 1 or 2. The interior domains $\Omega^{(1)}$ and $\Omega^{(2)}$ remain compatible and equilibrated within each sub-region. The equilibrium equations and boundary conditions for each region $\Omega^{(\alpha)}$ are supplemented with the discontinuity evolution equation and the balance of traction conditions along Γ_I. The Lagrangian form of balance of momentum and balance of energy then takes the form:

$$\dot{\boldsymbol{\phi}}^{(\alpha)}(\boldsymbol{X},t)=\boldsymbol{V}^{(\alpha)}(\boldsymbol{X},t) \qquad \text{in} \quad \Omega^{(\alpha)}\times]0,\mathrm{T}[,\ \alpha=1,2 \tag{6-2}$$

$$\rho_0 \ddot{\boldsymbol{\phi}}^{(\alpha)} = \mathrm{DIV}\, \boldsymbol{P}^{(\alpha)}\left(\boldsymbol{F}^{(\alpha)}\right) + \rho_o^{(\alpha)} \boldsymbol{B}^{(\alpha)} \qquad \text{in} \quad \Omega^{(\alpha)} \times]0, \mathrm{T}[, \ \alpha = 1,2 \tag{6-3}$$

$$\rho_0 C_F \dot{\theta}^{(\alpha)} = -\mathrm{DIV}\left(\boldsymbol{Q}^{(\alpha)}\right) + \mathcal{D}_{\mathrm{int}}^{(\alpha)} - \mathcal{H}_{\mathrm{EI}}^{(\alpha)} + R^{(\alpha)} \quad \text{in} \quad \Omega^{(\alpha)} \times]0, \mathrm{T}[, \ \alpha = 1,2 \tag{6-4}$$

$$\boldsymbol{\phi}^{(1)} - \boldsymbol{\phi}^{(2)} = \boldsymbol{\zeta} \qquad \text{on} \ \Gamma_{\mathrm{I}} \tag{6-5}$$

$$\theta^{(1)} - \theta^{(2)} = 0 \qquad \text{on} \ \Gamma_{\mathrm{I}} \tag{6-6}$$

$$-\boldsymbol{P}^{(1)} \cdot \boldsymbol{N}^{(1)} + \boldsymbol{\lambda}_1 = \boldsymbol{0} \qquad \text{on} \ \Gamma_{\mathrm{I}} \tag{6-7}$$

$$-\boldsymbol{P}^{(2)} \cdot \boldsymbol{N}^{(2)} - \boldsymbol{\lambda}_1 = \boldsymbol{0} \qquad \text{on} \ \Gamma_{\mathrm{I}} \tag{6-8}$$

$$\boldsymbol{Q}^{(1)} \cdot \boldsymbol{N}^{(1)} - \lambda_2 = \boldsymbol{0} \qquad \text{on} \ \Gamma_{\mathrm{I}} \tag{6-9}$$

$$\boldsymbol{Q}^{(2)} \cdot \boldsymbol{N}^{(2)} + \lambda_2 = \boldsymbol{0} \qquad \text{on} \ \Gamma_{\mathrm{I}} \tag{6-10}$$

where $\boldsymbol{Q}^{(\alpha)}$ is the heat flux vector, $\mathcal{D}_{\mathrm{int}}$ is the internal dissipation, $R^{(\alpha)}$ is the heat resource. For a free energy function $\Psi\left(\boldsymbol{F}, \theta, \boldsymbol{G}\right)$ (per unit reference volume), $C_F := -\theta \partial_{\theta\theta}^2 \Psi$ is the specific heat at constant deformation, $\mathcal{H}_{\mathrm{EI}} := -\underbrace{\theta \partial_{\theta \boldsymbol{F}}^2 \Psi : \dot{\boldsymbol{F}}}_{\text{Elasitc}} - \underbrace{\theta \partial_{\theta \boldsymbol{G}}^2 \Psi : \dot{\boldsymbol{G}}}_{\text{Inelastic}}$ is the elastic-inelastic structural heating, $\boldsymbol{G}$ is a general set of internal variables representing the inelastic response of the material. The relative temperature with respect to the reference temperature can be defined as $\vartheta^{(\alpha)} = \theta^{(\alpha)} - \theta_{\mathrm{ref}}^{(\alpha)}$.

Eqn. (6-5) facilitates the non-conforming evolution of the interfaces that are subject to impenetrability constraint and phenomenological and/or physics based interfacial kinematics. Eqn. (6-6) constraints the continuity of the temperature field over the two adjoining domains. In (6-1) to (6-10), $\boldsymbol{B}^{(\alpha)}$ is the mass-specific body force, $\rho_o^{(\alpha)} > 0$ is the referential mass density, $\mathrm{DIV}(\bullet) = \mathrm{tr}\left[\mathrm{GRAD}(\bullet)\right]$ is the material divergence operator, and $\boldsymbol{N}^{(\alpha)}$ is the unit outward normal to the interface boundary Γ_{I}. The first Piola-Kirchhoff stress tensor is denoted by $\boldsymbol{P}^{(\alpha)}$, and we restrict our discussion to hyperelastic materials such that $\boldsymbol{P} = \partial_{\boldsymbol{F}} \mathcal{W}$ is derived from an associated strain energy density function $\mathcal{W}^{(\alpha)}\left(\boldsymbol{F}^{(\alpha)}; \boldsymbol{X}\right)$. The Lagrange multipliers $\boldsymbol{\lambda}_1$ and λ_2 are introduced to enforce the equilibrium of the tractions and the equilibrium of the heat flux across the interface Γ_{I}. The traction terms are only operational when the two subdomains are in contact at Γ_{I}. Once fully debonded, the traction terms vanish automatically and uniformly.

The case of multiple interfaces can be accommodated by a straightforward generalization. We specify the functional spaces as follows:

$$\mathcal{S}_{\phi}^{(\alpha)} = \left\{ \boldsymbol{\phi}^{(\alpha)} \;\middle|\; \begin{array}{l} \boldsymbol{\phi}^{(\alpha)} \in \left[H^1\left(\Omega^{(\alpha)}\right) \right]^{n_{\mathrm{sd}}},\ \det\left(\boldsymbol{F}^{(\alpha)}\right) > 0, \boldsymbol{\phi}^{(\alpha)}\big|_{\Gamma^{(\alpha)}\setminus\Gamma_{\mathrm{I}}} = \boldsymbol{X}^{(\alpha)}, \\ \boldsymbol{\phi}^{(\alpha)}\left(\cdot,0\right) = \boldsymbol{\phi}_0^{(\alpha)} \end{array} \right\} \tag{6-11}$$

$$\mathcal{S}_{\theta}^{(\alpha)} = \left\{ \theta^{(\alpha)} \;\middle|\; \theta^{(\alpha)} \in \left[H^1\left(\Omega^{(\alpha)}\right) \right]^{n_{\mathrm{sd}}}, \theta^{(\alpha)}\left(\cdot,0\right) = \theta_0^{(\alpha)} \right\} \tag{6-12}$$

$$\mathcal{V}_{\phi}^{(\alpha)} = \left\{ \boldsymbol{\eta}_o^{(\alpha)} \;\middle|\; \boldsymbol{\eta}_o^{(\alpha)} \in \left[H_o^1\left(\Omega^{(\alpha)}\right) \right]^{n_{\mathrm{sd}}},\ \boldsymbol{\eta}_o^{(\alpha)}\big|_{\Gamma^{(\alpha)}\setminus\Gamma_{\mathrm{I}}} = \boldsymbol{0} \right\} \tag{6-13}$$

$$\mathcal{V}_{\theta}^{(\alpha)} = \left\{ \omega_o^{(\alpha)} \;\middle|\; \omega_o^{(\alpha)} \in \left[H_o^1\left(\Omega^{(\alpha)}\right) \right],\ \omega_o^{(\alpha)}\big|_{\Gamma^{(\alpha)}\setminus\Gamma_{\mathrm{I}}} = 0 \right\} \tag{6-14}$$

$$\mathcal{Q}_{\phi} = \left\{ \boldsymbol{\lambda}_1 \;\middle|\; \boldsymbol{\lambda}_1 \in \left[H^{-\frac{1}{2}}\left(\Gamma_{\mathrm{I}}\right) \right]^{n_{\mathrm{sd}}} \right\} \tag{6-15}$$

$$\mathcal{Q}_{\theta} = \left\{ \lambda_2 \;\middle|\; \lambda_2 \in \left[H^{-\frac{1}{2}}\left(\Gamma_{\mathrm{I}}\right) \right] \right\} \tag{6-16}$$

$$\mathcal{P}_{\phi} = \left\{ \boldsymbol{\mu}_1 \;\middle|\; \boldsymbol{\mu}_1 \in \left[H^{-\frac{1}{2}}\left(\Gamma_{\mathrm{I}}\right) \right]^{n_{\mathrm{sd}}} \right\} \tag{6-17}$$

$$\mathcal{P}_{\theta} = \left\{ \mu_2 \;\middle|\; \mu_2 \in \left[H^{-\frac{1}{2}}\left(\Gamma_{\mathrm{I}}\right) \right] \right\} \tag{6-18}$$

A formal statement of the standard weak form is: Find $\left\{ \boldsymbol{\phi}^{(\alpha)}, \theta^{(\alpha)}, \boldsymbol{\lambda}_1, \lambda_2 \right\} \in \mathcal{S}_{\phi}^{(\alpha)} \times \mathcal{S}_{\theta}^{(\alpha)} \times \mathcal{Q}_{\phi} \times \mathcal{Q}_{\theta}$ such that for all $\left\{ \boldsymbol{\eta}_o^{(\alpha)}, \omega_0^{(\alpha)}, \boldsymbol{\mu}_1, \mu_2 \right\} \in \mathcal{V}_{\phi}^{(\alpha)} \times \mathcal{V}_{\theta}^{(\alpha)} \times \mathcal{P}_{\phi} \times \mathcal{P}_{\theta}$:

(i) Weak form of balance of momentum

$$\begin{aligned} &\sum_{\alpha=1}^{2} \int_{\Omega^{(\alpha)}} \left[\rho_0 \ddot{\boldsymbol{\phi}}^{(\alpha)} \cdot \boldsymbol{\eta}_o^{(\alpha)} + \mathrm{GRAD}\, \boldsymbol{\eta}_o^{(\alpha)} : \boldsymbol{P}^{(\alpha)} - \rho_o^{(\alpha)} \boldsymbol{B}^{(\alpha)} \cdot \boldsymbol{\eta}_o^{(\alpha)} \right] \mathrm{d}V \\ &- \sum_{\alpha=1}^{2} \int_{\Gamma^{(\alpha)}\setminus\Gamma_{\mathrm{I}}} \boldsymbol{T}^{(\alpha)} \cdot \boldsymbol{\eta}_o^{(\alpha)} \mathrm{d}A - \int_{\Gamma_{\mathrm{I}}} \boldsymbol{\lambda}_1 \cdot [\![\boldsymbol{\eta}_o]\!] \, \mathrm{d}\Gamma_{\mathrm{I}} = 0 \end{aligned} \tag{6-19}$$

(ii) Continuity equation for the displacement field

$$-\int_{\Gamma_{\mathrm{I}}} \boldsymbol{\mu}_1 \cdot \left([\![\boldsymbol{\phi}]\!] - \boldsymbol{\zeta} \right) \mathrm{d}\Gamma_{\mathrm{I}} = 0 \tag{6-20}$$

(iii) Balance of energy

$$\sum_{\alpha=1}^{2}\int_{\Omega^{(\alpha)}}\left[-\rho_0 C_F\,\dot{\theta}\cdot\omega_o^{(\alpha)}+\mathrm{GRAD}\,\omega_o^{(\alpha)}\cdot\boldsymbol{Q}^{(\alpha)}-\mathcal{H}_{\mathrm{EI}}\cdot\omega_o^{(\alpha)}+\mathcal{D}_{\mathrm{int}}\cdot\omega_o^{(\alpha)}+R^{(\alpha)}\cdot\omega_o^{(\alpha)}\right]\mathrm{d}V$$
$$-\sum_{\alpha=1}^{2}\int_{\Gamma^{(\alpha)}\setminus\Gamma_{\mathrm{I}}}\bar{Q}^{(\alpha)}\cdot\omega_o^{(\alpha)}\,\mathrm{d}A-\underbrace{\int_{\Gamma_{\mathrm{I}}}\lambda_2\cdot\left[\!\left[\omega_o\right]\!\right]\mathrm{d}\Gamma_{\mathrm{I}}}_{\text{heat flux cont.}}=0 \tag{6-21}$$

(iv) Continuity equation for temperature

$$\underbrace{-\int_{\Gamma_{\mathrm{I}}}\mu_2\cdot\left(\left[\!\left[\theta\right]\!\right]\right)\mathrm{d}\Gamma_{\mathrm{I}}}_{\text{temperature cont.}}=0 \tag{6-22}$$

where $\boldsymbol{T}=\boldsymbol{P}\cdot\boldsymbol{N}$ is the traction and $\bar{Q}=\boldsymbol{Q}\cdot\boldsymbol{N}$ is the heat flux at boundaries $\Gamma\setminus\Gamma_{\mathrm{I}}$.

The Lagrange multiplier field $\boldsymbol{\lambda}_1$ in (6-19) has the connotation of the traction field while λ_2 in Eqn. (6-21) has the connotation of heat flux at Γ_{I}. Eqn. (6-20) and (6-22) weakly enforce the jump continuity for the corresponding fields where $\left[\!\left[\bullet\right]\!\right]=(\bullet)^{(1)}-(\bullet)^{(2)}$ is the jump operator defined for vector-valued fields on interface Γ_{I}. Although this definition depends on the ordering of the domains as in [84], the final weak form is independent of sub-domain ordering.

We make two assumptions to simplify the thermal interfacial sub-problem. Firstly, we assume that the system obeys the Fourier's law for heat conduction which is motivated by the experimental observations [66] to ensure the satisfaction of the Clausius-Duhem inequality. Thus, the spatial heat flux vector or Cauchy heat flux vector in the current configuration is given by

$$\boldsymbol{q}=-\boldsymbol{k}(\theta)\nabla\theta \tag{6-23}$$

where $\nabla\theta$ is the spatial temperature gradient. By using Nanson's formula to directly equate the heat energy rate of the reference configuration with respect to the current configuration [66] the heat flux term in the reference configuration is served as a pull-back of Cauchy heat flux term, i.e. $\boldsymbol{Q}=J\boldsymbol{F}^{-1}\boldsymbol{q}$. By substituting (6-24) into it, the Piola–Kirchhoff heat flux term $\boldsymbol{Q}$ is taken to be

$$\boldsymbol{Q}=-\boldsymbol{k}^{*}(\theta)\boldsymbol{C}^{-1}\mathrm{GRAD}\theta \tag{6-24}$$

where $\boldsymbol{C}=\boldsymbol{F}^{\mathrm{T}}\boldsymbol{F}$ is the right Cauchy-Green tensor, and $\boldsymbol{k}^{*}=k^{*}\mathbf{I}$ is the thermal conductivity tensor with respect to the reference configuration, i.e. $\boldsymbol{k}^{*}=J\boldsymbol{k}(\theta)$, and coefficient k^{*} is taken of the form:

$$k^*(\theta) = k^*(\theta_{\text{ref}})\left[1 - \beta_k(\theta - \theta_{\text{ref}})\right] \tag{6-25}$$

where $k^*(\theta_{\text{ref}})$ is the thermal conductivity at $T = \theta_{\text{ref}}$ and β_k is the softening parameter. The pull-back thermal conductivity $\boldsymbol{K}_\theta$ is expressed in terms of the current thermal conductivity as $\boldsymbol{K}_\theta = J\boldsymbol{F}^{-1}\boldsymbol{k}(\theta)\boldsymbol{F}^{-T}$ [154]. The relation between the reference $\boldsymbol{k}_0$, spacial $\boldsymbol{k}$, and the pull back $\boldsymbol{K}_\theta$ is very critical when pushing forward from the reference configuration to the current configuration.

Secondly, we assume there is no internal dissipation or plastic structural heating; i.e., $\boldsymbol{G} = \boldsymbol{0}$ and $\mathcal{D}_{\text{int}} = 0$ in Eqn. (6-21). This assumption leads to a simplification of the elastic-inelastic structural heating $\mathcal{H}_{EI}$, namely, the second term in this equation drops and $\mathcal{H}_{\text{EI}} := \underbrace{-\theta\mathcal{D}^2_{\theta\boldsymbol{F}}\Psi : \dot{\boldsymbol{F}}}_{\text{Elasitc}}$. Quasi-static condition is considered such that $\ddot{\boldsymbol{\phi}} = \boldsymbol{0}$.

For the clarity of ideas we first focus on the derivation of the stabilized interface thermal formulation. In our earlier works in Chapter 3 we presented stabilized interface formulation for the mechanical field. Accordingly, for the stabilized coupled formulation we draw from Chapter 3, we modify the method accordingly. We then bring it together with the stabilized interfacial mechanical problem Chapter 3 in the context of finite thermoelasticity and present the fully coupled formulation.

6.3 The Stabilized Interface Form of the Thermal Problem

Following the work in Chapter 3 and [101], we decompose the solution fields for both temperature and deformation map into coarse scale and fine scale fields, as illustrated via a computational mapping in Figure 6.2. We assume an overlapping decomposition of the deformation map $\boldsymbol{\phi}^{(\alpha)}$ in each region $\Omega^{(\alpha)}$ consisting of a fine-scale deformation $\tilde{\boldsymbol{\phi}}^{(\alpha)}$ superimposed upon a coarse-scale deformation $\hat{\boldsymbol{\phi}}^{(\alpha)}$, where the coarse-scale deformation $\hat{\boldsymbol{\phi}}^{(\alpha)}$ contains both thermal deformation map $\boldsymbol{\phi}_\theta$ and mechanical deformation map $\overline{\boldsymbol{\phi}}$. This deformation can be expressed in terms of the multiscale displacement field as follows:

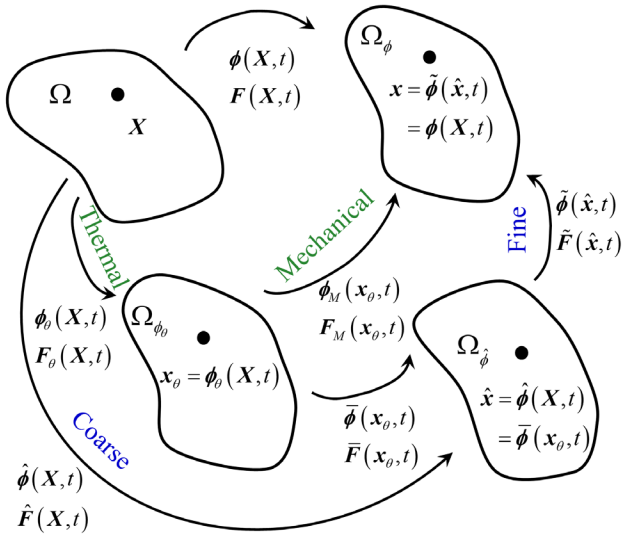

Figure 6.2. Multiscale composition of mappings $\boldsymbol{\phi}(\boldsymbol{x},t)$ for region Ω.

$$\hat{\boldsymbol{\phi}}(\boldsymbol{X},t)=\bar{\boldsymbol{\phi}}\circ\boldsymbol{\phi}_\theta=\boldsymbol{X}+\hat{\boldsymbol{u}}=\boldsymbol{x}_\theta+\bar{\boldsymbol{u}}=\boldsymbol{X}+\boldsymbol{u}_\theta+\bar{\boldsymbol{u}}\equiv\hat{\boldsymbol{x}} \tag{6-26}$$

$$\boldsymbol{\phi}(\boldsymbol{X},t)=\tilde{\boldsymbol{\phi}}\circ\bar{\boldsymbol{\phi}}\circ\boldsymbol{\phi}_\theta=\tilde{\boldsymbol{\phi}}\circ\hat{\boldsymbol{\phi}}=\boldsymbol{X}+\boldsymbol{u}_\theta+\bar{\boldsymbol{u}}+\tilde{\boldsymbol{u}}=\boldsymbol{X}+\hat{\boldsymbol{u}}+\tilde{\boldsymbol{u}} \tag{6-27}$$

From (6-26) and (6-27), we arrive at a relation between the total displacement and its coarse and fine-scale displacement components as follows:

$$\hat{\boldsymbol{u}}=\boldsymbol{u}_\theta+\bar{\boldsymbol{u}} \tag{6-28}$$

$$\boldsymbol{u}=\hat{\boldsymbol{u}}+\tilde{\boldsymbol{u}} \tag{6-29}$$

As highlighted in [101], a multiplicative decomposition of the deformation gradient $\boldsymbol{F}^{(\alpha)}$ follows from substituting (6-26) and (6-28) into (6-1):

$$\begin{aligned}\boldsymbol{F}(\boldsymbol{X},t)&=\frac{\partial\boldsymbol{x}}{\partial\boldsymbol{X}}=\frac{\partial\boldsymbol{x}}{\partial\bar{\boldsymbol{x}}}\frac{\partial\bar{\boldsymbol{x}}}{\partial\boldsymbol{x}_\theta}\frac{\partial\boldsymbol{x}_\theta}{\partial\boldsymbol{X}}\\&=\underbrace{\left[\boldsymbol{1}_{\tilde{\phi}}+\nabla_{\bar{\boldsymbol{x}}}\tilde{\boldsymbol{u}}\right]}_{\text{Fine-mech}}\underbrace{\left[\boldsymbol{1}_{\bar{\phi}}+\nabla_{\boldsymbol{x}_\theta}\bar{\boldsymbol{u}}\right]}_{\text{Coarse-mech}}\underbrace{\left[\boldsymbol{1}_{\phi_\theta}+\nabla_{X}\boldsymbol{u}_\theta\right]}_{\text{Thermal}}\\&\equiv\tilde{\boldsymbol{F}}\bar{\boldsymbol{F}}\boldsymbol{F}_\theta\\&=\tilde{\boldsymbol{F}}\hat{\boldsymbol{F}}\left(\text{fine and coarse scales}\right)\\&=\boldsymbol{F}_m\boldsymbol{F}_\theta\left(\text{mechanical and thermal fields}\right)\end{aligned} \tag{6-30}$$

where $\hat{\boldsymbol{F}}=\bar{\boldsymbol{F}}\boldsymbol{F}_\theta$ is the deformation gradient based decomposition of the coarse scales into mechanical and thermal fields. In terms of the physical fields, this deformation gradient can be

expressed as $\boldsymbol{F}\left(\boldsymbol{X},t\right)=\boldsymbol{F}_m\boldsymbol{F}_\theta$ where $\boldsymbol{F}_m=\tilde{\boldsymbol{F}}\bar{\boldsymbol{F}}$, as shown in (6-30).

In our recent developments, we elected to represent the coarse-scale field $\hat{\boldsymbol{\phi}}^{(\alpha)}$ using piecewise continuous finite element functions in each region $\Omega^{(\alpha)}$. The fine-scale field $\tilde{\boldsymbol{\phi}}^{(\alpha)}$ is treated as being local to the interface in a manner similar to [100] as well as in Chapter 3 and Chapter 4.

The multiscale decomposition for the thermal part is shown in Figure 6.3. As temperature is a scale field, we assume the total solution is a combination of the coarse scale solution $\hat{\theta}$ and a fine scale solution $\tilde{\theta}$ with the following relations:

$$\theta=\hat{\theta}+\tilde{\theta} \tag{6-31}$$

The same decomposition applies to the weighing function ω_o:

$$\omega_o=\hat{\omega}_o+\tilde{\omega}_o \tag{6-32}$$

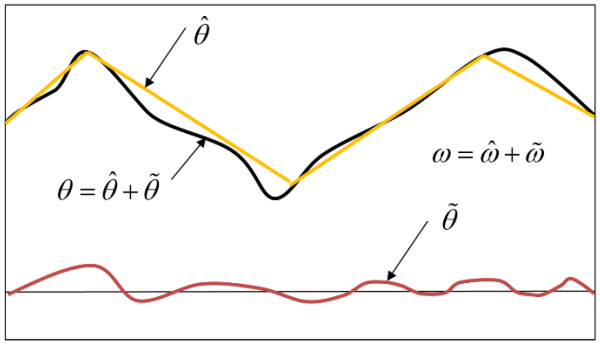

Figure 6.3. Multiplicative split of the temperature field θ.

Though the displacement field is assumed additively decomposed, and in the nonlinear regime this decomposition is to be viewed in the sense of projections, the Lagrange multiplier fields are not decomposed and therefore weak enforcement of jump continuity only contributes to the coarse scale model. Accordingly, the weak forms (6-21) and (6-22) can be separated into the following interfacial sub problems.

Balance of Energy and Continuity of Temperature:

Coarse-Scale Problem $\mathcal{C}_T$

$$
\begin{aligned}
&\hat{R}_\theta\left(\hat{\omega}_o^{(\alpha)};\hat{\theta}^{(\alpha)},\tilde{\theta}^{(\alpha)},\lambda_2\right)\\
&=\sum_{\alpha=1}^{2}\int_{\Omega^{(\alpha)}}\left[-\rho_0 C_F\left(\dot{\hat{\theta}}^{(\alpha)}+\dot{\tilde{\theta}}^{(\alpha)}\right)\cdot\hat{\omega}_o^{(\alpha)}+\mathrm{GRAD}\,\hat{\omega}_o^{(\alpha)}\cdot\boldsymbol{Q}^{(\alpha)}-\mathcal{H}_{\mathrm{EI}}\cdot\hat{\omega}_o^{(\alpha)}+R\cdot\hat{\omega}_o^{(\alpha)}\right]\mathrm{d}V\\
&-\sum_{\alpha=1}^{2}\int_{\Gamma^{(\alpha)}\setminus\Gamma_{\mathrm{I}}}\bar{Q}^{(\alpha)}\cdot\hat{\omega}_o^{(\alpha)}\,\mathrm{d}A-\underbrace{\int_{\Gamma_{\mathrm{I}}}\lambda_2\cdot\left[\!\left[\hat{\omega}_o\right]\!\right]\mathrm{d}\Gamma_{\mathrm{I}}}_{\text{heat flux cont.}}=0
\end{aligned}
\tag{6-33}
$$

$$
R_{\mu_2}\left(\mu_2,\hat{\theta}^{(\alpha)},\tilde{\theta}^{(\alpha)}\right)=\underbrace{-\int_{\Gamma_{\mathrm{I}}}\mu_2\cdot\left(\left[\!\left[\hat{\theta}\right]\!\right]+\left[\!\left[\tilde{\theta}\right]\!\right]\right)\mathrm{d}\Gamma_{\mathrm{I}}}_{\text{temperature cont.}}=0
\tag{6-34}
$$

Fine-Scale Problem $\mathcal{F}_T$

$$
\begin{aligned}
&\tilde{R}_\theta\left(\tilde{\omega}_o^{(\alpha)};\hat{\theta}^{(\alpha)},\tilde{\theta}^{(\alpha)},\lambda_2\right)\\
&=\sum_{\alpha=1}^{2}\int_{\Omega^{(\alpha)}}\left[-\rho_0 C_F\left(\dot{\hat{\theta}}^{(\alpha)}+\dot{\tilde{\theta}}^{(\alpha)}\right)\cdot\tilde{\omega}_o^{(\alpha)}+\mathrm{GRAD}\,\tilde{\omega}_o^{(\alpha)}\cdot\boldsymbol{Q}^{(\alpha)}+R\cdot\tilde{\omega}_o^{(\alpha)}\right]\mathrm{d}V\\
&-\sum_{\alpha=1}^{2}\int_{\Gamma^{(\alpha)}\setminus\Gamma_{\mathrm{I}}}\bar{Q}^{(\alpha)}\cdot\tilde{\omega}_o^{(\alpha)}\,\mathrm{d}A-\underbrace{\int_{\Gamma_{\mathrm{I}}}\lambda_2\cdot\left[\!\left[\tilde{\omega}_o\right]\!\right]\mathrm{d}\Gamma_{\mathrm{I}}}_{\text{heat flux cont.}}=0
\end{aligned}
\tag{6-35}
$$

With the assumption that scale split is local to Γ_{I}, the fine-scale sub problems are defined only over a narrow band across the interface Γ_{I}.

As in eqn. (6-33) to (6-35), the Lagrange multiplier λ_2 and the coarse and fine temperature field $\hat{\theta}^{(\alpha)}$ and $\tilde{\theta}^{(\alpha)}$ are unknowns. Since the coupled equations (6-19) and (6-20) with the mechanical unknowns $\boldsymbol{\phi}^{(\alpha)}$ in equations, and equations (6-21) and (6-22) contain both the Lagrange multiplier and the solution field temperature unknowns $\theta^{(\alpha)}$ to solve for, we adopt a strategy that is similar to our earlier work in the context of mechanical field [101,162] and Chapter 3. Since stabilization of the mechanical field is presented in [101,162], in this work we focus our attention primarily to the thermal problem. Then, in section 6.3.2 we bring together the combined thermomechanical stabilized interface formulation.

6.3.1. Derivation of Stabilized Form for the Thermal Sub-problem

In the following section, the objective is to develop a stabilized form for a thermal problem which is achieved through a three-stage modeling process. First, the fine-scale equation (6-35) is localized to the vicinity of the interface Γ_{I} and subsequently linearized to obtain a closed-form

expression for $\tilde{\theta}^{(\alpha)}$ in terms of $\hat{\theta}^{(\alpha)}$ and λ_2. Second, this fine-scale model is substituted into (6-34) to yield a piecewise expression for λ_2 in terms of $\hat{\theta}^{(\alpha)}$. Finally, these models for λ_2 and $\hat{\theta}^{(\alpha)}$ are consistently embedded into (6-33) to remove the explicit appearance of $\tilde{\theta}^{(\alpha)}$ and λ_2 while modeling their effects.

***Remark**: To keep the fine scales simple, the structural elastic heating $\mathcal{H}_{\mathrm{EI}}$ appears in coarse scale problem equation (6-33) only.*

6.3.2. Modeling of Fine Scales

At this point our objective is to develop a model for the fine-scale temperature field in the vicinity of Γ_{I}. To keep the modeling effort simple, we assume a piece-wise constant-in-time approximation for the fine-scale temperature field, i.e., $\dot{\tilde{\theta}}^{(\alpha)} = 0$. This helps drop the time rate of change of temperature field from (6-35). In this case, $\dot{\hat{\theta}}^{(\alpha)} = \dot{\theta}^{(\alpha)}$. In addition, we assume $\dot{\tilde{\boldsymbol{F}}}_{\theta} = \mathbf{0}$ for the fine-scale problem which means that we are ignoring $\mathcal{H}_{\mathrm{EI}}$ in our fine scale variational problem.

***Remark:** $\dot{\tilde{\boldsymbol{F}}}_{\theta} = \mathbf{0}$ amounts to fine scale thermal field helping in stabilizing the thermal interface problem with negligible effect on the geometric deformation of the interface Γ_{I}.*

As adopted in [162] and Chapter 3, we approximate the fine scales using edge bubble functions which are only supported within the sectors $\pi_s^{(\alpha)}$ next to the interface segments γ_s. The expressions for incremental fine scales and weighting functions as edge bubble functions are as follows:

$$\Delta\tilde{\theta}^{(\alpha)}\Big|_{\pi_s^{(\alpha)}} = \Delta\beta_s^{\theta(\alpha)} b_s^{\theta(\alpha)}(\boldsymbol{X}), \qquad \tilde{\omega}_o^{(\alpha)}\Big|_{\pi_s^{(\alpha)}} = \chi_s^{\theta(\alpha)} b_s^{\theta(\alpha)}(\boldsymbol{X}) \tag{6-36}$$

We linearize (6-35) with respect to the fine scales $\tilde{\theta}^{(\alpha)}$.The fine scale is treated as an incremental of the coarse scale solution and represented as $\Delta\tilde{\theta}$. First, we linearize the heat flux term $\boldsymbol{Q}^{(\alpha)}$ as follows:

$$\mathrm{D}_{\tilde{\theta}}[\boldsymbol{Q}]\cdot\Delta\tilde{\theta} = \mathrm{D}_{\tilde{\theta}}\left[-\boldsymbol{K}_{\theta}\cdot\mathrm{GRAD}\theta\right]\cdot\Delta\tilde{\theta} = \beta_k k_0 \boldsymbol{I}\Delta\tilde{\theta}\cdot\mathrm{GRAD}\theta - \boldsymbol{K}_{\theta}\cdot\mathrm{GRAD}\Delta\tilde{\theta} \tag{6-37}$$

Therefore, the linearization of (6-35) is

$$\begin{aligned}&\mathrm{D}_{\tilde{\theta}}\tilde{R}_{\theta}\left(\tilde{\omega}_o^{(\alpha)};\hat{\theta}^{(\alpha)},\tilde{\theta}^{(\alpha)},\boldsymbol{\lambda}_2\right)\cdot\Delta\tilde{\theta}=-\tilde{R}_{\theta}\left(\tilde{\omega}_o^{(\alpha)};\hat{\theta}^{(\alpha)},\tilde{\theta}^{(\alpha)},\boldsymbol{\lambda}_2\right)\\&=\sum_{\alpha=1}^{2}\int_{\omega_s^{(\alpha)}}-\mathrm{GRAD}\,\tilde{\omega}_o^{(\alpha)}\cdot\left(-\beta_k k_0\boldsymbol{I}\Delta\tilde{\theta}\cdot\mathrm{GRAD}\theta+\boldsymbol{K}_{\theta}\cdot\mathrm{GRAD}\Delta\tilde{\theta}\right)\mathrm{d}V\end{aligned}\tag{6-38}$$

For simplicity, we drop the contribution of the softening term $-\beta_k k_0\boldsymbol{I}\Delta\tilde{\theta}\cdot\mathrm{GRAD}\theta$ in (6-38).

Next, we substitute the expressions (6-35) into (6-38), and apply the divergence theorem:

$$\begin{aligned}&\sum_{\alpha=1}^{2}\int_{\omega_s^{(\alpha)}}\mathrm{GRAD}\,\tilde{\omega}_o^{(\alpha)}\cdot\boldsymbol{K}_{\theta}\cdot\mathrm{GRAD}\Delta\tilde{\theta}\,\mathrm{d}V\\&=\sum_{\alpha=1}^{2}\int_{\Omega^{(\alpha)}}\left[-\rho_0 C_F\dot{\theta}^{(\alpha)}\cdot\tilde{\omega}_o^{(\alpha)}+\mathrm{GRAD}\,\tilde{\omega}_o^{(\alpha)}\cdot\boldsymbol{Q}^{(\alpha)}+R\cdot\tilde{\omega}_o^{(\alpha)}\right]\mathrm{d}V\\&\quad-\sum_{\alpha=1}^{2}\int_{\Gamma^{(\alpha)}\setminus\Gamma_{\mathrm{I}}}\bar{Q}^{(\alpha)}\cdot\tilde{\omega}_o^{(\alpha)}\,\mathrm{d}A-\underbrace{\int_{\Gamma_{\mathrm{I}}}\lambda_2\cdot\left[\!\left[\tilde{\omega}_o\right]\!\right]\mathrm{d}\Gamma_{\mathrm{I}}}_{\text{heat flux cont.}}\\&\underline{\underline{\text{Divergence Theorem}}}\sum_{\alpha=1}^{2}\int_{\omega_s^{(\alpha)}}\tilde{\omega}_o^{(\alpha)}\cdot\left(-\rho_0 C_F\dot{\theta}^{(\alpha)}-\mathrm{DIV}\left(\boldsymbol{Q}^{(\alpha)}\right)+R\right)\mathrm{d}V\\&\quad+\int_{\gamma_s}\left(\boldsymbol{Q}^{(1)}\boldsymbol{N}^{(1)}-\lambda_2\right)\cdot\tilde{\omega}_o^{(1)}\,\mathrm{d}\gamma_s+\int_{\gamma_s}\left(\lambda_2+\boldsymbol{Q}^{(2)}\boldsymbol{N}^{(2)}\right)\cdot\tilde{\omega}_o^{(2)}\,\mathrm{d}\gamma_s\end{aligned}\tag{6-39}$$

We then solve for (6-39) by substituting the expression for fine scales and weighting functions (6-36).

$$\begin{aligned}&\sum_{\alpha=1}^{2}\int_{\omega_s^{(\alpha)}}\mathrm{GRAD}\left(\chi_s^{\theta(\alpha)}b_s^{\theta(\alpha)}\right)\cdot\boldsymbol{K}_{\theta}\cdot\mathrm{GRAD}\left(\Delta\beta_s^{\theta(\alpha)}b_s^{\theta(\alpha)}\right)\mathrm{d}V\\&=\sum_{\alpha=1}^{2}\int_{\omega_s^{(\alpha)}}\left(\chi_s^{\theta(\alpha)}b_s^{\theta(\alpha)}\right)\cdot\left(-\rho_0 C_F\dot{\theta}^{(\alpha)}-\mathrm{DIV}\left(\boldsymbol{Q}^{(\alpha)}\right)+R\right)\mathrm{d}V\\&+\int_{\gamma_s}\left(\boldsymbol{Q}^{(1)}\boldsymbol{N}^{(1)}-\lambda_2\right)\cdot\left(\chi_s^{\theta(1)}b_s^{\theta(1)}\right)\mathrm{d}\gamma_s+\int_{\gamma_s}\left(\lambda_2+\boldsymbol{Q}^{(2)}\boldsymbol{N}^{(2)}\right)\cdot\left(\chi_s^{\theta(2)}b_s^{\theta(2)}\right)\mathrm{d}\gamma_s\end{aligned}\tag{6-40}$$

Since the fine scale variational problem (6-40) holds for all admissible weighting functions, we obtain the incremental fine scale solution coefficient $\Delta\beta_s^{\theta(\alpha)}$ as follows

$$\begin{aligned}\Delta\beta_s^{\theta(\alpha)}=&\left(\int_{\omega_s^{(\alpha)}}\mathrm{GRAD}\left(b_s^{\theta(\alpha)}\right)\cdot\boldsymbol{K}_{\theta}\cdot\mathrm{GRAD}\left(b_s^{\theta(\alpha)}\right)\mathrm{d}V\right)^{-1}\cdot\\&\left(\begin{array}{l}\displaystyle\int_{\omega_s^{(\alpha)}}\left(b_s^{\theta(\alpha)}\right)\cdot\left(-\rho_0 C_F\dot{\theta}^{(\alpha)}-\mathrm{DIV}\left(\boldsymbol{Q}^{(\alpha)}\right)+R\right)\mathrm{d}V\\\displaystyle+\int_{\gamma_s}\left(\boldsymbol{Q}^{(\alpha)}\boldsymbol{N}^{(\alpha)}+(-1)^{(\alpha)}\lambda_2\right)\cdot\left(b_s^{\theta(\alpha)}\right)\mathrm{d}\gamma_s\end{array}\right)\end{aligned}\tag{6-41}$$

As adopted in [162] and Chapter 3, the following assumptions are applied to further simplify Eqn.

(6-41). Firstly, we apply the mean value theorem to the residual of Euler-Lagrange equation over each sector $\pi_s^{(\alpha)}$ to extract it out of the integral. Specifically, we consider a piecewise constant L_2 projection of the interface residual term $\left(\boldsymbol{Q}^{(\alpha)}\boldsymbol{N}^{(\alpha)}+\left(-1\right)^{(\alpha)}\lambda_2\right)$ over the sector boundaries. Secondly, although the bubble function $b_s^{\theta(\alpha)}$ is not an exactly residual free bubble, we assume the fine scale edge bubbles are orthogonal to the internal residual. Consequently, we assume $\int_{\pi_s^{(\alpha)}}\left(b_s^{\theta(\alpha)}\right)\cdot\left(-\rho_0 C_F\dot{\theta}^{(\alpha)}-\mathrm{DIV}\left(\boldsymbol{Q}^{(\alpha)}\right)+R\right)\mathrm{d}V\approx 0$. Thirdly, one attribute of VMS-based stabilization is that arbitrary combinations of interpolation functions can be employed for expanding the temperature and Lagrange multiplier fields. Lastly, we focus on the trace of the fine scales along the interface and make the following assumption analogous to employing the average value of the bubble function on the element boundaries.

$$\int_{\gamma_s}\left(b_s^{\theta(\alpha)}\right)\mathrm{d}\gamma_s = meas\left(\gamma_s\right)^{-1}\left(\int_{\gamma_s}\left(b_s^{\theta(\alpha)}\right)\mathrm{d}\gamma_s\right)^2 \tag{6-42}$$

Applying (6-42) to (6-41) and substituting back in Eqn. (6-38), the fine scale solution $\Delta\tilde{\theta}$ is obtained as follows

$$\Delta\tilde{\theta}^{(\alpha)} = \tau_s^{\theta(\alpha)}\cdot\left(\left(-1\right)^{\alpha}\lambda_2+\boldsymbol{Q}^{(\alpha)}\cdot\boldsymbol{N}^{(\alpha)}\right) \tag{6-43}$$

where:

$$\tau_s^{\theta(\alpha)} = \left[\mathrm{meas}\left(\gamma_s\right)\right]^{-1}\left(\int_{\gamma_s} b_s^{(\alpha)}\,\mathrm{d}\gamma_s\right)^2\tilde{\tau}_s^{\theta(\alpha)} \tag{6-44}$$

$$\tilde{\tau}_s^{\theta(\alpha)} = \left[\int_{\pi_s^{(\alpha)}}\mathrm{GRAD}\,b_s^{(\alpha)}\cdot\boldsymbol{K}_{\theta}^{(\alpha)}\cdot\mathrm{GRAD}\,b_s^{(\alpha)}dV\right]^{-1} \tag{6-45}$$

One significant attribute of this method is that the expression for the fine scale $\Delta\tilde{\theta}$ is similar in form to the expression given in [38]. The key contribution here is that the residual based fine scale solution incorporates the effects of evolving thermal nonlinearity from either side of the interface through the appearance of the conductivity tensor $\boldsymbol{K}_{\theta}^{(\alpha)}$. These dependencies play a key role in the mathematical properties of the numerical flux and penalty parameter derived in the next section.

Remark: *The fine scale derivation stays form identical to our previous work in Chapter 3 and [160] in the finite strain regime. Interested readers are referred to [162] for the evolution of the fine scales for different PDEs.*

6.3.3. Variational Embedding in the Coarse-scale Problem

The fine scale temperature field $\Delta\tilde{\theta}^{(\alpha)}$ in (6-43) is a function of the Lagrange multiplier field λ_2 which is still an unknown. We therefore focus on the continuity equation (6-34) to obtain an expression for the Lagrange multiplier field λ_2. Following our earlier work in Chapter 3, we require that (6-34) holds for all Lagrange multiplier field μ_2 locally along the interface. We take piecewise constant projection of μ_2 over element interfaces, the integral in (6-34) must vanish sector wise.

$$\left(\left[\!\left[\hat{\theta}\right]\!\right]+\left[\!\left[\Delta\tilde{\theta}\right]\!\right]\right)=0 \tag{6-46}$$

Noting that $\left[\!\left[\cdot\right]\!\right]=(\cdot)^{(1)}-(\cdot)^{(2)}$ and solving (6-46) for λ_2 by substituting (6-43), we arrive at an explicit form for λ_2 as a function of heat flux term $\boldsymbol{Q}^{(\alpha)}$ and coarse scale temperature field $\hat{\theta}$:

$$\lambda_2=\left[\delta_s^{\theta(1)}\cdot\boldsymbol{Q}^{(1)}\cdot\boldsymbol{N}^{(1)}-\delta_s^{\theta(2)}\cdot\boldsymbol{Q}^{(2)}\cdot\boldsymbol{N}^{(2)}\right]+\tau_s^{\theta}\cdot\left(\left[\!\left[\hat{\theta}\right]\!\right]\right) \tag{6-47}$$

where $\tau_s^{\theta}=\left(\tau_s^{\theta(1)}+\tau_s^{\theta(2)}\right)^{-1}$ is the stability tensor term and $\delta_s^{\theta(\alpha)}=\tau_s^{\theta}\cdot\tau_s^{\theta(\alpha)}$ is the flux weighting tensor consisting of the stabilization tensor from both subdomains.

Remark: *We wish to emphasize that this consistent derivation that variationally embeds the interfacial kinematic models is crucial to the derivation of consistent tangent tensors that are fundamental to obtaining quadratic convergence rates when employed in Newton Raphson method.*

By substituting λ_2 into (6-43), a simplified expression for the fine scales results:

$$\Delta\tilde{\theta}^{(\alpha)}=\delta_s^{\theta}\left[\boldsymbol{Q}^{(1)}\cdot\boldsymbol{N}^{(1)}+\boldsymbol{Q}^{(2)}\cdot\boldsymbol{N}^{(2)}\right]+(-1)^{(\alpha)}\delta_s^{\theta(\alpha)T}\cdot\left(\left[\!\left[\hat{\theta}\right]\!\right]\right) \tag{6-48}$$

where

$$\delta_s^{\theta}=\tau_s^{\theta(1)}\cdot\delta_s^{\theta(2)}=\tau_s^{\theta(2)}\cdot\delta_s^{\theta(1)} \tag{6-49}$$

Now we focus on the coarse-scale problem (6-33), and linearize it with respect to fine scale solution $\Delta\tilde{\theta}$ for the heat flux term:

$$
\begin{aligned}
-\hat{R}_\theta\left(\hat{\omega}_o^{(\alpha)};\hat{\theta}^{(\alpha)},\tilde{\theta}^{(\alpha)},\boldsymbol{\lambda}_2\right) &= \mathcal{D}_{\tilde{\theta}}\hat{R}_\theta\left(\hat{\omega}_o^{(\alpha)};\hat{\theta}^{(\alpha)},\tilde{\theta}^{(\alpha)},\boldsymbol{\lambda}_2\right)\cdot\Delta\tilde{\theta} = \mathcal{D}_{\tilde{\theta}}\left[\mathrm{GRAD}\,\hat{\omega}_o^{(\alpha)}\cdot\boldsymbol{Q}\right]\cdot\Delta\tilde{\theta} \\
&= \sum_{\alpha=1}^{2}\int_{\Omega^{(\alpha)}}\mathrm{GRAD}\,\hat{\omega}_o^{(\alpha)}\cdot\boldsymbol{K}_\theta^{(\alpha)}\cdot\mathrm{GRAD}\tilde{\theta}^{(\alpha)}\,\mathrm{d}V \\
&= -\sum_{\alpha=1}^{2}\int_{\Omega^{(\alpha)}}\mathrm{DIV}\left(\mathrm{GRAD}\,\hat{\omega}_o^{(\alpha)}\cdot\boldsymbol{K}_\theta^{(\alpha)}\right)\cdot\tilde{\theta}^{(\alpha)}\,\mathrm{d}V \\
&\quad + \sum_{\alpha=1}^{2}\int_{\Gamma_\mathrm{I}}\left(\mathrm{GRAD}\,\hat{\omega}_o^{(\alpha)}\cdot\boldsymbol{K}_\theta^{(\alpha)}\right)\boldsymbol{N}^{(\alpha)}\cdot\tilde{\theta}^{(\alpha)}\mathrm{d}\Gamma_\mathrm{I}
\end{aligned}
\tag{6-50}
$$

where

$$
\begin{aligned}
&\hat{R}_\theta\left(\hat{\omega}_o^{(\alpha)};\hat{\theta}^{(\alpha)},\tilde{\theta}^{(\alpha)},\lambda_2\right) \\
&= \sum_{\alpha=1}^{2}\int_{\Omega^{(\alpha)}}\left[-\rho_0 C_F\left(\dot{\hat{\theta}}^{(\alpha)}+\dot{\tilde{\theta}}^{(\alpha)}\right)\cdot\hat{\omega}_o^{(\alpha)} + \mathrm{GRAD}\,\hat{\omega}_o^{(\alpha)}\cdot\boldsymbol{Q}^{(\alpha)} - \mathcal{H}_{\mathrm{EI}}\cdot\hat{\omega}_o^{(\alpha)} + R\cdot\hat{\omega}_o^{(\alpha)}\right]\mathrm{d}V \\
&\quad - \sum_{\alpha=1}^{2}\int_{\Gamma^{(\alpha)}\setminus\Gamma_\mathrm{I}}\bar{Q}^{(\alpha)}\cdot\hat{\omega}_o^{(\alpha)}\,\mathrm{d}A - \underbrace{\int_{\Gamma_\mathrm{I}}\lambda_2\cdot\left[\!\left[\hat{\omega}_o\right]\!\right]\mathrm{d}\Gamma_\mathrm{I}}_{\text{heat flux cont.}}
\end{aligned}
\tag{6-51}
$$

Incorporating the expressions (6-47) for λ_2 and the fine-scale fields $\Delta\tilde{\theta}^{(\alpha)}$ (6-48) into the linearized coarse-scale problem (6-51) yields the following stabilized interface formulation (6-53) for finite deformations

$$
\begin{aligned}
R_\phi\left(\boldsymbol{\eta}_o^{(\alpha)},\boldsymbol{\phi}^{(\alpha)}\right) &= \sum_{\alpha=1}^{2}\int_{\Omega^{(\alpha)}}\left[\mathrm{GRAD}\,\boldsymbol{\eta}_o^{(\alpha)}:\boldsymbol{P}^{(\alpha)} - \boldsymbol{\eta}_o^{(\alpha)}\cdot\rho_o^{(\alpha)}\boldsymbol{B}^{(\alpha)}\right]\mathrm{d}V \\
&\quad - \sum_{\alpha=1}^{2}\int_{\Gamma^{(\alpha)}\setminus\Gamma_\mathrm{I}}\boldsymbol{T}^{(\alpha)}\cdot\boldsymbol{\eta}_o^{(\alpha)}\mathrm{d}A + \int_{\Gamma_\mathrm{I}}\left[\!\left[\boldsymbol{\eta}_o\right]\!\right]\cdot\left(-\left\{\boldsymbol{P}\cdot\boldsymbol{N}\right\} + \boldsymbol{\tau}_s\cdot\left(\left[\!\left[\boldsymbol{\phi}\right]\!\right]-\boldsymbol{\zeta}\right)\right)\mathrm{d}\Gamma_\mathrm{I} \\
&\quad - \int_{\Gamma_\mathrm{I}}\left\{\left(\mathrm{GRAD}\,\boldsymbol{\eta}_o:\mathbf{A}\right)\cdot\boldsymbol{N}\right\}\cdot\left(\left[\!\left[\boldsymbol{\phi}\right]\!\right]-\boldsymbol{\zeta}\right)\mathrm{d}\Gamma_\mathrm{I} = 0
\end{aligned}
\tag{6-52}
$$

$$
\begin{aligned}
R_\theta\left(\omega_o^{(\alpha)};\theta^{(\alpha)}\right) &= \sum_{\alpha=1}^{2}\int_{\Omega^{(\alpha)}}\left[\rho_0 C_F\dot{\theta}^{(\alpha)}\cdot\omega_o^{(\alpha)} - \mathrm{GRAD}\,\omega_o^{(\alpha)}\cdot\boldsymbol{Q}^{(\alpha)} + \mathcal{H}_{ei}\cdot\omega_o^{(\alpha)} - R\cdot\omega_o^{(\alpha)}\right]\mathrm{d}V \\
&\quad + \sum_{\alpha=1}^{2}\int_{\Gamma^{(\alpha)}\setminus\Gamma_\mathrm{I}}\bar{Q}^{(\alpha)}\cdot\omega_o^{(\alpha)}\,\mathrm{d}A + \int_{\Gamma_\mathrm{I}}\left[\!\left[\omega_o\right]\!\right]\cdot\left(\left\{\boldsymbol{Q}\cdot\boldsymbol{N}\right\} + \boldsymbol{\tau}_s^{\theta}\cdot\left(\left[\!\left[\theta\right]\!\right]\right)\right)\mathrm{d}\Gamma_\mathrm{I} \\
&\quad - \int_{\Gamma_\mathrm{I}}\left\{\left(\mathrm{GRAD}\,\omega_o^{(\alpha)}\cdot\boldsymbol{K}_\theta^{(\alpha)}\right)\cdot\boldsymbol{N}\right\}\left(\left[\!\left[\theta\right]\!\right]\right)\mathrm{d}\Gamma_\mathrm{I} = 0
\end{aligned}
\tag{6-53}
$$

The stabilized residual form (4-27) has the inelastic gap $\boldsymbol{\zeta}$ term inside the integral expression which plays a key role for debond evolution [39]. In this Chapter, the damage phenomena which shows strong discontinuity in the mechanical field is validated in the following numerical sections. Interested readers are referred to [39] for the evolution of the damage internal variables. Variationally consistent updating of these tensors results in a stabilized formulation that yields a

robust numerical method as shown via numerical test cases in section 6.4.

Remark: *For the time evolution term* $\dot{\theta}^{(\alpha)}$ *shown in (6-53), backward Euler method is applied such that* $\dot{\theta}^{(\alpha)} = \dfrac{\theta_{n+1}^{(\alpha)} - \theta_n^{(\alpha)}}{\Delta t}$.

Remark: *The elastic heating term* $\mathcal{H}_{\mathrm{EI}} := -\theta \partial^2_{\theta \boldsymbol{F}} \Psi : \dot{\boldsymbol{F}}$ *where* $\dot{\boldsymbol{F}}$ *can be represented in terms of the velocity gradient* $\boldsymbol{L} = \dfrac{\partial \boldsymbol{v}}{\partial \boldsymbol{x}}$, *which leads to an index form of* $\dot{F}_{iI} = v_{i,j} F_{jI}$.

Remark: *The first Piola-Kirchhoff stress tensor* $\boldsymbol{P}^{(\alpha)} = \partial_{\boldsymbol{F}^{(\alpha)}} \Psi$ *where* Ψ *is the strain energy function which contains the thermomechanical coupling term* $M\left(J, \theta\right)$. *The detailed description of* $M\left(J, \theta\right)$ *is given in the numerical section 6.4.*

Remark: *The process to push forward (6-52) and (6-53) to the spatial configuration is summarized in Appendix D.*

6.4 Numerical Results

In this section we investigate the performance of the proposed thermomechanical interface method across a range of problems. We have employed standard Lagrange polynomials for linear triangle (T3) and linear quadrilateral (Q4) elements. All integral expressions over surfaces and volumes are evaluated using Gauss quadrature rules of sufficient by high degree.

Two methods are investigated: In the first method, continuity is weakly enforced at specific bi-material interfaces elements which corresponds to the formulation summarized in sections 4. The second method has weakly enforced continuity across every element boundary across all the elements, and this is the full discontinuous Galerkin (DG) formulation for interfacial thermoelasticity.

All integral expressions over surfaces and volumes are evaluated using Gauss quadrature rules of sufficient degree. A common thermoelastic constitutive model for regularized compressible neo-Hookean material is given by the uncoupled free energy function [6] as follows:

$$\Psi\left(\boldsymbol{C}, \theta\right) = W\left(\bar{\boldsymbol{C}}\right) + U\left(J\right) + M\left(J, \theta\right) + T\left(\theta\right) \tag{6-54}$$

where $\bar{\boldsymbol{C}} = J^{-2/3} \boldsymbol{F}^{\mathrm{T}} \boldsymbol{F}$. The elastic stored energy functions are specified as follows:

$$W\left(\bar{C}\right)=\frac{1}{2}\mu\left(\mathrm{tr}\left(\bar{C}\right)-3\right) \tag{6-55}$$

$$U\left(J\right)=\frac{1}{2}\kappa\log^2 J \tag{6-56}$$

The thermomechanical coupling term as well as the pure thermal term are taken as:

$$M\left(J,\theta\right)=-3\kappa\beta_0\left(\theta-\theta_{ref}\right)\ln J \tag{6-57}$$

$$T\left(\theta\right)=C_0\left[\left(\theta-\theta_{ref}\right)-\theta\ln\left(\frac{\theta}{\theta_{ref}}\right)\right] \tag{6-58}$$

Then we could arrive the expression for the volumetric heat capacity (VHC) $\rho_0 C_F := -\theta\partial^2_{\theta\theta}\Psi = C_0$ and $\mathcal{H}_{\mathrm{EI}} := -\theta\partial^2_{\theta\boldsymbol{F}}\Psi : \dot{\boldsymbol{F}} = 3\theta\kappa\beta_0\boldsymbol{F}^{-\mathrm{T}} : \dot{\boldsymbol{F}} = 3\theta\kappa\beta_0\boldsymbol{F}^{-1}_{Ii}v_{i,j}F_{jI} = 3\theta\kappa\beta_0 v_{i,i}$.

We first present results for test cases wherein continuity is weakly enforced at specific bi-material interfaces and thus corresponds to the formulation derived in Sections 6.2 and 6.3. Numerical tests are also performed using fully discontinuous approximations across all elements through section 6.4.1 to 6.4.3, and section 6.4.5.

6.4.1 Thermo-mechanical coupled problem: Quasi-static long-term behavior

In this section, as shown in Figure 6.4, we set the same boundary conditions as stated in section 2.5.2 while geometric and material nonlinearity is taken into account. For section 6.4.1 to section 6.4.3, we study the steady state behavior of the temperature transient problem, which means $t = \infty$.

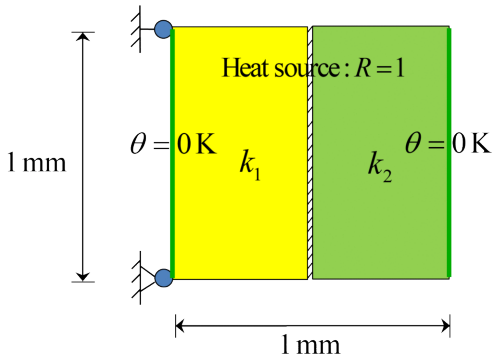

Figure 6.4. Problem description for the thermo-mechanical coupled problem.

All Material properties are listed in Table 6.1. The difference is that now we set a high enough number of the thermal expansion coefficient β_0 as listed in Table 6.1 to have a high influence of the thermal field on the mechanical deformation.

Table 6.1. Material properties for the thermo-mechanical coupled problem.

Material properties	Symbol	value
Young's modulus	E	100 MPa
Poisson's ratio	ν	0.25
Thermal conductivity	k_2	$0.5\ \mathrm{N/s{\cdot}K}$
	k_1	$3\ \mathrm{N/s{\cdot}K}$
Expansion coefficient	β_0	$1.5\times10^{-1}\mathrm{K}^{-1}$
Softening parameter	β_k	$0\ \mathrm{K}^{-1}$

The σ_{11} contour plot is given in Figure 6.5 with a deformed configuration with a magnification coefficient of 5 to show the deformation of the displacement field. Three different FEM element types are presented: Q4, T3, and T3-Q4 composite element types. In this figure, a noticeable expansion of the block due to the thermal field can be seen with a relatively high value of the stress field at the top and bottom surface. Figure 6.6 shows the σ_{11} value along $x = 0.3\ \mathrm{mm}$ which is the line AB plotted in Figure 6.5. It shows that T3 element is stiffer compared with Q4, and the composite element stress plot matches with Q4 elements from point A to the middle point, and matches T3 element from the middle point to point B, as expected. As for this coupling problem, the mechanical deformation does not affect the thermal field for steady-state situation, the temperature plot given in Figure 6.7 still almost matches the previous closed-form expression as what we expected.

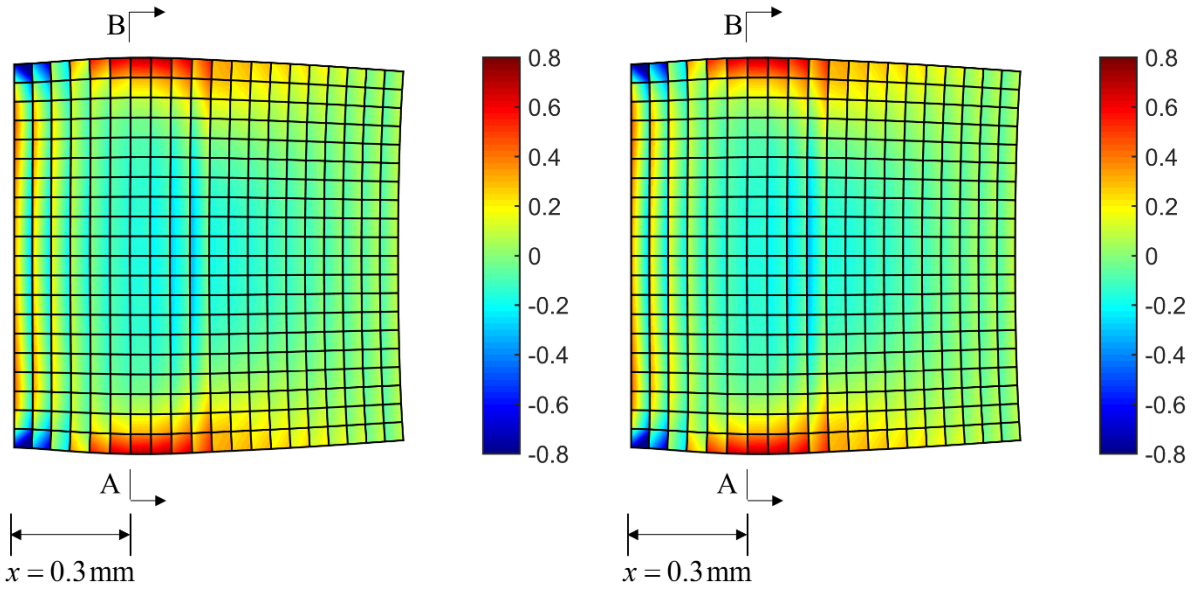

(a)

(b)

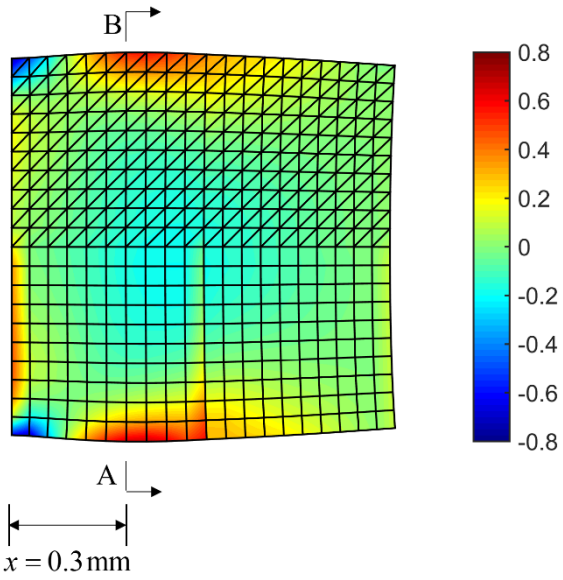

(c)

Figure 6.5. σ_{11} contour plot for the thermo-mechanical coupled problem: (a) Q4 element; (b) T3 element; (c) T3-Q4 composite element.

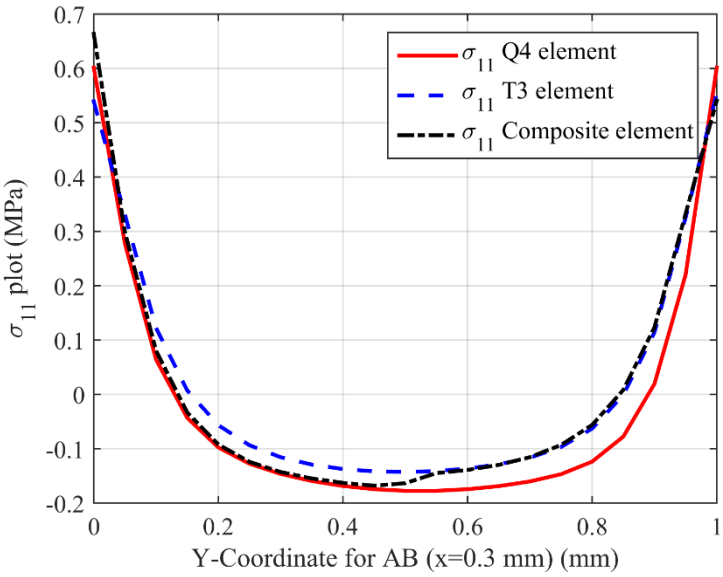

Figure 6.6. σ_{11} plot for line AB for various element types: Q4, T3, and T3-Q4 composite element.

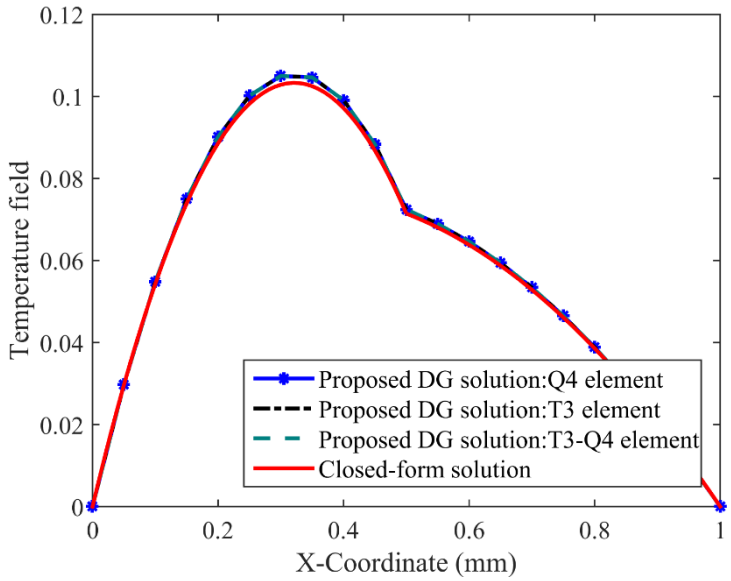

Figure 6.7. Temperature field plot for the thermo-mechanical coupled problem.

6.4.2 Stability tensor study

In this section, we aim to study the evolution of the stability tensors $\|\boldsymbol{\tau}_s\|$ and $\|\tau_s^{\theta}\|$ at the interface. As shown in Figure 6.8, we divide the domain into three different zones with different conductivity

parameters k_1, k_2, and k_3. We put DG element on every interface, including the region with same conductivity parameter to analyze the evolution of the stability tensors for both mechanical and thermal part.

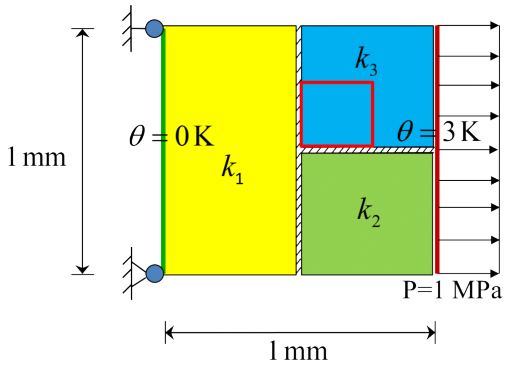

Figure 6.8. Geometry and boundary description for stability tensor study problem.

The material properties as listed in Table 6.2. In this problem, we do not have any external heat resource, and instead, the temperature at the boundary $x = 1\text{mm}$ is set to be 3 Kelvin. External mechanical deformation of $P = 1\text{MPa}$ is also applied to the right surface, as shown in Figure 6.8.

Table 6.2. Material properties for stability tensor study problem.

Material properties	Symbol	value
Young's modulus	E	100 MPa
Poisson's ratio	ν	0.25
Thermal conductivity	k_1	0.5 N/ s·K
	k_2	3 N/ s·K
	k_3	1 N/ s·K
Expansion coefficient	β_0	$1.5\times10^{-3}\,\text{K}^{-1}$
Softening parameter	β_k	$0\,\text{K}^{-1}$

The contour plots of the σ_{11} stress and thermal field are shown in Figure 6.9 (a) and (b), with an expansion on the right surface due to the higher temperature boundary condition.

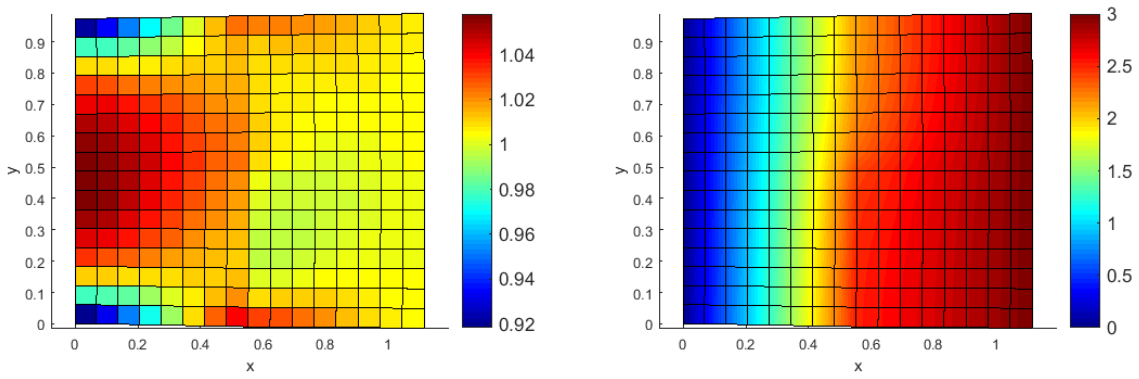

(a) (b)

Figure 6.9. Contour plot for stability tensor study problem: (a) σ_{11} stress; (b) temperature field.

As a unique feature of this framework, we plot the norm of stability tensors, namely $\left\|\tau_s^{\theta}\right\|$ and $\left\|\boldsymbol{\tau}_s\right\|$ at the interface elements in Figure 6.10 and Figure 6.11. The equation of the mechanical stability tensor $\left\|\boldsymbol{\tau}_s\right\|$ is given in Chapter 2. As given in Eqn. (6-49), the thermal stability tensor $\left\|\tau_s^{\theta}\right\|$ is a function of the thermal conductivity tensor and the geometry nonlinearity. Thus, this parameter evolves with element size and regions with different thermal conductivity parameter as shown in Figure 6.10. Note that these values are naturally derived without any tunable parameters which update with the evolution of the problem. For the mechanical part, because of the one-way coupling feature and the choice of the coupling term thermal expansion β to be a small number, the mechanical part is not affected much by the thermal field. Therefore, the stability term $\left\|\boldsymbol{\tau}_s\right\|$ shown in Figure 6.11 is uniformly distributed in the y-axis and decreasing element-wise through the x-axis.

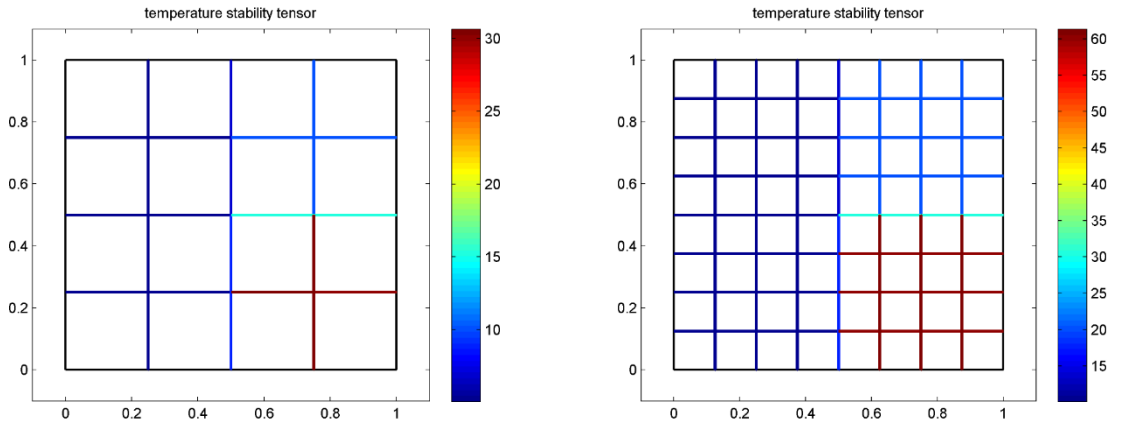

(a) (b)

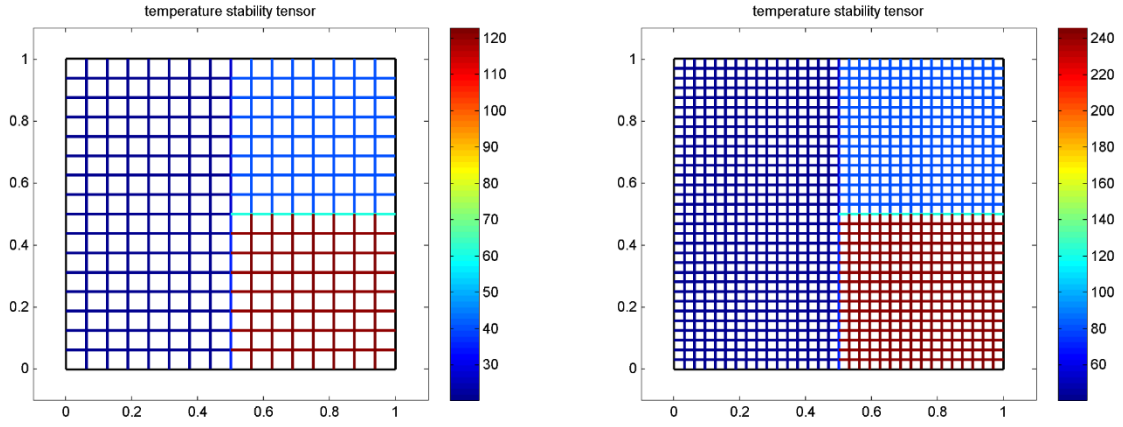

(c) (d)

Figure 6.10. stability tensor $\left\|\tau_s^{\theta}\right\|$ plot for different mesh refinement: (a) $n=4$, (b) $n=8$, (c) $n=16$, (d) $n=32$.

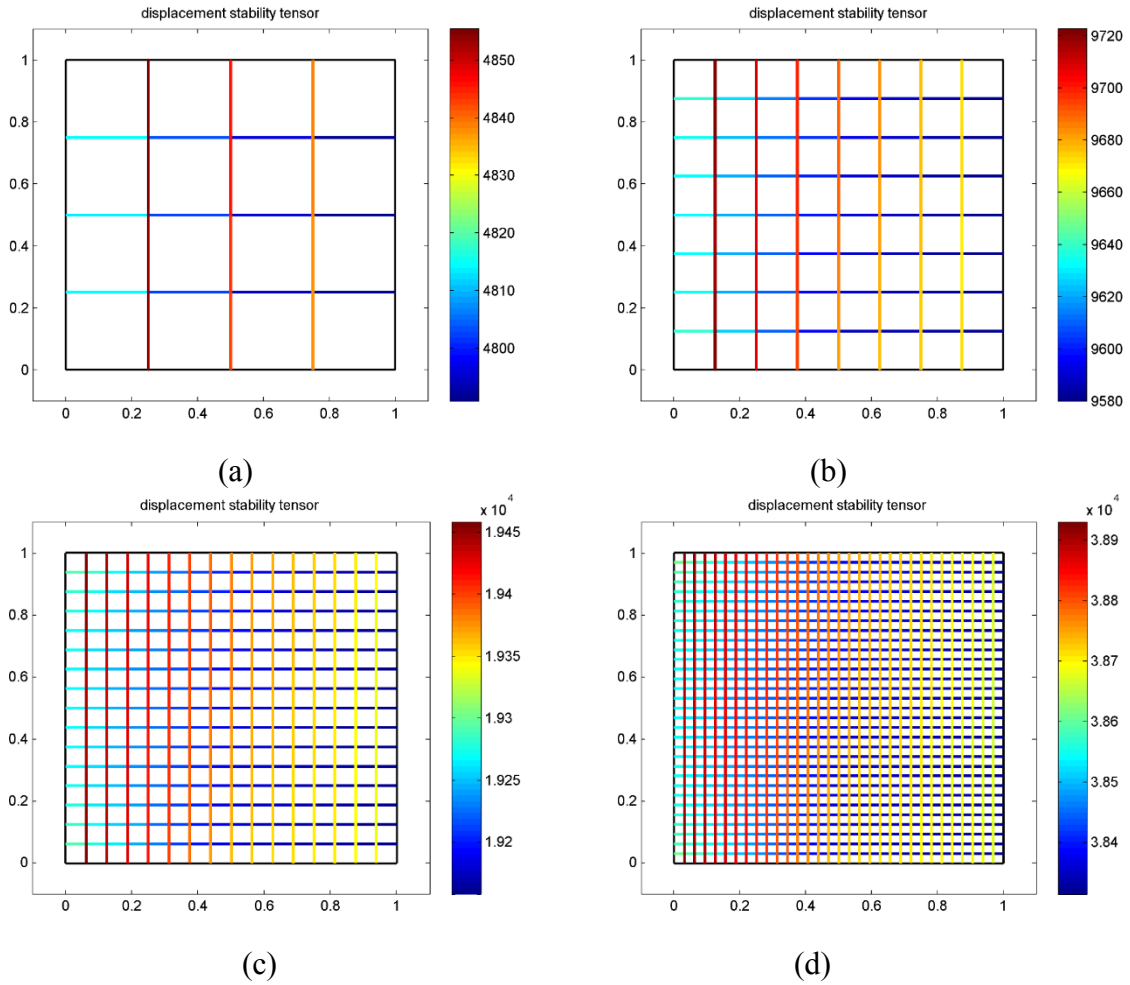

Figure 6.11. stability tensor $\|\boldsymbol{\tau}_s\|$ plot for different mesh refinement: (a) $n=4$, (b) $n=8$, (c) $n=16$, (d) $n=32$.

Now we focus on the coarse mesh size $h=1/4$ and analysis the stability tensor $\|\tau_s^{\theta}\|$ and $\|\boldsymbol{\tau}_s\|$ at different element interfaces for the element labeled in red in Figure 6.8 and in Figure 6.12 (a) and (b). The interface numbering system for the four sides of the targeted interior elements is listed in Figure 6.12. The tabulated numbers of these parameters are summarized in Table 6.3. The values for the stability tensors $\|\tau_s^{\theta}\|$ and $\|\boldsymbol{\tau}_s\|$ show that for different interface elements, the numbers are different due to different material nonlinearity, namely, the thermal conductivity and the acoustic tensor, and the geometric nonlinearity due to the large deformation. It indicates the naturally evolved feature of the stability parameter for both the thermal and mechanical part.

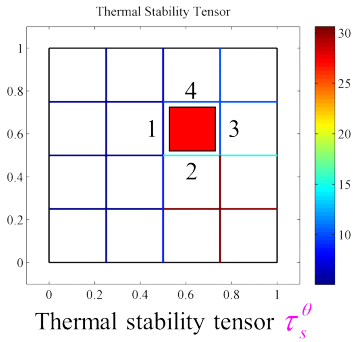

(a)

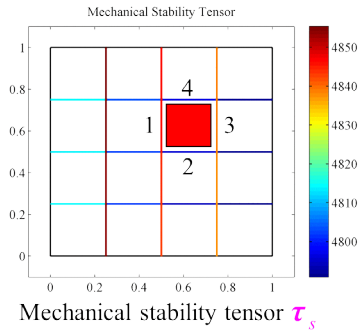

(b)

Figure 6.12. Stability tensor $\|\tau_s^\theta\|$ and $\|\boldsymbol{\tau}_s\|$ plot with specification of interface element number: (a) thermal stability tensor; (b) mechanical stability tensor.

Table 6.3. Stability parameter $\|\tau_s^\theta\|$ and $\|\boldsymbol{\tau}_s\|$ for different interface element number.

Interface element number	Stability parameter $\|\tau_s^\theta\|$	Stability parameter $\|\boldsymbol{\tau}_s\|$
1	6.8355	4.8455×10^3
2	15.1376	4.7948×10^3
3	10.2208	4.8387×10^3
4	10.0951	4.7959×10^3

6.4.3 Thermo-mechanical problem with damage phenomenon: Quasi-static long-term behavior

In this section, we merge the thermo-mechanical formulations with the damage model we have in Chapter 4. Nonconforming meshes are used for this problem to show the various use of our proposed DG method. The boundary conditions are given in Figure 6.13 with a displacement of 0.1 mm applied to the right surface and a different temperature applied to the two different surfaces.

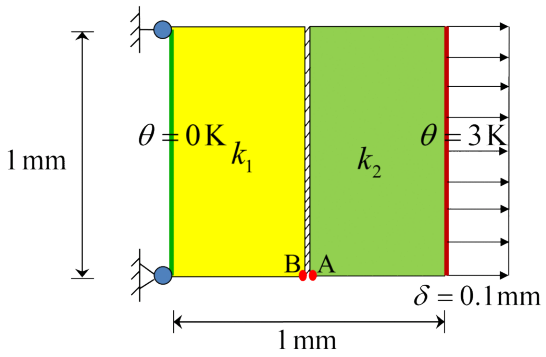

Figure 6.13. Geometry and boundary description for damage evolution problem.

The material properties given in Table 6.4 are the same to the problem sets in section 6.4.1, with the additional damage parameters given to enable the damage evolution. Interest readers can refer to Chapter 4 for a detailed discussion of these parameters.

Table 6.4. Material properties for damage evolution problem.

Material properties	Symbol	Value
Critical stress	P_c	5 MPa
Critical inelastic gap	δ_c	0.1 mm
Friction coefficient	μ_f	0.52

The contour plots for the axial stress σ_{11} and the temperature field are shown in Figure 6.14 (a) and Figure 6.15 (b). Nonconforming mesh is used for this test problem. The stress σ_{11} field is almost constant, which matches the result we have in Chapter 4 and [39]. Small variation in σ_{11} contours is due to the temperature variation. The gap in mechanical field is shown in Figure 6.15 (a) and (b) and it appears when the traction at Γ_1 exceeding the critical stress. This is accompanied with a corresponding gradual unloading of the mechanical stresses in the damaged regions. The thermal field remains continuous as shown in both Figure 6.14 (b) and Figure 6.15 (b). Plot of stress σ_{11} at node B versus the gap function ζ between nodes A and B is shown in Figure 6.16 and is compared with the exact solution.

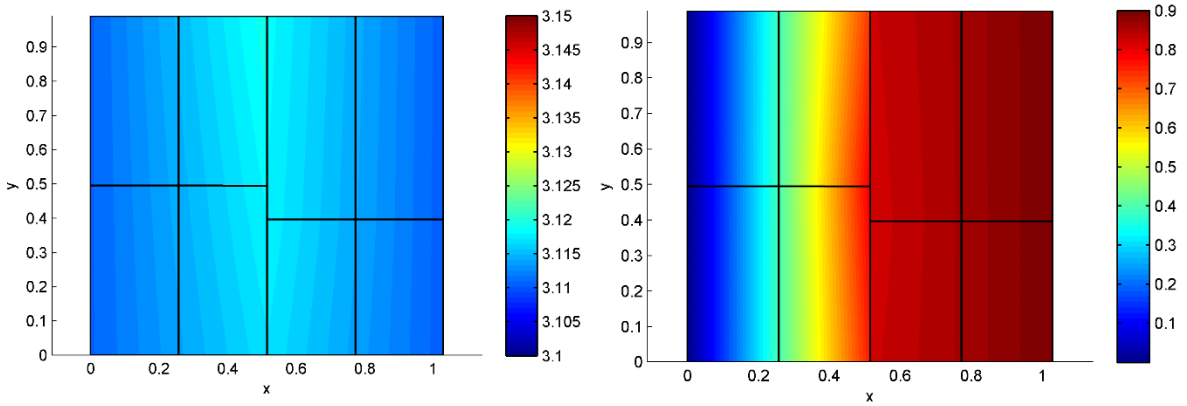

(a) (b)

Figure 6.14. Contour plot for damage evolution for $\delta = 0.03\,\text{mm}$: (a) σ_{11} stress; (b) temperature field.

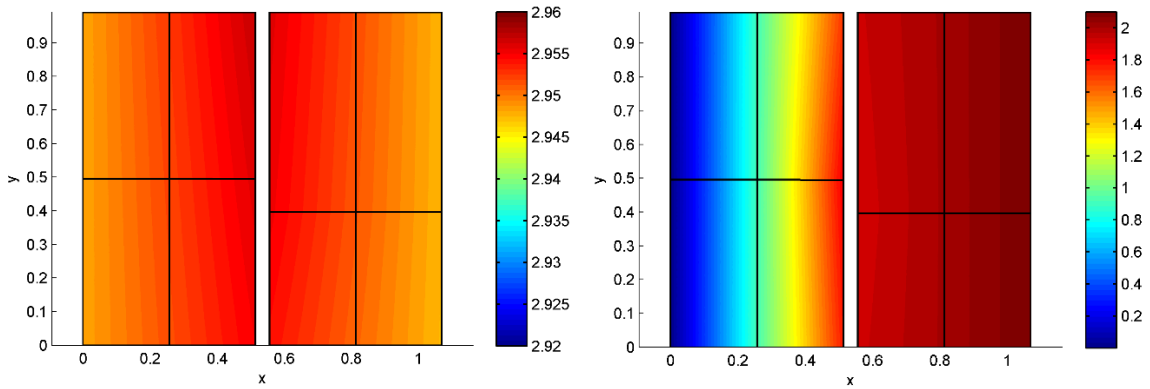

(a) (b)

Figure 6.15. Contour plot for damage evolution for $\delta = 0.07\,\text{mm}$: (a) σ_{11} stress; (b) temperature field.

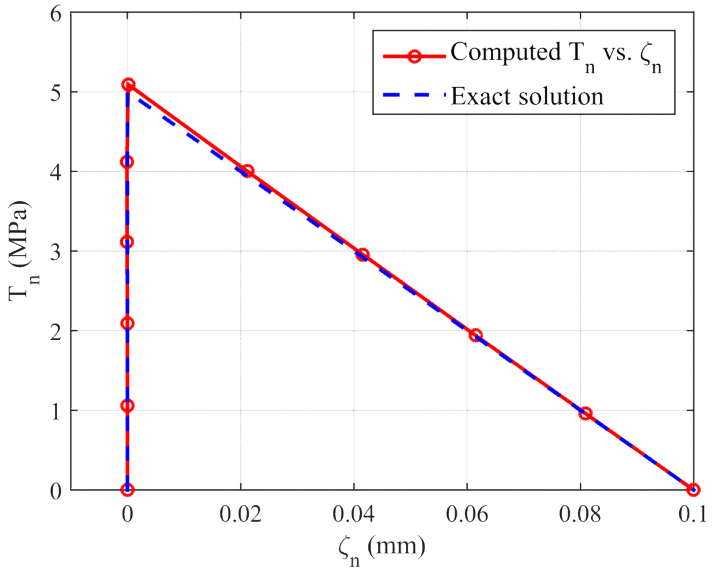

Figure 6.16. Normal traction T_n versus the gap function ζ_n plot.

6.4.4 Transient Heat Flux Test Problem

In this test problem, we adopt the problem presented in [135]. The geometry taken from [135] is described in Figure 6.17 with a constant heat flux acting on the right end of the rod. The temperature field is kept as constant on the left end. The DG element is put in the middle where $l = 7.5$ mm. The problem is completely thermal driven and the material properties are stated in Table 6.5.

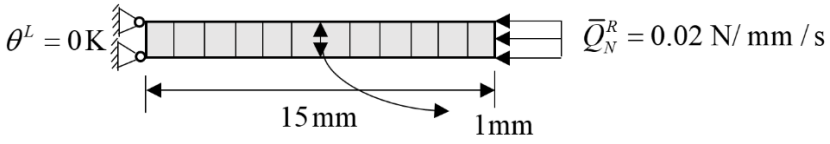

Figure 6.17. Problem description of the constant heat flux test case.

Table 6.5. Material properties for the constant heat flux problem.

Material properties	Symbol	value
Young's modulus	E	998.55 MPa
Poisson's ratio	v	0.30
Thermal conductivity	k	1.0 N/ s·K
Expansion coefficient	β_0	$1.0\times10^{-4}\,\mathrm{K}^{-1}$
Specific heat capacity	C_F	$0.2\ \mathrm{mm}^2/\mathrm{s}^2\cdot\mathrm{K}$
Density	ρ_0	$1.0\,\mathrm{Ns}^2/\mathrm{mm}^4$

The problem is simulated with a time increment $\Delta t = 0.1\,\mathrm{sec}$ for heat flux and $\Delta t = 0.5\,\mathrm{sec}$ for temperature which are both larger compared with $\Delta t = 0.02\,\mathrm{sec}$ in [135]. The line plot of the temperature field at $t = 5\,\mathrm{sec}$ and the heat flux Q term at $t = 1\,\mathrm{sec}$ are presented in Figure 6.18 and Figure 6.19. The steady states where $t = \infty$ for both temperature and heat flux terms are also presented. Instead of using adaptive meshing as stated in [135], a fixed mesh refinement of 60×1 is used which is much coarser compared with the initial mesh provided in [135]. As shown in Figure 6.18 and Figure 6.19, both the temperature and heat flux term match the exact solution given in [135]. The result using backward Euler finite difference method [135] is taken to compare the result, which shows that the presented method is capturing the exact solution much better. The steady state is plotted for $t = \infty$, where the temperature transient term is not affecting the results. As shown in Figure 6.18 and Figure 6.19, the temperature field is linear, and the heat flux is constant.

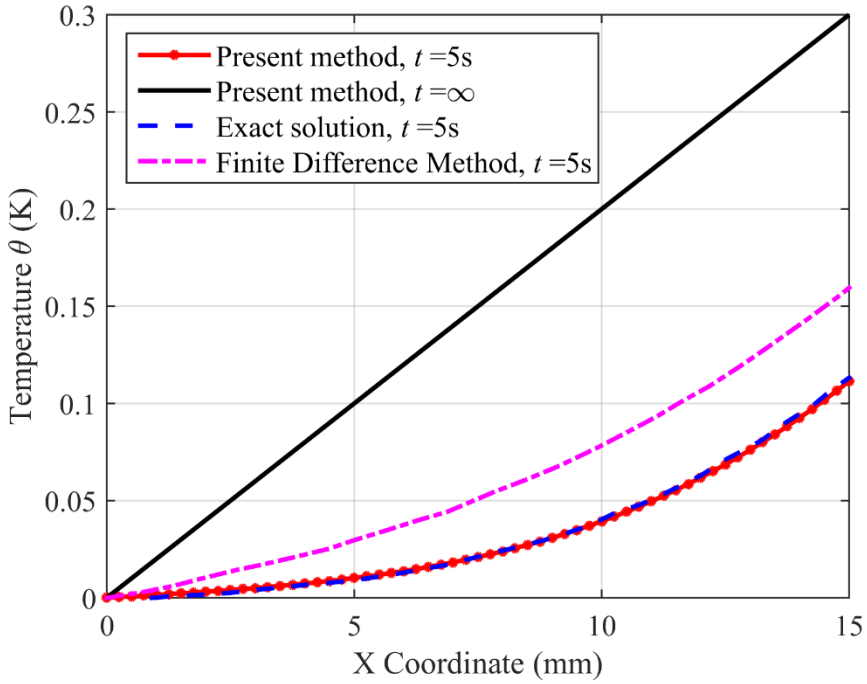

Figure 6.18. Temperature field for various locations of the rod for $t = 5\,\text{sec}$ and $t = \infty$.

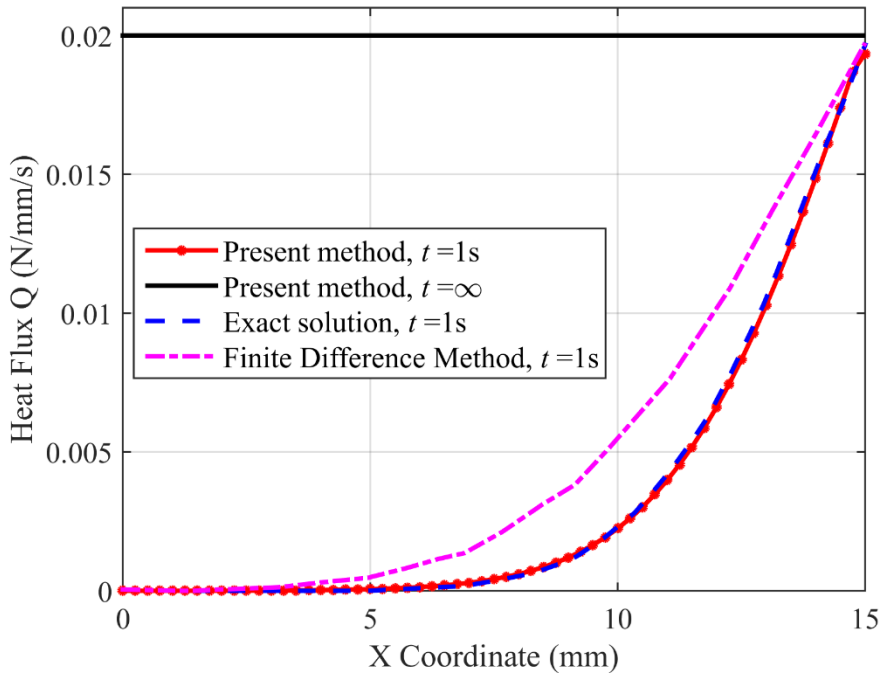

Figure 6.19. Heat flux field for various locations of the rod for $t = 1\,\text{sec}$ and $t = \infty$.

Remark: *For this problem, the interface element is inserted at every element boundary, which induces the oscillation of the results when enforcing the continuity of the temperature field at*

element boundary. Thus, the derived stability term $\tau_s^{\theta} = \left(\tau_s^{\theta(1)} + \tau_s^{\theta(2)}\right)^{-1}$ *derived in section 6.3.2 which serves as a penalty parameter in Eqn. (6-53) is multiplied by a constant penalty coefficient* $\mathrm{A} = 4$ *to avoid the oscillation.*

6.4.5 Fully coupled simulation for functionally graded materials with evolving properties concerning temperature fields

In this section, we discuss a problem of an axisymmetric cylinder in the small deformation region with functionally graded materials (FGM) as given in [134]. The problem description is given in Figure 6.20. At the inner surface with the radius $r_a = 1.27\,\mathrm{cm}$, a convective heat transfer $q = h_c\left(\theta_{\text{source}} - \theta_a\right)$ and fixed radial displacement $u_r = 0$ are applied. This convective heat transfer [134] shown in Figure 6.20 is to simulate hot gases passing through a hollow cylinder and experiencing high temperature variation. The high temperature of the gases is set to be $\theta_{\text{source}} = 2000\,\mathrm{K}$ and the heat transfer coefficient $h_c = 750\,\mathrm{W/m^2K}$. The reference temperature is $\theta_{\text{ref}} = \theta_a - \vartheta_a = 298.15\ \mathrm{K}$ and θ_a is the current unknown temperature field of the inner surface as the problem evolves with time. At the outer surface with the radius $r_b = 2.54\,\mathrm{cm}$, isolated and stress-free boundary conditions are applied as shown in Figure 6.20. The geometries, as well as boundary conditions, are taken to match the problem statement presented in [134]. Interface elements are set at all element boundaries.

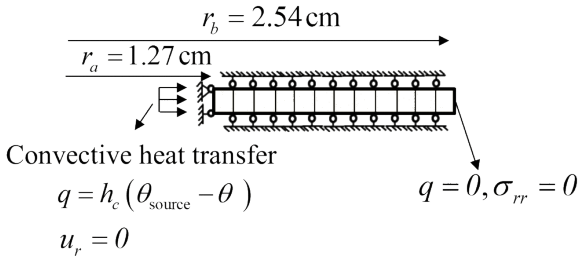

Figure 6.20. Problem description of the FGM cylinder.

The nonlinearity arises from the evolving material properties regarding the temperature field. As presented in [156] and later adopted by Reddy and Chin [134], all material properties can be expressed in a cubic fit as the following.

$$P = P_0\left(\frac{P_{-1}}{\theta} + 1 + P_1\theta + P_2\theta^2 + P_3\theta^3\right) \tag{6-59}$$

where θ is the absolute temperature field, P_{-1} through P_3 are constant parameters. For the current FGM problem, silicon nitride (ceramic) and stainless steel (metal) (Si_3N_4/SUS304) are adopted for comparison with the results presented in [134]. The coefficients P_{-1} through P_3 which define the material properties given in [134] are summarized below in Table 6.6 and Table 6.7 for completion.

Table 6.6. Constant coefficients shown in Eqn. (6-64) for silicon nitride (Si_3N_4).

Material type: Silicon nitride	P_0	P_{-1}	P_1	P_2	P_3
Thermal conductivity $k_\theta\left(\mathrm{W/mK}\right)$	13.723	0	-1.032×10^{-3}	5.466×10^{-7}	-7.876×10^{-11}
Thermal expansion $\beta\left(\mathrm{1/K}\right)$	5.8723×10^{-6}	0	9.095×10^{-4}	0	0
Elastic modulus $E\left(\mathrm{Pa}\right)$	348.43×10^{9}	0	-3.070×10^{-4}	2.160×10^{-7}	-8.946×10^{-11}
Poisson's ratio ν	0.2400	0	0	0	0
Specific heat $c_F\left(\mathrm{J/kgK}\right)$	555.11	0	1.016×10^{-3}	2.920×10^{-7}	-1.670×10^{-10}
Density $\rho\left(\mathrm{kg/m^3}\right)$	0	2370	0	0	0

Table 6.7. Constant coefficients shown in Eqn. (6-64) for stainless steel (SUS304).

Material type: Silicon nitride	P_0	P_{-1}	P_1	P_2	P_3
Thermal conductivity $k_\theta\left(\mathrm{W/mK}\right)$	15.379	0	-1.264×10^{-3}	2.092×10^{-6}	-7.223×10^{-10}
Thermal expansion $\beta\left(1/\mathrm{K}\right)$	12.330×10^{-6}	0	8.086×10^{-4}	0	0
Elastic modulus $E\left(\mathrm{Pa}\right)$	201.04×10^{9}	0	3.079×10^{-4}	-6.534×10^{-7}	0
Poisson's ratio v	0.3262	0	-2.002×10^{-4}	3.797×10^{-7}	0
Specific heat $c_F\left(\mathrm{J/kgK}\right)$	496.56	0	-1.151×10^{-3}	1.636×10^{-6}	-5.863×10^{-10}
Density $\rho\left(\mathrm{kg/m^3}\right)$	0	8166	0	0	0

Remark: *Density ρ for both stainless steel and silicon nitride is chosen to be constant though temperature.*

Based on the coefficients given in Table 6.6 and Table 6.7 and the expression in Eqn. (6-59), the plots of various material properties versus the temperature field are given in Figure 6.21.

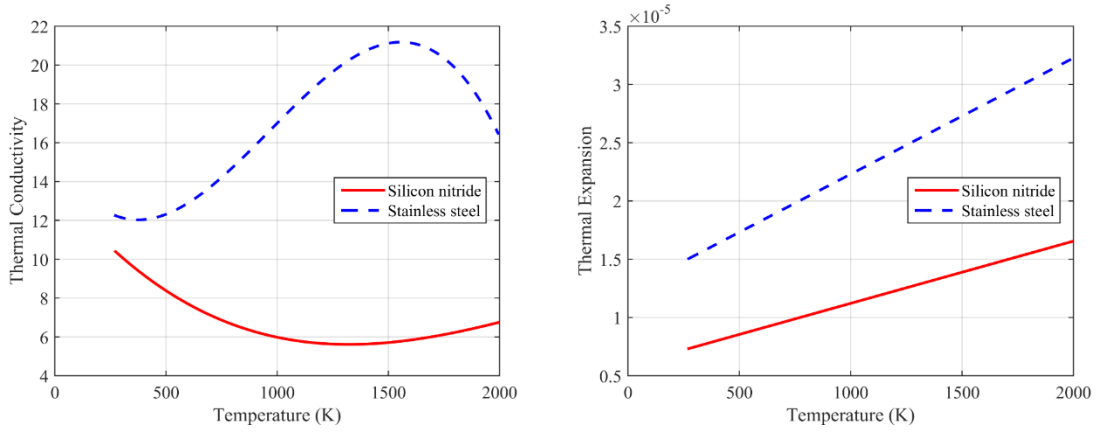

(a) (b)

Figure 6.21. Plots of different material properties versus temperature: (a) Thermal conductivity $k_\theta\left(\mathrm{W/mK}\right)$; (b) Thermal expansion $\beta\left(1/\mathrm{K}\right)$; (c) Elastic modulus $E\left(\mathrm{Pa}\right)$; (d) Poisson's ratio v; (e) Specific heat $c_F\left(\mathrm{J/kgK}\right)$; (f) Density $\rho\left(\mathrm{kg/m^3}\right)$.

Figure 6.21 continued.

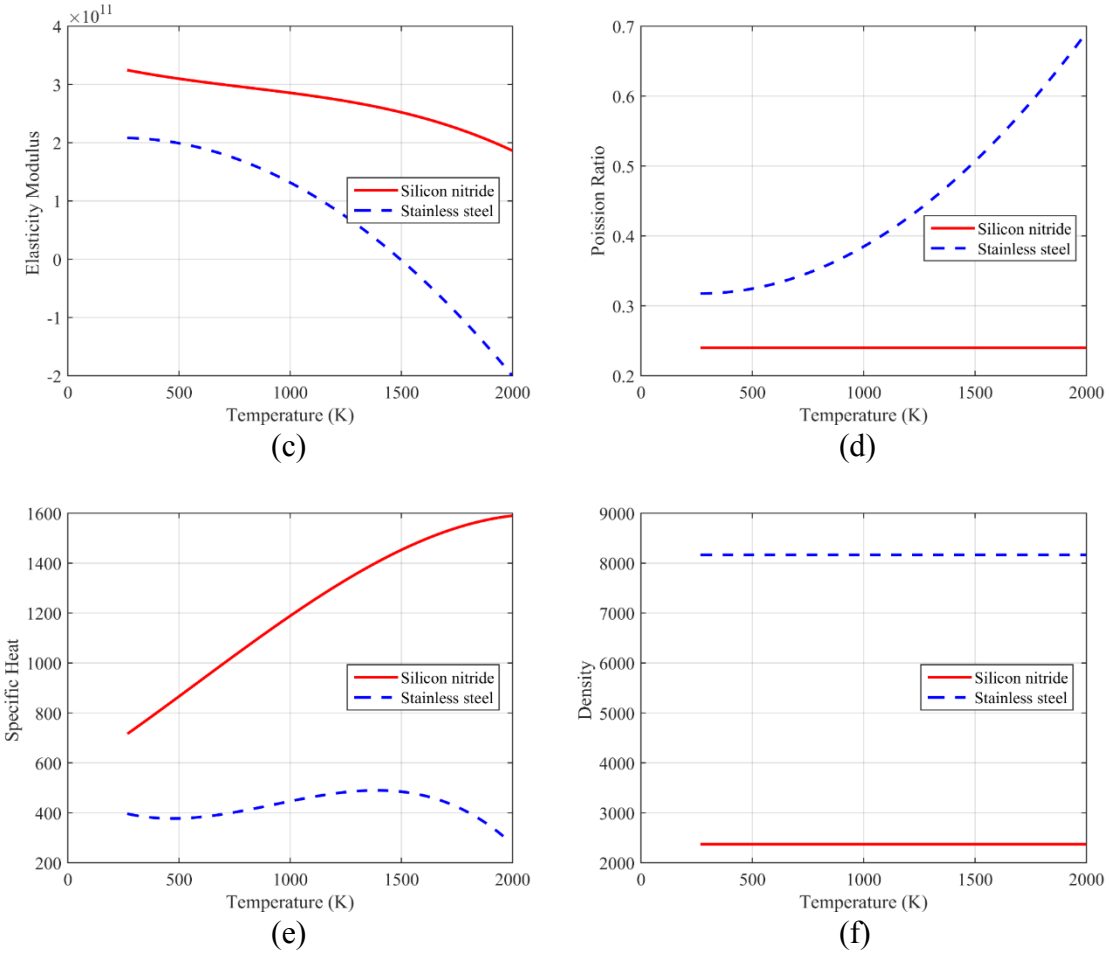

The construction of the FGM is based on the distance in the radial direction. As given in [134], the volume fraction for SUS304 and the relation of the volume fraction for Si_3N_4/SUS304 cylinder are given as

$$V_{\text{SUS304}} = \left(\frac{r - r_a}{r_b - r_a} \right)^n \qquad V_{Si_3N_4} + V_{\text{SUS304}} = 1.0 \tag{6-60}$$

where r_a and r_b are the inner and outer radius, respectively. n is the exponential ratio indicating the distribution of the FGM material in the radial direction. When $n = 0$ and $V_{\text{SUS304}} = 1$, the FGM cylinder is entirely made of metal. Based on the representation in Eqn. (6-60), the inner surface is ceramic-rich and the outer surface is metal-rich [134]. The effective material property P_{eff} given

in [134] is expressed as a function of the volume fraction V_{SUS304} and $V_{\text{Si}_3\text{N}_4}$, and the material properties of the stainless steel and silicon nitride.

$$P_{\text{eff}} = V_{\text{SUS304}}(r)\,P_{\text{SUS304}}(T) + V_{\text{Si}_3\text{N}_4}(r)\,P_{\text{Si}_3\text{N}_4}(T) \tag{6-61}$$

For the axisymmetric problem, specific treatment of the governing equations (6-3)-(6-4) is employed. Since this problem evolves with only material nonlinearity, the small strain version of the governing equations is listed as follows:

$$\frac{\partial \sigma_r^{(\alpha)}}{\partial r} + \frac{\left(\sigma_r^{(\alpha)} - \sigma_\theta^{(\alpha)}\right)}{r} = 0 \tag{6-62}$$

$$\rho^{(\alpha)} c_F^{(\alpha)} \dot{\vartheta}^{(\alpha)} = -\frac{\partial q^{(\alpha)}}{\partial r} - \frac{1}{r} q^{(\alpha)} - m^{(\alpha)} : \left(\frac{\partial v^{(\alpha)}}{\partial r} + \frac{v^{(\alpha)}}{r} \right) \tag{6-63}$$

where c_F is the specific heat. The hoop stress and the radial stress are summarized as

$$\sigma_r^{(\alpha)} = E^{(\alpha)}(\theta)\,\varepsilon_r^{(\alpha)} + \lambda^{(\alpha)}(\theta)\,\varepsilon_\theta^{(\alpha)} - m^{(\alpha)}(\theta)\,\vartheta^{(\alpha)} \tag{6-64}$$

$$\sigma_\theta^{(\alpha)} = \lambda^{(\alpha)}(\theta)\,\varepsilon_r^{(\alpha)} + E^{(\alpha)}(\theta)\,\varepsilon_\theta^{(\alpha)} - m^{(\alpha)}(\theta)\,\vartheta^{(\alpha)} \tag{6-65}$$

where two strains are represented as $\varepsilon_r^{(\alpha)} = \dfrac{\partial u^{(\alpha)}}{\partial r}$, and $\varepsilon_\theta^{(\alpha)} = \dfrac{u^{(\alpha)}}{r}$. $m^{(\alpha)} = 3\kappa^{(\alpha)}\beta^{(\alpha)}$ is the thermomechanical coupling term and $\kappa^{(\alpha)} = \lambda^{(\alpha)} + 2/3\mu^{(\alpha)}$ is the bulk modulus and $\beta^{(\alpha)}$ is the coefficient of thermal expansion as listed in Table 6.6 and Table 6.7.

Remark: *All the material properties $E^{(\alpha)}$, $\lambda^{(\alpha)}$, and $m^{(\alpha)}$ shown in Eqn. (6-64) and (6-65) are functions of the temperature field. The calculation of each material property is based on substituting the right coefficients given in Table 6.6 and Table 6.7 into Eqn. (6-59).*

The temperature distribution is depicted in Figure 6.22 to Figure 6.24. The development of the stress field primarily results from the high temperature variation [134]. Figure 6.22 shows the temperature versus radial distance plot for different power exponent values $n = 0$, $n = 1$, $n = 25$. According to Eqn. (6-60), The cylinder is more ceramic-rich than metal-rich as the power exponent value n is larger. The gradient of the temperature field versus radial distance is significant. The temperature distribution versus time plot for the inner surface is attained in Figure 6.23 for the time period $t = (0\sim50)\,\text{sec}$. The temperature field does not reach a steady state during this time

period. The relation between the temperature field of the inner surface and volumetric fraction for ceramic $V_{Si_3N_4}$ for different time steps is shown in Figure 6.24. From Figure 6.22 to Figure 6.23, the results obtained from the proposed method capture almost exactly the numerical results from Reddy and Chin [134] for power exponent value $n=1, n=25$. As shown in Figure 6.24, the results match Reddy and Chin [134] very well when ceramic volume fraction is not zero and $t \geq 5\,\text{sec}$.

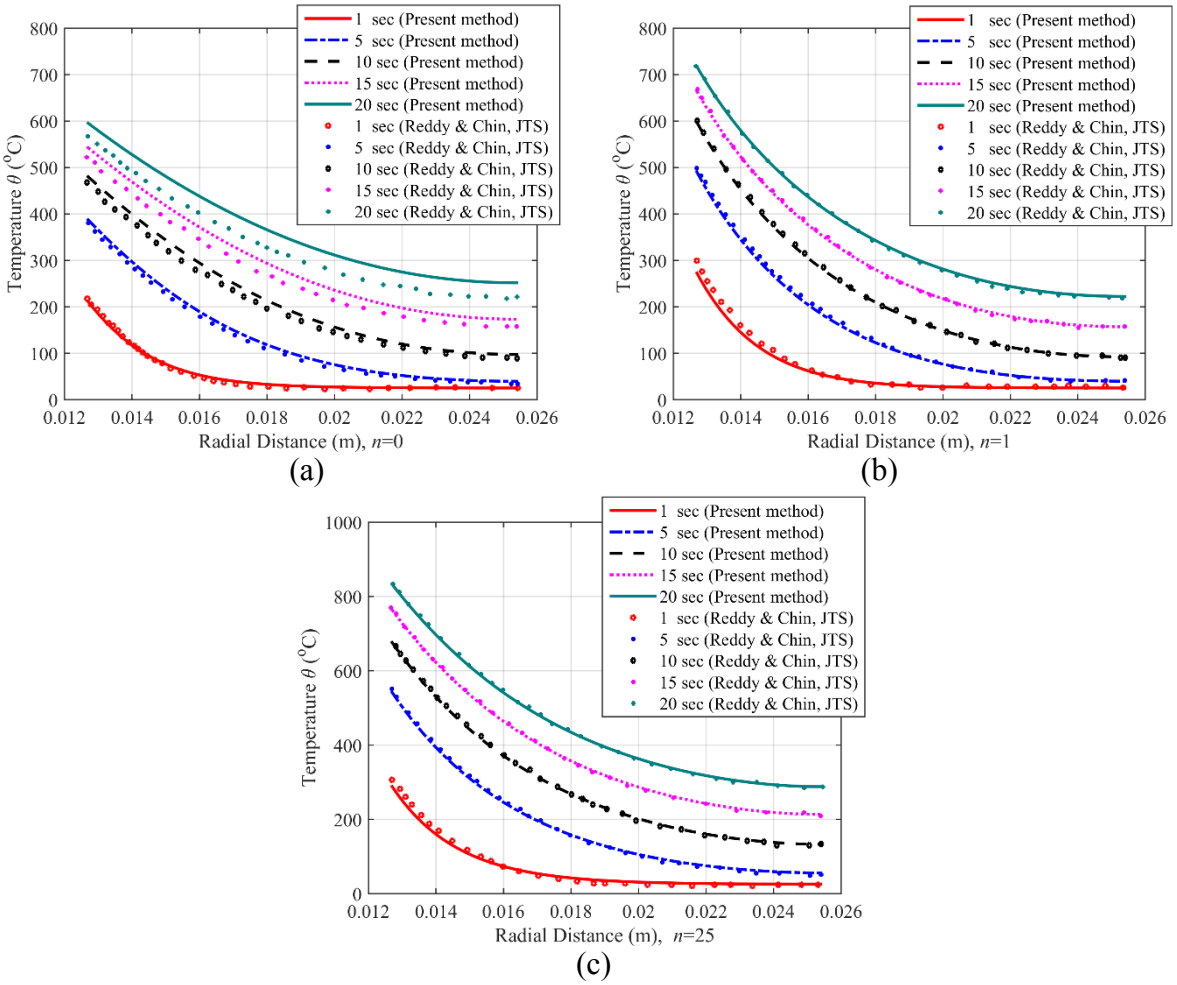

Figure 6.22. Relation between temperature and radial distance for various exponent coefficients: (a) $n=0$; (b) $n=1$; (c) $n=25$.

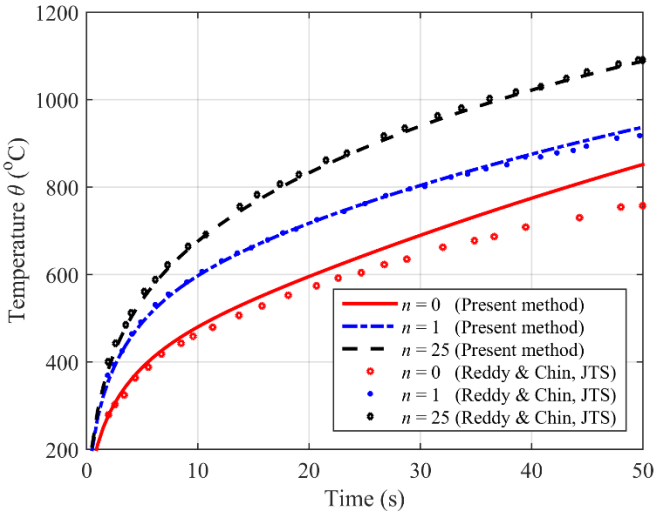

Figure 6.23. Relation between temperature field and time for various exponent coefficients: $n = 0$, $n = 1$, $n = 25$.

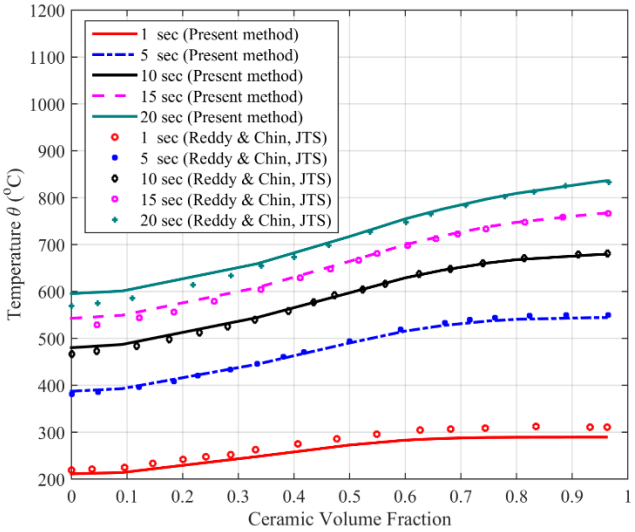

Figure 6.24. Relation between temperature field and ceramic volume fraction $V_{Si_3N_4}$ for various time levels: $t = 1\,\text{s}$, $t = 5\,\text{s}$, $t = 10\,\text{s}$, $t = 15\,\text{s}$, $t = 20\,\text{s}$.

The plot of hoop stress distribution versus radial distance is presented in Figure 6.25 with a comparison between the current method and numerical results in [134].

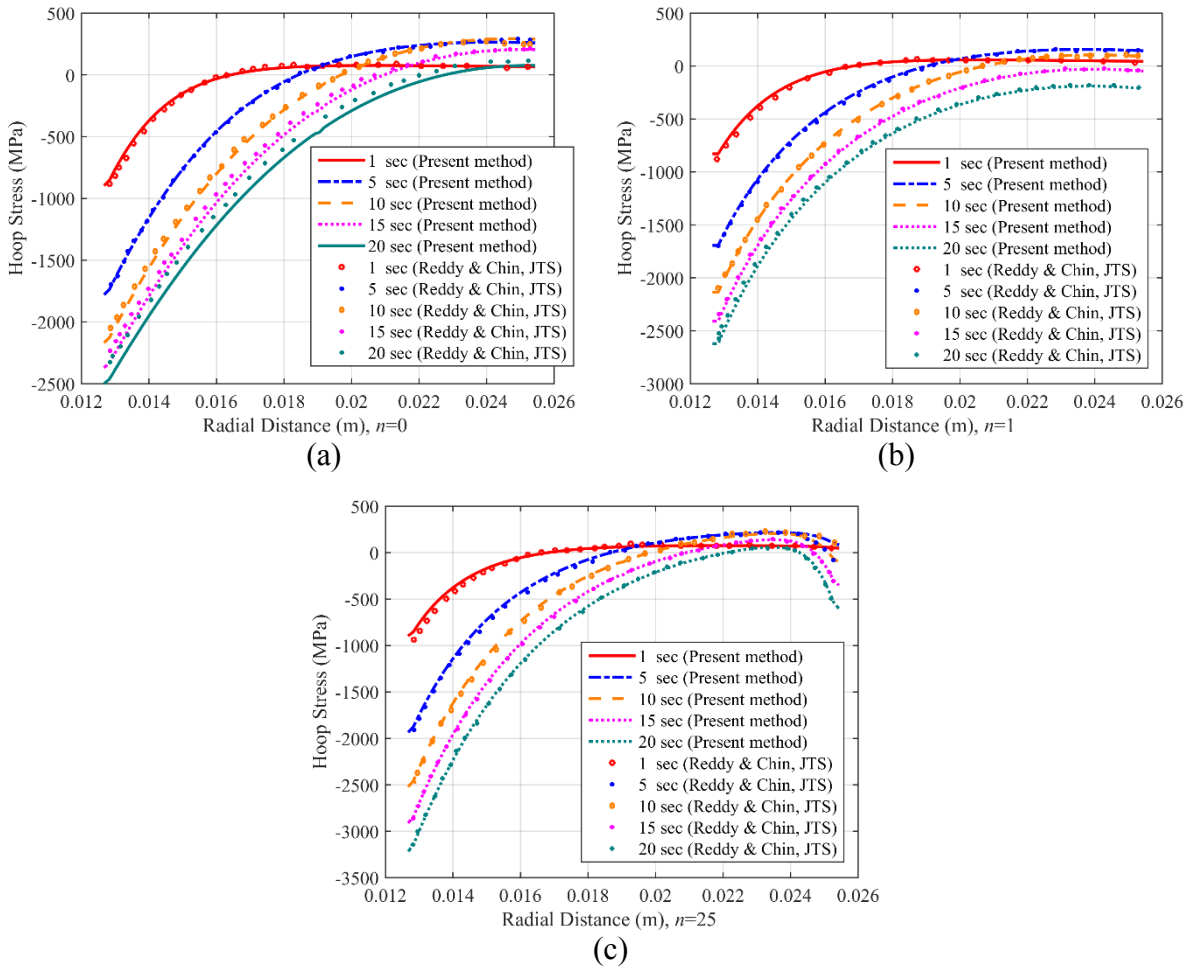

Figure 6.25. Plot of hoop stress versus radial distance for different exponent coefficients: (a) $n=0$; (b) $n=1$; (c) $n=25$.

6.4.6 Finite Strain Thermoelastic Expansion

This is a benchmark problem first proposed by Armero and Simo [6] to study the thermoelastic behavior of a thick-walled cylinder when subjected to radial expansion. The cylinder is assumed to be long enough and by assuming plane strain, the example can be reduced to a 2D problem. Instead of using the unit band of axisymmetric elements as given in [6,72], we keep the cross section as a shape of a disk and due to the symmetry condition, only one-quarter of the cross section is considered [88] as shown in Figure 6.26 with the spatial mesh. To simulate the internal pressure applied on the inner surface, a prescribed radial displacement with a constant speed $\dot{u}=1\,\text{mm/s}$ is applied at the inner radius $r=a=10\,\text{mm}$ until the displacement $u=20\,\text{mm}$. On the outer surface $r=b=20\,\text{mm}$, the temperature field is fixed as $\theta=\theta_{\text{ref}}=293\,\text{K}$ through the

process and traction free is assigned. The initial temperature for the cylinder is set to be $\theta_{\text{initial}} = 293\,\text{K}$. The problem clearly involves finite strains [6] since the final inner surface strain $\varepsilon = 200\%$ and is driven by thermal initial condition, prescribed temperature field and radial expansion [88].

Interface elements are placed on either the red solid (radial direction) or black dash line (circumferential direction) shown in Figure 6.26 to express two types of the interfaces. The first interface type (red solid line) can be used to model the bursting of pipe in the radial direction. The second interface type (black dash line) is used for the layered deposition process involved in additive manufacturing.

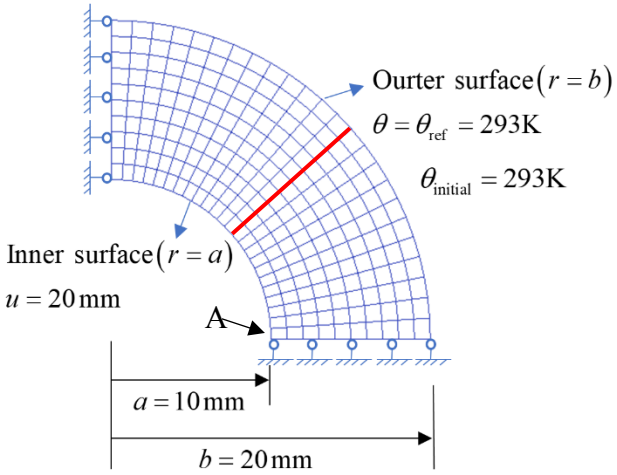

Figure 6.26. Problem description of the thick-walled cylinder.

Material Properties are summarized in Table 6.8, with two expansion coefficients to simulate weak and strong coupling between thermal and mechanical effects. The thermoelastic constitutive model is given in Eqn. (6-54).

Table 6.8. Material properties for the thick-walled cylinder problem.

Material properties	Symbol	value
Young's modulus	E	206899.94 MPa
Poisson's ratio	ν	0.29
Thermal conductivity	k_0	45.0 N/ s·K
Expansion coefficient	β_0	$1.5\times10^{-5}\,\text{K}^{-1}$ or $1.5\times10^{-4}\,\text{K}^{-1}$
Heat capacity	C_F	$0.46\times10^{9}\ \text{mm}^2/\text{s}^2\cdot\text{K}$
Density	ρ_0	$7.8\times10^{-9}\ \text{Ns}^2/\text{mm}^4$

Remark: *To match the results shown in [6], the material properties adopted in Table 6.8 are reference material properties with the following relation with the spatial material properties:* $\{\bullet\}_{\text{Reference}} = J \times \{\bullet\}_{\text{Spatial}}$ *, namely, the reference material property is the spatial material property multiplies the Jacobian.*

For the first expansion coefficient $\beta_0 = 1.5\times10^{-5}\,\text{K}^{-1}$, two different time steps $\Delta t = 1.0\,\text{s}$ and $\Delta t = 1.0\,\text{s}$ are chosen. Figure 6.27 presents the temperature distribution at instants $\text{t} = 1\,\text{s}, 5\,\text{s}, 10\,\text{s}, 15\,\text{s}$ and $20\,\text{s}$ with the deformed configuration. Large deformation can be observed in Figure 6.27. The thickness of the disk decrease during the simulation due to the difference of the expansion between the inner and outer surface [88]. For the second case with $\beta_0 = 1.5\times10^{-4}\,\text{K}^{-1}$, the temperature distribution is presented in Figure 6.28. Compared with the temperature variation shown in Figure 6.27, the case with a higher expansion coefficient has a stronger interaction between thermal and mechanical part which results in a higher variation of temperature field.

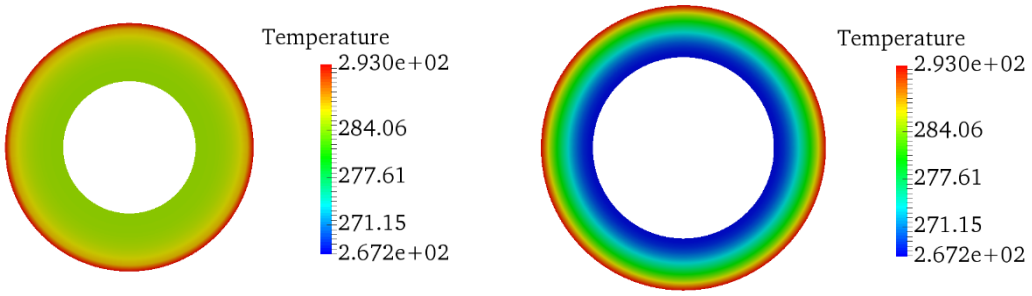

(a) (b)

Figure 6.27. Contour plot of temperature field for the deformed configuration of the thick-walled cylinder at different time steps with $\beta_0 = 1.5\times10^{-5}\,\text{K}^{-1}$: (a) $\text{t} = 1\,\text{s}$; (b) $\text{t} = 5\,\text{s}$; (c) $\text{t} = 10\,\text{s}$; (d) $\text{t} = 15\,\text{s}$; (e) $\text{t} = 20\,\text{s}$.

Figure 6.27 continued.

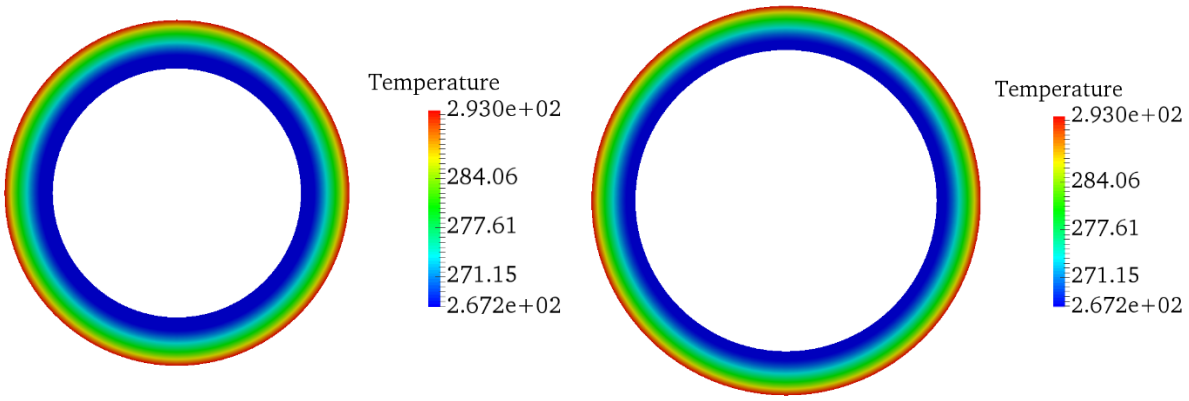

(c)

(d)

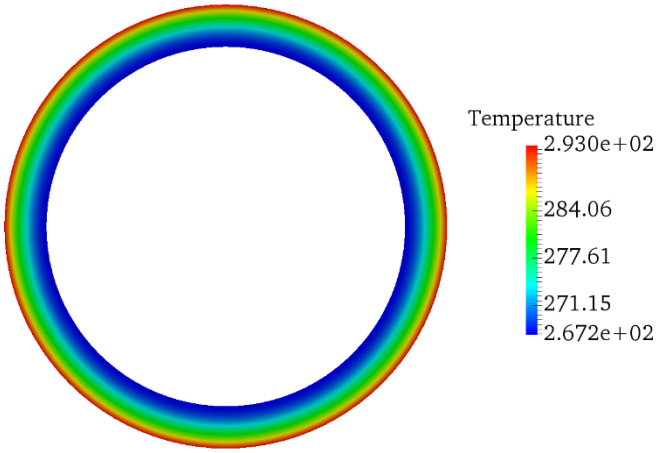

(e)

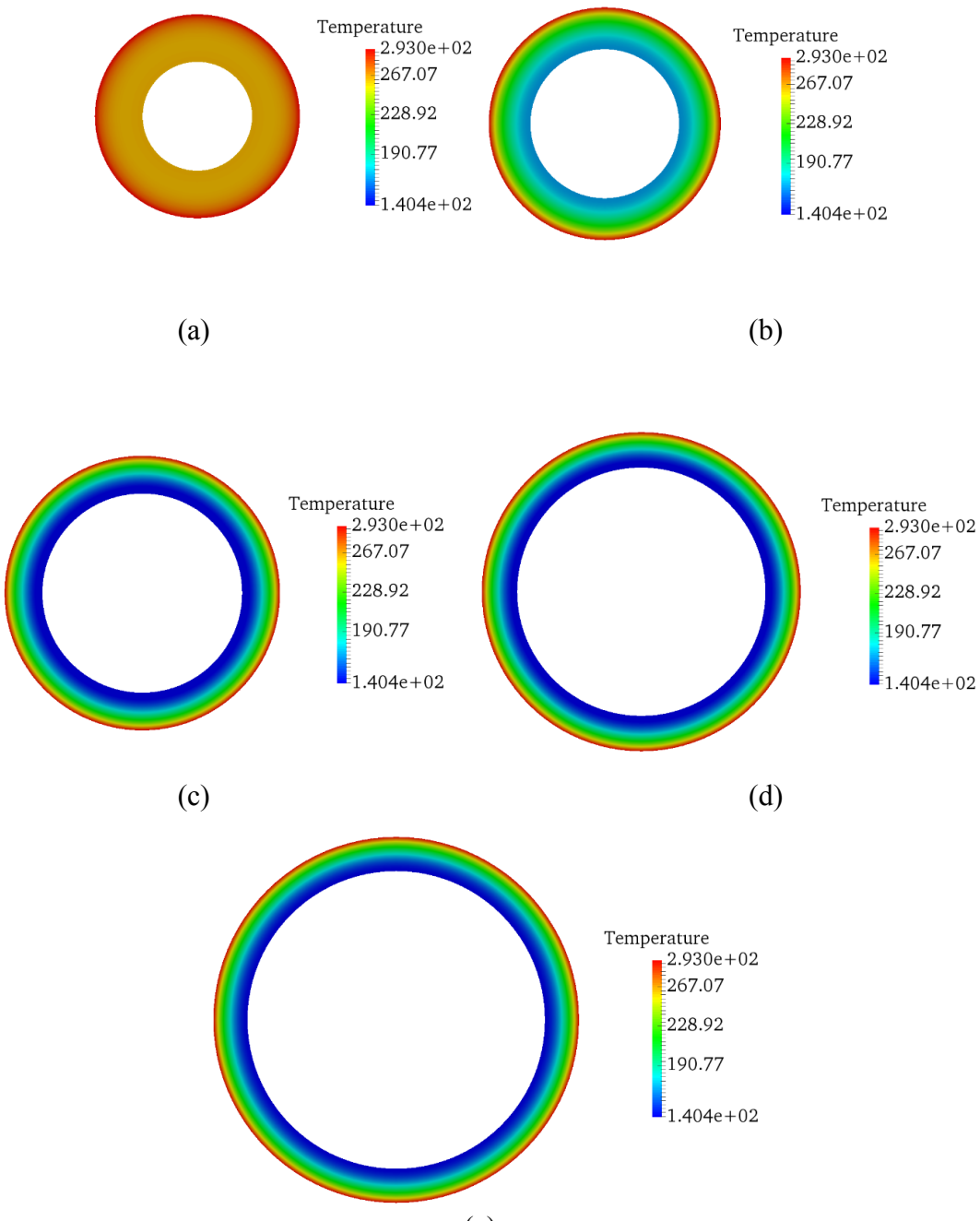

Figure 6.28. Contour plot of temperature field for the deformed configuration of the thick-walled cylinder at different time steps with $\beta_0 = 1.5 \times 10^{-4}\,\mathrm{K}^{-1}$: (a) $t = 1\,\mathrm{s}$; (b) $t = 5\,\mathrm{s}$; (c) $t = 10\,\mathrm{s}$; (d) $t = 15\,\mathrm{s}$; (e) $t = 20\,\mathrm{s}$.

Figure 6.29 represents the evolution of the relative temperature field ϑ_A at point A on the inner

surface as shown in Figure 6.26. As shown in Figure 6.29 (a), for weakly coupled case, while comparing the results with the numerical results from Armero and Simo [6], very good agreement is achieved, for $\Delta t = 0.1\text{s}$. The results are slightly overestimated by the proposed method for $\Delta t = 1\text{s}$ case. For the strongly coupled problem as shown in Figure 6.29 (b), the proposed method tends to slightly overestimate the temperature field compared with the results given in [6].

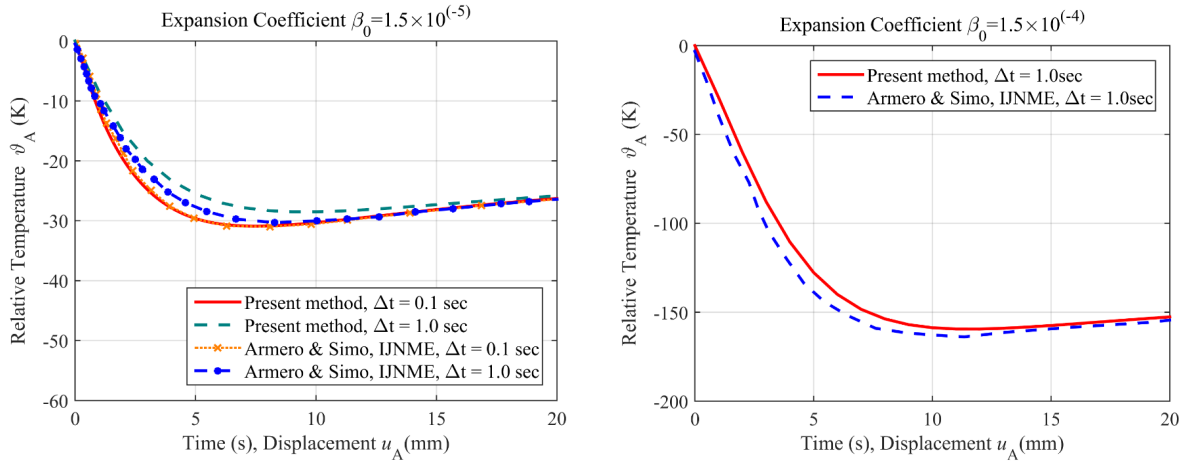

(a) (b)

Figure 6.29. Evolution of the relative temperature ϑ_A at the inner surface point A with different thermal expansion coefficient: (a) $\beta_0 = 1.5\times10^{-5}\,\text{K}^{-1}$; (b) $\beta_0 = 1.5\times10^{-4}\,\text{K}^{-1}$.

For both interface locations, the $\sigma_{\theta\theta}$ stress contour plots are shown in Figure 6.30. $\sigma_{\theta\theta}$ stress line plots in the circumferential direction AB for the red solid line interface, and radial direction AC for the black dash line interface shown in Figure 6.31. As shown in Figure 6.31 (a), the stress is constant in the circumferential direction AB on the inner surface for a given time step regarding the existence of the interfaces. In Figure 6.31 (b), at $\text{t} = 15\,\text{s}$ and $\text{t} = 20\,\text{s}$, a small jump in the stress field is observed in the stress $\sigma_{\theta\theta}$ line plot.

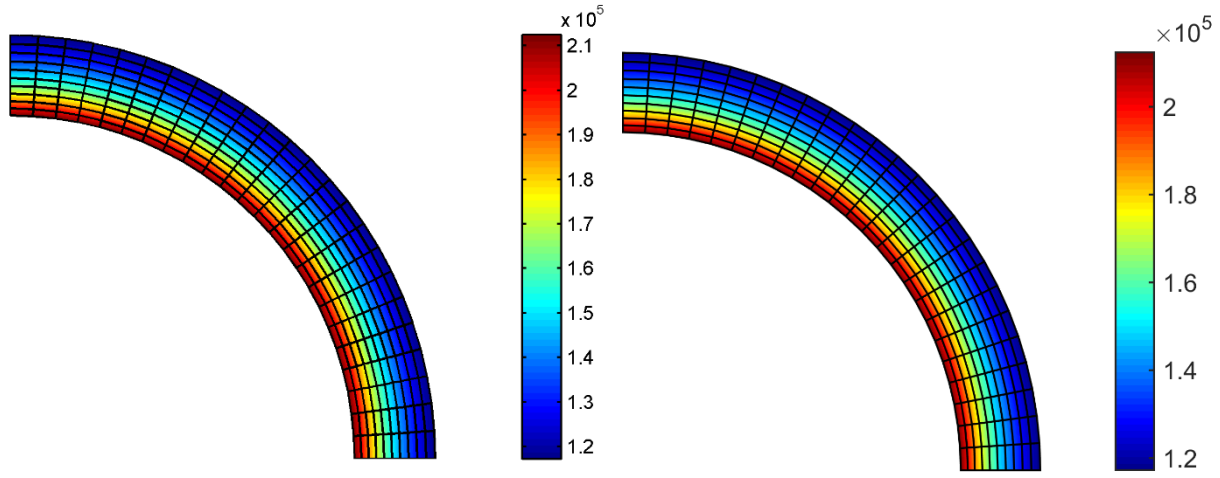

(a) (b)

Figure 6.30. $\sigma_{\theta\theta}$ plot for interface locations for thermal expansion coefficient $\beta_0 = 1.5\times10^{-5}\,\mathrm{K}^{-1}$: (a) Interface placed in the radial direction; (b) Interface placed in the circumferential direction.

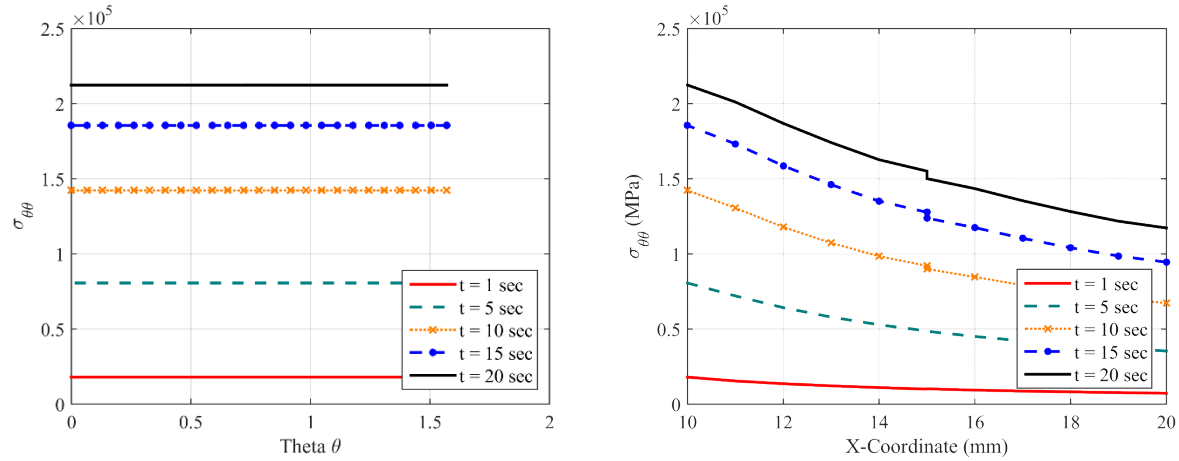

(a) (b)

Figure 6.31. $\sigma_{\theta\theta}$ plot for different interface locations for thermal expansion coefficient $\beta_0 = 1.5\times10^{-5}\,\mathrm{K}^{-1}$ along two interfaces:(a) Interface line AB; (b) Interface line AC.

For the problem with circumferential interface (black dash line), different material properties are assigned for the inner and outer rings of the cylinder as tabulated in Table 6.9. This situation typically arises in the modeling of additively manufactured cylinders employing materials with different properties. As given in Table 6.9, the outer ring is softer material as compared with the

inner ring of the cylinder.

Table 6.9. Material properties for the bi-material thick-walled cylinder problem.

Material properties	Symbol	value	Symbol	value
Young's modulus	E_{inner}	206899.94 MPa	E_{outer}	103449.97 MPa
Poisson's ratio	ν_{inner}	0.29	ν_{outer}	0.29
Thermal conductivity	$k_{0,\text{inner}}$	45.0 N/ s·K	$k_{0,\text{outer}}$	22.5 N/ s·K
Expansion coefficient	$\beta_{0,\text{inner}}$	$1.5\times10^{-5}\,\text{K}^{-1}$	$\beta_{0,\text{outer}}$	$3.0\times10^{-5}\,\text{K}^{-1}$
Heat capacity	$C_{F,\text{inner}}$	$0.46\times10^{9}\ \text{mm}^2/\text{s}^2\cdot\text{K}$	$C_{F,\text{outer}}$	$0.92\times10^{9}\ \text{mm}^2/\text{s}^2\cdot\text{K}$
Density	$\rho_{0,\text{inner}}$	$7.8\times10^{-9}\,\text{Ns}^2/\text{mm}^4$	$\rho_{0,\text{outer}}$	$7.8\times10^{-9}\,\text{Ns}^2/\text{mm}^4$

Figure 6.32 shows the $\sigma_{\theta\theta}$ contour plot and the line plot along interface AC for this bimaterial test case and a sharp jump at the bi-material interfaces can clearly be seen.

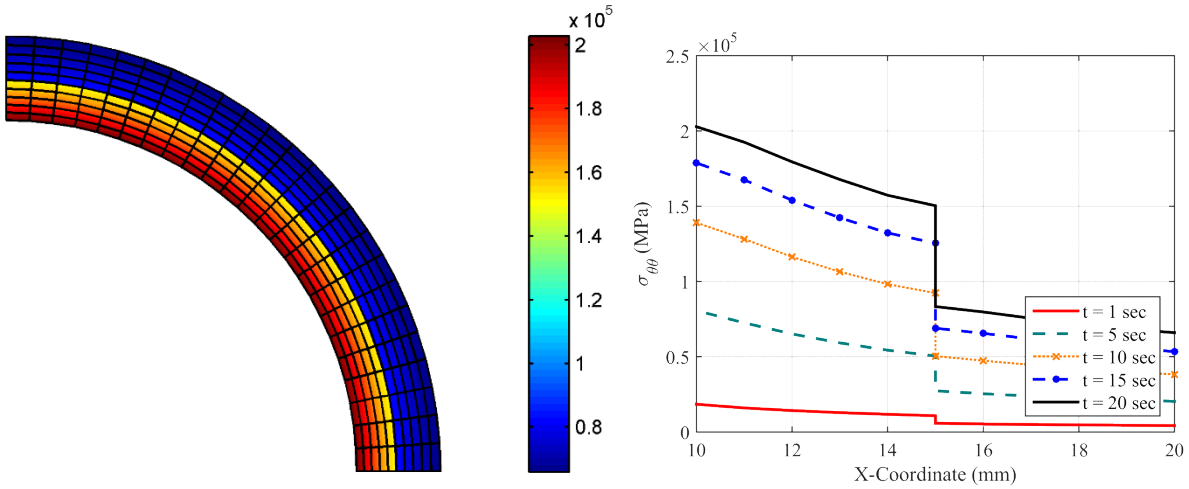

(a) (b)

Figure 6.32. Bi-material test:(a) $\sigma_{\theta\theta}$ contour plot; (b) $\sigma_{\theta\theta}$ line plot along interface line AC.

6.5 Conclusions

This Chapter focuses on thermo-mechanical problems on multiple elastic bodies interacting at the common interface across which thermal and mechanical fields interact. It presents a new interface coupling framework for mechanical and thermal fields on adjoining subdomains by embedding Discontinuous Galerkin (DG) ideas in the Continuous Galerkin (CG) method within the context

of Stabilized Methods. Starting from a thermo-mechanically coupled formulation over the elastic domain, a Lagrange multiplier method that couples fields along the interface is developed. Employing ideas from VMS based stabilization, the interfacial fine-scale problem is expanded via edge bubbles and resolved locally to extract an analytical expression for Lagrange multipliers. The derived expressions are a function of the evolving mechanical and thermal fields and therefore the resulting stabilized formulation contains numerical flux and stability tensor, while being free of user-defined parameters. Several test cases are presented to validate the method. The method is applied to model engineered materials governed by a spectrum of isotropic and anisotropic constitutive equations in the finite strain range to illustrate its versatility and applicability.

CHAPTER 7: CONCLUDING REMARKS AND FUTURE WORK

7.1 Concluding Remarks

The motivation of our work is to develop a variational framework and associated Computational Method for a simulation-based material design that can model the onset of weak and strong discontinuities in a mathematically consistent manner.

This dissertation has presented a stabilized framework to model mathematically nonsmooth problems including interface damage and fatigue evolution at finite strain regime. This work makes a major contribution to research on AM by demonstrating the framework with consistently evolved stabilization and opens a new way to solve the interface problems which has a broad application in material modeling and research of newly designed structures. Following the idea of the VMS stabilization, the standard primal solution fields (coarse scales) are enhanced through the existence of the fine scales which are solutions that are unresolved by coarse scales. The hallmark of this VMS based stabilization is that all the necessary terms are derived in a variational consistent manner. For problems evolve large deformation, a key feature with the present method is the naturally derived stability parameters and numerical flux terms. This feature provides the flexibility to embed the damage variable without loss of the stability and robustness of the method. By embedding different types of constitutive models for damage evolution, a unified formulation which treats damage in tension, compression and friction in compression in a consistent fashion is developed which can track various interfacial kinematics. Another objective of this dissertation is to develop a fully coupled thermomechanical formulation for interface problems. Analogously, the VMS method is employed to derive a couple of stabilized interface formulations by eliminating Lagrange multipliers for both thermal and mechanical fields.

The main contributions of the present dissertation are summarized as follows:

- Fully coupled thermomechanical interface formulations are developed in Chapter 2 and the formulations are extended to finite strain region in Chapter 6. The Lagrange multipliers are eliminated via VMS method for constraining both temperature and displacement fields. Problems with highly heterogeneous material properties and functionally graded materials are conducted to validate the robustness of the formulation.

- A VMS-based stabilized interface coupling framework is developed from an underlying Lagrange multiplier method. Fine-scale problem is residual driven which leads to a consistent formulation.
- The so-called numerical flux and the penalty or evolved stabilization parameters are consistently derived via a fine-scale problem where the fine scale solutions are represented by edge bubble functions. In the context of finite deformation, these terms play a crucial role in the robustness and efficiency of the interface formulation.
- The derived stability tensors are updated accordingly with material properties and element types, the geometry of the problems, and process the features of area-weighting and stress-weighting.
- The stabilized interface formulation accommodates any combinations of element types and order of polynomial functions, non-conforming meshes, and full DG elements.
- Error convergence analyses were conducted for problems with analytical solutions, and the convergence of the discretization error confirmed the stability of the proposed interface method.
- The stabilized DG formulation is extended for simulating the debonding process in general bimaterial interface at finite strains. The algorithmic interface parameters are updated automatically as the nonlinear problem evolves. For the class of problems that have been addressed with the new method, i.e., process modeling of the damage and fracture, different interfacial damage constitutive models and the flow rules for interfacial mechanics are adopted that combined interfacial debonding in tension (damage), compression (damage and friction) in a unified way.
- In Chapter 4, Appearance of the gap function in the expression for the Lagrange multiplier and therefore in the evolving finite-scales provides a natural mechanism to embed physics based models as well as phenomenological models for progressive failure under various loading scenarios.
- In Chapter 5, fatigue effects are embedded via a different interfacial fatigue constitutive model which is capable of capturing the damage accumulation and material degradation along with a cohesive damage envelope to capture the nucleation.

- In Chapter 6, the stabilized fully coupled thermomechanical interface framework is established and it has been shown that the thermomechanical coupling term plays an important role for problems involving high transient temperature gradient, and for problems with finite strains.
- Benchmark problems are presented to show the robustness and accuracy of the interface method. L_2 and H_1 convergence rate studies are shown for a series of 3D large rotation problems, 2D bending problems and thermomechanical coupled problems. The proposed interface formulation is also validated through a series of numerical test cases and compared with both numerical and experimental results in the literature.

7.2 Future Work

7.2.1 Mixed Interfacial Formulation for Nearly Incompressible Elasticity

To fit for a broader class of material types, a new mixed framework for a class of problems of incompressible linear elasticity with the existence of interfaces needs to be developed. In this framework, we have both displacement and pressure as unknown fields. To satisfy the inf-sup condition and use the standard Galerkin shape functions, a novel stabilized formulation is derived. The key contribution will be the combination of both interiors and interface stabilization. Since the fine scale solution is residual driven and is inherently derived, we have this naturally derived build-in explicit error which can be used to evaluate the accuracy of the proposed method. By combining this formulation with the previous interface damage model, several large-scale problems are planned to validate the solving capacity of the proposed method. This extension develops the variety of the material class to next level and maintains the possibilities of simulating different types of materials.

As a first step, we consider a problem with the geometry consists of a square domain which is subsequently deformed into a trapezoid by raising the upper right-hand corner. The problem is taken from Chapter 3 but modified for incompressible material and is validated for interior VMS stabilization framework given in [101]. A single pure-displacement quadrilateral element can represent this deformation mode, as shown in Figure 7.1 (b). The analytical solution is reproduced below in Cartesian coordinates in terms of the vertical displacement δ of the corner node:

$$x = X, \qquad y = \delta XY + Y, \qquad z = Z \tag{7-1}$$

The deformation gradient and Jacobian are given as:

$$\boldsymbol{F} = \begin{bmatrix} 1 & 0 & 0 \\ \delta Y & \delta X + 1 & 0 \\ 0 & 0 & 1 \end{bmatrix}, \qquad J = \delta X + 1 \tag{7-2}$$

Considering the stored elastic strain energy function, the first Piola-Kirchhoff stress tensor follows:

$$\boldsymbol{P} = \begin{bmatrix} \delta\lambda JX & \delta\mu Y/J - \delta^2\lambda XY & 0 \\ \delta\mu Y & \left[\delta X\left(\lambda J + \mu + \mu J\right)\right]/J & 0 \\ 0 & 0 & \delta\lambda JX \end{bmatrix} \tag{7-3}$$

The expression of the body force term below:

$$\rho_o \boldsymbol{B} = -\text{DIV}\ \boldsymbol{P} = \left[-\left(\delta\mu/J + \delta\lambda J\right) \quad 0 \quad 0\right]^T \tag{7-4}$$

The material parameters are taken as $\lambda = \mu = 40$ and the load parameter as $\delta = 1.01$. To investigate this problem in the numerical setting, we apply fixed boundary conditions on the lower edge and apply the analytical tractions arising from Eqn. (7-3) on the other edges, as depicted in Figure 7.1 (a). The exact pressure field is presented in Figure 7.1 (b). Due to the appearance of $J = \delta X + 1$ in the denominator of (7-3) and (7-4), the integrands within the finite element residual vector and the tangent matrix will contain rational polynomials that are not precisely evaluated through low-order Gauss quadrature. To obtain the exact solution to numerical precision, we employ higher-order rules using 10 × 10 quadrature points for element-interior integrals and 10 points for boundary or interface integrals.

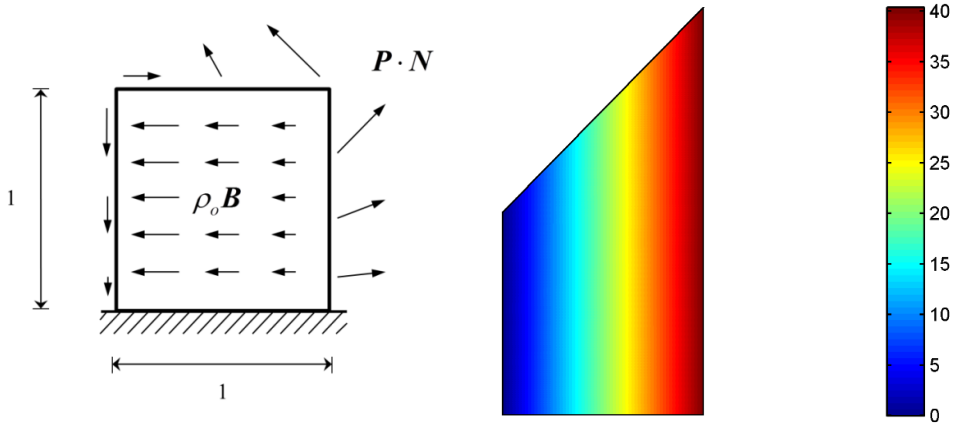

(a) (b)

Figure 7.1. Trapezoidal deformation problem: (a) problem domain; (b) exact pressure field on deformed configuration.

A nonconforming mesh shown in Figure 7.2 with the lower region is represented using two quadratic triangular elements in the lower-left and one biquadratic element in the lower-right; the upper region contains three bilinear quadrilaterals such that the interface is nonconforming.

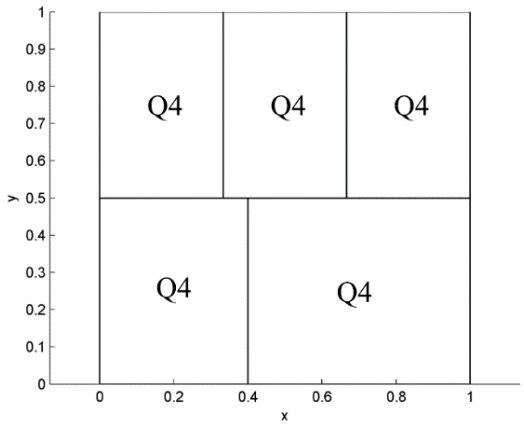

Figure 7.2. Nonconforming meshes: bilinear quadrilaterals.

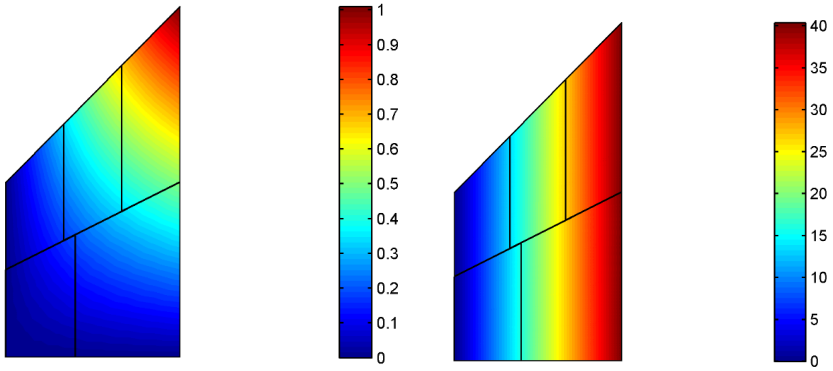

(a) (b)

Figure 7.3. Vertical displacement and pressure contours on deformed configuration: (a) vertical displacement; (b) pressure field.

The pressure field presented in Figure 7.3 is exactly the same as the exact solution shown in Figure 7.1.

7.2.2 CG-DG Coupling Formulation

When modeling the damage behavior of composite materials for large-scale problems, board applications are limited by computational cost. Developing a hierarchical coupling technique to merge the discrete constituent model with a homogenized model is with the objective to capture local effects with comparable computational costs. As shown in Figure 7.4, the green region represents a homogenized domain where no local delamination or debonding initiates, which necessitates a lower order of mesh refinement with a homogenized theory. The blue region with detailed mesh represents the domain with local damage where the proposed interface formulation is adopted. It is possible that two regions have different systems of governing equations and levels of mesh refinements. Thus, a heterogeneous multiscale method can be employed here [97]. The challenge is how to consistently combine the detailed region with the coarse region in a unified fashion. Meanwhile, the development framework should be able to merge the homogenized model with the discrete model by mixing element types and accommodating non-conforming meshes.

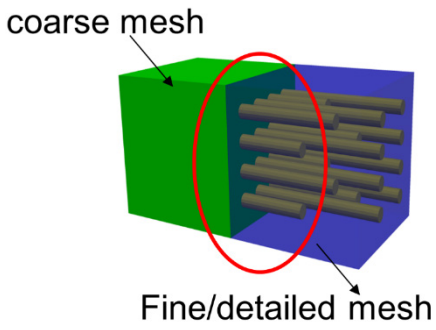

Figure 7.4. Hierarchical coupling of coarse and fine mesh.

7.2.3 Multiphysics problem

7.2.3.1 Degradation process of Lithium-ion battery: Chemical and Thermal Reactions

High strength, high durability, and light weight are the hallmark attributes of composites with fibrous layouts and Nano-particulate inclusions. These engineered materials are therefore becoming the materials of choice in many applications. By carefully selecting the properties of reinforcing constituents and inclusions, one can enhance material properties in preferred directions, and the embedded constituents can act as internal energy dissipation devices. With designed layouts of embedded constituents, researchers can directionally channel the energy for the design of impact absorbing materials (e.g., bulletproof vests and panels), or for converting mechanical

energy into electrical energy as the case is in hybrid mechanical devices.

While the VMS method has been validated through many benchmark problems in both solid and fluid mechanics, a potential for applying this method for Multiphysics is obvious. Simulating Multiphysics problems which involve multiple physical phenomena remains as one of the most challenging fields to date. While single field problems can be solved via general finite element method, multi-field problems may encounter stability issues when different partial differential equations are solved simultaneously. With the existence of the additional stabilization terms, the goal is to solve Multiphysics problems within standard, continuous or discontinuous finite element spaces and limit massive mesh refinements.

This topic can be elaborated as the extension to model the degradation of layered oxide Lithium-ion (Li-ion) battery materials. The degradation is caused by the fatigue effects in the operating process, or material aging in the rest process, and takes place in a microscope or atomistic level. As discussed in [165], the normal degradation mechanisms for cathode composites include cracking or debonding of particles at interfaces and structural disordering of the particle-inclusion system. Li-ion batteries are very unstable in the context of thermodynamics. During the charging and uncharging process or the rest process, chemical or electronic reactions and phrase change may occur. This plays an important role in the performance of the batteries and therefore, defines the irreversible loss of the capacity [62].

In the past few years [67], a new class of techniques has been put forward which allows controlling the creation of spatially heterogeneous interphases over individual particles, resulting in the so-called “patchy” particles; see, e.g., Figure 7.5. Owing to their inherently anisotropic chemical and physical properties, interest in such interphases is growing rapidly, and investigations into a number of novel engineering and medical applications have started [173]. Despite these advances in the synthesis of organic materials with highly controllable nanostructures, it remains an open problem to measure the mechanical/physical properties of the interphases that are eventually created and the distribution of charges (or other source terms) that they may contain. An even more critical open problem from an applications perspective is to determine how such interphases with source terms manifest themselves at macroscopic length scales.

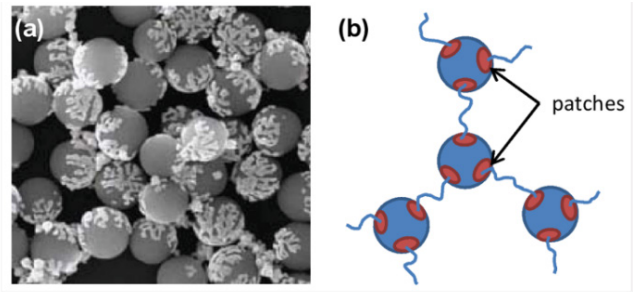

(a) (b)

Figure 7.5. (a) Micrograph; (b) schematic of patchy particles illustrating the ability of current synthesis techniques to form different types of interphases over different parts of individual particles.

In all these engineered materials a significant issue is the reliability of the material interphases, debonding at the material interfaces, or fracture of particles that can severely limit the functional life of the material. A robust framework with the ability to accurately model the interphases will open doors to the modeling of interfacial fatigue effects in engineered materials which is a fundamental issue to be addressed in the development of resilient infrastructure systems for advanced engineering applications.

A model problem of this particle inclusion case is shown in Figure 7.6 with single particle inside of a brick matrix. The material properties are given in Table 7.1, which are taken from [40] for epoxy matrix and glass bead inclusion material. The interface maximum stress and critical gap are taken to match the first debonding point from the experimental data given in [40]. From Figure 7.6, a clear debonding at the particle-matrix interfaces is shown with a stress concentration at the particle tips where the particle and matrix are still bonded together.

Table 7.1. Material properties and damage parameters for single spherical particle inclusion.

Material	E (GPa)	ν	P_c (MPa)	δ_c (mm)
Vinyl Epoxy	3.5	0.35	-	-
Glass Bead	70	0.25	-	-
Interface	-	-	50	0.2

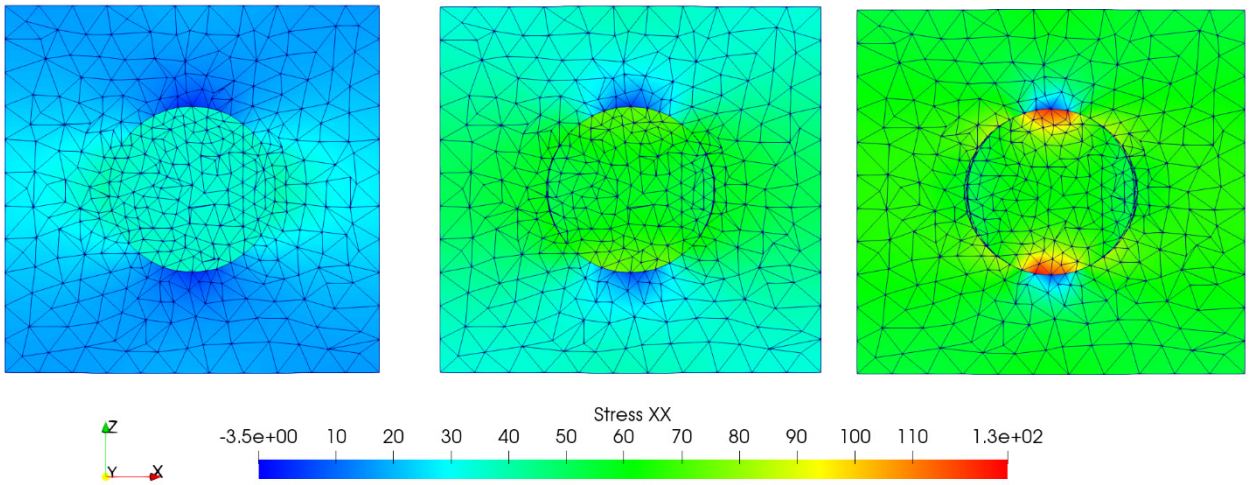

Figure 7.6. Stress σ_{11} and the evolution of the deformation along the center slice of the cube.

A comparison of the opening angle versus the applied strain plot is presented in Figure 7.7. As we refine the mesh, the current numerical results are approaching the experimental results given in Cho et al. [40].

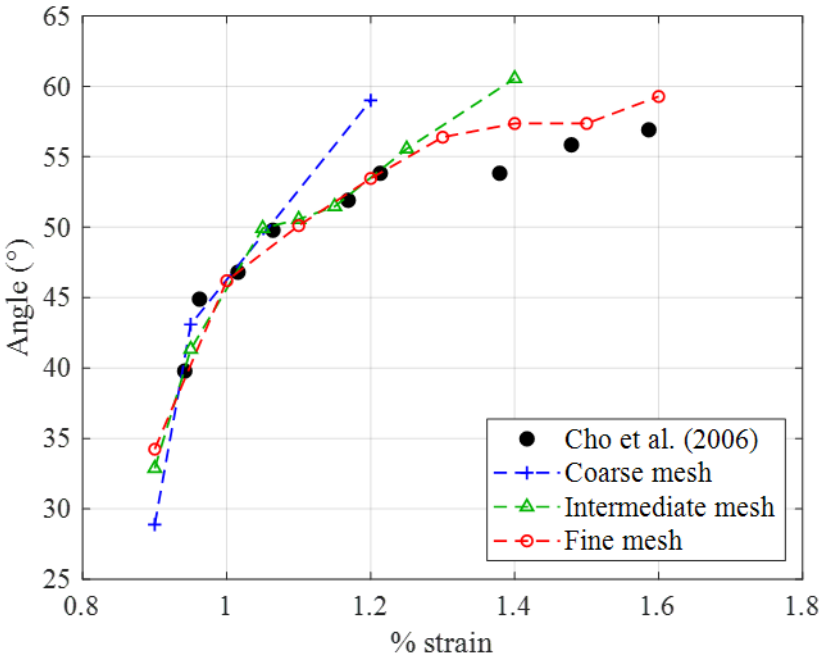

Figure 7.7. Comparison between experimental result and numerical result.

A multiple particle inclusion test problem is shown in Figure 7.8 with the axial stress plots for both particles and matrix.

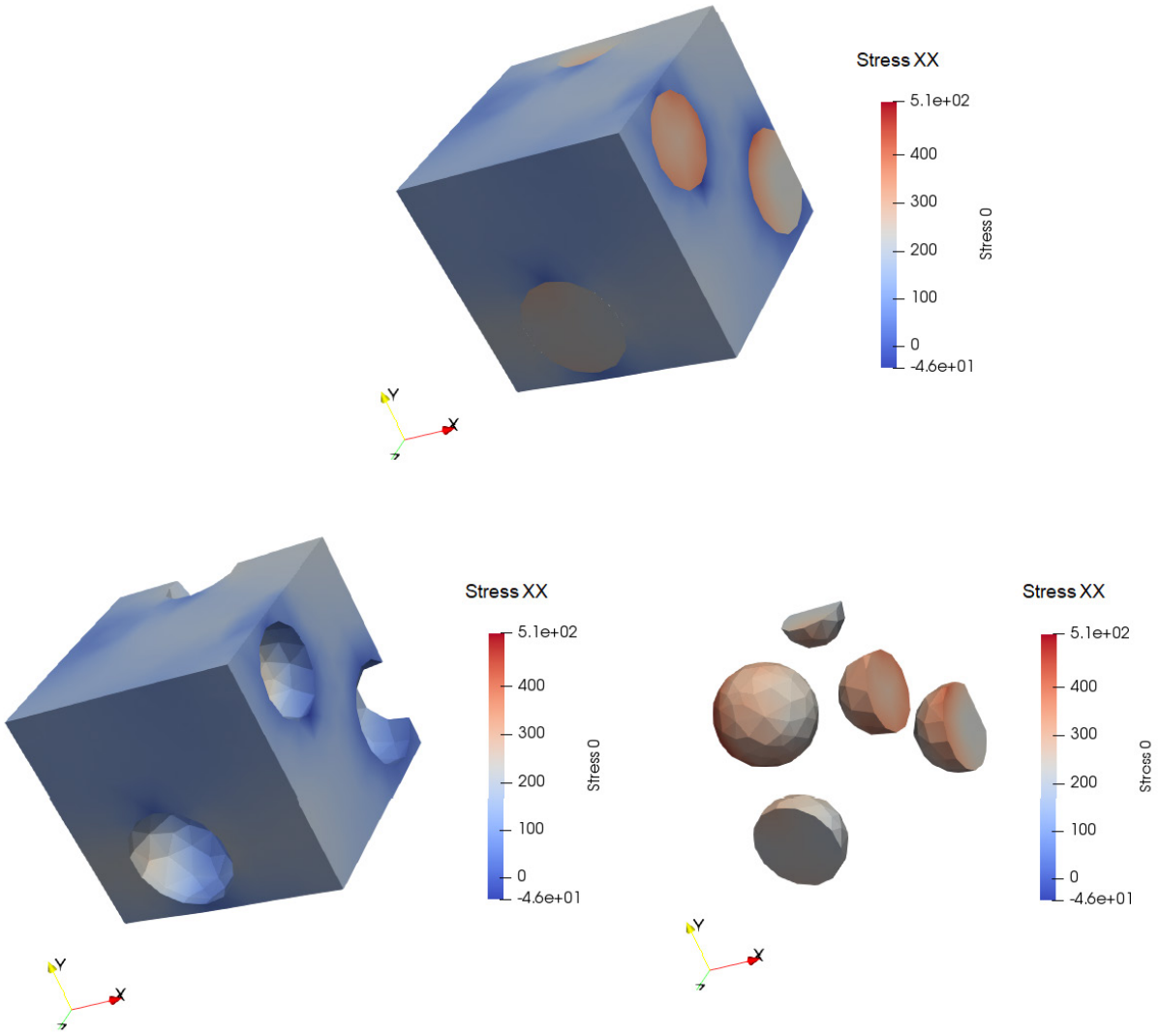

Figure 7.8. Multiple particle inclusions: Stress σ_{11} for both matrix and particles.

7.2.4 Additive Manufacturing in Civil Infrastructure

As stated in Chapter 2 and Chapter 5, additive manufacturing technique allows for using composite materials, functionally graded materials (FGM), recycled materials and smart materials for rapid building construction which significantly save the labor and construction period. While the traditional construction is still mostly a manual task, 3D printing technique provides a platform for using the computer aided design (CAD) and precisely printing different construction components and resembling into real civil infrastructure buildings. While large-scale 3D printing for cement-based [56] is applied to civil engineering with complex geometries, the challenge is how to develop a 3D printing technique to construct performance-based material properties which secure an

enhanced behavior. Another challenge is once the deposited structure is ready, the measurement of the current strength of the structure during various loading conditions. While the ACI code exists for traditional buildings and materials, a systematic and reliable method is to be developed such that the behavior of the additive manufactured structure can be predicted through analogy to the traditional masonry or concrete buildings.

REFERENCES

1. M. Abbasi, M. Sabbaghian, and M. Reza Eslami, Exact closed-form solution of the dynamic coupled thermoelastic response of a functionally graded Timoshenko beam. J Mech. Mater. Struct. 5 (2010) 79–94.
2. G. Alfano, E. Sacco, Combining interface damage and friction in a cohesive-zone model. Int. J Numer. Methods Eng. 68 (2006) 542–582.
3. A. M. Dychne, Conductivity of a two-phase two-dimensional system, Exper. And Theor. Phys. 59 (1970) 110–115
4. C. Annavarapu, M. Hautefeuille, and J. E. Dolbow, A Nitsche stabilized finite element method for frictional sliding on embedded interfaces. Part I: Single interface. Comput. Methods Appl. Mech. Eng. 268 (2014) 417–436.
5. C. Annavarapu, M. Hautefeuille, J.E. Dolbow, A robust Nitsche's formulation for interface problems. Comput. Methods Appl. Mech. Eng. 225 (2012) 44-54.
6. F. Armero, J.C. Simo, A new unconditionally stable fractional step method for non-linear coupled thermomechanical problems. Int. J Numer. Methods Eng. 35 (1992) 737-766.
7. I. Arias, S. Serebrinsky, M. Ortiz. A phenomenological cohesive model of ferroelectric fatigue. Acta Materialia. 54 (2006) 975-984.
8. D. N. Arnold, An interior penalty finite element method with discontinuous elements. SIAM J. Numer. Anal. 19 (1982) 742-760.
9. D. N. Arnold, F. Brezzi, B. Cockburn, and L. D. Marini, Unified analysis of discontinuous Galerkin methods for elliptic problems. SIAM J. Numer. Anal. 39 (2002) 1749–1779.
10. M. Ayub and A. Masud, A new stabilized formulation for convective-diffusive heat transfer. Numer. Heat Tr. 44 (2003) 1-23.
11. C. Baiocchi, F. Brezzi, L.D. Marini, Stabilization of Galerkin methods and applications to domain decomposition, in: Future Tendencies in Computer Science. Control Appl. Math. (1992) 343–355.
12. R. Becker, P. Hansbo, and R. Stenberg, A finite element method for domain decomposition with non-matching grids. Esaim Math. Model. Numer. Anal. 37 (2003) 209–225.
13. S.A. Berggren, D. Lukkassen, A. Meidell, L. Simula, A new method for numerical solution of checkerboard fields, J. Appl. Math. 1 (2001) 157–173.

14. H. J. C. Barbosa and T. J. R. Hughes, The finite element method with Lagrange multipliers on the boundary: circumventing the Babuška-Brezzi condition. Comput. Methods Appl. Mech. Eng. 85 (1991) 109–128.
15. H. J. C. Barbosa and T. J. R. Hughes, Boundary Lagrange multipliers in finite element methods: Error analysis in natural norms. Numer. Math. 62 (1992) 1–15.
16. G.I. Barenblatt, The Mathematical Theory of Equilibrium Cracks in Brittle Fracture, Adv. Appl. Mech. 7 (1962) 55–129.
17. C. E. Baumann and J. T. Oden, A discontinuous hp finite element method for convection—diffusion problems. Comput. Methods Appl. Mech. Eng. 175 (1999) 311–341.
18. Y. Bazilevs, C. Michler, V. M. Calo, T. J. R. Hughes, Weak Dirichlet boundary conditions for wall-bounded turbulent flows. Comput. Methods Appl. Mech. Eng. 196 (2007) 4853-4862.
19. V. T. Bechel, N. R. Sottos, A comparison of calculated and measured debond lengths from fiber push-out tests. Compos. Sci. Technol. 58 (1998) 1727–1739.
20. R. Becker, P. Hansbo, and R. Stenberg, A finite element method for domain decomposition with non-matching grids. Esaim Math. Model. Numer. Anal. 37 (2003) 209–225.
21. T. Belytschko, W. K. Liu, B. Moran, K. Elkhodary, Nonlinear Finite Elements for Continua and Structures. Wiley: Hoboken, New Jersey, 2014.
22. B. Berman, 3-D printing: The new industrial revolution, Business Horizons. 55 (2012) 155–162.
23. C. Bernardi, Y. Maday, A. T. Patera, A new nonconforming approach to domain decomposition: The mortar element method. Nonlinear Partial Differential Equations and their Applications, Pitman and Wiley. (1992) 13–51.
24. N. Bonora and G. M. Newaz, Low cycle fatigue life estimation for ductile metals using a nonlinear continuum damage mechanics model. Int. J Solids Struct, 35 (1998) 1881–1894.
25. R. de Borst, J. J. C. Remmers, and A. Needleman, Mesh-independent discrete numerical representations of cohesive-zone models. Eng. Fract. Mech. 73 (2006) 160-177.
26. F. Brezzi, On the existence, uniqueness and approximation of saddle-point problems arising from lagrangian multipliers. Esaim Math. Model. Numer. Anal. - Modélisation Mathématique et Analyse Numérique, 8 (1974) 129-151.

27. F. Brezzi, M.-O. Bristeau, L. P. Franca, M. Mallet, and G. Rogé, A relationship between stabilized finite element methods and the Galerkin method with bubble functions. Comput. Methods Appl. Mech. Eng. 96 (1992) 117-129.
28. F. Brezzi and M. Fortin, Mixed and Hybrid Finite Element Methods,. New York, NY: Springer, 1991.
29. F. Brezzi, T. J. R. Hughes, L. D. Marini, and A. Masud, Mixed Discontinuous Galerkin Methods for Darcy Flow. J Sci Comput. 22–23 (2005) 119–145.
30. G. T. Camacho, M. Ortiz, Computational modelling of impact damage in brittle materials. Int. J Solids Struct. 33 (1996) 2899-2938.
31. P. Castillo, Performance of Discontinuous Galerkin Methods for Elliptic PDEs. SIAM J Sci. Comput. 24 (2002) 524-547.
32. P. Castillo, B. Cockburn, I. Perugia, and D. Schötzau, An A Priori Error Analysis of the Local Discontinuous Galerkin Method for Elliptic Problems. SIAM J. Numer. Anal. 38 (2000) 1676–1706.
33. J. L. Chaboche. Une loi differentielle d'endommagement de fatigue avec cumulation non lineaire. Rev. Fr.Mec. (1974) 50-51.
34. J. Chaboche, Lifetime Predictions and Cumulative Damage under High-Temperature Conditions. ASTM International. (1982) 81-104.
35. J. L. Chaboche, Continuum Damage Mechanics: Part I—General Concepts. J. Appl. Mech. 55 (1988) 59–64.
36. J. L. Chaboche, Continuum Damage Mechanics: Part II—Damage Growth, Crack Initiation, and Crack Growth. J. Appl. Mech. 55 (1988) 65–72.
37. J. L. Chaboche, R. Girard, A. Schaff. Numerical analysis of composite systems by using interphase/interface models. Comput. Mech. 20 (1997) 3-11.
38. P. Chen, A. Masud, A General Framework for Thermoelasticity with Embedded Discontinuities:Linearized Coupled Formulations. Int. J Numer. Methods Eng., Submitted, 2018.
39. P. Chen, T. J. Truster, and A. Masud, Interfacial stabilization at finite strains for weak and strong discontinuities in multi-constituent materials. Comput. Methods Appl. Mech. Eng. 328 (2018) 717–751.

40. J. Cho, M.S. Joshi, C.T. Sun, Effect of inclusion size on mechanical properties of polymeric composites with micro and nano particles, Compos. Sci. and Technol. 66 (2006) 1941–1952.
41. B. Cockburn, J. Gopalakrishnan, and R. Lazarov, Unified Hybridization of Discontinuous Galerkin, Mixed, and Continuous Galerkin Methods for Second Order Elliptic Problems. SIAM J. Numer. Anal. 47 (2009) 1319–1365.
42. R. Codina, J. Baiges, Weak imposition of essential boundary conditions in the finite element approximation of elliptic problems with non-matching meshes, Int. J Numer. Methods Eng. 104 (2015) 624–654.
43. R. V. Craster and Y. V. Obnosov, Checkerboard composites with separated phases. J. Math. Phys. 42 (2011) 5379–5388.
44. A. De-Andrés, J.L. Pérez. M. Ortiz. Elastoplastic finite element analysis of three-dimensional fatigue crack growth in aluminum shafts subjected to axial loading. Int. J. Solids Struct. 36 (1999) 2231-2258.
45. J. E. Dolbow, L. P. Franca, Residual-free bubbles for embedded Dirichlet problems. Comput. Methods Appl. Mech. 197 (2008) 3751-3759.
46. D. S. Dugdale, Yielding of steel sheets containing slits. J. Mech. Phys. Solids. 8 (1960) 100–104.
47. R. Echle, G.Z. Voyiadjis. Simulation of damage evolution in a uni-directional titanium matrix composite subjected to high cycle fatigue. Int. J. Fatigue. 21 (1999) 909-923.
48. M. Elices, G. V. Guinea, J. Gómez, and J. Planas, The cohesive zone model: advantages, limitations and challenges. Eng. Fract. Mech. 69 (2002) 137–163.
49. A. Embar, J. Dolbow, and I. Harari, Imposing Dirichlet boundary conditions with Nitsche's method and spline-based finite elements. Int. J Numer. Methods Eng. 83 (2010) 877–898.
50. R. E. Ewing, J. Wang, and Y. Yang, A stabilized discontinuous finite element method for elliptic problems. Numer. Linear Algebra Appl. 10 (2003) 83–104.
51. A. T. Eyck, F. Celiker, and A. Lew, Adaptive stabilization of discontinuous Galerkin methods for nonlinear elasticity: Analytical estimates. Comput. Methods Appl. Mech. Eng. 197 (2008) 2989-3000.

52. A.T. Eyck, F. Celiker, and A. Lew, Adaptive stabilization of discontinuous Galerkin methods for nonlinear elasticity: Motivation, formulation, and numerical examples. Comput. Methods Appl. Mech. Eng. 197 (2008) 3605-3622.
53. A. T. Eyck, A. Lew, Discontinuous Galerkin methods for non-linear elasticity. Int. J Numer. Methods Eng. 2006. 67 (9) 1204-1243.
54. J. Fish, Q. Yu. Computational mechanics of fatigue and life predictions for composite materials and structures. Computer methods in applied mechanics and engineering. 191 (2002) 4827-4849.
55. L.P. Franca, T.E Tezduyar and A. Masud, Finite Element Methods: 1970's and Beyond. CIMNE, Barcelona, Spain 2004. ISBN 84-95999-49-8.
56. C. Gosselin, R. Duballet, P. Roux, N. Gaudillière, J. Dirrenberger, P. Morel, Large-scale 3D printing of ultra-high performance concrete – a new processing route for architects and builders, Materials & Design. 100 (2016) 102–109.
57. M. Griebel and M. A. Schweitzer, A Particle-Partition of Unity Method Part V: Boundary Conditions, in Geometric Analysis and Nonlinear Partial Differential Equations, Springer, Berlin, Heidelberg. (2003) 519–542.
58. A. Hansbo and P. Hansbo, An unfitted finite element method, based on Nitsche's method, for elliptic interface problems. Comput. Methods Appl. Mech. Eng. 191 (2002) 5537-5552.
59. P. Hansbo, K. Salomonsson. A discontinuous Galerkin method for cohesive zone modelling. Finite Elem. Anal. Des. 102-103 (2015) 1-6.
60. P. Hansbo and M. G. Larson, Discontinuous Galerkin methods for incompressible and nearly incompressible elasticity by Nitsche's method. Comput. Methods Appl. Mech. Eng. 191 (2002) 1895-1908.
61. P. Hansbo, C. Lovadina, I. Perugia, and G. Sangalli, A Lagrange multiplier method for the finite element solution of elliptic interface problems using non-matching meshes. Numer. Math. 100 (2005) 91-115.
62. R. Hausbrand, G. Cherkashinin, H. Ehrenberg, M. Gröting, K. Albe, C. Hess, W. Jaegermann, Fundamental degradation mechanisms of layered oxide Li-ion battery cathode materials: Methodology, insights and novel approaches, Mater. Sci. Eng. C. 192 (2015) 3–25.

63. M. Hautefeuille, C. Annavarapu, J.E. Dolbow. Robust imposition of Dirichlet boundary conditions on embedded surfaces. Int. J Numer. Methods Eng. 90 (2012) 40-64.
64. J. Helsing, The effective conductivity of random checkerboards, J. Comput. Phys. 230 (2011) 1171–1181.
65. A. Hillerborg, M. Modéer, and P.-E. Petersson, Analysis of crack formation and crack growth in concrete by means of fracture mechanics and finite elements. Cem. Concr. Res. 6 (1976) 773–781.
66. G.A. Holzapfel, J.C. Simo, Entropy elasticity of isotropic rubber-like solids at finite strains, Comput. Methods Appl. Mech. Eng. 132 (1996) 17–44.
67. B. Huixin, P. Wolfgang and T. R. Klupp, One‐Pot Colloidal Synthesis of Plasmonic Patchy Particles, Advanced Materials. 23 (2011) 2644–2649.
68. T. J. R. Hughes, G. R. Feijóo, L. Mazzei, and J.-B. Quincy. The variational multiscale method—a paradigm for computational mechanics. Comput. Methods Appl. Mech. Eng. 166 (1998) 3–24.
69. T. J. R. Hughes, Multiscale phenomena: Green's functions, the Dirichlet-to-Neumann formulation, subgrid scale models, bubbles and the origins of stabilized methods. Comput. Methods Appl. Mech. Eng.127 (1995) 387-401.
70. T. J. R. Hughes, A. Masud, and J. Wan, A stabilized mixed discontinuous Galerkin method for Darcy flow. Comput. Methods Appl. Mech. Eng. 195 (2006) 3347–3381.
71. L. N. T. Huynh, N. C. Nguyen, J. Peraire, and B. C. Khoo, A high-order hybridizable discontinuous Galerkin method for elliptic interface problems. Int. J Numer. Methods Eng. 93 (2012) 183–200.
72. A. Ibrahimbegovic, L. Chorfi, and F. Gharzeddine, Thermomechanical coupling at finite elastic strain: covariant formulation and numerical implementation, Commun. Numer. Methods Eng. 17 (2001) 275–289.
73. C. Johnson, U. Nävert, and J. Pitkäranta, Finite element methods for linear hyperbolic problems. Comput. Methods Appl. Mech. Eng. 45 (1984) 285-312.
74. L. M. Kachanov, Time of the Rupture Process Under Creep Conditions. IVZAkadNauk, S.S.R., Otd Tech Nauk, 8 (1958).

75. H. Khoramishad, A.D. Crocombe, K.B. Katnam, and I.A. Ashcroft, Predicting fatigue damage in adhesively bonded joints using a cohesive zone model. Int. J. Fatigue. 32 (2010) 1146–1158.
76. D. Krajcinovic, G.U. Fonseka. The continuous damage theory of brittle materials, part 1: general theory. Journal of applied Mechanics. 48 (1981) 809-815.
77. L. M. Kachanov. Time of the rupture process under creep conditions. IVZ Akad. Nauk, S.S.R., Otd Tech Nauk No.8, 26-31 (1958).
78. P. I. Kattan, G.Z. Voyiadjis. A coupled theory of damage mechanics and finite strain elasto-plasticity—I. Damage and elastic deformation. Int. J. Engng. Sci. 28 (1990) 421-435.
79. T.A. Laursen, Computational Contact and Impact Mechanics. Springer, 2003.
80. P. Le Tallec, T. Sassi, Domain decomposition with nonmatching grids: augmented Lagrangian approach. Math. Comp. 64 (1995) 1367–1396.
81. J. Lemaitre, A Continuous Damage Mechanics Model for Ductile Fracture. J. Eng. Mater. Technol, 107 (1985) 83–89.
82. S. Li and S. Ghosh, Modeling interfacial debonding and matrix cracking in fiber reinforced composites by the extended Voronoi cell FEM. Finite Elem. Anal. Des. 43 (2007) 397-410.
83. G. Lin, P. H. Geubelle, and N. R. Sottos, Simulation of fiber debonding with friction in a model composite pushout test. Int. J Solids Struct. 38 (2001) 8547-8562.
84. R. Liu, M. F. Wheeler, I. Yotov, On the spatial formulation of discontinuous Galerkin methods for finite elastoplasticity. Comput. Methods Appl. Mech. Eng. 253 (2012) 219-236.
85. E. Lorentz, A mixed interface finite element for cohesive zone models. Comput. Methods Appl. Mech. Eng. 198 (2008) 302–317.
86. D.S. Malkus, Eigenproblems associated with the discrete LBB condition for incompressible finite elements, Int. J Eng. Sci. 19 (1981) 1299–1310.
87. Marsden JE, Hughes TJR. Mathematical Foundations of Elasticity (Dover Civil and Mechanical Engineering). Dover Publications: Mineola, New York, 1994.
88. J. M. P. Martins, D. M. Neto, J. L. Alves, M. C. Oliveira, H. Laurent, A. Andrade-Campos, L. F. Menezes, A new staggered algorithm for thermomechanical coupled problems, Int. J. Solids Struct. 122–123 (2017) 42–58.

89. A. Masud, A multiplicative finite strain finite element framework for the modeling of semicrystalline polymers and polycarbonates. Int. J Numer. Methods Eng. 47 (2000) 1887-1908.
90. A Masud, Peface: Recent advances in stabilized and multiscale finite element methods. Comput. Methods Appl. Mech. Eng. 193 (2004) iii-iv.
91. A. Masud, A 3-D Model of Cold Drawing in Engineering Thermoplastics. Mechanics of Advanced Materials and Structures. 12 (2005) 457-469.
92. A. Masud, R. Calderer, A variational multiscale method for incompressible turbulent flows: Bubble functions and fine scale fields. Comput. Methods Appl. Mech. Eng. 200 (2011) 2577-2593.
93. A Masud, R Kannan, B-splines and NURBS based finite element methods for Kohn–Sham equations. Comput. Methods Appl. Mech. 241 (2012) 112-127.
94. A. Masud, R.A. Khurram, A multiscale/stabilized finite element method for the advection--diffusion equation. Comput. Methods Appl. Mech. Eng. 193 (2004) 1997-2018.
95. A Masud, L.A Bergman, Solution of the four dimensional Fokker–Planck equation: still a challenge. ICOSSAR 2005, 1911-16.
96. A. Masud, M. Panahandeh, F. Aurrichio, A finite-strain finite element model for the pseudoelastic behavior of shape memory alloys. Comput. Methods Appl. Mech. Eng. 148 (1997) 23–37.
97. A. Masud, G. Scovazzi, A heterogeneous multiscale modeling framework for hierarchical systems of partial differential equations. Int. J. Numer. Methods Fluids. 65 (2011) 28-42.
98. A. Masud, C.L. Tham, Three-Dimensional co-rotational framework for finite deformation elasto-plastic analysis of multilayered composite shells. AIAA J. 38 (2000) 2320-2327.
99. A. Masud, T. Truster, L.A. Bergman, A variational multiscale a-posteriori error estimation method for mixed-form of nearly incompressible elasticity. Comput. Methods Appl. Mech. Eng. 200 (2011) 3453–3481.
100. A. Masud, T. Truster, and L.A. Bergman, A unified formulation for interface coupling and frictional contact modeling with embedded error estimation. Int. J Numer. Methods Eng. 92 (2012) 141-177.

101. A. Masud, T. Truster, A framework for residual-based stabilization of incompressible finite elasticity: Stabilized formulations and $\overline{F}$ methods for linear triangles and tetrahedra. Comput. Methods Appl. Mech. Eng. 267 (2013) 359–399.
102. A. Masud, K. Xia. A stabilized mixed finite element method for nearly incompressible elasticity. J. Appl. Mech. 72 (2005) 711-720.
103. A. Masud, Z. Zhang, J. Botsis, Strength of composites with long-aligned fibers: fiber–fiber and fiber–crack interaction, Composites Part B: Engineering. 29 (1998) 577–588.
104. A.T. McBride, B.D. Reddy. A discontinuous Galerkin formulation for gradient plasticity at finite strains. Comput. Methods Appl. Mech. Eng. 198 (2008) 1805-1820.
105. T. W. McDevitt, T. A. Laursen, A mortar-finite element formulation for frictional contact problems. Int. J. Numer. Meth. Eng. 48 (2000) 1525–1547.
106. J. Mergheim, E. Kuhl, and P. Steinmann, A hybrid discontinuous Galerkin/interface method for the computational modelling of failure. Comput. Methods Appl. Mech. Eng. 20 (2004) 511-519.
107. J. Mergheim, P. Steinmann, A geometrically nonlinear FE approach for the simulation of strong and weak discontinuities. Comput. Methods Appl. Mech. Eng. 195 (2006) 5037-5052.
108. C. Miehe, Entropic thermoelasticity at finite strains. Aspects of the formulation and numerical implementation. Comput. Methods Appl. Mech. Eng. 120 (1995) 243–269.
109. N. Moës, J. Dolbow, and T. Belytschko, A finite element method for crack growth without remeshing. Int. J. Numer. Meth. Eng. 46 (1999) 131–150.
110. J.P. Moore, C.B. Williams, Fatigue properties of parts printed by PolyJet material jetting, Rapid Prototyping Journal. 21 (2015) 675–685.
111. H.M Mourad, J. Dolbow, I. Harari. A bubble-stabilized finite element method for Dirichlet constraints on embedded interfaces. Int. J. Numer. Meth. Eng. 69 (2007) 772-793.
112. L. Mu, J. Wang, Y. Wang, and X. Ye, A computational study of the weak Galerkin method for second-order elliptic equations. Numer Algor. 63 (2013) 753–777.
113. L. Mu, J. Wang, G. Wei, X. Ye, and S. Zhao, Weak Galerkin methods for second order elliptic interface problems. J. Comput. Phys. 250 (2013) 106–125.
114. L. Mu, J. Wang, X. Ye, and S. Zhao, A new weak Galerkin finite element method for elliptic interface problems. J. Comput. Phys. 325 (2016) 157–173.

115. A. Needleman, A Continuum Model for Void Nucleation by Inclusion Debonding. J. Appl. Mech, 54 (1987) 525–531.
116. N. Nguyen-Thanh, K. Zhou, X. Zhuang, P. Areias, H. Nguyen-Xuan, Y. Bazilevs, and T. Rabczuk, Isogeometric analysis of large-deformation thin shells using RHT-splines for multiple-patch coupling. Comput. Methods Appl. Mech. Eng. 316 (2017) 1157–1178.
117. O. Nguyen, E. A. Repetto, M. Ortiz, and R. A. Radovitzky, A cohesive model of fatigue crack growth. Int. J. Fract. 110 (2001) 351–369.
118. V.D. Nguyen, G. Becker, L. Noels, Multiscale computational homogenization methods with a gradient enhanced scheme based on the discontinuous Galerkin formulation. Comput. Methods Appl. Mech. Eng. 260 (2013) 63-77.
119. V. P. Nguyen, Discontinuous Galerkin/extrinsic cohesive zone modeling: Implementation caveats and applications in computational fracture mechanics. Eng. Fract. Mech. 128 (2014) 37-68.
120. J. Nitsche, Über ein Variationsprinzip zur Lösung von Dirichlet-Problemen bei Verwendung von Teilräumen, die keine Randbedingungen untervorfen sind. Abhandlungen in der Mathematik an der Universität Hamburg 36 (1971) 9-15.
121. I. Nistor, M. L. E Guiton, P. Massin, N. Mo¨es, S. G´eniaut, An X-FEM approach for large sliding contact along discontinuities. Int. J. Numer. Meth. Eng. 78 (2009) 1407-1435
122. L. Noels, R. Radovitzky, A general discontinuous Galerkin method for finite hyperelasticity. Formulation and numerical applications. Int. J. Numer. Meth. Eng. 68 (2006) 64-97.
123. Y. V. Obnosov, Exact solution of a boundary-value problem for a rectangular checkerboard field. Proc. R. Soc. Lond. A. 452 (1996) 2423–2442.
124. R.W. Ogden. Non-Linear Elastic Deformations. Dover Publications: Mineola, New York, 1997.
125. C. Ortner, E. Süli, Discontinuous Galerkin Finite Element Approximation of Nonlinear Second-Order Elliptic and Hyperbolic Systems. SIAM J. Numer. Anal. 45 (2007) 1370–1397.
126. C. Oskay, J. Fish. Multiscale modeling of fatigue for ductile materials. Int. J. Multiscale Comput. Eng. 2 (2004) 329-353.

127. M. H. J. W. Paas, P. J. G Schreurs, and W. A. M Brekelmans. A continuum approach to brittle and fatigue damage: Theory and numerical procedures. Int. J. Solids Struct. 30 (1993) 579-599.

128. L. Pichler, A. Masud and L. A. Bergman, Numerical solution of the Fokker–Planck equation by finite difference and finite element methods—a comparative study. Comput. Methods Stoch. Dyn. (2013) 69-85.

129. M. Prechtel, P. Ronda Leiva, R. Janisch, A. Hartmaier, G. Leugering, P. Steinmann, M. Stingl, Simulation of fracture in heterogeneous elastic materials with cohesive zone models. Int. J Fract. 168 (2011) 15-29.

130. Properties of wrought aluminum and aluminum alloys. In: ASM metals handbook. vol. 2, Properties and selection: nonferrous alloys and special-purpose materials, 10th ed., Materials Park, OH: ASM International. (1990) 62 – 122.

131. M. A. Puso, T. A. Laursen, A mortar segment-to-segment contact method for large deformation solid mechanics. Comput. Methods Appl. Mech. Eng. 193 (2004) 601–629.

132. R. Radovitzky, A. Seagraves, M. Tupek, and L. Noels, A scalable 3D fracture and fragmentation algorithm based on a hybrid, discontinuous Galerkin, cohesive element method. Comput. Methods Appl. Mech. Eng. 200 (2011) 326-344.

133. P. Raghavan, S. Ghosh, A continuum damage mechanics model for unidirectional composites undergoing interfacial debonding. Mech. Mater. 37 (2005) 955-979.

134. J.N. Reddy, C.D. Chin, Thermomechanical Analysis of Functionally Graded Cylinders and Plates, J. Therm. Stresses. 21 (1998) 593–626.

135. A. Rieger, P. Wriggers, Adaptive methods for thermomechanical coupled contact problems. Int. J. Numer. Meth. Eng. 59 (2004) 871–894.

136. K. L. Roe, T. Siegmund, An irreversible cohesive zone model for interface fatigue crack growth simulation. Eng. Fract. Mech.. 70 (2003) 209–232.

137. I. Romero, Thermodynamically consistent time-stepping algorithms for non-linear thermomechanical systems. Int. J. Numer. Meth. Eng. 79 (2009) 706–732.

138. I. Romero, Algorithms for coupled problems that preserve symmetries and the laws of thermodynamics. Comput. Methods Appl. Mech. Eng. 199 (2010) 1841–1858.

139. S. Sadik, A. Yavari, Geometric nonlinear thermoelasticity and the time evolution of thermal stresses. Math. Mech. Solids. 22 (2017) 1546–1587.

140. J. D. Sanders, T. A. Laursen, and M. A. Puso, A Nitsche embedded mesh method. Comput. Mech. 49 (2012) 243-257.

141. J. D. Sanders, M. A. Puso, An embedded mesh method for treating overlapping finite element meshes. Int. J. Numer. Meth. Eng. 91 (2012) 289-305.

142. A. Seagraves, R. Radovitzky, Large-scale 3D modeling of projectile impact damage in brittle plates. J. Mech. Phys. Solids. 83 (2015) 48-71.

143. S. Serebrinsky, M. Ortiz, A hysteretic cohesive-law model of fatigue-crack nucleation. Scr. Mater. 53 (2005) 1193–1196.

144. A. R. Shahani, S. M. Nabavi, Analytical solution of the quasi-static thermoelasticity problem in a pressurized thick-walled cylinder subjected to transient thermal loading. Appl. Math. Model. 31 (2007) 1807–1818.

145. J. C. Simo, F. Armero, Geometrically non-linear enhanced strain mixed methods and the method of incompatible modes. Int. J. Numer. Meth. Eng. 33 (1992) 1413-1449.

146. J. C. Simo, T. J. R. Hughes, Computational Inelasticity. New York: Springer-Verlag, 1998.

147. J. C. Simo, T.A. Laursen, An augmented Lagrangian treatment of contact problems involving friction. Comput. Struct. 42 (1992) 97-116.

148. J. C. Simo, R. L. Taylor, and K. S. Pister, Variational and projection methods for the volume constraint in finite deformation elasto-plasticity. Comput. Methods Appl. Mech. Eng. 51 (1985) 177-208.

149. J. C. Simo, R. L. Taylor, Quasi-Incompressible finite elasticity in principal stretches. Continuum basis and numerical algorithms, Comput. Methods Appl. Mech. Eng. 85 (1991) 273-310.

150. D. W. Spring, O. Giraldo-Londoño, G. H. Paulino, A study on the thermodynamic consistency of the Park–Paulino–Roesler (PPR) cohesive fracture model, Mechanics Research Communications. 78 (2016) 100–109.

151. R. Stenberg, On some techniques for approximating boundary conditions in the finite element method. J. Comput. Appl. Math. 63 (1995) 139–148.

152. M. Sugavaneswaran, G. Arumaikkannu, Modelling for randomly oriented multi material additive manufacturing component and its fabrication, Materials & Design (1980-2015). 54 (2014) 779–785.

153. N. Sukumar, N. Moës, B. Moran, and T. Belytschko, Extended finite element method for three-dimensional crack modelling. Int. J Numer. Methods Eng. 48 (2000) 1549–1570.
154. W. Sun, A stabilized finite element formulation for monolithic thermo-hydro-mechanical simulations at finite strain, Int. J. Numer. Meth. Engng. 103 (2015) 798–839.
155. C. L. Tham, Z. Zhang and A. Masud, An elastoplastic damage model cast in a corotational kinematic framework for large deformation analysis of laminated composite shells. Comput. Methods Appl. Mech. 194 (2005) 2641-2660.
156. Y. S. Touloukian, Thermophysical properties of high temperature solid materials., Macmillan, New York, 1967.
157. T. Truster, A stabilized, symmetric Nitsche method for spatially localized plasticity, Comput. Mech. 57 (2016) 75-103.
158. T. Truster, On interface element insertion into three-dimensional meshes, Eng. Fract. Mech. 153 (2016) 171-174.
159. T. Truster, P. Chen, A. Masud, Finite strain primal interface formulation with consistently evolving stabilization. Int. J Numer. Methods Eng. 102 (2015) 278-315.
160. T. Truster, P. Chen, A. Masud, On the algorithmic and implementational aspects of a Discontinuous Galerkin method at finite strains. Comput. Math. Appl. 70 (2015) 1266-1289.
161. T. Truster, A. Masud, A Discontinuous/continuous Galerkin method for modeling of interphase damage in fibrous composite systems. Comput. Mech. 52 (2013) 499–514.
162. T. Truster, A. Masud, Primal interface formulation for coupling multiple PDEs: A consistent derivation via the Variational Multiscale method. Comput. Methods Appl. Mech. Eng. 268 (2014) 194-224.
163. T.J. Truster, A. Masud, Discontinuous Galerkin Method for Frictional Interface Dynamics, J. Eng. Mech. 142 (2016) 04016084.
164. M. Vaezi, S. Chianrabutra, B. Mellor, S. Yang, Multiple material additive manufacturing – Part 1: a review: This review paper covers a decade of research on multiple material additive manufacturing technologies which can produce complex geometry parts with different materials. Virtual and Physical Prototyping. 8 (2013) 19–50.

165. J. Vetter, P. Novák, M.R. Wagner, C. Veit, K.-C. Möller, J.O. Besenhard, M. Winter, M. Wohlfahrt-Mehrens, C. Vogler, A. Hammouche, Ageing mechanisms in lithium-ion batteries, J. Power Sources. 147 (2005) 269–281.

166. G. Z. Voyiadjis and R. Echle, High cycle fatigue damage evolution in uni-directional metal matrix composites using a micro-mechanical approach. Mechanics of Materials, 30 (1998) 91–110.

167. C. Wang, J. Wang, R. Wang, and R. Zhang, A locking-free weak Galerkin finite element method for elasticity problems in the primal formulation. J. Comput. Appl. Math. 307 (2016) 346–366.

168. J. Wang, X. Ye, A weak Galerkin finite element method for second-order elliptic problems. J. Comput. Appl. Math. 241 (2013) 103–115.

169. Y. Wang, H. Waisman, From diffuse damage to sharp cohesive cracks: A coupled XFEM framework for failure analysis of quasi-brittle materials. Comput. Methods Appl. Mech. Eng. 299 (2016) 57–89.

170. J. P. Whiteley, Discontinuous Galerkin finite element methods for incompressible non-linear elasticity. Comput. Methods Appl. Mech. Eng. 198 (2009) 3464-3478.

171. P. Wriggers, O. Scherf, Adaptive finite element techniques for frictional contact problems. Comput. Methods Appl. Mech. Eng. 151 (1998) 593–603.

172. L. Wu, D. Tjahjanto, G. Becker, A. Makradi, A. Jérusalem, and L. Noels, A micro–meso-model of intra-laminar fracture in fiber-reinforced composites based on a discontinuous Galerkin/cohesive zone method. Eng. Fract. Mech. 104 (2013) 162-183.

173. M. Yoshida, J. Lahann, Smart Nanomaterials, ACS Nano. 2 (2008) 1101–1107.

174. J. Zhao, M.A. Bessa, J. Oswald, Z.Liu, and T. Belyschko. A method for modeling the transition of weak discontinuities to strong discontinuities: from interfaces to cracks. Int. J Numer. Methods Eng. 105 (2016) 834-854.

175. Z. (Jenny) Zhang, G. H. Paulino, and W. Celes, Extrinsic cohesive modelling of dynamic fracture and microbranching instability in brittle materials. Int. J Numer. Methods Eng. 72 (2007) 893–923.

APPENDIX A: IMPLEMENTATION OF METHODS IN CHAPTER 2

A.1 1D Coupled Thermal-Mechanical System Matrices

In this problem shown in Figure A.1, we employ the 1D elemental matrices and vectors developed in section 2.2 for the coupled response of the system. We employ Dirichlet boundary conditions and evaluate the system eigenvalues.

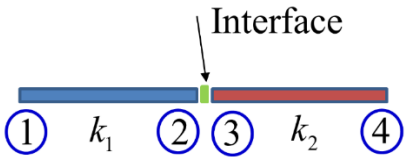

Figure A.1. Two element mesh with interface (2-node linear elements).

- Elasticity term

$$\left(\boldsymbol{\varepsilon}\left(\boldsymbol{\eta}^{(\alpha)}\right), \boldsymbol{m}^{(\alpha)}\theta^{(\alpha)}\right) = \delta\eta^T \underbrace{\left(N_{\mathrm{a,x}}, mN_{\mathrm{b}}\right)}_{K^{ab}_{\text{Mech-Couple}}} \delta\theta \tag{A-1}$$

$$K^{(\alpha)}_{\text{Elasticity}} = E\int_{\Omega^{(\alpha)}} N_{\mathrm{a},x} N_{\mathrm{b,x}} \mathrm{d}V = E\int_{x_1}^{x_2} \frac{(-1)^a}{h^e}\frac{(-1)^b}{h^e}\mathrm{d}V = \frac{E\mathrm{A}}{h^e}(-1)^a(-1)^b$$
$$= \frac{E\mathrm{A}}{h^e}\begin{bmatrix} 1 & -1 \\ -1 & 1 \end{bmatrix} \tag{A-2}$$

- Coupling term in mechanical phase

$$\left(\boldsymbol{\varepsilon}\left(\boldsymbol{\eta}^{(\alpha)}\right), \boldsymbol{m}^{(\alpha)}\theta^{(\alpha)}\right) = \delta\eta^T \underbrace{\left(N_{\mathrm{a,x}}, mN_{\mathrm{b}}\right)}_{K^{ab}_{\text{Mech-Couple}}} \delta\theta \tag{A-3}$$

$$K^{(\alpha)}_{\text{Mech-Couple}} = m\int_{\Omega^{(\alpha)}} N_{\mathrm{a},x} N_{\mathrm{b}} \mathrm{d}V = m\int_{x_1}^{x_2} \frac{(-1)^a}{h^e}\frac{1}{2}(1+\xi_b\xi)\mathrm{d}V = \frac{m\mathrm{A}}{2}(-1)^a$$
$$= \frac{m\mathrm{A}}{2}\overbrace{\begin{bmatrix} -1 & -1 \\ 1 & 1 \end{bmatrix}}^{(\theta_1 \;\; \theta_2)}\begin{matrix} d_1 \\ d_2 \end{matrix} \tag{A-4}$$

Assembling the interior contribution inside each element adjoining the interface, which in the present context is the common node between the elements.

$$K^{(1)}_{\text{Interior}} = \mathrm{A}\overbrace{\begin{bmatrix} \frac{E^{(1)}}{h^e} & \frac{m^{(1)}}{2} & -\frac{E^{(1)}}{h^e} & \frac{m^{(1)}}{2} \\ 0 & 0 & 0 & 0 \\ -\frac{E^{(1)}}{h^e} & -\frac{m^{(1)}}{2} & \frac{E^{(1)}}{h^e} & -\frac{m^{(1)}}{2} \\ 0 & 0 & 0 & 0 \end{bmatrix}}^{\begin{matrix} d_1 & \theta_1 & d_2 & \theta_2 \end{matrix}} \tag{A-5}$$

$$K^{(2)}_{\text{Interior}} = \mathrm{A}\overbrace{\begin{bmatrix} \frac{E^{(2)}}{h^e} & \frac{m^{(2)}}{2} & -\frac{E^{(2)}}{h^e} & \frac{m^{(2)}}{2} \\ 0 & 0 & 0 & 0 \\ -\frac{E^{(2)}}{h^e} & -\frac{m^{(2)}}{2} & \frac{E^{(2)}}{h^e} & -\frac{m^{(2)}}{2} \\ 0 & 0 & 0 & 0 \end{bmatrix}}^{\begin{matrix} d_3 & \theta_3 & d_4 & \theta_4 \end{matrix}} \tag{A-6}$$

- Coupling term in thermal phase:

$$\left(\omega_o^{(\alpha)}, m^{(\alpha)} \nabla v_{n+1}^{(\alpha)}\right) = \delta\omega^T \underbrace{\left(N_{\mathrm{a}}, m^{(\alpha)} \frac{1}{\Delta t} N_{\mathrm{b},x}\right)}_{K^{ab}_{\text{Thermal Couple}}} \delta u \tag{A-7}$$

$$\begin{aligned} K^{(\alpha)}_{\text{Thermal Couple}} &= \frac{m^{(\alpha)}}{\Delta t} \int_{\Omega^{(\alpha)}} N_{\mathrm{a}} N_{\mathrm{b},x} \mathrm{d}V = \frac{m^{(\alpha)}}{\Delta t} \int_{x_1}^{x_2} \frac{1}{2}\left(1+\xi_a \xi\right) \frac{(-1)^b}{h^e} \mathrm{A}\,\mathrm{dx} \\ &= \frac{m^{(\alpha)} \mathrm{A}}{2\Delta t} \overbrace{\begin{bmatrix} -1 & 1 \\ -1 & 1 \end{bmatrix}}^{\begin{matrix} d_1 & d_2 \end{matrix}} \begin{matrix} \theta_1 \\ \theta_2 \end{matrix} \end{aligned} \tag{A-8}$$

Assembling the interior contribution $\mathbb{B}^{\text{Gal}}_{\text{thermal}}$:

$$K^{(1)}_{\text{Interior\_th}} = \mathrm{A}\overbrace{\begin{bmatrix} 0 & 0 & 0 & 0 \\ -\frac{m^{(1)}}{2\Delta t} & \frac{\overline{c}^{(1)} h^e}{2\Delta t} + \frac{\overline{k}^{(1)}}{h^e} & \frac{m^{(1)}}{2\Delta t} & -\frac{\overline{k}^{(1)}}{h^e} \\ 0 & & 0 & 0 \\ -\frac{m^{(1)}}{2\Delta t} & -\frac{\overline{k}^{(1)}}{h^e} & \frac{m^{(1)}}{2\Delta t} & \frac{\overline{c}^{(1)} h^e}{2\Delta t} + \frac{\overline{k}^{(1)}}{h^e} \end{bmatrix}}^{\begin{matrix} d_1 & \theta_1 & d_2 & \theta_2 \end{matrix}} \tag{A-9}$$

$$K^{(2)}_{\text{Interior\_th}} = \mathrm{A}\overbrace{\begin{bmatrix} 0 & 0 & 0 & 0 \\ -\dfrac{m^{(2)}}{2\Delta t} & \dfrac{\overline{c}^{(2)}h^e}{2\Delta t}+\dfrac{\overline{k}^{(2)}}{h^e} & \dfrac{m^{(2)}}{2\Delta t} & -\dfrac{\overline{k}^{(2)}}{h^e} \\ 0 & 0 & 0 & 0 \\ -\dfrac{m^{(2)}}{2\Delta t} & -\dfrac{\overline{k}^{(2)}}{h^e} & \dfrac{m^{(2)}}{2\Delta t} & \dfrac{\overline{c}^{(2)}h^e}{2\Delta t}+\dfrac{\overline{k}^{(2)}}{h^e} \end{bmatrix}}^{d_3 \quad \theta_3 \quad d_4 \quad \theta_4} \tag{A-10}$$

Assembling the interior and interface contribution together, the total stiffness matrices are summarized as follows.

$$K_{n+1} = K^{(1)}_{\text{Interior}} + K^{(2)}_{\text{Interior}} - K^{1}_{\text{Interface}} - K^{2}_{\text{Interface}} + K^{2.2}_{\text{Interface}} + K^{3}_{\text{Interface}} \tag{A-11}$$

$$K_{n} = K^{(1)}_{\text{Interior\_n}} + K^{(2)}_{\text{Interior\_n}} \tag{A-12}$$

where

$$K^{(1)}_{\text{Interior}} = \mathrm{A}\overbrace{\begin{bmatrix} \dfrac{E^{(1)}}{h^e} & \dfrac{m^{(1)}}{2} & -\dfrac{E^{(1)}}{h^e} & \dfrac{m^{(1)}}{2} \\ -\dfrac{m^{(1)}}{2\Delta t} & \dfrac{\overline{k}^{(1)}}{h^e}+\dfrac{\overline{c}^{(1)}h^e}{2\Delta t} & \dfrac{m^{(1)}}{2\Delta t} & -\dfrac{\overline{k}^{(1)}}{h^e} \\ -\dfrac{E^{(1)}}{h^e} & -\dfrac{m^{(1)}}{2} & \dfrac{E^{(1)}}{h^e} & -\dfrac{m^{(1)}}{2} \\ -\dfrac{m^{(1)}}{2\Delta t} & -\dfrac{\overline{k}^{(1)}}{h^e} & \dfrac{m^{(1)}}{2\Delta t} & \dfrac{\overline{k}^{(1)}}{h^e}+\dfrac{\overline{c}^{(1)}h^e}{2\Delta t} \end{bmatrix}}^{d_1 \quad \theta_1 \quad d_2 \quad \theta_2} \tag{A-13}$$

$$K^{(2)}_{\text{Interior}} = \mathrm{A}\overbrace{\begin{bmatrix} \dfrac{E^{(2)}}{h^e} & \dfrac{m^{(2)}}{2} & -\dfrac{E^{(2)}}{h^e} & \dfrac{m^{(2)}}{2} \\ -\dfrac{m^{(2)}}{2\Delta t} & \dfrac{\overline{k}^{(2)}}{h^e}+\dfrac{\overline{c}^{(2)}h^e}{2\Delta t} & \dfrac{m^{(2)}}{2\Delta t} & -\dfrac{\overline{k}^{(2)}}{h^e} \\ -\dfrac{E^{(2)}}{h^e} & -\dfrac{m^{(2)}}{2} & \dfrac{E^{(2)}}{h^e} & -\dfrac{m^{(2)}}{2} \\ -\dfrac{m^{(1)}}{2\Delta t} & -\dfrac{\overline{k}^{(2)}}{h^e} & \dfrac{m^{(2)}}{2\Delta t} & \dfrac{\overline{k}^{(2)}}{h^e}+\dfrac{\overline{c}^{(2)}h^e}{2\Delta t} \end{bmatrix}}^{d_3 \quad \theta_3 \quad d_4 \quad \theta_4} \tag{A-14}$$

$$K^{(1)}_{\text{Interior\_n}} = \mathrm{A}\overbrace{\begin{bmatrix} 0 & 0 & 0 & 0 \\ -\dfrac{m^{(1)}}{2\Delta t} & \dfrac{\overline{c}^{(1)}h^e}{2\Delta t} & \dfrac{m^{(1)}}{2\Delta t} & 0 \\ 0 & 0 & 0 & 0 \\ -\dfrac{m^{(1)}}{2\Delta t} & 0 & \dfrac{m^{(1)}}{2\Delta t} & \dfrac{\overline{c}^{(1)}h^e}{2\Delta t} \end{bmatrix}}^{d_1 \quad \theta_1 \quad d_2 \quad \theta_2} \tag{A-15}$$

$$K^{(2)}_{\text{Interior\_n}} = \mathrm{A}\overbrace{\begin{bmatrix} 0 & 0 & 0 & 0 \\ -\dfrac{m^{(2)}}{2\Delta t} & \dfrac{\overline{c}^{(2)}h^e}{2\Delta t} & \dfrac{m^{(1)}}{2\Delta t} & 0 \\ 0 & 0 & 0 & 0 \\ -\dfrac{m^{(2)}}{2\Delta t} & 0 & \dfrac{m^{(2)}}{2\Delta t} & \dfrac{\overline{c}^{(2)}h^e}{2\Delta t} \end{bmatrix}}^{d_1 \quad \theta_1 \quad d_2 \quad \theta_2} \tag{A-16}$$

Interface terms:

$$K^{1}_{\text{Interface}} = \frac{l^3 t^3}{4h^e A}\overbrace{\begin{bmatrix} 0 & 0 & -\tau_s & 0 & \tau_s & 0 & 0 & 0 \\ 0 & 0 & 0 & -\tau_s^{\theta} & 0 & \tau_s^{\theta} & 0 & 0 \\ 0 & 0 & \tau_s & 0 & -\tau_s & 0 & 0 & 0 \\ 0 & 0 & 0 & \tau_s^{\theta} & 0 & -\tau_s^{\theta} & 0 & 0 \\ 0 & 0 & -\tau_s & 0 & \tau_s & 0 & 0 & 0 \\ 0 & 0 & 0 & -\tau_s^{\theta} & 0 & \tau_s^{\theta} & 0 & 0 \\ 0 & 0 & \tau_s & 0 & -\tau_s & 0 & 0 & 0 \\ 0 & 0 & 0 & \tau_s^{\theta} & 0 & -\tau_s^{\theta} & 0 & 0 \end{bmatrix}}^{d_1 \quad \theta_1 \quad d_2 \quad \theta_2 \quad d_3 \quad \theta_3 \quad d_4 \quad \theta_4} \tag{A-17}$$

$$K^{2}_{\text{Interface}} = \left(K^{1}_{\text{Interface}}\right)^T \tag{A-18}$$

$$K^{2.2}_{\text{Interface}} = \frac{lt}{2}\overbrace{\begin{bmatrix} 0 & 0 & 0 & 0 & 0 & 0 & 0 & 0 \\ 0 & 0 & 0 & 0 & 0 & 0 & 0 & 0 \\ 0 & 0 & 0 & \delta m^{(1)} & 0 & -\delta m^{(2)} & 0 & 0 \\ 0 & 0 & 0 & 0 & 0 & 0 & 0 & 0 \\ 0 & 0 & 0 & -\delta m^{(1)} & 0 & \delta m^{(2)} & 0 & 0 \\ 0 & 0 & 0 & 0 & 0 & 0 & 0 & 0 \\ 0 & 0 & 0 & 0 & 0 & 0 & 0 & 0 \\ 0 & 0 & 0 & 0 & 0 & 0 & 0 & 0 \end{bmatrix}}^{d_1 \quad \theta_1 \quad d_2 \quad \theta_2 \quad d_3 \quad \theta_3 \quad d_4 \quad \theta_4} \tag{A-19}$$

$$K^{3}_{\text{Interface}} = \frac{lt}{2}\overbrace{\begin{bmatrix} 0 & 0 & 0 & 0 & 0 & 0 & 0 & 0 \\ 0 & 0 & 0 & 0 & 0 & 0 & 0 & 0 \\ 0 & 0 & \tau_s & 0 & -\tau_s & 0 & 0 & 0 \\ 0 & 0 & 0 & \tau_s^{\theta} & 0 & -\tau_s^{\theta} & 0 & 0 \\ 0 & 0 & -\tau_s & 0 & \tau_s & 0 & 0 & 0 \\ 0 & 0 & 0 & -\tau_s^{\theta} & 0 & \tau_s^{\theta} & 0 & 0 \\ 0 & 0 & 0 & 0 & 0 & 0 & 0 & 0 \\ 0 & 0 & 0 & 0 & 0 & 0 & 0 & 0 \end{bmatrix}}^{d_1 \quad \theta_1 \quad d_2 \quad \theta_2 \quad d_3 \quad \theta_3 \quad d_4 \quad \theta_4} \tag{A-20}$$

where $\delta m^{(\alpha)} = \delta_s^{(\alpha)} m^{(\alpha)}$.

APPENDIX B: IMPLEMENTATION OF METHODS IN CHAPTER 3

B.1 Derivation of the Consistent Tangent and Push Forward to the Current Configuration

The derivations in section 3.3 have been carried out in the reference configuration in terms of the first Piola-Kirchhoff stress $\boldsymbol{P}$ and the acoustic tensor $\mathbf{A}$ so that the resulting interface formulation (3-48) can be expressed in a form closely resembling the small strain counterpart [162]. An entirely equivalent representation can be written using the second Piola-Kirchhoff stress $\boldsymbol{S}$ and the material tangent tensor $\mathbf{C}$ by recourse to transformations from continuum mechanics [87,148]:

$$P_{iJ} = F_{iI} S_{IJ} \tag{B-1}$$

$$\mathsf{A}_{iIjJ} = g_{ij} S_{IJ} + F_{iK} F_{jL} \mathsf{C}_{KILJ} \tag{B-2}$$

where $\boldsymbol{g}$ is the spatial metric tensor and throughout the following discussion lower-case and upper-case subscripts refer to components expressed in current and reference coordinate systems, respectively. Expressions for $\boldsymbol{S}$ and $\mathbf{C}$ arise in the usual manner by differentiating the strain energy density function W with respect to the Green-Lagrange strain tensor $\boldsymbol{E}$. By carefully differentiating (B-2), we obtain the following relation for the sixth-order material tangent tensor $\mathbf{D}$ that was defined in [87]:

$$\Xi_{iIjJkK} = g_{ij} F_{kL} \mathsf{C}_{IJLK} + g_{ik} F_{jL} \mathsf{C}_{KILJ} + g_{jk} F_{iL} \mathsf{C}_{JKLI} + F_{iL} F_{jM} F_{kN} \mathsf{D}_{LIMJNK} \tag{B-3}$$

Notice that $\boldsymbol{\Xi}$ possesses major symmetry for each pair of dual-basis components due to the symmetries of $\mathbf{C}$ and $\mathbf{D}$.

To obtain the spatial counterpart of the weak form (3-48) and the linearized form (3-49), we require the following transformation relations for the Cauchy stress tensor $\boldsymbol{\sigma}$, spatial tangent tensor $\boldsymbol{c}$, and spatial sixth-order tensor $\boldsymbol{d}$:

$$J\sigma_{ij} = F_{iI} S_{IJ} F_{jJ}, \quad Jc_{ijkl} = F_{iI} F_{jJ} \mathsf{C}_{IJKL} F_{kK} F_{lL}, \quad Jd_{ijklmn} = F_{iI} F_{jJ} F_{kK} \mathsf{D}_{IJNKLMN} F_{lL} F_{mM} F_{nN} \tag{B-4}$$

Where $J = \det(\boldsymbol{F})$. Furthermore, we will use the following transformation of area and surface infinitesimal elements as well as the unit normal vector $\boldsymbol{N}$:

$$\mathrm{d}v = J\mathrm{d}V, \quad \boldsymbol{n}\mathrm{d}a = J\boldsymbol{F}^{-T}\boldsymbol{N}\mathrm{d}A, \quad \mathrm{d}a/\mathrm{d}A \equiv \vartheta_A^{-1} = J\left\|\boldsymbol{F}^{-T}\boldsymbol{N}\right\| \tag{B-5}$$

where $\boldsymbol{n}$ is the unit outward normal to the deformed domain $\boldsymbol{\phi}(\Omega)$. The last expression (B-5) has a very important implication: in the discrete setting, the mapped unit vectors $\boldsymbol{n}^{(\alpha)}$ in the spatial configuration on either side of the interface Γ_{I} will not be identical in general. This observation is due to the dependence of the unit normal on the deformation gradient $\boldsymbol{n}^{(\alpha)}$ which may take distinct values across the interface when continuity and equilibrium are enforced only in a weak sense through (3-4) and (3-5). Therefore, numerical integration in the deformed configuration must take this consideration into account. Additionally, the differential area element $\mathrm{d}a$ for each side of the interface may also be different due to the discontinuity of $\boldsymbol{F}$.

We omit the details of substituting the transformations (B-1) – (B-5) within the weak form (3-48) and provide the final results:

$$
\begin{aligned}
R\left(\boldsymbol{\eta}^{(\alpha)},\boldsymbol{\phi}^{(\alpha)}\right) &= \sum_{\alpha=1}^{2}\int_{\phi^{(\alpha)}\left(\Omega^{(\alpha)}\right)}\left[\nabla^{\mathrm{s}}\boldsymbol{\eta}^{(\alpha)}:\boldsymbol{\sigma}^{(\alpha)}-\boldsymbol{\eta}^{(\alpha)}\cdot\rho^{(\alpha)}\boldsymbol{B}^{(\alpha)}\right]\mathrm{d}v \\
&-\sum_{\alpha=1}^{2}\int_{\phi^{(\alpha)}(\Gamma_{\mathrm{I}})}\left(-1\right)^{\alpha-1}[\![\boldsymbol{\eta}]\!]\cdot\left(\boldsymbol{\delta}_{s}^{(\alpha)}\cdot\boldsymbol{\sigma}^{(\alpha)}\cdot\boldsymbol{n}^{(\alpha)}\right)\mathrm{d}a \\
&-\sum_{\alpha=1}^{2}\int_{\phi^{(\alpha)}(\Gamma_{\mathrm{I}})}\left(-1\right)^{\alpha-1}\left[\boldsymbol{\delta}_{s}^{(\alpha)}\cdot\left(\nabla^{\mathrm{s}}\boldsymbol{\eta}^{(\alpha)}:\boldsymbol{c}^{(\alpha)}\right)\cdot\boldsymbol{n}^{(\alpha)}\right]\cdot[\![\boldsymbol{\phi}]\!]\,\mathrm{d}a \\
&+\sum_{\alpha=1}^{2}\int_{\phi^{(\alpha)}(\Gamma_{\mathrm{I}})}\left(-1\right)^{\alpha-1}\boldsymbol{\eta}^{(\alpha)}\cdot\boldsymbol{\tau}_{s}\cdot[\![\boldsymbol{\phi}]\!]\,\vartheta_{A}\mathrm{d}a=0
\end{aligned}
\tag{B-6}
$$

where $\boldsymbol{\eta}^{(\alpha)}=\boldsymbol{\eta}_{o}^{(\alpha)}\circ\left(\boldsymbol{\phi}^{(\alpha)}\right)^{-1}$ is the spatial displacement variation, $\nabla(\bullet)=\partial(\bullet)/\partial\boldsymbol{x}$ is the spatial gradient, $\nabla^{\mathrm{s}}(\bullet)=\frac{1}{2}\left[\nabla(\bullet)+\left(\nabla(\bullet)\right)^{T}\right]$, and $\rho=J^{-1}\rho_{o}$ is the spatial density. The values of the stabilization tensors $\boldsymbol{\tau}_{s}$ and $\boldsymbol{\delta}_{s}^{(\alpha)}$ are unaffected by the transformation. However, if desired, the stability tensors $\boldsymbol{\tau}_{s}^{(\alpha)}$ may be evaluated in the spatial configuration by pushing forward (3-33) as follows:

$$
\tilde{\boldsymbol{\tau}}_{s}^{(\alpha)}=\left[\int_{\phi^{(\alpha)}\left(\omega_{s}^{(\alpha)}\right)}\nabla\boldsymbol{b}_{s}^{(\alpha)}\cdot\left(\boldsymbol{\sigma}^{(\alpha)}\cdot\nabla\boldsymbol{b}_{s}^{(\alpha)}\right)+\nabla\boldsymbol{b}_{s}^{(\alpha)}:\boldsymbol{c}^{(\alpha)}:\nabla\boldsymbol{b}_{s}^{(\alpha)}\;\mathrm{d}v\right]^{-1}
\tag{B-7}
$$

Finally, the spatial counterpart of the linearized weak form (3-49) is expressed as below:

$$
\begin{aligned}
K\left(\boldsymbol{\eta}^{(\alpha)},\Delta\boldsymbol{u}^{(\alpha)};\boldsymbol{\phi}^{(\alpha)}\right) &= \sum_{\alpha=1}^{2}\int_{\phi^{(\alpha)}\left(\Omega^{(\alpha)}\right)}\left(\nabla\boldsymbol{\eta}^{(\alpha)}\cdot\left(\boldsymbol{\sigma}^{(\alpha)}\cdot\nabla\boldsymbol{\eta}^{(\alpha)}\right)+\nabla^{\mathrm{s}}\boldsymbol{\eta}^{(\alpha)}:\boldsymbol{c}^{(\alpha)}:\nabla^{\mathrm{s}}\boldsymbol{\eta}^{(\alpha)}\right)\mathrm{d}v \\
&+\sum_{\alpha=1}^{2}\int_{\phi^{(\alpha)}(\Gamma_1)}(-1)^{\alpha-1}\,\boldsymbol{\eta}^{(\alpha)}\cdot\boldsymbol{\tau}_s\cdot[\![\Delta\boldsymbol{u}]\!]\,\vartheta_A\mathrm{d}a \\
&-\sum_{\alpha=1}^{2}\int_{\phi^{(\alpha)}(\Gamma_1)}(-1)^{\alpha-1}[\![\boldsymbol{\eta}]\!]\cdot\left[\boldsymbol{\delta}_s^{(\alpha)}\cdot\left(\boldsymbol{c}^{(\alpha)}:\nabla^{\mathrm{s}}\left(\Delta\boldsymbol{u}^{(\alpha)}\right)\right)\cdot\boldsymbol{n}^{(\alpha)}\right]\mathrm{d}a \\
&-\sum_{\alpha=1}^{2}\int_{\phi^{(\alpha)}(\Gamma_1)}(-1)^{\alpha-1}\left[\boldsymbol{\delta}_s^{(\alpha)}\cdot\left(\nabla^{\mathrm{s}}\boldsymbol{\eta}^{(\alpha)}:\boldsymbol{c}^{(\alpha)}\right)\cdot\boldsymbol{n}^{(\alpha)}\right]\cdot[\![\Delta\boldsymbol{u}]\!]\,\mathrm{d}a \\
&-\sum_{\alpha=1}^{2}\int_{\phi^{(\alpha)}(\Gamma_1)}(-1)^{\alpha-1}\left[\boldsymbol{\delta}_s^{(\alpha)}\cdot K_{uu}\left(\boldsymbol{\eta}^{(\alpha)},\Delta\boldsymbol{u}^{(\alpha)};\boldsymbol{\phi}^{(\alpha)}\right)\cdot\boldsymbol{n}^{(\alpha)}\right]\cdot[\![\boldsymbol{\phi}]\!]\,\mathrm{d}a
\end{aligned}
\tag{B-8}
$$

and the additional stiffness term is defined as follows, where the superscripts (α) have been suppressed:

$$
\begin{aligned}
K_{uu}\left(\boldsymbol{\eta},\Delta\boldsymbol{u};\boldsymbol{\phi}\right) &= \nabla\boldsymbol{\eta}\cdot\left[\boldsymbol{c}:\nabla^{\mathrm{s}}\left(\Delta\boldsymbol{u}\right)\right]+\nabla\left(\Delta\boldsymbol{u}\right)\cdot\left[\boldsymbol{c}:\nabla^{\mathrm{s}}\boldsymbol{\eta}\right] \\
&+\left[\left(\boldsymbol{d}:\nabla^{\mathrm{s}}\left(\Delta\boldsymbol{u}\right)\right):\nabla^{\mathrm{s}}\boldsymbol{\eta}\right]+\boldsymbol{c}:\left[\left(\nabla\left(\Delta\boldsymbol{u}\right)\right)^{T}\cdot\nabla\boldsymbol{\eta}\right]
\end{aligned}
\tag{B-9}
$$

B.2 Expression for the Material Tensors

Here we provide expressions for the material tensors corresponding to the strain energy density function (3-56); a similar material model was considered in [107].

First Piola-Kirchoff stress tensor $\boldsymbol{P}$:

$$
P_{iI}=\mu\left(F_{Ii}^{-1}+F_{iI}\right)+\lambda J\left(J-1\right)F_{Ii}^{-1} \tag{B-10}
$$

Acoustic tensor $\mathbf{A}$:

$$
\mathsf{A}_{iIjJ}=\mu\left(F_{Ij}^{-1}F_{Ji}^{-1}+g_{ij}G_{IJ}^{-1}\right)+\lambda\left[J\left(2J-1\right)F_{Ii}^{-1}F_{Jj}^{-1}-J\left(J-1\right)F_{Ij}^{-1}F_{Ji}^{-1}\right] \tag{B-11}
$$

Sixth-order material tensor $\boldsymbol{\Xi}$:

$$
\begin{aligned}
\Xi_{iIjJkK} &= \left[\lambda J\left(J-1\right)-\mu\right]\left(F_{Jk}^{-1}F_{Ki}^{-1}F_{Ij}^{-1}+F_{Ji}^{-1}F_{Ik}^{-1}F_{Kj}^{-1}\right)+\lambda\left[J\left(4J-1\right)F_{Ii}^{-1}F_{Jj}^{-1}F_{Kk}^{-1}\right] \\
&-\lambda J\left(2J-1\right)\left[F_{Ik}^{-1}F_{Ki}^{-1}F_{Jj}^{-1}+F_{Ii}^{-1}F_{Jk}^{-1}F_{Kj}^{-1}+F_{Kk}^{-1}F_{Ji}^{-1}F_{Ij}^{-1}\right]
\end{aligned}
\tag{B-12}
$$

where $\boldsymbol{G}^{-1}$ is the inverse of the material metric tensor. The spatial constitutive tensors take a much simpler form.

Cauchy stress tensor $\boldsymbol{\sigma}$:

$$J\sigma_{ij} = \mu\left(g_{ij} + F_{iI}F_{jI}\right) + \lambda J\left(J-1\right)g_{ij} \tag{B-13}$$

Spatial tangent tensor $\boldsymbol{c}$:

$$Jc_{ijkl} = \mu\left(g_{ik}g_{jl} + g_{il}g_{jk}\right) + \lambda\left[J\left(2J-1\right)g_{ij}g_{kl} - J\left(J-1\right)\left(g_{ik}g_{jl} + g_{il}g_{jk}\right)\right] \tag{B-14}$$

Sixth-order material tensor $\boldsymbol{d}$:

$$\begin{aligned} Jd_{ijklmn} = &\left[\lambda J\left(J-1\right) - \mu\right]\left(\boldsymbol{d}_3\right)_{ijklmn} + \lambda\left[J\left(4J-1\right)\left(\boldsymbol{d}_1\right)_{ijklmn}\right] \\ &+\lambda J\left(2J-1\right)\left(\boldsymbol{d}_2\right)_{ijklmn} \end{aligned} \tag{B-15}$$

where the tensors $\boldsymbol{d}_1$, $\boldsymbol{d}_2$, and $\boldsymbol{d}_3$ are defined in [101], and the values of their components in a Cartesian coordinate frame are listed in Table B.1.

Table B.1. Components of spatial sixth-order volumetric tensor.

Component	Value	Condition
$\left[\boldsymbol{d}_1\right]_{\text{iijjkk}}$	1	None
$\left[\boldsymbol{d}_2\right]_{\text{iiiiii}}$	-6	None
$\left[\boldsymbol{d}_2\right]_{\text{iiiijj}}$	-2	$i \neq j$
$\left[\boldsymbol{d}_2\right]_{\text{iijkjk}}$	-1	$j \neq k$
$\left[\boldsymbol{d}_3\right]_{\text{iiiiii}}$	8	None
$\left[\boldsymbol{d}_3\right]_{\text{iiijij}}$	2	$i \neq j$
$\left[\boldsymbol{d}_3\right]_{\text{ijjkki}}$	1	$i \neq j \neq k$

APPENDIX C: IMPLEMENTATION OF METHODS IN CHAPTER 4

C.1 Consistent Linearization of the Damage Part

To achieve quadratic convergence with the Newton-Raphson method for the nonlinear equation (4-85), we need consistent linearization of the term which is related to the damage part. Note that the rest of the terms in Eqn. (4-85) is linearized in Appendix B.1.

$$\frac{\partial}{\partial \boldsymbol{T}}\left(\Delta\gamma \boldsymbol{n}\right) = \frac{\partial \Delta\gamma}{\partial \boldsymbol{T}} \otimes \boldsymbol{n} + \gamma \frac{\partial \boldsymbol{n}}{\partial \boldsymbol{T}} = \frac{\partial \Delta\gamma}{\partial T_i} n_j + \Delta\gamma \frac{\partial n_i}{\partial T_j} \tag{C-1}$$

According to section 4.5.1.1 and 4.5.2.1, the return mapping algorithms and the corresponding expression for the damage consistency parameter $\Delta\gamma$ and the unit normal $\boldsymbol{n}$ are different for different loading scenarios. Therefore, we first consider the case of damage in tension. Note that compression damage case follows a similar pattern. For the case of damage in tension, from the expressions in Box 4.2, the yield function f and the damage consistency parameter $\Delta\gamma$ are expressed in (4-67) and (4-68), equation (C-1) becomes:

$$\frac{\partial}{\partial \boldsymbol{T}}\left(\Delta\gamma \boldsymbol{n}\right) = \frac{1}{r_P - H_c}\left(\boldsymbol{I} - \frac{P_c - Q_n}{\left\| \boldsymbol{T} \right\|}\left(\boldsymbol{I} - \boldsymbol{n} \otimes \boldsymbol{n} \right) \right) \tag{C-2}$$

For compression friction case, the yield function and the damage consistency parameter are expressed in (4-77) and (4-79):

Thus Eqn. (C-1) becomes:

$$\frac{\partial}{\partial \boldsymbol{T}}\left(\Delta\gamma \boldsymbol{n}\right) = \frac{1}{r_p}\left[\boldsymbol{I} + \frac{\mu_f \left\| T_N \right\|}{\left\| T_T \right\|}\left(\boldsymbol{I} - \boldsymbol{n}_T \otimes \boldsymbol{n}_T \right) \right]\left(\boldsymbol{I} - \boldsymbol{N} \otimes \boldsymbol{N} \right) + \frac{1}{r_p}\mu_f \boldsymbol{n}_T \otimes \boldsymbol{N} \tag{C-3}$$

APPENDIX D: IMPLEMENTATION OF METHODS IN CHAPTER 6

D.1 Push Forward the Thermomechanical Coupled Residual Form to the Current Configuration

Following the same idea in [159] and [39], the transformation of surface and volume between spatial and material configuration is given as follows.

$$\mathrm{d}v = JdV\ ,\ \boldsymbol{n}da = J\boldsymbol{F}^{-T}\boldsymbol{N}d\,A\ ,\ \frac{da}{d\,A} = \mathcal{V}_A^{-1} = J\left\|F^{-T}\boldsymbol{N}\right\| \tag{D-1}$$

The residual forms (6-52) and (6-53) are pushed forward to the current configuration as follows.

$$\begin{aligned} r_{\phi}\left(\boldsymbol{\eta}_o^{(\alpha)},\boldsymbol{\phi}^{(\alpha)}\right) &= \sum_{\alpha=1}^{2}\int_{\mathrm{v}^{(\alpha)}}\left[\nabla\boldsymbol{\eta}_o^{(\alpha)}:\boldsymbol{\sigma}^{(\alpha)} - \boldsymbol{\eta}_o^{(\alpha)}\cdot\rho^{(\alpha)}\boldsymbol{b}^{(\alpha)}\right]\mathrm{d}v \\ &\quad - \sum_{\alpha=1}^{2}\int_{\gamma^{(\alpha)}\setminus\gamma_{\mathrm{I}}}\boldsymbol{t}^{(\alpha)}\cdot\boldsymbol{\eta}_o^{(\alpha)}\mathrm{d}a - \int_{\gamma_{\mathrm{I}}}[\![\boldsymbol{\eta}_o]\!]\cdot\{\boldsymbol{\sigma}\cdot\boldsymbol{n}\}\,\mathrm{d}\gamma_{\mathrm{I}} + \int_{\gamma_{\mathrm{I}}}[\![\boldsymbol{\eta}_o]\!]\cdot\boldsymbol{\tau}_s\cdot\left([\![\boldsymbol{\phi}]\!]-\boldsymbol{\zeta}\right)\mathcal{V}_A\,\mathrm{d}\gamma_{\mathrm{I}} \\ &\quad - \int_{\gamma_{\mathrm{I}}}\left\{\left(\nabla^s\boldsymbol{\eta}_o:\mathbf{c}\right)\cdot\boldsymbol{n}\right\}\cdot\left([\![\boldsymbol{\phi}]\!]-\boldsymbol{\zeta}\right)\mathrm{d}\gamma_{\mathrm{I}} - \int_{\gamma_{\mathrm{I}}}\left\{\left(\nabla\boldsymbol{\eta}_o\,\boldsymbol{\sigma}\right)\cdot\boldsymbol{n}\right\}\cdot\left([\![\boldsymbol{\phi}]\!]-\boldsymbol{\zeta}\right)\mathrm{d}\gamma_{\mathrm{I}} = 0 \end{aligned} \tag{D-2}$$

$$\begin{aligned} r_{\theta}\left(\omega_o^{(\alpha)};\theta^{(\alpha)}\right) &= \sum_{\alpha=1}^{2}\int_{\mathrm{v}^{(\alpha)}}\left[\frac{1}{J}\rho_0 C_F\dot{\theta}^{(\alpha)}\cdot\omega_o^{(\alpha)} - r\cdot\omega_o^{(\alpha)}\right]\mathrm{d}v \\ &\quad + \sum_{\alpha=1}^{2}\int_{\mathrm{v}^{(\alpha)}}\left[\nabla\omega_o^{(\alpha)}\cdot\left(\frac{1}{J}\boldsymbol{k}_0(\theta)\right)\cdot\nabla\theta^{(\alpha)} + 3\kappa\left(\frac{1}{J}\beta_0\right)\cdot\theta\cdot\mathrm{tr}\left(\nabla\boldsymbol{v}\right)\cdot\omega_o^{(\alpha)}\right]\mathrm{d}v \\ &\quad + \sum_{\alpha=1}^{2}\int_{\gamma^{(\alpha)}\setminus\gamma_{\mathrm{I}}}\overline{q}^{(\alpha)}\cdot\omega_o^{(\alpha)}\,\mathrm{d}a - \int_{\gamma_{\mathrm{I}}}[\![\omega_o]\!]\cdot\left\{\frac{1}{J}\boldsymbol{k}_0(\theta)\cdot\nabla\theta^{(\alpha)}\cdot\boldsymbol{n}\right\}\mathrm{d}\gamma_{\mathrm{I}} \\ &\quad + \int_{\gamma_{\mathrm{I}}}[\![\omega_o]\!]\cdot\boldsymbol{\tau}_s^{\theta}\cdot\left([\![\theta]\!]\right)\mathcal{V}_A\mathrm{d}\gamma_{\mathrm{I}} - \int_{\gamma_{\mathrm{I}}}\left\{\left(\nabla\omega_o\cdot\frac{1}{J}\boldsymbol{k}_0(\theta)\right)\cdot\boldsymbol{n}\right\}\left([\![\theta]\!]\right)\mathrm{d}\gamma_{\mathrm{I}} = 0 \end{aligned} \tag{D-3}$$